



N U R S U L T A N K A I N B A Y E V

**I N F L U E N C E O F
A L U M I N A D O P A N T S O N
T H E M I C R O S T R U C T U R E
A N D I O N I C
C O N D U C T I V I T Y O F
S C A N D I A S T A B I L I Z E D
Z I R C O N I U M O X I D E
T H I N F I L M S**

D O C T O R A L D I S S E R T A T I O N

K a u n a s
2 0 2 2

KAUNAS UNIVERSITY OF TECHNOLOGY

NURSULTAN KAINBAYEV

INFLUENCE OF ALUMINA DOPANTS ON
THE MICROSTRUCTURE AND IONIC
CONDUCTIVITY OF SCANDIA STABILIZED
ZIRCONIUM OXIDE THIN FILMS

Doctoral dissertation
Natural Sciences, Physics (N 002)

Kaunas, 2022

This doctoral dissertation was prepared at Kaunas University of Technology, Faculty of Mathematics and Natural Sciences, Department of Physics during the period of 2017–2022. The studies were supported by the Research Council of Lithuania.

The doctoral right has been granted to Kaunas University of Technology together with University of Southern Denmark.

Scientific Supervisor

Prof. Dr. Giedrius LAUKAITIS (Kaunas University of Technology, Department of Physics, Natural Sciences, Physics, N 002).

Edited by: English language editor Brigita Brasienė (Publishing House *Technologija*), Lithuanian language editor Aurelija Gražina Rukšaitė (Publishing House *Technologija*).

Dissertation Defense Board of Physics Science Field:

Prof. Hab. Dr. Sigitas TAMULEVIČIUS (Kaunas University of Technology, Natural Sciences, Physics, N 002) – **chairperson**;

Prof. Dr. Liutauras MARCINAUSKAS (Kaunas University of Technology, Natural Sciences, Physics, N 002);

Dr. Šarūnas MEŠKINIS (Kaunas University of Technology, Natural Sciences, Physics, N 002);

Assoc. Prof. Dr. Pavels ONUFRIJEVS (Riga Technical University, Latvia, Natural Sciences, Physics, N 002);

Assoc. Prof. Dr. Tomas ŠALKUS (Vilnius University, Technological Sciences, Materials Engineering, T 008).

The official defense of the dissertation will be held at 10 a.m. on 14 December, 2022 at the public meeting of Dissertation Defense Board of Physics Science Field in M7 Hall at The Campus Library of Kaunas University of Technology.

Address: Studentu 48–M7, Kaunas, LT-51367, Lithuania.

Tel. no. (+370) 608 28 527; e-mail doktorantura@ktu.lt

Doctoral dissertation was sent on 14 November, 2022.

The doctoral dissertation is available on the internet <http://ktu.edu> and at the libraries of Kaunas University of Technology (K. Donelaičio 20, Kaunas, LT-44239, Lithuania) and University of Southern Denmark (Campusvej 55, Odense M, DK-5230, Denmark).

© N. Kainbayev, 2022

KAUNO TECHNOLOGIJOS UNIVERSITETAS

NURSULTAN KAINBAYEV

ALIUMINIO OKSIDO PRIEMAIŠŲ ĮTAKA
CIRKONIO OKSIDO, STABILIZUOTO
SKANDŽIO OKSIDU, PLONŲ DANGŲ
MIKROSTRUKTŪRAI IR JONINIAM LAIDŽIUI

Daktaro disertacija
Gamtos mokslai, fizika (N 002)

Kaunas, 2022

Disertacija rengtą 2017–2022 metais Kauno technologijos universiteto Matematikos ir gamtos mokslų fakultete, Fizikos katedroje. Mokslinius tyrimus rėmė Lietuvos mokslo taryba.

Doktorantūros teisė Kauno technologijos universitetui suteikta kartu su Pietų Danijos universitetu.

Mokslinis vadovas

prof. dr. Giedrius LAUKAITIS (Kauno technologijos universitetas, gamtos mokslai, fizika, N 002).

Redagavo: anglų kalbos redaktorė Brigita Brasienė (leidykla „Technologija“), lietuvių kalbos redaktorė Aurelija Gražina Rukšaitė (leidykla „Technologija“).

Fizikos mokslo krypties disertacijos gynimo taryba:

prof. habil. dr. Sigitas TAMULEVIČIUS (Kauno technologijos universitetas, gamtos mokslai, fizika, N 002) – **pirmininkas**;

prof. dr. Liutauras MARCINAUSKAS (Kauno technologijos universitetas, gamtos mokslai, fizika, N 002);

dr. Šarūnas MEŠKINIS (Kauno technologijos universitetas, gamtos mokslai, fizika, N 002);

doc. dr. Pavels ONUFRIJEVS (Rygos technikos universitetas, Latvija, gamtos mokslai, fizika, N 002).

doc. dr. Tomas ŠALKUS (Vilniaus universitetas, technologijos mokslai, medžiagų inžinerija, T 008).

Disertacija bus ginama viešame Fizikos mokslo krypties disertacijos gynimo tarybos posėdyje 2022 m. gruodžio 14 d. 10 val. Kauno technologijos universiteto Studentų miestelio bibliotekoje, salėje M7.

Adresas: Studentų g. 48–M7, Kaunas, LT-51367, Lietuva.

Tel. (+370) 37 30 00 42; el. paštas doktorantura@ktu.lt

Disertacija išsiųsta 2022 m. lapkričio 14 d.

Su disertacija galima susipažinti interneto svetainėje <http://ktu.edu> ir Kauno technologijos universiteto (K. Donelaičio g. 20, Kaunas, LT-44239, Lietuva) ir Pietų Danijos universiteto (Campusvej 55, Odense M, DK-5230, Danija) bibliotekose.

© N. Kainbayev, 2022

TABLE OF CONTENTS

LIST OF FIGURES	8
LIST OF TABLES	12
LIST OF ABBREVIATIONS	14
INTRODUCTION	15
1. LITERATURE OVERVIEW	19
1.1. Zirconium oxide based ceramics (ZrO_2).....	19
1.1.1. Zirconium dioxide (ZrO_2) crystal structure	19
1.1.2. Phase transformation of zirconia (ZrO_2).....	21
1.1.3. Doping of zirconia (ZrO_2)	23
1.2. Scandia stabilized zirconia (ScSZ)	26
1.3. Ternary system and dopant influence of ZrO_2 based ceramics.....	28
1.3.1. Ternary system of scandia and yttrium stabilized zirconia (ScSZ and YSZ).....	28
1.3.2. ZrO_2 based systems doping with CeO_2 and Ceria based systems	29
1.3.3. ZrO_2 based system doping with Y_2O_3 and CeO_2	30
1.3.4. ZrO_2 based system doping Sc_2O_3 and CeO_2	30
1.3.5. Influence of Al_2O_3 on ScSZ.....	31
1.4. Nanocrystalline solid ceramics	33
1.5. Thin films fabrication, conductive and microstructure properties of ScSZ thin films.....	34
1.5.1. Thin films deposition of electrolyte.....	34
1.5.2. Influence of technical parameters	36
1.5.3. Conductive properties of ScSZ thin films	37
1.5.4. Microstructure and densification of ScSZ thin films.....	38
1.6. Conductivity degradation of solid ceramics	39
1.7. Features of the crystalline structure nature and phase content of electrolytes based on ZrO_2 oxides	39
1.8. Conclusions	45
2. INSTRUMENTS AND METHODS	46
2.1. Electron beam evaporation	46
2.2. X-ray diffraction analysis (XRD)	48
2.3. Scanning electron microscopy (SEM)	49
2.4. Energy-dispersive X-ray spectrometry (EDS).....	50
2.5. Atomic force microscopy	51
2.6. X-ray photoelectron spectroscopy (XPS)	52
2.7. Raman spectroscopy	55
2.8. Electrochemical impedance spectroscopy (EIS).....	58
2.9. Thin film thickness via profilometer	60
RESULTS AND DISCUSSIONS	62

3.	STRUCTURE AND CONDUCTIVITY STUDIES OF (Sc ₂ O ₃) _{0.10} (ZrO ₂) _{0.90} SCANDIA-STABILIZED ZIRCONIA AND (Sc ₂ O ₃) _{0.10} (Al ₂ O ₃) _{0.01} (ZrO ₂) _{0.89} SCANDIA-STABILIZED ZIRCONIA CO-DOPED WITH ALUMINA THIN FILMS.....	62
	3.1. X-ray diffraction analysis of initial powders and investigation of the crystalline structure of formed ScSZ and ScSZAl thin films	62
	3.2. Analysis of Raman spectroscopy measurements data.....	67
	3.3. Investigation of electrical properties of the formed thin films (EIS) ..	70
	3.4. Results and conclusions	72
4.	STRUCTURAL AND ELECTROCHEMICAL PROPERTIES OF SCANDIA ALUMINA STABILIZED ZIRCONIA (Sc ₂ O ₃) _{0.06} (Al ₂ O ₃) _{0.01} (ZrO ₂) _{0.93} THIN FILMS.....	73
	4.1. Determination of elemental composition of Zr based thin films and influence on microstructure.....	73
	4.1.1. Elemental analysis (EDS) of ScAlSZ thin films formed at 300 °C and 600 °C substrate temperatures	73
	4.1.2. Elemental analysis (EDS) of ScAlSZ thin films formed at 450 °C substrate temperature.....	74
	4.2. Chemical analysis by X-ray photoelectron spectrometer XPS	75
	4.3. X-ray diffraction analysis and investigation of the crystal structure of formed thin films.....	78
	4.3.1. X-ray diffraction analysis of the initial powder.....	78
	4.3.2. X-ray diffraction analysis and crystallinity ScAlSZ thin films	78
	4.3.3. X-ray diffraction analysis of ScAlSZ thin films at different Al concentrations	80
	4.3.4. XRD analysis of thin films after thermal annealing	81
	4.4. Surface roughness analysis of formed thin films.....	82
	4.5. Analysis of Raman spectra	85
	4.5.1. Raman spectra analysis of ScAlSZ initial powder and formed thin films.....	86
	4.5.2. Raman spectra analysis of ScAlSZ thin films at different Al concentrations	89
	4.5.3. Raman spectra analysis of ScAlSZ thin films at different Al concentrations after thermal annealing	90
	4.6. Investigation of the surface morphology of thin films by scanning electron microscopy	91
	4.7. Investigation of electrical properties of formed thin films	95
	4.7.1. Impedance for ScAlSZ thin films.....	95
	4.7.2. Impedance for ScAlSZ thin films formed with different Al concentration.....	97
	4.8. Results and conclusions.....	101
	MAIN RESULTS	103
	CONCLUSIONS	105

SANTRAUKA	107
REFERENCES	130
CURRICULUM VITAE	149
LIST OF PUBLICATIONS AND SCIENTIFIC CONFERENCES	150
Appendix 1.	152

LIST OF FIGURES

Fig. 1.1. Types of crystal lattices of zirconia (a) monoclinic, (b) tetragonal, (c) cubic [11, 12]	19
Fig. 1.2. (a) Phase diagrams of the $ZrO_2 - YO_{1.5}$ systems on the degree of containing phases against the amount of stabilizing Y_2O_3 dopants and temperature, (b) fracture through a column of a coating deposited by EB-PVD [21]	22
Fig. 1.3. The interactions of ionic conductivity against the ionic ratio of the dopants [32]	24
Fig. 1.4. Phase diagram of (a) $Y_2O_3-ZrO_2$ and (b) $MgO-ZrO_2$ system [11]	25
Fig. 1.5. The ionic conductivity against the temperature of (a) ZrO_2 based ceramics and other solid ceramic systems (b) ZrO_2 stabilized with different dopants and co-dopants [40]	26
Fig. 1.6. Phase diagram of the scandia stabilized zirconia system [7, 33]	27
Fig. 1.7. Arrhenius plots of ScSZ ionic conductivity [52]	28
Fig. 1.8. Rare-earth oxide-stabilized ZrO_2 conductivity [52]	29
Fig. 1.9. Crystal structure of doped and un-doped ceria [64]	30
Fig. 1.10. The dopants ionic radius against the lattice parameter and ionic conductivity of ZrO_2 based systems [68]	31
Fig. 1.11. Arrhenius plot of YSZ/ Al_2O_3 ionic conductivity [52, 83]	32
Fig. 1.12. 16YSZ Single-crystal, bulk microcrystal, and nano-crystal electrical conductivity [52, 85, 86]	33
Fig. 1.13. Summary of the variations as function of the Al concentration (a) root-mean-square roughness (AFM) image and (b) grain size against the Al content in HfO_2 and ZrO_2 based thin films [106]	37
Fig. 1.14. (a) Electrochemical impedance spectroscopy (EIS) spectra and (b) activation energy of ScSZ electrolyte [108, 109]	38
Fig. 1.15. Ionic conductivity through the hopping mechanism in solid electrolytes [109, 111]	38
Fig. 1.16. (a) Fluorite structure, (b) the displacements of cations and anions is demonstrated by the Zr-shift structure model; at interstitials, the oxygens (in red) are displaced in six directions along the cubic axes, while the Zr atoms (turquoise) are displaced along eight cubic body diagonals relative to Y (purple) [123]	40
Fig. 1.17. Schematics of ZrO_2 based ceramics (a) fluorite structure and (b) rhombohedral phase of ZrO_2 based compound; large dark spheres are Zirconia and dopants ions; small spheres are oxygen ions [119]	41
Fig. 1.18. Raman spectra of the tetragonal (top) and monoclinic (bottom) phases of ZrO_2 [124]	42
Fig. 1.19. Different zirconia samples: (a) XRD patterns, (b) Raman spectra [122].	43
Fig. 1.20. Raman peak intensity ratio of $470\text{ cm}^{-1}/640\text{ cm}^{-1}$ peaks [127]	44
Fig. 2.1. (a) E-Beam Evaporator, EB-PVD 75 Kurt J. Lesker Company, Pittsburg, PA, USA, (b) vacuum chamber illustration of PVD system [137]	46
Fig. 2.2. XRD setup, Bragg–Brentano geometry [140]	49

Fig. 2.3. Sectional view of Scanning Electron Microscope Hitachi S-3400N column and internal components [141]	50
Fig. 2.4. Typical curve of the Van der Waals interaction force on the distance between the cantilever and the sample surface [142]	51
Fig. 2.5. (a) Overhead view of the instrument "PHI 5000 Versaprobe", (b) XPS Spectra of ZrO ₂ : overview and Zr 3d orbits, (c) schematic illustration of inner-shell ionization [144–146]	53
Fig. 2.6. ZrO ₂ based thin films XPS spectra: overview and Zr 3d orbits and deconvoluted peaks of O1s [147]	54
Fig. 2.7. (a) Energy level diagram for Rayleigh and Raman (Stokes and Anti-Stokes) scattering processes, the difference in the vibrational or rotational energy levels of that molecule is represented by $\Delta E = hv_{vi}$, adapted from [149]; (b) types of scattering processes [150]	55
Fig. 2.8. Illustration of the key components of Renishaw inVia confocal Raman microscope [151]	57
Fig. 2.9. (a) Ideal equivalent circuit and (b) impedance spectrum [52]	59
Fig. 2.10. Nyquist scheme of the complex impedance	59
Fig. 2.11. Profile of ScSZAl thin films	61
Fig. 3.1. X-ray diffraction patterns of initial powders: ScSZ and ScAlSZ [50]	63
Fig. 3.2. X-ray diffraction patterns of thin films obtained by evaporation process (a) ScSZ and (b) ScSZAl; deposition rate: 0.4 nm/s; substrate: alloy 600 [50]	64
Fig. 3.3. The lattice constant against the substrate temperature of ScSZ and ScSZAl thin films deposited on SiO ₂ substrates using 0.4 nm/s deposition rate	65
Fig. 3.4. Rietveld full-profile analysis of x-ray diffraction pattern from ScSZAl thin films; substrate: alloy 600; deposition rate: 0.4 nm/s [50]	65
Fig. 3.5. Dependency of the crystallite size on the substrate temperatures of ScSZAl thin films; substrate: alloy 600; deposition rate: by 0.2 nm/s to 1.6 nm/s [50]	66
Fig. 3.6. Raman spectra of initial powder (ScAlSZ - red, ScSZ- black) [50], monoclinic [130, 126, 131], tetragonal [10, 117, 118, 131, 133], rhombohedral [130, 10], cubic [130, 10, 126, 117]	67
Fig. 3.7. Raman spectra of (a) ScSZ and (b) ScSZAl thin films; substrate: alloy 600; deposition rate: 0.4 nm/s [50]; monoclinic [126, 130, 131]; tetragonal [10, 117, 118, 131, 133]; rhombohedral [10, 130]; cubic [10, 117, 126, 130]	68
Fig. 3.8. (a) Arrhenius plots of ScSZAl thin films, (b) vacancy activation energy of ScSZAl thin films against the substrate temperature; substrate: Al ₂ O ₃ ; deposition rate: 0.4 nm/s [50]	70
Fig. 4.1. Al concentration in ScAlSZ thin films against the deposition rate: (a) $T_d = 300$ °C and (b) $T_d = 600$ °C [102]	74
Fig. 4.2. XPS spectra of ScAlSZ thin films ($v_d = 0.2$ nm/s, $T_d = 300$ °C): (a) survey, (b) Zr O1s, (c) Zr 3d, (d) Al 2p, (e) Sc 2p [102]	76
Fig. 4.3. XPS spectra of ScAlSZ thin films: (a) Zr 3d, (b) O 1s, and (c) full surveys of ScAlSZ thin films with 1.6 at.% and 15.9 at.% Al content [159]	77
Fig. 4.4. X-ray diffraction (XRD) patterns of ScAlSZ powders [102]	78

Fig. 4.5. XRD patterns (measured at room temperature) of ScAlSZ thin films deposited on alloy 600 substrates using (a) 300 °C and (b) 600 °C substrate temperature and different deposition rate from 0.2 nm/s to 1.6 nm/s [102].....	80
Fig. 4.6. XRD patterns (measured at room temperature) of ScAlSZ thin films deposited on alloy 600 substrates using 450 °C substrate temperature and different Al concentration: 1.6 at.%, 3.8 at.%, 15.9 at.%, and 22.2 at.% [159].....	81
Fig. 4.7. XRD patterns of ScAlSZ thin films during annealing process containing different Al concentration: (a) 15.9 at.%, (b) 22.2 at.% [159].....	82
Fig. 4.8. 3D-images of top view and surface roughness (AFM) of ScAlSZ thin films: a) $c_{Al} = 1.6$ at.%, b) $c_{Al} = 3.8$ at.%, c) $c_{Al} = 15.9$ at.%, d) $c_{Al} = 22.2$ at.% [159].....	83
Fig. 4.9. 3D-images of top view and surface roughness (AFM) of ScAlSZ thin films after annealing: a) $c_{Al} = 1.6$ at.%, b) $c_{Al} = 3.8$ at.%, c) $c_{Al} = 15.9$ at.%, d) $c_{Al} = 22.2$ at.%.....	84
Fig. 4.10. Surface roughness of ScAlSZ thin films: ○ as-deposited and ○ after annealing [159].....	85
Fig. 4.11. Raman spectra of ScAlSZ initial powder [102], monoclinic [10, 50, 122, 126, 130–132, 133], tetragonal [10, 50, 117, 118, 122, 126, 131, 132, 133], rhombohedral [50, 130, 154], Cubic [10, 50, 117, 122, 126, 130–132].....	86
Fig. 4.12. Raman spectra of ScAlSZ thin films deposited on alloy 600 substrates using (a) 300 °C and (b) 600 °C substrate temperature and different deposition rate from 0.2 nm/s by 1.6 nm/s [102], monoclinic [10, 50, 122, 126, 130–133], tetragonal [10, 50, 117, 118, 122, 126, 131–133], rhombohedral [50, 130, 154], Cubic [10, 50, 117, 122, 126, 130–132].....	87
Fig. 4.13. Raman spectra of ScAlSZ thin films [159], monoclinic [50, 118, 122, 126, 130, 134], tetragonal [50, 118, 122, 126, 130, 132, 134], rhombohedral [50, 118], cubic [50, 118, 122, 126, 130, 134, 174].....	89
Fig. 4.14. Raman spectra measurements of ScAlSZ thin ceramic films deposited on Alloy600 in the annealing process (30–900 °C): containing 15.9 at.% and 22.2 at.% of Al consisted (a) range of 100 cm^{-1} to 550 cm^{-1} , (b) range of 100 cm^{-1} to 900 cm^{-1} [159], monoclinic [50, 118, 122, 126, 130, 134], tetragonal [50, 118, 122, 126, 130, 132, 134], rhombohedral [50, 118], cubic [50, 118, 122, 126, 130, 134, 174].....	91
Fig. 4.15. Topographic images view (SEM) of ScAlSZ thin films formed at 300 °C and 600 °C at different deposition rate: (a) 0.2 nm/s, (b) 0.4 nm/s, (c) 0.8 nm/s, (d) 1.2 nm/s, (e) 1.6 nm/s.....	93
Fig. 4.16. Cross section images view (SEM) of ScAlSZ thin films formed at (a) 300 °C substrate temperature and 1.6 nm/s deposition rate, (b) 600 °C substrate temperature and 1.6 nm/s deposition rate.....	94
Fig. 4.17. Topographic and cross section images view (SEM) of ScAlSZ thin films formed with different Al concentrations in 300 °C and 600 °C at different deposition rate: (a) 0.2 1.6 at.%, (b) 3.8 at.%, (c) 15.9 at.%, (d) 22.2 at.%.....	95
Fig. 4.18. Dependencies of $Im(Z) = Z''$ ($Re(Z) = Z'$) ScAlSZ formed thin films deposition rate of 0.4 nm/s at different temperatures.....	96
Fig. 4.19. The bulk ionic conductivity as a function of temperature at different deposition rates from 0.2 nm/s to 1.6 nm/s: (a) substrates temperature 300 °C, (b) substrates temperature 600 °C.....	96

Fig. 4.20. Nyquist plots of ScAlSZ thin films with 15.9 at.% and 1.6 at.% of Al at 560 °C temperature [159] 98
Fig. 4.21. Arrhenius plots of ScAlSZ thin films with different Al concentrations [159] 99

LIST OF TABLES

Table 1.1. The structural parameters of the various phases of ZrO ₂ and coordination [16]	20
Table 1.2. Lattice parameters of m-monoclinic, t-tetragonal, and c-cubic phases of ZrO ₂ of various ceramic systems [11]	20
Table 1.3. The temperature of the beginning of m-ZrO ₂ ↔t-ZrO ₂ and t-ZrO ₂ ↔m-ZrO ₂ phase transitions depending on the purity of the ZrO ₂ and stabilizing dopants [19]	21
Table 1.4. Ionic radii of metals in their oxides [35].....	24
Table 1.5. Element, coordination, and length of atoms [33].....	27
Table 1.6. Thin film formation methods and characteristic features of the methods [105]	35
Table 1.7. The main Raman peaks of ZrO ₂ based ceramics	44
Table 2.1. Characteristic of commercial initial powders [138].....	47
Table 2.2. Technical characteristics of e-beam evaporator.....	48
Table 2.3. The main technical parameters of X-Ray diffractometer “Bruker D8 Discover” (XRD, Bruker, Billerica, MA, USA).....	49
Table 2.4. SEM measurements scanning parameters.....	50
Table 2.5. Primary XPS regions of Zr 3d, Sc2p, Al 2p, O1s and binding energies of common chemical states [144]	53
Table 2.6. Basic operating parameters of XPS spectrometer.....	54
Table 2.7. InVia Renishaw general specifications, adapted from [152]	57
Table 2.8. Technical characteristics of Ambios XP-200 [160].....	61
Table 3.1. Dependency of the crystallite size on the substrate temperatures of ScSZAl thin films; substrate: alloy 600; deposition rate: by 0.2 nm/s to 1.6 nm/s ..	66
Table 3.2. Evaluation of containing phase ratio for ScSZ and ScSZAl thin films [50]	69
Table 3.3. Ionic conductivity (S/cm) of ScSZ and ScSZAl thin films deposited using different substrate temperature and 0.4 nm/s deposition rate [50]	71
Table 3.4. Activation energy (E_a , eV) of ScSZAl thin films deposited using different substrate temperature and 0.4 nm/s deposition rate.....	72
Table 4.1. The elemental composition (EDS) of the thin film surface of ScAlSZ, where v_d is the deposition rate, T_d - substrate temperature, and c_x - atomic concentration of investigating elements [102].....	73
Table 4.2. The elemental composition (EDS) of the thin film surface of ScAlSZ thin films formed at 450 °C substrates temperature, where v_d is the deposition rate, and c_x - atomic concentration of investigating elements [159]	75
Table 4.3. The dependence of crystallite size ($\langle d \rangle$, nm) with substrate temperature 300 °C and 600 °C at different deposition rate for thin films formed on alloy 600 .	79
Table 4.4. Surface roughness of ScAlSZ thin films ◦as-deposited and ◦ after annealing samples.....	85
Table 4.5. The ratio of cubic, tetragonal, and monoclinic phases in the ScAlSZ thin films [102]	88

Table 4.6. The ratio of monoclinic, tetragonal, and cubic phases of deposited ScAlSZ thin films [159]	90
Table 4.7. The ratio of monoclinic, tetragonal and rhombohedral, and cubic phases of annealed ScAlSZ thin films [159].....	91
Table 4.8. Bulk ionic conductivity (σ_{bulk}) at 800 °C temperature and their activation energy (E_a) of ScAlSZ thin ceramic films formed at different deposition rate	97
Table 4.9. Resistance and capacitance for grain and grain boundary process, the composition ScAlSZ thin films with 15.9 at.% and 1.6 at.% of Al at 560 °C temperature	98
Table 4.10. Bulk ionic conductivity (σ_{bulk}) at 520 °C and 800 °C temperatures and their activation energy (E_a) of ScAlSZ thin ceramic films formed at the different aluminum concentration (c_{Al}) [159].....	99
Table 4.11. Total conductivities of ZrO ₂ based compounds (σ_{tot}), highest total conductivities in the study ($\sigma_{3.8 \text{ at.}\%}$) [159]	100

LIST OF ABBREVIATIONS

AFM	Atomic force microscope
ALD	Atomic layer depositions
ASR	Area-specific resistance
CCD	Charge-coupled device
CSD	Chemical solution deposition
CVD	Chemical vapor deposition
DLC	Diamond-like coatings
EB-PVD	Electron beam physical vapor deposition
EDS	Electron dispersive spectroscopy
EIS	Electrochemical impedance spectroscopy
ESD	Electrostatic deposition
FSZ	Fully stabilized ZrO ₂
FWHM	Full width half maximum
PSZ	Partially stabilized ZrO ₂
PVD	Physical vapor deposition
PVD	Physical vapor deposition
Rwp	Weighted-profile R-factor
ScAISZ	Scandia Alumina stabilized zirconia (6% Sc ₂ O ₃ , 1% Al ₂ O ₃ , 93% ZrO ₂)
ScSZ	Scandia stabilized zirconia
ScSZAl	Scandia Alumina stabilized zirconia (10% Sc ₂ O ₃ , 1% Al ₂ O ₃ , 89% ZrO ₂)
SDC	Cerium oxide doped with samarium
SEM	Scanning electron microscope
SOFC	Solid oxide fuel cells
TZP	Tetragonal ZrO ₂ polycrystals
XPS	X-ray photoelectron spectroscopy
XRD	X-ray diffraction
YDC	Cerium oxide doped with yttrium
YSZ	Yttrium-stabilized zirconia

INTRODUCTION

The ceramics based on zirconium oxide stabilized by scandium (ScSZ) are widely used in fuel cells and gas sensors [1–3]. This is influenced by the combination of mechanical, thermal and electrochemical properties, such as: high strength, thermal stability, ionic conductivity, etc. The ceramics based on zirconia have unipolar conductivity due to the oxygen ion in a broad pressure and temperatures range. It is this property that made it possible to realize in oxygen sensors, electrochemical oxygen loads, and high-temperature fuel cells. The conductivity of ceramics based on zirconia is provided by the vacancy mechanism, while the increase in the number of vacancies and, consequently, the conductivity value is noted up to sufficiently high temperatures (up to 1200 °C).

One of the ways to improve the properties of solid ceramic is the additive (co-doping) to the ScSZ of the third component, which results in structural changes, and hence stability and mechanical properties as well as change in the mobility of ions and oxygen vacancies concentration [4–6]. The features of the conductivity and structure in solid solutions, containing three components, are complex and have not been studied well enough, even though the knowledge of the conventional two-component solid solutions properties, as well as the additional oxides properties, help in predicting the ternary solid solution properties [7]. Additionally, the predictions are strict for a single crystal system only. In connection with a significant fraction of grain boundaries in polycrystalline materials, the parameters of the solid solution structure may differ from the linear function of the parameters of the structure of the initial oxides. There are no detailed experimental statistics on the phase compositions of three-component oxide systems over a wide temperature range; there are data either from a small set of temperatures for each system over a wide range of compositions or data on certain small additives but for sufficiently broad-ranged conditions [8]. The third component addition can notably change the structure of the crystal lattice of the electrolyte and, consequently, the contribution of various changes to the conductivity. Thus, the stabilization of a cubic phase solid ceramics based on zirconium oxide simultaneously with cerium and scandium oxides or alumina and scandium oxides leads to leveling out the contributions of grain boundaries resistance to the entire conductivity of the ceramic [9, 10].

Based on the foregoing, the purpose of this work was to investigate the alumina dopants effect on the microstructure, crystallinity, and ionic conductivity of scandium stabilized zirconium oxide thin films that were formed by using e-beam deposition technique, i.e., to investigate such ternary systems as follows:

- $(\text{Sc}_2\text{O}_3)_{0.10}(\text{ZrO}_2)_{0.90}$ (10% Sc_2O_3 , 90% ZrO_2) Scandia Stabilized Zirconia (ScSZ)
- $(\text{Sc}_2\text{O}_3)_{0.10}(\text{Al}_2\text{O}_3)_{0.01}(\text{ZrO}_2)_{0.89}$ (10% Sc_2O_3 , 1% Al_2O_3 , 89% ZrO_2) Scandia Alumina Stabilized Zirconia (ScSZAl)

- $(\text{Sc}_2\text{O}_3)_{0.06}(\text{Al}_2\text{O}_3)_{0.01}(\text{ZrO}_2)_{0.93}$ (6% Sc_2O_3 , 1% Scandia Alumina
 Al_2O_3 , 93% ZrO_2) Stabilized Zirconia
 (ScAlSZ)

Research problem

The main problem of the research is the absence of a detailed analysis of physical and technological properties, the effect of the ratio of components, morphology of particles, phase composition, parameters of the crystal structure of phases in thin films of the Sc_2O_3 - ZrO_2 - Al_2O_3 systems obtained by the electron beam (e-beam) physical vapor deposition technique, controlling the substrate temperature and deposition rate.

Research aim and objectives

The **research aim** is to systematically and comprehensively investigate the influence of alumina dopants on the microstructure, crystallinity, and ionic conductivity of scandia stabilized zirconium oxide thin films that were formed by using e-beam deposition technique.

Research objectives:

1. To form thin ceramic films of Sc_2O_3 - ZrO_2 - Al_2O_3 systems using e-beam physical vapor deposition technique by changing the technological parameters, such as substrate temperature and deposition rate.
2. To study the influence of compositions of initial powders on phase compositions, crystal structures and microstructure of formed thin films evaporating $(\text{Sc}_2\text{O}_3)_{0.06}(\text{Al}_2\text{O}_3)_{0.01}(\text{ZrO}_2)_{0.93}$, $(\text{Sc}_2\text{O}_3)_{0.10}(\text{Al}_2\text{O}_3)_{0.01}(\text{ZrO}_2)_{0.89}$, $(\text{Sc}_2\text{O}_3)_{0.10}(\text{ZrO}_2)_{0.90}$ powders using e-beam deposition.
3. To study the crystal phase composition of the formed thin films of ZrO_2 - Sc_2O_3 and ZrO_2 - Sc_2O_3 - Al_2O_3 systems using Raman spectroscopy.
4. To study the crystallographic nature of formed thin films ZrO_2 - Sc_2O_3 and ZrO_2 - Sc_2O_3 - Al_2O_3 systems using X-ray diffraction analysis (XRD).
5. To study the ionic conductivity of the formed thin films of ZrO_2 - Sc_2O_3 and ZrO_2 - Sc_2O_3 - Al_2O_3 systems.

Scientific novelty and practical value

Although the two-component ZrO_2 - M_xO_y systems have been studied quite fully, the information on three-component oxide systems is extremely small. The structure and properties of three-component systems cannot be considered a strictly additive function of the structure and properties of individual components. The possible effect of the co-dopants on the structure and conductivity of grain boundaries should be noted separately, which is clearly manifested in the case of the Al_2O_3 - ScSZ system. The focus is on scandia-stabilized zirconia (ScSZ) systems to explore novel possibilities of control and investigate the phase stability and ionic conductivity of ScSZ by co-doping by alumina, which can be applied at different techniques as oxygen sensors, electrochemical oxygen deposits and high

temperature fuel cells. It is very important to cover a range of novel description of phase content and ionic conductivity properties of Sc_2O_3 - ZrO_2 - Al_2O_3 systems, because co-doping of a third component to ScSZ system can lead to a change in the structure and hence the mechanical properties and stability, as well as a change in the number and mobility of oxygen vacancies. Raman spectroscopy data has described the phase content and microstructural properties of ScAlSZ thin films that were formed using e-beam deposition in detail. Furthermore, in order to acquire an accurate understanding of the possibilities of changing the conductivity, there was separately considered the effect of the structure of a polycrystalline electrolyte on its conductivity. Moreover, as a new study, the effect of Aluminum concentration in ZrO_2 - Sc_2O_3 - Al_2O_3 systems on the surface roughness of thin films was formed by using e-beam deposition technique.

The key statements for the defense

1. The ScSZAl thin films cubic phase starts to stabilize and form at temperatures above 50 °C; the subsequent ramping of the temperature does not have any significant effect on the formation and the amount of the cubic phase.
2. Small displacement of atoms in the fluorite structure of ZrO_2 - Sc_2O_3 - Al_2O_3 systems can be determined by using Raman spectroscopy analysis.
3. The ScAlSZ thin films are uniform and with lower surface roughness at higher 15.9 at.% and 22.2 at.% Al concentrations.
4. Higher ionic conductivity can be achieved in thin films of ZrO_2 - Sc_2O_3 - Al_2O_3 systems formed at higher substrate temperatures of 600 °C and lower alumina concentrations.
5. The Raman peak position shift for cubic phase towards the higher wavenumber values are related to oxygen sub-lattice disorder associated by Sc_2O_3 and Al_2O_3 doping and co-doping, respectively.
6. The high concentration 15.9 and 22.2 at.% of Al co-dopant slows down the stabilization of cubic phase.

Dissertation structure

The structure of the dissertation is composed to follow the set research objectives and consists of 5 main chapters: an introduction, literature overview, instruments and methods, results and discussion, and conclusions. The first chapter is a literature overview of ZrO_2 based ceramics, covering its structure, materials, methods of formation. Chapter 2 presents the instruments and methods employed in this thesis. As a result of the complex nature of evaporating material and different approaches of investigating methods, it was decided to split the results part into two chapters. Chapter 3 and 4 present the obtained results with the following discussion. The conclusions of the main results are presented in the last chapter. The summary of the dissertation in Lithuanian language, a list of references, curriculum vitae of the author, list of publications and scientific conferences are presented at the end of the dissertation. The volume of the dissertation is 156 pages, including 60 figures, 30 tables, 22 numbered equations, and 203 references.

Contribution of the author and others

The author of this thesis made the major part of the experimental work: ceramic system depositions, investigations, measurements and calculations of obtained data. The author's contribution includes:

- Deposition of Sc_2O_3 - ZrO_2 - Al_2O_3 thin film ceramic systems and electrochemical impedance spectroscopy measurements in collaboration with Dr. D. Virbukas.
- Investigation and analysis data using scanning electron microscope in collaboration with Dr. M. Sriubas.
- Measurements, investigation, analysis of Raman spectra and numerical calculations of the obtained data using Raman spectroscopy.
- Investigation and analysis of the obtained data using atomic force microscope in collaborations with Dr. M. Sriubas.
- Overall analysis and interpretation of the obtained results; writhing scientific articles and presentations of the results in scientific conferences.

The results and measurements presented in this work were supervised by Prof. Dr. G. Laukaitis. The experiments and the methodology of the scientific plan were done in collaboration with all co-authors: Dr. K. Bočkutė, Assos. Prof. Ž. Rutkūnienė and Prof. Dr. G. Laukaitis. The investigation and analysis of deposition, electrochemical impedance spectroscopy measurements were done by Dr. D. Virbukas. The investigation and analysis X-ray diffraction, energy-dispersive X-ray spectroscopy, X-ray photoelectron spectroscopy were done in collaboration with Dr. M. Sriubas and Dr. D. Virbukas. The measurements of the Scanning electron microscope were made by Dr. M. Sriubas.

1. LITERATURE OVERVIEW

1.1. Zirconium oxide based ceramics (ZrO_2)

1.1.1. Zirconium dioxide (ZrO_2) crystal structure

Zirconium dioxide (ZrO_2) by nature is a polymorphic material existing in three crystal modifications: monoclinic phase m- ZrO_2 , tetragonal phase t- ZrO_2 , cubic phase c- ZrO_2 . All three-phase modifications are mutually reversible and transform one into another at a certain temperature: m- ZrO_2 monoclinic: (25–1370 °C) \leftrightarrow t- ZrO_2 tetragonal: (1370–2320 °C) \leftrightarrow c- ZrO_2 cubic: (2320–2680 \pm 50 °C melting point).

In addition to the above-mentioned phases of ZrO_2 , there is as well a special rhombohedral modification, which forms at high pressures of the order of 23×10^9 Pa and is metastable under normal conditions. The tetragonal phase exists at middle temperature ranges (1370–2320 °C) because of its monoclinic structure, low specific ionic conductivity, vacancies number, and high ionic conductivity above 1370 °C. The cubic phase, which is highly conductive forms only at 2320 °C, and the melting point is 2680 ± 50 °C. The crystallite lattice phase transition against the temperature is presented below (Fig. 1.1).

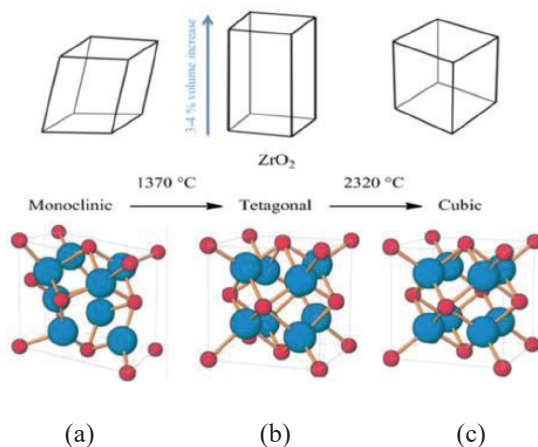


Fig. 1.1. Types of crystal lattices of zirconia (a) monoclinic, (b) tetragonal, (c) cubic) [11, 12]

Pure ZrO_2 oxide does not form in nature, and it is extracted from various complex minerals, baddeleyite and zircon $ZrSiO_4$, which is containing around ~65% of ZrO_2 oxide [13]. The density of baddeleyite crystals is 5.4–6.02 g/cm³, and it contain from ~96.5 to 98.5 wt% of ZrO_2 [14, 15]. The structural parameters of the various phases of ZrO_2 and coordination numbers of the Zr and O atoms, which is indicating the number of bonds that the central atom has in the coordination in a crystal, are presented in Table 1.1.

Table 1.1. The structural parameters of the various phases of ZrO₂ and coordination [16]

Phase	Space group	Lattice parameter, (Å)	T, (°C)	Coordination		
				Zr	O1	O2
Cubic	Fm3m	a = 5.139 V _{cell} = 135.62	2320–2680 ± 50	8	4	4
Tetragonal	P42/nmc	a = b = 3.629 c = 5.297 V _{cell} = 69.76	1370–2320	8	4	4
Monoclinic	P21/c	a = 5.169 b = 5.232 c = 5.341 Z = 4 V _{cell} = 144.44	25–1370	7	3	3

All three-phase modifications of ZrO₂ are mutually reversible. The crystal lattices of the monoclinic and tetragonal phases appear as derivatives of the cubic phase. Phase transition of t-ZrO₂ ↔ c-ZrO₂ occurs due to a specific rearrangement of the cubic oxygen sub-lattice (at which one-half of the oxygen atoms shifts relative to the other) and the unit cell elongation in the direction of displacement of oxygen atoms. Thus, in t-ZrO₂ ↔ c-ZrO₂ phase transitions, no essential restructuring occurs in the crystal lattice [17]. The ZrO₂ by the stabilizing level can be categorized into three groups: the first group FSZ is fully stabilized ZrO₂; the second group PSZ is partially stabilized ZrO₂; the third group TZP includes tetragonal ZrO₂ polycrystals [8].

The cubic phase of zirconia has a fluorite type crystalline structure (Fig. 1.1 c), and lattice parameters of cubic, tetragonal, and monoclinic phases of ZrO₂ are presented in Table 1.2. Spatial groups are “Fm3m” oxygen that has 4 coordination number; the zirconium in oxygen has 8 coordination numbers [18].

Table 1.2. Lattice parameters of m-monoclinic, t-tetragonal, and c-cubic phases of ZrO₂ of various ceramic systems [11]

Composition (mol%)	Lattice parameters (Å)						
	a _c	a _t	c _t	a _m	b _m	c _m	β
9.4Mg (PSZ)	5.080	5.077	5.183	5.117	5.117	5.303	98.91
8.4Ca (PSZ)	5.132	5.094	5.18	5.156	5.191	5.304	98.8
12Ce (TZP)		5.132	5.228	5.193	5.204	5.362	98.8
4.5Y (PSZ)	5.130	5.116	5.157				
3Y (TZP)		5.102	5.176				

1.1.2. Phase transformation of zirconia (ZrO₂)

The transformation of the phase t-ZrO₂ → m-ZrO₂ is a conversion martensitic type (displacive phase transition). Thus, the monoclinic phase is formed from the tetragonal by shear deformation and large volume increase of the whole unit cell. The large volume increases at t-ZrO₂↔m-ZrO₂ appear due to the large difference in densities between monoclinic and tetragonal modifications of ZrO₂. The shear deformation and large volume collectively establish the internal stress, which could lead to the cracking of the ceramics (fracture through a column). As mentioned above, during the t-ZrO₂↔c-ZrO₂ phase transitions, no essential restructuring occurs in the crystal lattice, and this is the main difference between these two-phase transformations of ZrO₂ [8]. In addition to the above-mentioned temperature dependents of phase transitions, there is one more factor, which is external pressure.

There are several fundamental ways to fully or partially stabilize tetragonal or cubic modifications of ZrO₂ to prevent polymorphic modifications or cracking of the ceramics, one of which is the introduction of stabilizing additives oxides (dopant). Stabilizing dopants can be metal oxides that form zirconium dioxide solutions of interstitial or substitution Y₂O₃, CaO, MgO, which became widely promoted dopants and more oxides with a very low solubility as several mole percent or not forming solid solutions based on ZrO₂, such additives include Al₂O₃. The temperature of the phase transition from m-ZrO₂↔t-ZrO₂ and t-ZrO₂↔m-ZrO₂ of zirconium oxide-based ceramics as a function of the type of the stabilizing dopants and the purity of the initial materials are presented in Table 1.3.

Table 1.3. The temperature of the beginning of m-ZrO₂↔t-ZrO₂ and t-ZrO₂↔m-ZrO₂ phase transitions depending on the purity of the ZrO₂ and stabilizing dopants [19]

Content	Phase transformation temperature, °C	
	<i>m</i> → <i>t</i>	<i>t</i> → <i>m</i>
ZrO ₂ (ex. pure)	1100	1023
ZrO ₂ (ex. pure)+MgO	1056	930
ZrO ₂ (ex. pure)+CaO	662	937
ZrO ₂ (ex. pure)+Y ₂ O ₃	530	796
Baddelyte+Y ₂ O ₃	512	730
ZrO ₂ (tech)+Y ₂ O ₃	524	N.d.
The content of stabilizing additives is 1%		

According to (Table 1.3), the temperature of m-ZrO₂ → t-ZrO₂ directly depends on the dopant; the temperature of the phase transformation of pure ZrO₂ is 1100 °C (t-ZrO₂ → m-ZrO₂ -1023 °C). During the alloying of stabilizing dopants, such as MgO, CaO, Y₂O₃, this value of t-ZrO₂ → m-ZrO₂ transition temperatures decreases.

The zirconia phase diagrams include many variations of the ZrO₂ - Y₂O₃ phase diagrams. Since the 1951 original phase diagram by Duwez, many works have been published regarding the ZrO₂ - Y₂O₃ system [8, 20, 21]. The experimental data that

have been obtained were very contradictory, and many of the phase diagrams are still not reliable enough. This has to do with the problem of temperatures below 1400 °C: the diffusion of ZrO₂ cations becomes so slow that the equilibrium is difficult to achieve [8]. The classic phase diagram of the ZrO₂-YO_{1.5} systems on the degree of containing phases against the amount stabilizing Y₂O₃ dopants and temperature are presented in Fig. 1.2 a.

The shown monoclinic phase (M) exists at low temperatures. With an increase in temperature above the region of the monoclinic phase appears mixed monoclinic and tetragonal phase so-called metastable tetragonal. The metastable line itself that is presented by equilibria of tetragonal to monoclinic, as the lines of phase boundaries (Fig. 1.2 a), was obtained by optimizing experimental calculations of the phase boundaries of phase equilibrium and indicated as T₀(T/M). At higher concentrations of yttrium oxide, there is a phase region presented by equilibria of cubic and tetragonal phases T₀(C/T). A further increase in the concentration of Y₂O₃ leads to the formation of a single-phase cubic ceramics (Fig. 1.2 a).

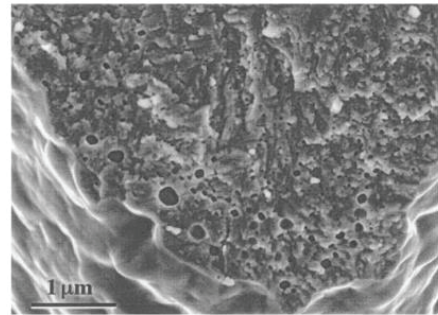
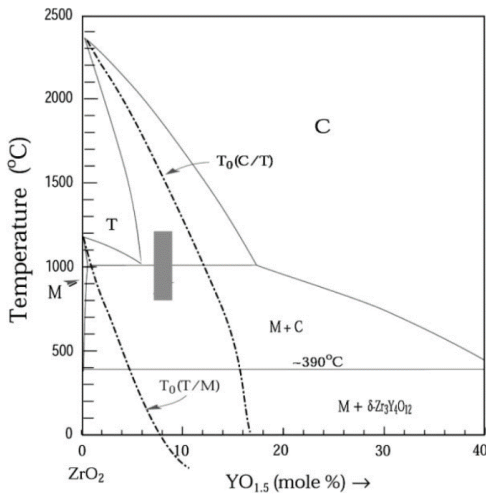


Fig. 1.2. (a) Phase diagrams of the ZrO₂ - YO_{1.5} systems on the degree of containing phases against the amount of stabilizing Y₂O₃ dopants and temperature, (b) fracture through a column of a coating deposited by EB-PVD [21]

The metastable tetragonal phase is formed during the cooling of materials. Hence, the metastable tetragonal phase could be the result of preventing diffusion processes by heating the samples in the region of the formation of the cubic phase, and then, a rapid cooling could lead to such phase. In this system, metastable tetragonal phase exists in the range of compositions from 0 to 8 mol% YO_{1.5}. The cross-sections of the columns that are resulting from fracturing indicate that the diffusional smoothing is restricted to the surface, where a distinct skin appears to have formed, while internal porosity just below the surface remains such as shown in Fig. 1.2 b [8, 21] The phase stabilization of ZrO₂ based ceramics is as well

possible by varying technological parameters of the deposition process, such as substrate temperature, methods of deposition, rate of deposition, etc.

1.1.3. Doping of zirconia (ZrO_2)

Ceramic materials, which are pretending to the role of oxygen ion-conducting electrolytes, must satisfy a lot of numerical requirements [22–24]: 1) high ionic values and low minimum electronic conductivity values in the working temperature ranges and the chemical potential of oxygen; 2) thermodynamic and thermo-mechanical stability in these states; 3) thermal and chemical resistance; 4) gas tightness; 5) high rates of interphase exchange of oxygen and lack of a blocking effect on the interface with electrode material and gas phases; 6) adequate mechanical properties of ceramic, ensuring its reliability in coatings, solid oxide fuel cell assembly (SOFC) and subsequent procedures [25]. When the electrolytes do not meet these requirements of porosity, gas diffusion occurs and will reduce the ionic conductivity of the electrolyte [26]. The most common solid electrolyte is zirconium dioxide that is stabilized by yttrium (YSZ) [24, 27, 28]. The latest studies have shown that some other candidates replace YSZ. Higher ionic conductivity might be attained by stabilizing the cubic phase of ZrO_2 by the simultaneous introduction of Sc^{3+} and other relatively small cations, such as Ce^{4+} or Al^{3+} [29, 30].

A fluorite structure is a better conductor with the initial higher oxygen vacancies concentration. Thus, doped fluorite has better conductivity when there is no strain and distortion in the cubic lattice [2, 31, 32]. In order to stabilize the zirconia before adding dopant, there are some factors that can affect the zirconia:

- minimum content of vacancies number;
- concentration, size, and charge of dopant ions;
- dopant oxide crystal structure;
- electronic energy levels [32, 33].

The materials, such as Sc_2O_3 , Y_2O_3 , MgO , and CaO , are the stabilizers added in a certain amount in the cubic zirconia solid solution with fluorite type structure, which improve the conductivity in oxygen ions [33]. Oxygen vacancy mechanics in ZrO_2 based ceramics could be presented as follows:



The ZrO_2 based ceramics, the addition of metal oxides with a valence and charge of an ion is less than that of zirconium, i.e., with a valence of two M^{2+} and M^{3+} three features of the structure and electrical conductivity of various complex oxide systems, will be discussed below.

The ZrO_2 oxide doping with the rare-earth and metal oxides, as CaO , MgO , Al_2O_3 , Y_2O_3 , Sc_2O_3 , Gd_2O_3 , Sm_2O_3 , Dy_2O_3 , CeO_2 , show a great impact on the crystalline structure parameters, such as lattice parameters and crystallite sizes. It as well enables the preserving of high-temperature ZrO_2 modification and prevents the polymorphic transformations modifications at high temperature to monoclinic at a low temperature because of the oxygen vacancies creation. Therefore, in the ZrO_2 - Y_2O_3 system, as an example, the tetravalent Zr^{4+} cations replacement with the trivalent Y^{3+} ions can result in one oxygen vacancy creation for every two yttrium

ions to balance the charges [4–6, 33].

Oxygen vacancies are created with the replacement of Zr^{4+} cations with the Gd^{3+} , Sm^{3+} , Al^{3+} , Dy^{3+} , Sc^{3+} , Y^{3+} , Ca^{2+} , and Mg^{2+} and assist in restoring the balance between the electrical charge of the system and allow O_2 ions migrations through the electrolyte. The structure can be fully stabilized to fluorite type by the addition of divalent dopants at a higher temperature around $\sim 1300\text{--}1500\text{ }^\circ\text{C}$ by 16 mol% MgO and 12–13, 20 mol% of CaO or trivalent dopants by 8.5 mol% of Y_2O_3 and above 9 mol% or 12.5–12.73 mol% of Sc_2O_3 that is presented as the ideal level of doping concentrations into the zirconia lattice [5, 31].

The required amount of dopant is Y_2O_3 around $\sim 2\text{--}3$ mol% and some rare-earth oxides for tetragonal phase stabilization. This is a metastable phase, and it has transformed to monoclinic when undergoing stress. The tetragonal phase is considered to have high toughness and strength [32, 34]. The selection of the dopants is mainly determined by the classification rule of Goldschmidt elements. The average ionic radii of the elements, according to the Shannon–Prewitt Ionic Radius systems, are provided in Table 1.4, and the interactions of ionic conductivity against the ionic ratio of the dopants are presented in Fig. 1.3 [32, 35].

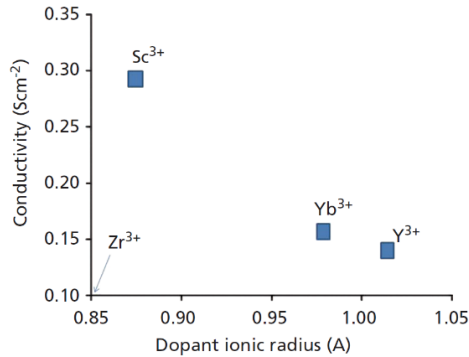


Fig. 1.3. The interactions of ionic conductivity against the ionic ratio of the dopants [32]

Table 1.4. Ionic radii of metals in their oxides [35]

Oxide	Ionic radius, (Å)
ZrO ₂	0.84
CeO ₂	0.97
CaO	0.10
MgO	0.72
Sc ₂ O ₃	0.75
Y ₂ O ₃	0.87
HfO ₂	0.83
Sm ₂ O ₃	0.96
Nd ₂ O ₃	0.98
Gd ₂ O ₃	0.94
Al ₂ O ₃	0.53

The stabilized tetragonal and stabilized cubic phases have a mixed composition of cubic and tetragonal and monoclinic precipitates sometimes and are known as partially stabilized zirconia. There is another phase around 3–7 mol% of M_2O_3 that is a dopant-rich metastable tetragonal, which has already been discussed. Hence, when trying to discuss some parts of the phase diagram, which are still not clear enough and are very contradictory, another version of the phase diagram of those systems was considered below (Fig. 1.4 a, b). When Y_2O_3 is dissolved and its concentration increases, a linear change in the values of the parameters of the tetragonal and cubic phases is observed (Fig. 1.4 a). During sintering, the final phase is as a cubic phase after the cooling of this phase to the room temperature. This rapid cooling is not usually required for ZrO_2 systems stabilized with Sc_2O_3 . The cubic and tetragonal phase could be reached at low concentrations of Sc_2O_3 dopant, and higher concentrations of Sc_2O_3 could be presented as β -rhombohedral structure. The phase transition limits those systems stabilized with Sc_2O_3 dopants that are from 8.2 to 10 mol%, β -rhombohedral to c-cubic [33, 34].

Zirconia has higher conductivity when it is doped with trivalent oxides or divalent oxides. However, more oxygen vacancies are formed when the dopant is divalent and has a lower ionic conductivity because of the higher defect-related tendency and has a lower thermodynamic stability of cubic-fluorite type solid solutions in ZrO_2 based systems. The ZrO_2 based system usually has lower conductivity and does not vary from composition to composition [34, 36–38]. However, according to the Y. Yin et al. [39], the replacement of Zr^{4+} cations with divalent CaO and MgO oxides has a great impact on the lattice parameters. It has been found that irrespective of temperature, CaO - ZrO_2 results in the increment of lattice parameters. However, in the MgO - ZrO_2 system, an increase in the amount of MgO, on the contrary, leads to a decrease in the lattice parameter. This circumstance is due to the reason that the radius of the Mg^{2+} cations is significantly smaller than the Zr^{4+} cations, as a result of which the lattice parameter c- ZrO_2 decreases as a result of substitution in the crystal lattice of Zr^{4+} [39]. The solid solution formation with a cubic structure in the ZrO_2 - MgO systems occurs with stabilizer content from 8–10 mol% and with a further increase (Fig. 1.4 b).

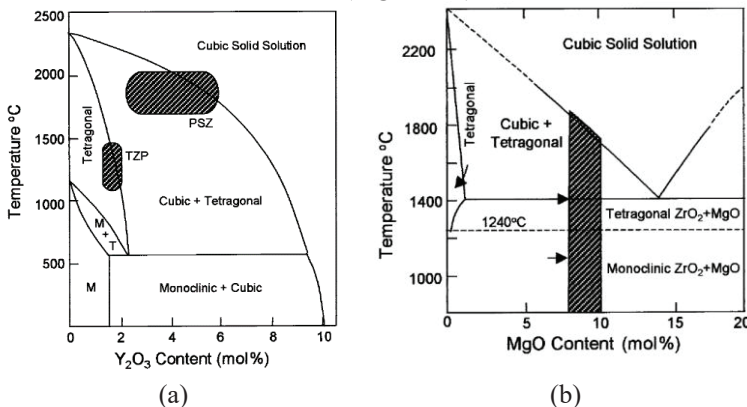


Fig. 1.4. Phase diagram of (a) Y_2O_3 - ZrO_2 and (b) MgO- ZrO_2 system [11]

1.2. Scandia stabilized zirconia (ScSZ)

ScSZ is considered a promising material for the application as an electrolyte at intermediate temperatures due to having one of the great electrochemical characteristics as higher ionic conductivity, lower electronic conductivity, unique electrical stability in reducing and oxidizing conditions. ScSZ has several times higher ionic conductivity at intermediate temperature 600–800 °C than that of YSZ systems and allows performing it at low temperatures. According to the literature [38], the 8ScSZ has an ionic conductivity of 0.159 S/cm, and for 8YSZ, it has 0.039 S/cm at 800 °C. The ionic conductivity against the temperature of ZrO₂ based ceramics doped and coped with different oxides and some other solid solutions that are presented in Fig. 1.5 a, b. The comparison of the conductivity properties shows that Sc₂O₃ ZrO₂ based ceramics is in the leading position.

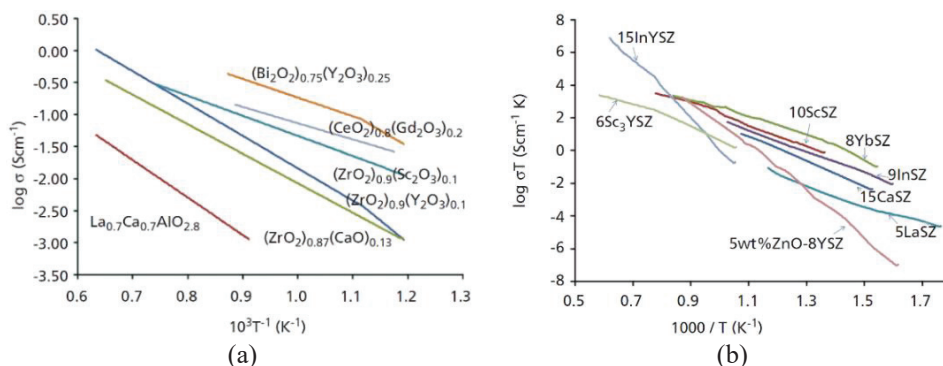


Fig. 1.5. The ionic conductivity against the temperature of (a) ZrO₂ based ceramics and other solid ceramic systems (b) ZrO₂ stabilized with different dopants and codopants [40]

The working intermediate temperature of ScSZ electrolytes is from 600 to 800 °C. The long-range materials can be utilized because of the operation at an intermediate temperature, such as stainless steel for interconnects. Furthermore, it reduces material degradation [41–44]. ScSZ can be used in electrochemical devices as catalytic membrane reactors and SOFCs because of its high ionic conductivity [45].

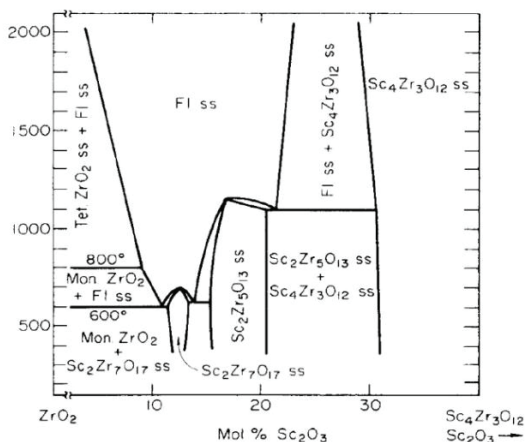
In such cases, some distortion occurs in the ZrO₂ crystal structure between the coordination number of 6 and 8. It can possess 8 coordination numbers of cubic fluorite structure, but mineral baddeleyite structure at room temperatures with 7 coordination number because of the borderline radius ratio (0.68 for 6 and 0.78 for 8) at high temperature 2000 °C [33]. In literature [46], it was mentioned that yttrium tends to have 8 coordination numbers, and zirconium tries to have 6 as scandium [33]. This behavior can be clarified by ionic radii sizes mentioned in Table 1.5.

Table 1.5. Element, coordination, and length of atoms [33]

Element, coordination	Length, pm
Y ³⁺ (8 coordinate)	115.9
Zr ⁴⁺ (6 coordinate)	86
Sc ³⁺ (6 coordinate)	88.5

Phase diagram of ScSZ

Scandium oxide Sc₂O₃ by ionic radius (Table 1.4) is presented as one of the best dopants for ZrO₂ oxide-based ceramics. There is a significant number of phase diagrams of this system, which sometimes contradict one another. Fig. 1.6 presents one of phase diagrams, which explains the nature of the temperature against the electrical properties of the ZrO₂-Sc₂O₃ system. It was reported in the literature [47] that there are same coordination number of Sc³⁺ and Zr⁴⁺, and the driving force is smaller for these cations distribution. The equilibrium phase diagram of Sc₂O₃-ZrO₂ has no clear agreement, and the literature [7] reported the Scandia stabilized zirconia equilibrium phase diagram.

**Fig. 1.6.** Phase diagram of the scandia stabilized zirconia system [7, 33]

When two scandium atoms are incorporated, one vacancy is formed [48]. The cubic phase cannot be stable at equilibrium below the temperature of 650 °C, and the phase transformation can occur on thermal cycling. Phase transformation is the main concern for ScSZ. When the acceptor-type dopants fraction is near to the lowest required fraction for stabilizing the cubic phases completely, the ZrO₂-based systems show maximum ionic conductivity. High conductivity has been observed in the pure cubic phase rather than the mixed phases [33, 34, 44].

1.3. Ternary system and dopant influence of ZrO₂ based ceramics

1.3.1. Ternary system of scandia and yttrium stabilized zirconia (ScSZ and YSZ)

ScSZ possesses a unipolar conductive nature, only as long as the oxygen ions are over the broad range of pressures and temperatures [3, 49]. The ionic conductivity of ZrO₂ based ceramics induced by oxygen vacancy is dominant sufficiently to the higher temperatures up to 1200 °C [50]. The Arrhenius Plots of ScSZ ionic conductivity is presented in Fig. 1.7. Therefore, the ionic conductivity of ScSZ can be higher than yttria-stabilized zirconia (YSZ) and can compete with it at intermediate temperatures of 600 °C [40]. The addition of dopants (co-doping) in small concentrations up to 1 to 2 mol% in ScSZ can help in increasing the amount of Scandia in ZrO₂ while maintaining the cubic structure correspondingly. The dopants added in ScSZ to avoid the phase transformation and hold the cubic fluorite structures in Scandia doped zirconia normally are Yb₂O₃, Bi₂O₃, CeO₂, CaO, MgO, and Ga₂O₃ Mn₂O₃, or Al₂O₃ [29, 49, 51].

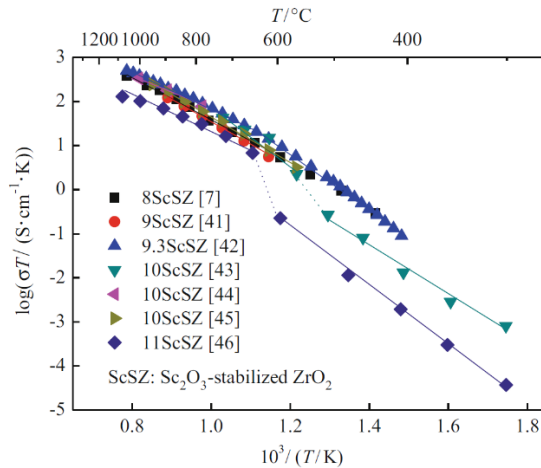


Fig. 1.7. Arrhenius plots of ScSZ ionic conductivity [52]

It was reported [53] that the conductivity of grains was observed to increase with 0 to 4% mol of x value in the $(\text{ZrO}_2)_{0.88}(\text{Y}_2\text{O}_3)_x(\text{CaO})_{0.12-x}$ system, but then it tends to decrease slightly with the increase in x value. Gong et al. [54, 55] have observed that $(\text{ZrO}_2)_{0.88-0.04x}(\text{Y}_2\text{O}_3)_{0.08x}(\text{CaO})_{0.12(1-x)}$ system conductivity has improved at higher temperatures but reduced at lower temperatures because of the defect formation. Fonseca et al. [56, 57] have observed that the MgO has a solubility limit in 10 mol% 8YSZ, and when more than 15 mol% MgO is added with 3YSZ, it shows stabilized ZrO₂ and MgO. The MgO can react with Al₂O₃ and SiO₂ impurities to create distinct MgAl₂O₄ and Mg₂SiO₄ grain in the electrolytes, respectively, and the grain boundaries of zirconia avoid the current blockings. The composite electrolyte conductivity is dependent on the phase continuity: if the phase continuity is high, the conductivity is high as well [52, 58].

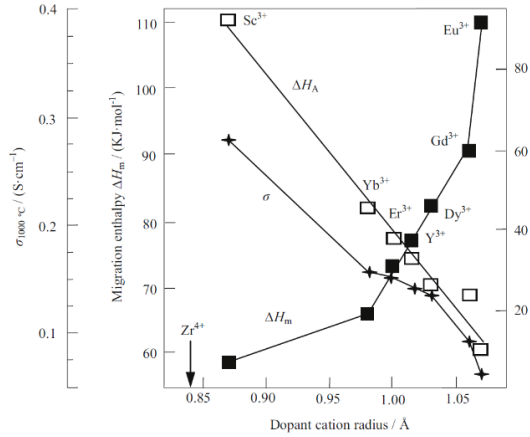


Fig. 1.8. Rare-earth oxide-stabilized ZrO_2 conductivity [52]

The structural stability of YSZ can be improved by adding 5 to 20mo% CeO_2 , but can as well decrease the ionic conductivity [59]. ZrO_2 based ceramics stabilized by doping with Y_2O_3 or CeO_2 may become as an oxide ion conductor [60] or oxide-ion/electron conductor [61] with change in composition, temperature, and fabrication method. Rare-earth oxide-stabilized ZrO_2 conductivity is presented in Fig. 1.8. The addition of CeO_2 content can increase the electronic conductivity of ZrO_2 -based materials. The densification can be decreased by adding a small amount of Fe_2O_3 in 8YSZ, and it can as well decrease the sintering temperature. In the YSZ lattice, the occupied position of Fe is depending on the vacancy concentrations of oxygen and phase at room temperature. The grain growth and densification of Y_2O_3 and Fe_2O_3 stabilized ZrO_2 are occurred by Fe^{3+} interstitial diffusion mechanism. The grain growth at grain boundaries is obstructed by Fe^{3+} segregation [52, 62].

The mechanical properties can be controlled by the segregation of vitreous phase at the grain boundary. The mechanical properties of zirconia ceramics are affected positively by sintering. Alumina is considered one of the most effective in enhancing the mechanical properties of zirconia-based materials by varying chemical composition at grain boundaries.

1.3.2. ZrO_2 based systems doping with CeO_2 and Ceria based systems

Ceria is a ceramic material that has a fluorite crystal structure and shows excellent stability up to the melting point. Oxygen vacancies are created within its crystal structure when doped with divalent or trivalent cations. However, these are important for the conduction of oxygen ions through the ceramic material. The presence of vacancies helps oxygen ions to insert in the lattice of the ceramic in oxygen-rich environments and extract in a low oxygen environment from it [63].



Fig. 1.9. Crystal structure of doped and un-doped ceria [64]

These properties have various applications in different technologies for example catalysts, chemical sensor and gas purification membrane. The application of this material is mainly focused on the use of this ceramic as an electrolyte in SOFC [63]. Furthermore, this material has applications as insulators, high refractive index materials and anticorrosive coatings. The properties of CeO_2 can vary under the influence of added dopants, stoichiometry change, fabrication technique and process parameters, such as pentavalent dopant produces p-type conductive material. The crystal structure of doped and un-doped Ceria is presented in Fig. 1.9. Vanadium doped ceria (CeVO_4) has application as counter electrodes for Li^+ ions storages in smart windows [65].

Pure ceria has a low oxygen ion conductivity of 5×10^{-5} S/cm at 600 °C [40]. The ionic conductivity is higher in non-stoichiometric CeO_{2-x} as compared to the pure ceria, because it has more oxygen vacancies. The normally used dopants materials are CaO, Na_2O , SrO, Y_2O_3 , Gd_2O_3 , La_2O_3 , and Sm_2O_3 [66]. Sm_2O_3 and Gd_2O_3 doped ceria has shown high potential for O^{2-} conductors at intermediate temperature. It has three times greater ionic conductivity than yttrium stabilized zirconium oxide (YSZ) from 500 °C to 600 °C temperature range with improved mechanical, thermal, and chemical compatibility with anodes and cathodes [67].

1.3.3. ZrO_2 based system doping with Y_2O_3 and CeO_2

Ceria-based systems have higher electrochemical characteristics due to the crystalline structure changes in the crystal lattice of cerium oxides as a result of the replacement of Ce^{4+} ions by Zr^{4+} ions. The difference between ionic radii in such systems plays beneficial role: the ionic radius of Ce^{4+} is ~ 0.97 Å, and the ionic radius Zr^{4+} is ~ 0.84 Å. The addition of Ce^{4+} in YSZ systems could lead to extreme distortion in the conduction paths, which reduces the activation energy for the diffusion of oxygen ions in the lattice. Hence, there is a possibility to create favorable conditions for oxygen-ion mobility. However, Y_2O_3 - ZrO_2 - CeO_2 systems that cerium oxide can be in different oxidation states Ce^{4+} and Ce^{3+} , and this feature allows low oxygen partial pressures at intermediate operating temperatures, hence, high levels of electronic conductivity [68, 69].

1.3.4. ZrO_2 based system doping Sc_2O_3 and CeO_2

(Sc_2O_3) - (ZrO_2) (CeO_2) systems have the highest ionic conductivity (0.066 S/cm) compared to $(\text{ZrO}_2$ - $\text{CeO}_2)$ based systems co-doping with other dopants, such

as Nd (0.009 S/cm), Gd (0.018 S/cm), Y (0.027 S/cm), and Yb (0.039 S/cm) [68]. However, co-doping of these component systems shows general decrease in ionic conductivity than two-component systems [68]. According to the Kimpton et al. [68] at intermediate operating temperature, the ionic conductivity of three-component ($\text{Sc}_2\text{O}_3\text{-ZrO}_2\text{-CeO}_2$) systems was 0.066 S/cm, i.e., two times lower compared to the two-components ($\text{ZrO}_2\text{-Sc}_2\text{O}_3$) systems, which was 0.12 S/cm. At three-component systems, the difference in the ionic ratio has a significant impact on the choice of additives (co-dopants) and stabilizing the structure. In addition, it was stated by Kimpton et al. [68] that lattice parameters are increased by increasing the ionic ratio of the dopants. The dopants ionic radius against the lattice parameter and ionic conductivity are presented in Fig. 1.10.

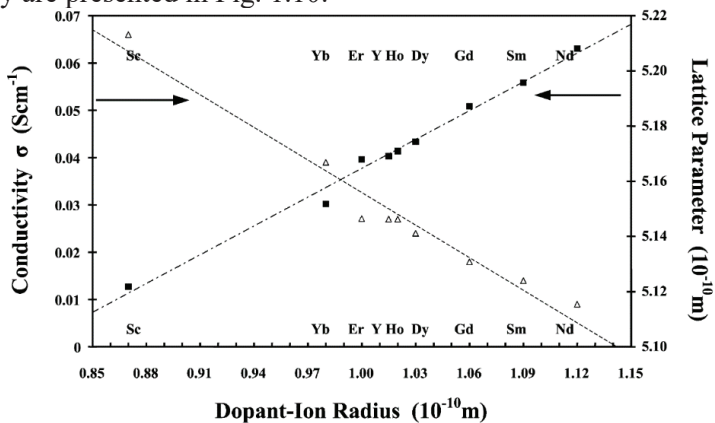


Fig. 1.10. The dopants ionic radius against the lattice parameter and ionic conductivity of ZrO_2 based systems [68]

1.3.5. Influence of Al_2O_3 on ScSZ

Many investigations have been conducted on the study of mechanical, electrical, and thermal properties of zirconium oxide-based systems co-doped with Al_2O_3 oxides [70–72]. Butler, Drennan et al. [72] state that the co-doping of Al_2O_3 oxides in stabilized zirconia-based systems influence the microstructure. It was suggested that Al_2O_3 acts as a scavenger for SiO_2 [73] and removes the siliceous phase from the vicinity of grain boundaries. The small amount of Al_2O_3 oxide addition around 0.5 mol% is soluble in stabilized zirconia. It was reported that the addition of Al_2O_3 has two dual functions, i.e., the resistivity of grain and grain boundaries increases, and the grain growth is restricted below the solubility limit, while above the solubility limit of Al_2O_3 , the resistivity decreases, and the grain growth is inhibited [74]. The addition of Al_2O_3 content up to 20 wt% resulted in an increase in strength and thermal conductivity of the composite, but the coefficient of thermal expansion decreased with increasing Al_2O_3 content [75, 76].

It has been observed that 1 wt% Al_2O_3 content can slightly increase the electrical conductivity and then a monotonic reduction with the increase of Al_2O_3 content follows. The required amount of co-dopants, such as CeO_2 and Y_2O_3 , to

stabilize the ScSZ is a well around $\sim 1\text{--}2$ mol%. The main role of co-dopings to the Scandia doped zirconia is to prohibit the phase transition and retain the cubic structure. The difference on ionic radius is playing a very important role in the selection of the second dopant. However, Scandium oxide Sc_2O_3 is presented as one of the best dopants for ZrO_2 oxide-based ceramics, when two scandium atoms are incorporated, one vacancy is formed [48]. The phase transformation is the main concern for ScSZ. Fluorite cubic phase of ScSZ system is not stable below the temperature of 650°C , and phase transformation can occur on thermal cycling. Ishii et al. [29] reported that the co-doping of aluminum by 0.4 at.% reduce the phase transition temperature from rhombohedral to cubic phase and make it stable. It has been reported [29] that the co-doping of ScSZ with a small amount of Sm^{3+} and Yb^{3+} reduce the phase transition temperature from rhombohedral to cubic structure; however, the phase transition temperature compared to aluminum co-doping was in the same range, i.e., around $500\text{--}550^\circ\text{C}$ [29].

Al_2O_3 is as well known as a cleaning agent of SiO_2 impurities that are present at grain boundaries. SiO_2 is normally believed to be toxic for YSZ and can decrease ionic conductivity at grain boundaries [52, 77, 78]. However, it is controversial whether the silica glassy phase segregate completely or partially at the grain boundaries and covers the grains [79]. It has been observed that the amorphous SiO_2 layer is re-precipitated around the grain of ZrO_2 while cooling from higher temperatures, but it is not created at the grain boundary [80]. SiO_2 can decrease the ionic conductivity of ZrO_2 -based electrolytes but can be increased by densification, sintering, super-plastic deformations, and co-doping with alumina. The addition of Al_2O_3 into stabilized zirconia material can decrease the detrimental effect and enhance the conductivity at grain boundaries. However, it has been observed that Al_2O_3 can have an adverse effect on the grain boundaries because of the impurities, which are introduced in powder synthesis and sintering processes [81]. The Arrhenius plot of YSZ/ Al_2O_3 systems ionic conductivity is shown in Fig. 1.11. The resistance of grain boundaries is as well closely associated with the trace siliceous phase distribution. In addition, trace Al_2O_3 reduces the sintering temperature of the sample and improves the hardness and fracture toughness of zirconia-based materials [82].

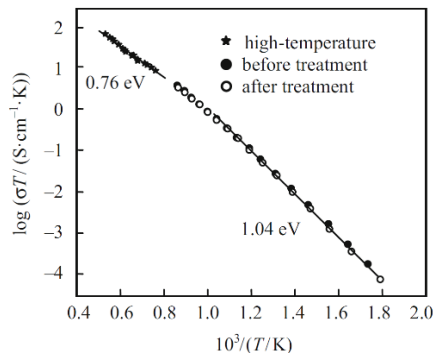


Fig. 1.11. Arrhenius plot of YSZ/ Al_2O_3 ionic conductivity [52, 83]

1.4. Nanocrystalline solid ceramics

Nano-crystalline oxides have exceptional electrical properties and chemical reactivity, unlike microcrystalline oxides. However, the previous investigations have shown that the conductivity of nano-crystalline materials has no considerable changes in comparison to the microcrystalline oxides. For instance, YSZ fully tetragonal phase ceramic with the grain size of $\sim 35\text{--}49\text{ nm}$ are observed to have no improvement in conductivity, and it can be the result of not small enough grain size [84]. It is well-known that the grain size has a major influence on the conductivity. Fig. 1.12 demonstrates the 16YSZ thin ceramics with the thickness of $\sim 1\text{ micron}$ fabricated on alumina, and the sapphire substrates through polymer spin coating method have improved conductivity against the grain size, while small grain size resulted in a high conductivity [85, 86]. The nano-crystalline YSZ film conductivity was one to two orders of magnitude higher than single-crystalline and bulk microcrystalline YSZ. It was suggested that the resistance of grain boundary determines the high-frequency resistance of nanocrystalline YSZ, and a remarkable reduction in the resistance of grain boundary appears because of the decrease in the number of impurities segregating at the grain boundary [52, 87].

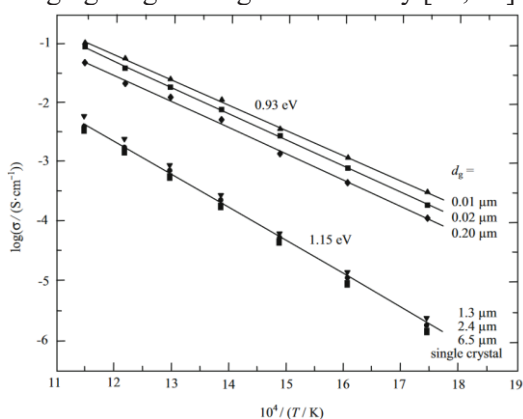


Fig. 1.12. 16YSZ Single-crystal, bulk microcrystal, and nano-crystal electrical conductivity [52, 85, 86]

Moreover, the ionic conductivity could be improved by the thin film thickness regulations. For instance, 9.5 mol% of YSZ thin ceramics were fabricated by pulsar laser ablation on MgO substrate. The in-plane ionic conductivity of these films was better at $>60\text{ nm}$ thickness. It has been reported as well that thin films have a positive trend towards interfacial conductivity with decreasing thin film thickness as a considerable contribution of MgO and YSZ. The interfacial conductivity was three orders magnitude higher at 1.6 nm thickness, compared to the lattice conductivity [52, 88]. The 8.7 mol% CaSZ/ Al_2O_3 multilayer thin films that are fabricated from pulsed laser deposition have conductivity that is parallel to the hetero-phase boundary improved by two orders of magnitude for a $0.78\ \mu\text{m}$ to 40 nm layer thickness: it could be due to the quite higher ionic mobility in the disordered core areas of incoherent interface than in the bulk [52, 89].

1.5. Thin films fabrication, conductive and microstructure properties of ScSZ thin films

1.5.1. Thin films deposition of electrolyte

There are many deposition methods for the formation of thin-film electrolytes for SOFCs with the purpose to minimize transport resistance from the solid electrolytes. These methods have two categories, i.e., vacuum methods and non-vacuum methods [90].

Vacuum methods: vacuum deposition methods could be split into two methods systems, i.e., chemical vapor deposition (CVD) and physical vapor deposition (PVD), which have defined control on film microstructure, growth rate, and stoichiometry during deposition [90, 91]. The sputtering and atomic layer depositions (ALD) are particularly used to prepare thin-film electrolytes for SOFCs [92–94]. However, these methods have some limitations, for example, slower process speed, strict deposition conditions, and high costs [95].

Non-vacuum methods: these depositions methods are comparatively simpler than vacuum process and may be classified as powder-based processes or solution-based processes for thin-film deposition. The wet chemical methods, as chemical solution deposition (CSD), have some benefits, for example, high deposition areas, low fabrication costs, and simple stoichiometry control [96]. There are other methods that are normally used for deposition, such as spin coating, dip coating, screen printing, and electrostatic deposition (ESD) [97–99].

It is known that sintering in a vacuum or atmosphere of inert gas has a stabilizing effect similar to that of stabilizing by additive, because additional vacancies of oxygen are formed in the ZrO_2 . Lattice leads to the stabilization of high-temperature phases due to the deficiency of oxygen [100, 101].

E-beam Physical Vapor Deposition for Solid Electrolyte (Ceramics): the phase transitions and stabilization properties ZrO_2 based ceramics have not been investigated well. The thin film properties are robustly dependent on the fabrication process and process parameters. E-beam physical vapor deposition process is considered a suitable method for creating ceramic layers. High temperature is the result of collisions of electrons and the material in crucibles and can be increased up to 3000 °C or more. The melting temperature of most of the metal oxides is lower than this temperature [102]. E-beam evaporation technique can adjust the deposition rate over a wide range, which is not possible with other methods for the metal oxides, such as the magnetron sputtering method. Thin films are normally dense and homogeneous by the e-beam method. Furthermore, the thin-film structures are not dependent on the initial material structure, for example, ZrO_2 based electrolytes are evaporated by partial dissociations. However, there are some limitations in this method, such as materials having various melting temperatures being evaporated at various rates. Therefore, the deposition of a thin film is hard with the required compositions with multi-component materials [103, 104]. Thin film formation methods and characteristic features are presented in Table 1.6.

Table 1.6. Thin film formation methods and characteristic features of the methods [105]

Thin film formation methods				
Method	Method implementation conditions of the methods	Main types of coatings	Advantages	Disadvantages
Electron beam evaporations	Working environment: vacuum 10^{-4} – 10^{-2} Pa; reagent. gases: N ₂ , O ₂ , CH ₄ .	Metallic coatings: Al, Ag, Cu, Ti, Cr, Ni, Co, Si. Ceramic coatings: Sc ₂ O ₃ , Al ₂ O ₃ , TiO ₂ , SiO ₂ , ZrO ₂ , ZrO ₂ / Y ₂ O ₃ .	High deposition rate; possibility of obtaining thin and thick coatings (1–2 up to 200 microns); high purity of coatings (minimum impurities); homogeneity.	Low degree of loading by materials in vacuum chamber.
Vacuum arc evaporation	Working environment: vacuum 10^{-3} – 10^{-2} Pa; reagent. gases: N ₂ , O ₂ , CH ₄ ; P = 0.01^{-1} Pa; T = 300–600 °C; evaporation of metals in the cathode spot of an arc discharge; deposition of highly ionic coatings.	Metal coatings: Ti, Zr, Hf, Cr, Ta, Ni, Co, Si. Ceramic coatings: TiO ₂ , ZrO ₂ . Nanocomposites: TiAlN / Si ₃ N ₄ , AlCrN / Si ₃ N ₄ .	High deposition rate; relative simplicity of technical implementation; effective ionic cleaning of products before coating; high properties of ceramic coatings.	The presence of a microdroplet metallic phase in the structure of coatings; relatively high deposition temperatures.
Magnetron sputtering	Working environment: pure gases: Ar, N ₂ , O ₂ , CH ₄ ; P = 0.05^{-1} Pa; T = 60–6000 °C.	Ion sputtering of metals in a magnetron discharge. Full range of metal coatings: Al, Ag, Au, Cu, Zn, Sn, Cd Ti, Zr, Ni, Co, Si, etc. Ceramic coatings: ZrN, CrN, TiAlN, TiO ₂ , ZrO ₂ , Al ₂ O ₃ , SiO ₂ . Nanocomposite	Dense micro-(nano-) crystalline structure of metal and ceramic coatings in complete absence of the droplet phase; possibility of coating heat-sensitive materials at low temperatures; the widest range	Relative complexity of technical implementation of method in the production of reactive (ceramic) coatings; relatively high cost of equipment.

		s: 3D: TiAlN / Si ₃ N ₄ , TiN / BN, AlCrN / 2D: TiN / NbN, TiN / CrN.	of coatings for various purposes; high deposition rate; high properties of metal and ceramic coatings.	
Laser vaporization (ablation)	Working environment: vacuum 10 ⁻⁵ -10 ⁻³ Pa; evaporation of materials of various compositions by a laser pulse of duration from μs to fs.	Coatings for microelectronic s: Sb ₂ S ₃ , As ₂ S ₃ , SrTiO ₃ , BaTiO ₃ , GaAs High performance diamond-like coatings (DLC).	Obtaining coatings of complex compounds; high purity of coatings (minimum impurities).	Complexity of implementation.

1.5.2. Influence of technical parameters

There is a considerable effect of technical parameters of e-beam deposition method, such as deposition rate, crystallinity, or substrate temperature on the properties of solid electrolytes. In the Al co-doped ScSZ, the concentration of Al changes non-homogeneously with increasing substrate temperature and deposition rates. At higher temperatures, the concentration of Al is slightly higher for thin films deposition. As the deposition rate increases, the crucible temperature increases as well and influences the changes in the vapor concentrations of elements, atoms and atomic clusters, and the evaporation rates. As the melting temperature reaches different elements, the concentration of Al decreases, and Al₂O₃ evaporates faster than Sc₂O₃ and ZrO₂. Furthermore, the fabrication process of thin-films is longer at lower deposition rates versus higher deposition rates. Therefore, at higher deposition, the smaller Al amount evaporates for the same thin-film thickness. At a higher deposition rate, the crystallinity is higher, i.e., the higher is the peak intensity, the larger are the crystallites. Thin-film crystallinity is correlated with the Al concentration and substrate temperatures. Crystallinity is increased with the decrease in Al concentration and an increase in substrate temperatures. At the grain boundaries of ScSZAl crystallites, the amorphous phases of Al or Al₂O₃ are formed, which act as impurities. Furthermore, the influence of Al concentrations on the crystallite Structure and Electrical Properties was studied by Yean Woo et al. [106]. However, according to the Yean Yoo et al., the grain growth is obscured at higher Al concentrations. The crystallinity reduces, and the root-mean-square roughness from the AFM images with an increase in Al concentration in ZrO₂ thin films prepared by the atomic layer deposition method are presented in Fig. 1.13 a, b [102, 106].

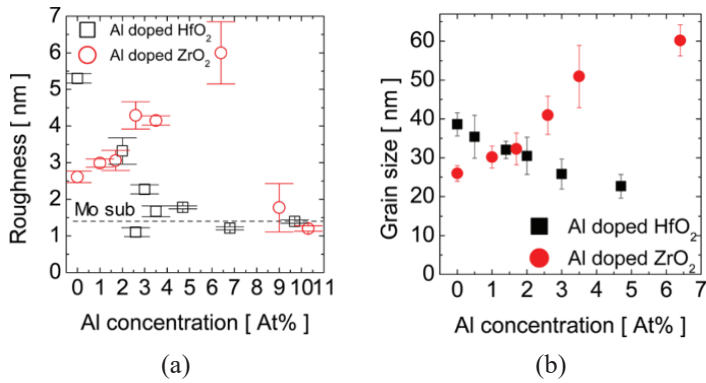


Fig. 1.13. Summary of the variations as function of the Al concentration (a) root-mean-square roughness (AFM) image and (b) grain size against the Al content in HfO₂ and ZrO₂ based thin films [106]

1.5.3. Conductive properties of ScSZ thin films

The fabrication of solid electrolytes in the thin film increases the ion conductivity towards lower operating temperatures of SOFCs. The solid ceramic electrolytes coatings thickness is normally from 10 to 100 μm . A thin-film electrolyte ($<1 \mu\text{m}$) reduces the Ohmic loss and is a practical method of reducing the operating temperatures of SOFCs, for instance, reduced solid electrolytes size can decrease the ohm resistance to effectively increase the oxide ions diffusions. Shin et al. [95] reported that post-heat treatment time for nano-sized electrolytes can be reduced by using the spin-coating process for ScSZ ceramic electrolyte thin film fabrication with the invention of the sintering method by flashlight irradiation. Yun et al. [107] reported that ionic conductivity, densification, and stability of the thin-film structure can be increased by introducing nickel additives as modifications in ScSZ electrolytes.

Solid electrolyte cells are capable of maintaining up to 500 hours of output at intermediate operating temperatures. Cho et al. [108] reported that thin-film ScSZ electrolyte of 280 nm thickness fabrication by sputtering method at room temperature can successfully establish the cubic phase crystal structure of the ScSZ electrolyte. The higher ionic conductivity of solid electrolytes can be achieved by the fabrication of the nano-sized grain of the ScSZ electrolytes; the grain size can be influenced by the excellent activation energy of the solid electrolytes. In Fig. 1.14 a, the electrical impedance results of the ScSZ electrolyte resistance are low, and the ionic resistance is reduced by increasing the operating temperature; therefore, the ionic conductivity is increased. In addition, the ionic conductivity results in good activation energy of ScSZ electrolyte, which implies that the cubic structure of the solid electrolyte is sustained during the operating condition (Fig. 1.14 b) [109].

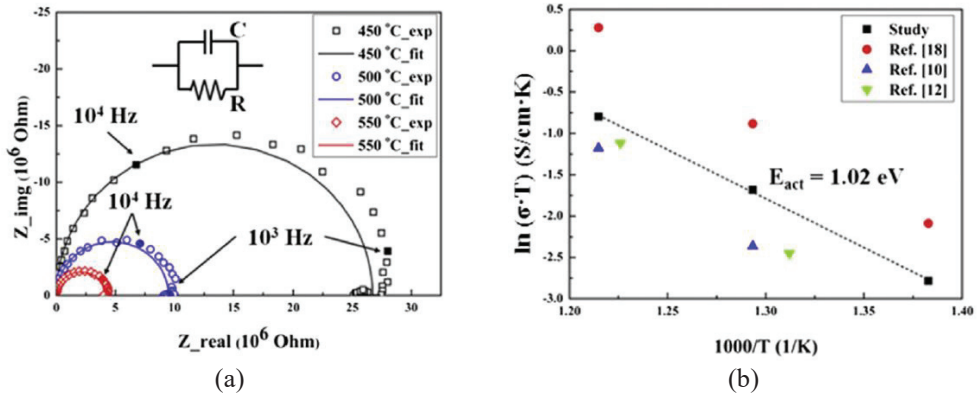


Fig. 1.14. (a) Electrochemical impedance spectroscopy (EIS) spectra and (b) activation energy of ScSZ electrolyte [108, 109]

1.5.4. Microstructure and densification of ScSZ thin films

The grain boundary formation is an important factor to maintain the high densification and compact structure of the ScSZ electrolytes. The grain sizes and grain boundaries of the ScSZ electrolytes can affect the ion conductivity and performance of the cell. The illustration of ionic conductivity through the hopping mechanism in solid electrolytes is shown in Fig. 1.15. The smaller size of particles of ScSZ powder can increase the resistance of grain boundaries, which considerably enhances the ionic conductivity of solid electrolytes at low temperatures. Hence, the ScSZ electrolyte can endure the ionic conductivity stability longer in the lower operating temperatures of intermediate temperature SOFCs [109, 110]. Therefore, the electron beam deposition (EBVD) method for the thin film fabrication can provide high densification and compact and dense microstructure ScSZ electrolytes by higher deposition rates and larger deposition areas of the solid electrolytes. The thin structures of the ScSZ electrolyte are beneficial for providing a simple path to ionic diffusions. For this reason, the ionic conductivity of the ScSZ electrolyte is improved by the e-beam deposition method [23, 109].

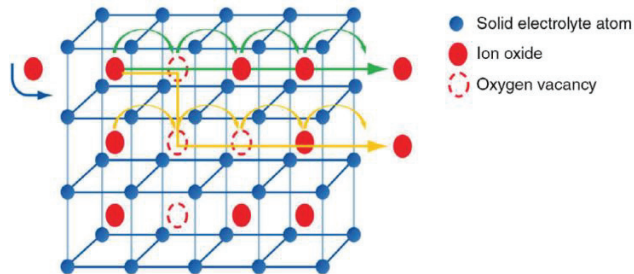


Fig. 1.15. Ionic conductivity through the hopping mechanism in solid electrolytes [109, 111]

1.6. Conductivity degradation of solid ceramics

The oxide-ion conductivity of ZrO₂-based electrolyte can be decreased in a long-term exposure to high temperatures, and it impacted the stability and accuracy of the sensor [112]. It is common for YSZ to encounter this phenomenon at temperatures of about 1000 °C with the yttria content of less than 9 mol%. For instance, the 8YSZ conductivity degradation is decreased by >50% after annealing at 1000 °C for 1000 hrs. This degradation effect decreased with the increase of yttria content and disappeared in the case of 10YSZ [113]. The impedance spectrum measurement showed that the grain boundary impedance remains unchanged and the bulk impedance increased after annealing at about 1000 °C [112]. The highly pure 8YSZ degradation is associated with bulk mechanisms. The conductivity degradation results from a decrease in mobile minority charge carriers' concentrations and/or their mobility. Bulk conductivity degradation mechanisms are proposed, which include a continuous phase transformation to a less-conductive phase, and vacancy trapping or "short-range ordering"; thus, the charge carrier in the electrolyte is not moved under Coulombic attractions between vacancies, positive charge fields, and the Y'_{Zr}, negative charge fields [52, 114]. However, the experimental verification is not sufficient enough, and most of the proposed mechanisms remain controversial. This is because of the complicated phase behaviors and multiple formations of metastable phases that are structurally similar; in the ZrO₂-based electrolytes, for example, ScSZ and YSZ are hard to be differentiated [52].

1.7. Features of the crystalline structure nature and phase content of electrolytes based on ZrO₂ oxides

The microstructure (crystalline structure) and phase content of zirconium-based ceramics can have an equally important effect on the electrical properties than the deposition method or technological parameters. Therefore, the study of the microstructure is a fundamentally important task. Zirconia-based electrolytes are polycrystalline material and their properties are significantly influenced by their microstructure, grain size, and grain boundaries. The characterization of the crystalline structure and phase composition of the ceramic electrolytes could be carried out by X-ray diffraction methods. As a result of XRD analyses, the peaks corresponding to the cubic phase could overlap with the peaks, which appear in the rhombohedral phase [50, 115, 116]. In these circumstances, a complementary analysis is required, and Raman spectroscopy analysis as an option that may be employed to appropriate solutions [117, 118]. Raman spectroscopy analysis is a powerful, highly integral, and sensitive method for analyzing the crystal structure of ceramic materials. Raman spectroscopy is the most sensitive to the change of the polarizability of oxygen cation vibrations and specific vibrational of containing atoms and molecules.

Despite the fact that the crystallographic of ZrO₂-based cubic ceramics has been studied in many works, their structure is still being determined ambiguously and is the subject of controversy. In several works, c-phase containing

polycrystalline and single crystals of Zirconium oxide-based ceramics was investigated by using X-ray diffraction methods and Neutron-scattering investigation [26, 116, 119–122].

The modeling of any displacement of single crystals anions and cations in the direction relative to each other $\langle 111 \rangle$ or $\langle 100 \rangle$ have been presented by Argyriou et al. [120]. It has been noted that some anions occur along the $\langle 100 \rangle$, $\langle 111 \rangle$, or both directions, but sometimes, a shift of cations along the $\langle 111 \rangle$ direction was observed, and they would be identified by the form of diffuse scattering or large values of the isotropic temperature factor [26, 120]. The pure ZrO_2 fluorite structure and ZrO_2 shift structure present the displacements of cations and anions illustrated in Fig. 16 a, b.

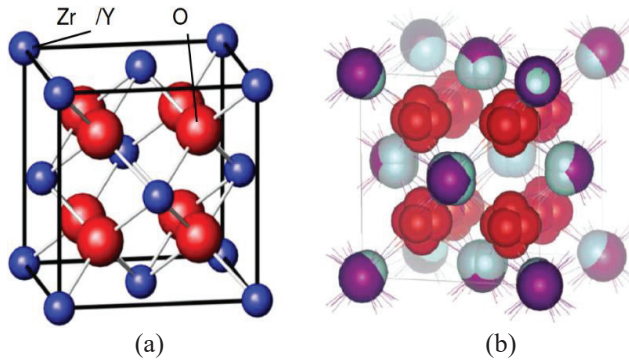


Fig. 1.16. (a) Fluorite structure, (b) the displacements of cations and anions is demonstrated by the Zr-shift structure model; at interstitials, the oxygens (in red) are displaced in six directions along the cubic axes, while the Zr atoms (turquoise) are displaced along eight cubic body diagonals relative to Y (purple) [123]

Goff et al. [119] notes that such displacement of oxygen in the anionic sublattice is a characteristic of the pure ZrO_2 phase, and such small displacement of oxygen atoms in the fluorite structure cannot be determined by using X-ray diffraction measurements. Therefore, as mentioned above, Raman spectroscopy is very sensitive to specific vibrational mode of fluorite containing ceramics atoms and molecules. However, in this work, Raman spectroscopy was used to reveal the features of the phase composition. Based on Clausen et al. [119], it was suggested that the appearance of additional forbidden reflections at the fluorite structure are presented as the results of the collective displacement of the anions along with the $\langle 111 \rangle$ directions. In this case, the cubic structure is preserved, but the structure has the $P43m$ -space group symmetry due to the loss of the face-center symmetry. It was suggested that the appearance of additional forbidden reflections at the fluorite structure should be presented as the results of the collective displacement of the anions, along the $\langle 111 \rangle$ directions. In this case, the cubic structure is preserved, but the structure has the $P-43m$ -space group symmetry due to the loss of the face-center symmetry.

The nature of the displacements manifests itself at a higher concentration of dopant: the displacement of orientations of $\langle 100 \rangle$: ions increases up to (0.31 Å),

while low dopant concentrations are (0.25 Å), and at $\langle 111 \rangle$ orientations, the opposite trend has been observed. Perhaps, this behavior is associated with anharmonic vibrations in the fluorite lattice. It is generally accepted that these vacancy pairs are the main structural phenomenon in the anion-deficient ordered fluorite-related structure. The inclusion of vacancy pairs and the presence of surrounding relaxation field displace fragments of the fluorite lattice. The other two types of defects correspond to the space group of the rhombohedral phase: one of them is at $\langle 111 \rangle$ fluorite related structure orientations, the next is presented at $\langle 112 \rangle$ preferential orientations (Fig. 1.17 a, b) [119].

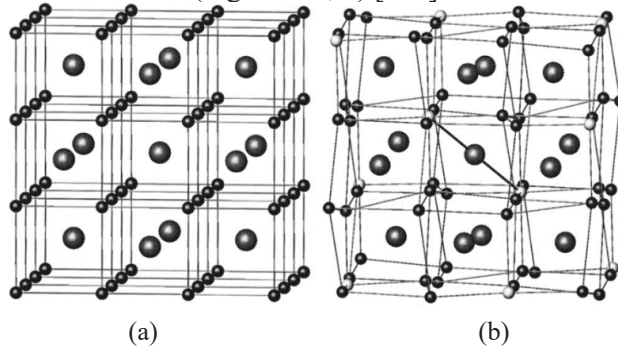


Fig. 1.17. Schematics of ZrO_2 based ceramics (a) fluorite structure and (b) rhombohedral phase of ZrO_2 based compound; large dark spheres are Zirconia and dopants ions; small spheres are oxygen ions [119]

The appearance of the Raman spectrum for different ceramic materials based on zirconium oxide and their various phase modifications, such as cubic, monoclinic, tetragonal, or rhombohedral, have their own unique characteristic Raman spectrum corresponding to each phase. The advantages and specific nature of the Raman spectrometry is the analysis of any displacement or strain and monitoring of influence of chemical composition on the structural properties. The Raman spectrum is as a set of prints, each of which accurately identifies the presence of a particular material or other compounds in a material. The Raman method allows calculating the content of this phase, and it is as well possible to qualitatively control the crystallization of materials by analyzing the Raman shift and peak intensity.

It is well known that the metal oxides are not always present in the crystalline form. Usually, Raman peaks, which are expressed by broad peaks, could be explained by the presence of the amorphous phase. Still, it might be corresponding to the crystallite structure content of these materials. The phase transition from the amorphous stage to the crystalline structure is one of the most important factors in the observation of ceramics. The amorphous stage could be explained by the distortion of interatomic bond angles. The long-range order is lost; however, the nearest-neighbor interactions could lead to the peak shift, and many of such particular vibrations (distortions) could be combined, and respectively, broad peaks might appear. In some cases, ZrO_2 could present multiple forms. It may result in atomic motion, which is higher than the interatomic spacing, and in these cases, lattice symmetry changes occur during the crystalline phase transition. While the

ZrO₂ atom sits on symmetry site, it may be presented as a cubic phase [124]. The Raman spectra and main characteristic peaks of tetragonal-ZrO₂ and monoclinic -ZrO₂ phases are presented in Fig. 1.18.

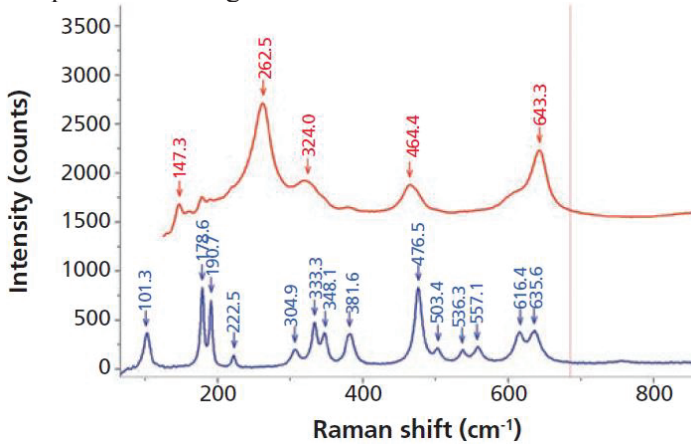


Fig. 1.18. Raman spectra of the tetragonal (top) and monoclinic (bottom) phases of ZrO₂ [124]

In several works, m-ZrO₂, t-ZrO₂, β -ZrO₂, and c - ZrO₂ phase containing polycrystalline and single crystals of ZrO₂-based ceramics have been investigated by using Raman spectroscopy measurements. Raman spectra of ZrO₂ have multiple forms of Raman peaks (Fig. 1.19 a). Literature data have shown that Raman peaks describing m- monoclinic nanocrystalline ZrO₂ were represented by 18 Raman modes [16]: (9A_g + 9B_g) that are pure monoclinic ZrO₂ Raman peaks expressed at 183, 301, 335, 381, 476, 536, 559, 613, 636 cm⁻¹ [122]. The strong bands were represented by 183, 335, and 476 cm⁻¹. According to the group theory, t-tetragonal ZrO₂ could be presented by six Raman active modes (A_{1g} + 2B_{1g} + 3E_g) and pure tetragonal ZrO₂ expressed at 149, 224, 292, 324, 407, 456, and 636 cm⁻¹. Raman bands for pure c-cubic phase were presented at narrow peak at 145 cm⁻¹, and broad peaks centered at 246 cm⁻¹, 301 cm⁻¹, 436 cm⁻¹, and 625cm⁻¹. According to Basahel et al. [122], some peaks belong to the tetragonal phase as well as the cubic phase, expressed at 145 cm⁻¹, and the cubic should be explained by the presence of intensive peaks, which should appear between 607 cm⁻¹ and 617 cm⁻¹. Furthermore, the presence of 625 cm⁻¹ peaks at c-ZrO₂ might be a consequence of disorders in the oxygen sublattice, while the t-ZrO₂ based samples display strong Raman peaks that were observed at 292 cm⁻¹ and 636 cm⁻¹ due to the symmetry reduction. The Raman mode cubic phase contains only one Raman active vibration peak that is presented at F_{2g} mode, expressed between ~605 and 630 cm⁻¹ [122]. The results that have been reported are quite in good agreement with the XRD results, which are presented in Fig. 1.19 b.

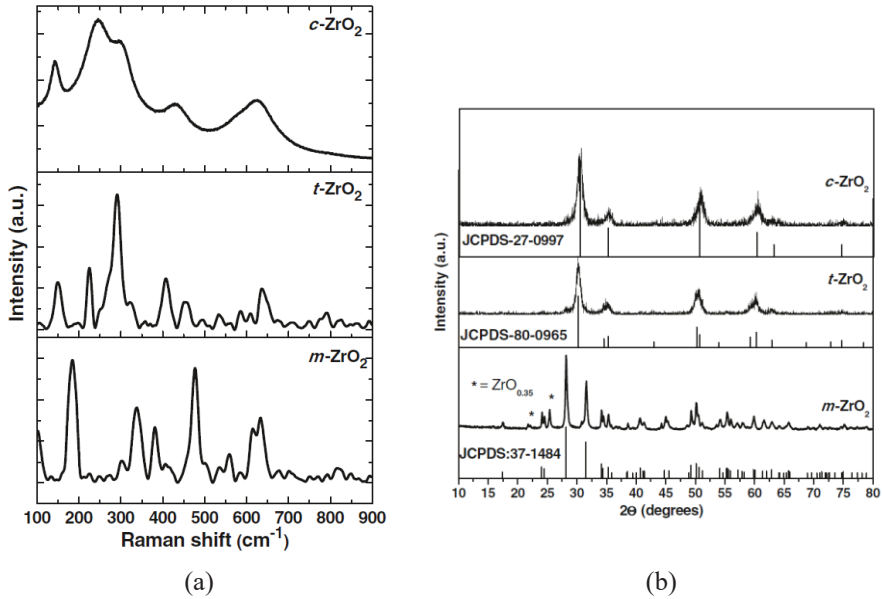


Fig. 1.19. Different zirconia samples: (a) XRD patterns, (b) Raman spectra [122]

The phase transition boundary of ZrO_2 is a disputed issue, and many factors could affect it, such as, technological parameters, sintering temperature, and stabilizing dopant concentrations [125]. For instance, during the increasing of dopant concentrations of Y_2O_3 , the intensity of bands, corresponding to the mixed phases, decreases continuously, and at 8 mol% Y_2O_3 , they completely disappeared, and only one broad peak was expressed at 607 cm^{-1} , which corresponds to the F_{2g} mode of cubic phase [126]. The boundary (level) of the transition from the t-tetragonal phase to the c-cubic phase is a controversial issue. According to Yashima et al. [127], a full phase transition from tetragonal lattice to the cubic fluorite structure occurs while the relationship of Raman bands at 640 and 470 cm^{-1} is 0. They have stated that the value of the ratio between the ~ 470 and 640 cm^{-1} modes is associated with the rearrangement of the vacancy positions of oxygen; as a result, a cubic phase could be formed [125]. As stated by Yashima et al. [127], the range of 10–11 mol% Y_2O_3 of this ratio tends to zero (Fig. 1.20).

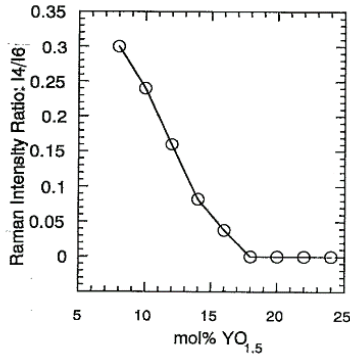


Fig. 1.20. Raman peak intensity ratio of 470 cm⁻¹/640 cm⁻¹peaks [127]

The substitution of ZrO₂ by Sc₂O₃ dopants could lead to the crystal lattice increases of zirconium oxide: a larger number of oxygen vacancies are formed [128], which affect the length and energy of the Zr - O bond [125]. The vacancies of oxygen are consolidated around the zirconium atoms and not near the scandium atoms. The oxygen vacancies increases can lead to disorders in the oxygen sublattice, which may easily be detected by a shift in the Raman spectra. High disorders in the oxygen sub-lattice can result in a violation of the selection rules, and therefore, allows the appearance of additional modes corresponding to the same changes of oxygen vacancy, which are forbidden for the cubic fluorite structure [129]. The main Raman peaks of ZrO₂ based ceramics are presented in Table 1.7. Furthermore, other corresponding Raman peaks of ZrO₂ based ceramics could be found by following references in Table 1.7.

Table 1.7. The main Raman peaks of ZrO₂ based ceramics

Phase	Peak position, cm ⁻¹	Raman mode	References
m - monoclinic	97, 115, 176, 179, 183 190, 191, 194, 223, 335, 347, 353, 354, 380, 473, 500, 536, 559, 564, 608	(9A _g + 9B _g) B _{1g}	[16, 122, 126, 130–132]
t - teragonal	147, 149, 155, 256, 259, 262, 264, 315, 321, 386, 422, 458, 480, 484, 485, 551, 600, 640, 643	(A _{1g} + 2B _{1g} + 3E _g)	[10, 117, 118, 131, 133]
c - cubic	145, 155, 604, 607, 613, 617, 620, 622, 626, 629, 631, 632	F _{2g}	[10, 50, 117, 118, 126, 130, 134]
β - rhombohedral	235, 411, 435, 507, 517, 523, 532, 540, 550, 585, 597, 600	A _g + B _g	[34, 130, 135]
Al ₂ O ₃	418	A _{1g}	[134, 136]

Raman method allows calculating the content of this phase, and it is as well possible to qualitatively control the crystallization of the materials by analyzing the

Raman shift and peak intensity. Further on, Raman spectroscopy analysis will be discussed in the experimental and results parts of this work.

1.8. Conclusions

The literature analysis of Zirconium oxide-based ceramics (ZrO_2) has shown that:

1. Zirconium oxide (ZrO_2) by nature is a polymorphic material and exists in three crystal modifications: monoclinic phase m- ZrO_2 , tetragonal phase t- ZrO_2 , cubic phase c- ZrO_2 .
2. The ZrO_2 by the stabilizing level can be categorized into three groups: the first group FSZ is fully stabilized ZrO_2 ; the second group is PSZ that is partially stabilized ZrO_2 ; the third group TZP is composed of tetragonal ZrO_2 polycrystals [8].
3. ScSZ has several times higher ionic conductivity at intermediate temperature 600–800 °C than that of YSZ systems and allows performing at low temperatures.
4. Scandium oxide Sc_2O_3 by ionic radius is one of the best dopants for ZrO_2 oxide-based ceramics.
5. Zirconium oxide-based ceramics can be applied at different techniques as oxygen sensors, electrochemical oxygen deposits, and high temperature fuel cells.
6. The co-doping of Al_2O_3 oxides in stabilized zirconia-based systems influence microstructure, and it has two dual functions, i.e., the resistivity of grain and grain boundaries increase, and the grain growth is restricted below the solubility limit, while above the solubility limit of Al_2O_3 , the resistivity decreases, and the grain growth is inhibited.
7. The addition of 1 at.% Al_2O_3 content can slightly increase the electrical conductivity.

The literature analysis of presented works shows that the study of microstructure and composition of ZrO_2 based ceramics, as well as the conductivity properties, is an urgent task nowadays. At the same time, the attention of researchers is still focused on the two-component systems. The information about three-component oxide systems is extremely sparse. The analysis of literature for this thesis has shown that one way to improve the properties of solid ceramic is the additive (co-doping) to the $ZrO - MxO_y$ of the third component, which results in structural changes, and hence, the stability and mechanical properties, and a change in the mobility of ions and oxygen vacancies concentration. The features of the conductivity and structure in solid solutions containing three components are complex and have not been studied well enough. The comprehensive study of three-component systems can significantly expand the existing understanding of the conduction structure and lead to the emergence of new functional materials.

2. INSTRUMENTS AND METHODS

2.1. Electron beam evaporation

Initial commercial ceramic powders of $(\text{Sc}_2\text{O}_3)_{0.10}(\text{ZrO}_2)_{0.90}(\text{ScSZ})$, $(\text{Sc}_2\text{O}_3)_{0.10}(\text{Al}_2\text{O}_3)_{0.01}(\text{ZrO}_2)_{0.89}(\text{ScSZAl})$, and $(\text{Sc}_2\text{O}_3)_{0.06}(\text{Al}_2\text{O}_3)_{0.01}(\text{ZrO}_2)_{0.93}(\text{ScAlSZ})$ (Nexceris, LLC, Fuelcellmaterials, Lewis Center, OH, USA) (Table 2.1) were compressed into pallets and used as evaporating materials. The concentration of the (Sc_2O_3) dopants were chosen to investigate the influence of alumina (Al_2O_3) co-dopant on the microstructure, crystallinity, and ionic conductivity of scandia stabilized zirconium oxide thin films that were formed by using e-beam deposition technique. The ceramic pallets were evaporated by the electron beam physical vapor deposition system “Kurt J. Lesker EB-PVD 75” (Kurt J. Lesker Company, Pittsburg, PA, USA) on Alloy 600 (Fe-Ni-Cr) and Al_2O_3 substrates. The deposition rate was from 0.2 nm/s to 1.6 nm/s. The thickness of the formed thin films (~1500–2000 nm) and the deposition rate during the deposition process was controlled via INFICON (Inficon, Bad Ragaz, Switzerland) crystal sensor. During the thin film deposition process, the temperature of substrates was changed from room temperature (20 °C) to 600 °C temperature, and the following temperatures were used: 50, 150, 300, 450, and 600 °C. The substrate was rotated during the deposition at 8 rotations per minute (rpm) speed to extract good homogenous thin films. In order to exclude the dust, the substrates were cleaned before deposition in an ultrasonic bath for 10–15 min and treated in Ar^+ ion plasma cleaning for 10 min. During the experiment, the voltage was constant at 7.9 kV. The main parameters of the e-beam physical vapor deposition system “Kurt J. Lesker EB-PVD 75” are presented in Table 2.2.

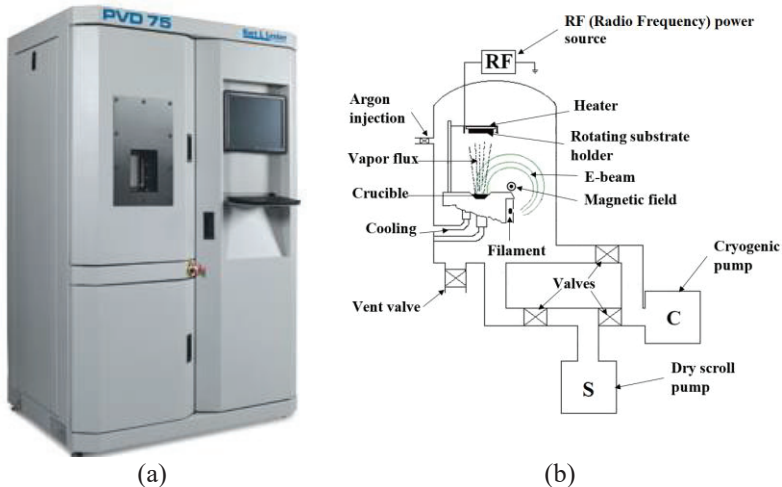


Fig. 2.1. (a) E-Beam Evaporator, EB-PVD 75 Kurt J. Lesker Company, Pittsburg, PA, USA, (b) vacuum chamber illustration of PVD system [137]

Table 2.1. Characteristic of commercial initial powders [138]

Part No.	Short code	Composition	Grade	Surface Area	PSD D50
312007	ScSZ-TC	$(\text{Sc}_2\text{O}_3)_{0.10}(\text{ZrO}_2)_{0.90}$	Tape-Cast	8–11 m ² /g	0.4–0.7 μm
312014	ScSZAl-TC	$(\text{Sc}_2\text{O}_3)_{0.10}(\text{Al}_2\text{O}_3)_{0.01}(\text{ZrO}_2)_{0.89}$	Tape-Cast	8–12 m ² /g	0.5–0.7 μm
312013	ScAlSZ-TC	$(\text{Sc}_2\text{O}_3)_{0.06}(\text{Al}_2\text{O}_3)_{0.01}(\text{ZrO}_2)_{0.93}$	Tape-Cast	8–10 m ² /g	0.5–0.7 μm

The thin film deposition by e-beam evaporation method is a world-wide used method. E-beam deposition system is one of the most widely used methods of thin film deposition. Moreover, EB-PVD materials are heated by the high energy of electrons, and the system itself has a good focusing of an electron beam, which enables manufacturers to get high concentration of power (up to $5 \cdot 10^8$ W/cm²), and high temperature, giving high rate of evaporation, and the thin-film porosity and thickness can be easily controlled even for the most refractory materials. EB-PVD system and vacuum chamber illustration is presented in Fig. 2.1 a, b. During the e-beam deposition processes, the current passes through the tungsten hairpin filament result in changes of the filament temperature and electron ejections. The ejected electrons accelerate by applying high voltage in the direction of evaporating materials; then, the accelerated electrons focus on the high magnetic fields, and an electron beam appears. When the electron beam achieves the evaporating materials energy, the transfer occurs, the consequence of which is the sublimation of the material into the substrate. During the deposition processes, there have been used two vacuum levels (first level $\sim 6.9 \times 10^{-4}$ Pa, second working level $\sim 2.0 \times 10^{-2}$ Pa) in a chamber, which were applied by rotary and cryogenic pumping systems. The high vacuum in the chamber during thin film deposition processes is very important to ensure the transport of electrons to the substrate and exclude their interaction with particles of the residual gas.

Table 2.2. Technical characteristics of e-beam evaporator

Electron beam source	Current tungsten filament	50A (when 10 kV)
	Accelerating voltage	4–10 kV \pm 0.5%
	Beam power	Up to 6 kW, voltage 10 kV
	Beam deflection	270°
	Beam shape	Sine, sawtooth, triangle, arbitrary
	Maximum electron beam current	600 mA
Crucible		15 sm^3 , 4 units (depending on the size)
System of automatic measurement of film thickness	Sensor type	Quartz oscillator, the frequency of 6 MHz
	Resolution	\pm 0.028 Hz
	Measurement interval	0.25 s
	Resolution of film thickness measurement	0.034 Å
Maximal vacuum		5×10^{-7} Torr
Heating block substrates		Heater with a maximum temperature of 600 °C
Diameter of the focused beam		3 mm
Maximum speed of evaporation in a vacuum		12000 Å/min
Working pressure		10^{-1} Pa, 10^{-6} Pa

2.2. X-ray diffraction analysis (XRD)

X-ray diffraction measurements were made by “Bruker D8 Discover” (XRD, Bruker, Billerica, MA, USA) system to analyze the crystalline structure characterization of the formed ceramic thin films at 2θ angle in a $20\text{--}70^\circ$ range using standard Bragg–Brentan θ/θ focusing geometry with Cu K_α ($\lambda = 0.154059$ nm) radiation, 0.01° step and 2θ and fixed divergence slits of $\frac{1}{2}^\circ$, and Lynx eye PSD detector. The main technological parameters of “Bruker D8 Discover” (XRD, Bruker, Billerica, MA, USA) are presented in Table 2.3. In the Bragg-Brentano scheme (Fig. 2.2), the sample is located in such a way that the investigated surface is stationary and the X-ray source and the detector move at equal angles to the substance during measurement. The high-temperature in-situ X-ray diffraction analysis, which makes it possible to measure the intensity of X-ray diffraction in-situ, was carried out in the Mri TC-basic chamber. Cu $K\alpha$ radiation was used as an X-ray source. The spectra were recorded in the temperature range from 30 to 900 °C, and during measurements, the following temperatures were used: 30, 300, 400, 500, 600, 700, 800, and 900 °C. The heating rate was 1 °C per minute, and the stabilization time of temperature was 20 min. Nevertheless, it has been noted that when working at such high temperatures, the choice of material for the sample holder becomes critical. In this work, a platinum holder was used, and the samples were placed on a Pt:Rh heating foil strip with an S-type thermocouple.

EVA Search–Match software and PDF-2 and “Sleve” PDF-4 databases were applied to examine the diffraction peaks. The size of the crystallites and lattice constants were estimated with the commercial TOPAS and TOPAS 4.1 software, respectively. The fitting procedure of diffraction patterns was done by Pawley’s method, and Scherrer equation [139] was used to estimate the crystallites size $\langle d \rangle$ of the initial powders and formed thin films:

$$d = \frac{0.9\lambda}{\beta \cos\theta}; \quad (2)$$

where λ is the wavelength of the X-rays (1.54059 nm), θ is the scattering angle of the main reflection, β is the corrected peak full width at half-maximum (FWHM) intensity.

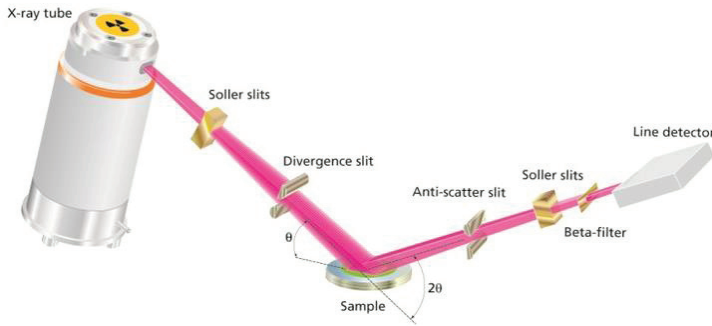


Fig. 2.2. XRD setup, Bragg–Brentano geometry [140]

The main technical parameters that were used in the measurements are listed in Table 2.3.

Table 2.3. The main technical parameters of X-Ray diffractometer “Bruker D8 Discover” (XRD, Bruker, Billerica, MA, USA)

Measuring angle, 2θ	20–70°
Detector	“Lynx eye” PSD detector
Working orientation	Horizontal or vertical
Possible configuration	Theta/2Theta, Theta/Theta
Goniometer diameter	435, 500, 600 mm, or any values in between
Angular analysis range (2θ)	From -110° up to 168° (depending on used parts)
Angular positioning	Stepper motor with optical switching
Lowest step size	0.01°
X-ray	Cu K_{α} ($\lambda = 0.154059$ nm)

2.3. Scanning electron microscopy (SEM)

Scanning electron microscopy (SEM) “Hitachi S-3400N, Hitachi High-Technologies Corporation, Tokyo, Japan” was used to investigate the microstructure of formed thin films as a presence of defects in the crystalline structure and obtain a topography image of the surface and section view images of the formed ceramics. The SEM device consists of a column and the following key components: electron

gun, tungsten hairpin filament, condenser lenses, electromagnetic compression lenses, objective lens movable aperture, objective lenses, focusing lenses, secondary electron detector, reflected electron detector, and sample holder (Fig. 2.3). The operation of the electron source is based on the emission phenomenon of electrons (thermionic emission) from a tungsten filament in a vacuum at a high temperature. The images were performed at room temperature. The SEM measurements scanning parameters are provided in Table 2.4.

Table 2.4. SEM measurements scanning parameters

Resolution	~9 nm using 5 kV acceleration voltage
Magnification	1000x, 20000x, 40000x, and 60000x
Cathode	Tungsten filament
Acceleration voltage	5 kV
Aperture	30 μm
Working distance	5 mm
Vacuum	$1.5 \cdot 10^{-3}$ Pa

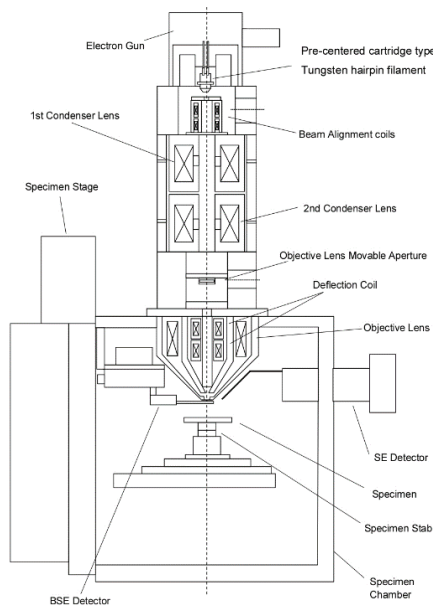


Fig. 2.3. Sectional view of Scanning Electron Microscope Hitachi S-3400N column and internal components [141]

2.4. Energy-dispersive X-ray spectrometry (EDS)

Energy-dispersive X-ray spectrometry (EDS) “BrukerXFlash QUAD 5040” has been used for the elemental analysis determination of the formed ceramics. The EDS measurements are based on the excitation of investigation material atoms, using an electron beam; this emits X-rays characteristic of each specific element.

The electron beam (electron probe) interacts with near-surface region of the sample that is approximately several microns deep. The depth of interaction depends on both the accelerating voltage and the density of the material. The interaction results in numerous signals that can be detected with a variety of detectors to obtain information about the sample. These signals include the emission of secondary electrons of low energy, the generation of Auger electrons, the emission of characteristic and bremsstrahlung X-rays, the emission of backscattered (reflected) electrons, cathode-luminescence, etc.

The scanning electron microscope has a prefix for the X-ray microanalysis, which is designed to determine the chemical content of solid ceramics. The detection limit is about 10–2 wt%; the minimal field of study is 1 micron for the elements. X-ray fluorescence analysis is for the elemental composition. The detection limit is about 10–5 wt%; the minimal field of study is 100 microns. The resolving power when using the secondary electron detector is 3.0 nm (accelerating voltage 30 kV, when working with a high degree of dilution) and 10 nm (3 kV accelerating voltage, when working with a high degree of dilution). The detector resolution of the detector when using backscattered electrons is 4.0 nm (accelerating voltage 30 kV, when working with a low degree of dilution).

2.5. Atomic force microscopy

The principle of operation of an AFM is based on the registration of force interaction between the atoms in the surface of investigated materials with the atoms of the probe. The force interaction of the tips atom between the atoms of the investigated materials implies the dependence of the energy of the Van der Waals interaction of two atoms located at a distance r from each other (Fig. 2.4). The forces of interaction of the tips atom between the atoms of investigated materials at small distances are repulsive, and with further increase in distance, they transform into forces of attraction. Three operating modes of the AFM can be divided based on the distance and type of forces between the cantilever and the sample surface:

1. Contact mode,
2. Non-contact mode,
3. Intermittent contact mode (tapping mode).

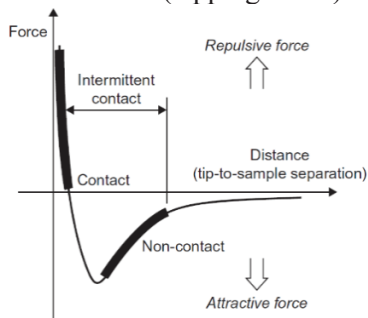


Fig. 2.4. Typical curve of the Van der Waals interaction force on the distance between the cantilever and the sample surface [142]

The atomic force microscope (AFM) (NT-206, Microtestmachines, Belarus) was used to build 3D images of the formed thin films. The 3D images of formed thin films were obtained by ($3.0\ \mu\text{m} \times 3.0\ \mu\text{m}$) scanning area. The AFM measurements were performed by using intermittent contact mode with 12 nm step size and oscillation frequency 45 kHz. The tips with Si-based by 16 μm high and 6 nm in diameter in pyramid shape were used while scanning. The numbers of measuring points were 128×128 . The vertical resolution was 0.1 nm. "Gwyddion 2.59" software was used to calculate the surface roughness value (R_q , nm).

The AFM NT-206 operates under the special software controller, which is delivered in a set of device, software executed on IBM PC-compatible computers [143].

2.6. X-ray photoelectron spectroscopy (XPS)

X-ray photoelectron spectroscopy measurements (XPS) were estimated to analyze the chemical composition and bonding state of the formed thin films. XPS, PHI Versaprobe 5000 consisted of a vacuum chamber, dual anode X-ray source, X-ray monochromator, energy analyzer, and ion gun (Fig. 2.5 a). During the experiments, the formed thin films were placed in a vacuum chamber. Then, high vacuum was created. During measuring, the surface of the sample was irradiated with monochromatic X-ray radiation: Al $K\alpha$ (1486.6 eV). The X-ray power was 23.2 W, the diameter was 100 mm, and the angle of incidence was 45° , and the pass energy was 187.580 eV, 1 eV resolution for Survey Spectrum, and for detailed chemical analysis, there was used extremely low energy 0.1 eV. XPS Spectra of ZrO_2 , Zr 3d Orbits are in general expressed by the non-symmetric peaks shape (Fig. 2.5 b) [144], and the schematic illustrations of inner-shell ionization were presented in Fig. 2.5 c. Zr 3d and binding energies of common chemical state parameters are presented in Table 2.5.

The charge neutralization conditions were compensated by the irradiation of low-energy electron beam surface of samples. When X-rays interact with the internal electrons of atoms on the surface of the investigating sample, the photoionization of the atoms occurs, and during these measurements, photoelectrons are emitted. The photoionization was accompanied by two other processes, i.e., X-ray fluorescence and Auger electron emission. The spin-orbit splitting changes with the chemical state [144].

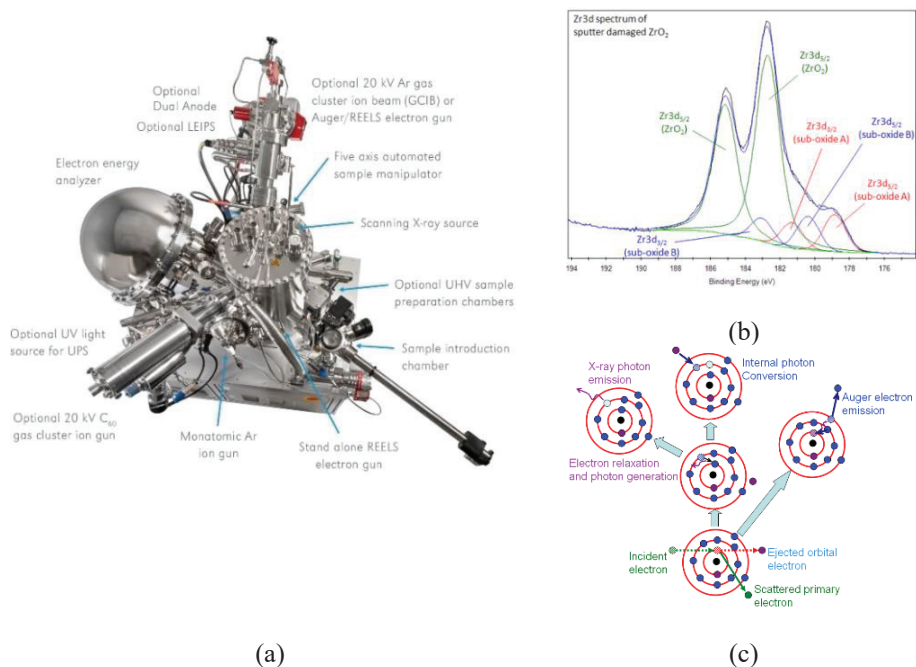


Fig. 2.5. (a) Overhead view of the instrument "PHI 5000 Versaprobe", (b) XPS Spectra of ZrO_2 : overview and Zr 3d orbits, (c) schematic illustration of inner-shell ionization [144–146]

Table 2.5. Primary XPS regions of Zr 3d, Sc 2p, Al 2p, O1s and binding energies of common chemical states [144]

Chemical state	Binding energy Zr 3d _{5/2} /eV
Zr metal	178.9
Sr sub-oxides	179–180.5
ZrO	182.3
Zr (IV) silicate ₂	182.7
Chemical state	Binding energy Sc 2p _{3/2} /eV
Sc metal	398.5
Sc ₂ O ₃	401.8
ScO (OH)	402.7
Chemical state	Binding energy Al 2p/eV
Al metal	72.6
Aluminosilicate	74.4
Al oxide	74.6
Al oxide on Al foil	75.6
Chemical state	Binding energy O1s/eV
Metal oxide	529–530
Metal carbonates	531.5–532

Al ₂ O ₃ (alumina)	531.1
SiO ₂	532.9
Organic C-O	531.5–532
Organic C=O	~533
O-F _x	~535

Before the analysis, the survey spectrum was shifted in a certain direction that the position of the carbon C1s peak coincided with that indicated in the manuals (182 eV) (Fig. 2.5 b) [144]. Then, a part of the spectrum corresponding to the background radiation was removed. Due to this, the Taugard method was used. After eliminating the background radiation, the theoretical positions of the peaks belonging to the Zr³⁺ ions in the spectrum of the Zr 3d orbit were noted [144]. XPS spectra of ZrO₂, Zr 3d orbits and deconvoluted peaks of O1s are presented in Fig. 2.6.

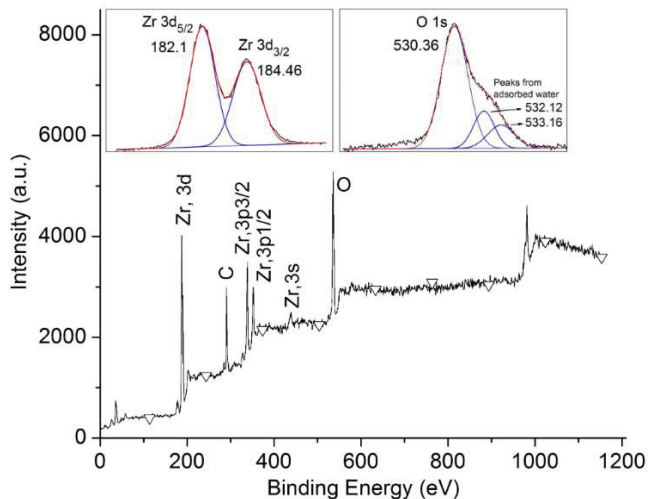


Fig. 2.6. ZrO₂ based thin films XPS spectra: overview and Zr 3d orbits and deconvoluted peaks of O1s [147]

XPS spectral analysis was performed using the CasaXPS software. The main operating parameters of XPS spectrometer are given in Table 2.6.

Table 2.6. Basic operating parameters of XPS spectrometer

X-rays beam	AlK α 1486.6 eV
X-ray beam power	23.2 W
X-ray beam diameter	100 mm
X-ray beam incidence angle	45°
Sample loading compensation	Launching low energy electrons
Surface cleaning	Not used in order to avoid the changing surface texture

2.7. Raman spectroscopy

Raman spectroscopy measurements as a technique were used in this study to provide a detailed examination of the formation and evolution of the phase composition of initial powders and formed thin films before and after the thermal annealing. Raman scattering is the inelastic interaction of monochromatic electromagnetic radiation with molecules of liquids, gases, and solids. The result of this interaction is a shift of the photon spectrum to lower (Stokes scattering) or higher (anti-Stokes scattering) frequency, which gives information about the vibrational modes of the system (Fig. 2.7 a). This shift reveals information about the low-frequency transitions in molecules, such as vibrational, rotational, and other low-frequency transitions [148, 149].

Stokes scattering: if the energy of the final level, on which the molecule falls, is higher than the energy of its initial level, the frequency of the scattered photon decreases, and such scattering is called Stokes $h(\nu_0 - \nu_{vib})$.

Anti-Stokes scattering: if the energy of the final level is less than the energy of its initial level, the frequency of the scattered photon increases, and such scattering is called anti-Stokes $h(\nu_0 + \nu_{vib})$.

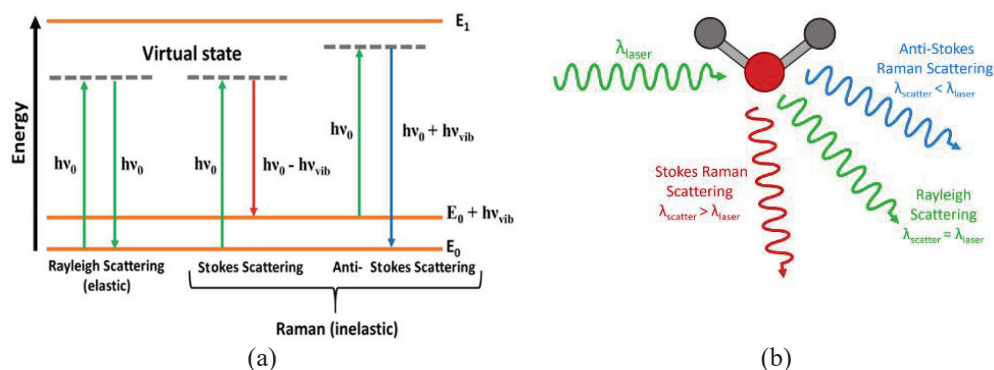


Fig. 2.7. (a) Energy level diagram for Rayleigh and Raman (Stokes and Anti-Stokes) scattering processes, the difference in the vibrational or rotational energy levels of that molecule is represented by $\Delta E = h\nu_{vib}$, adapted from [149]; (b) types of scattering processes [150]

When an incident photon $h\nu_0$ excites electrons from the ground states (E_0), which correspond to the lowest energy or rotational and vibrational energy levels, they briefly transition to the virtual levels before inelastic scattering occurs. In a case of inelastic scattering of a reflected photon, the energy does not correspond to the energy of the primary photon, in contrast to the elastic and Rayleigh scattering. The difference in the vibrational energies of molecules in the initial (main) and final (virtual) levels is the cause of change in the frequency of scattered photon and is called Rayleigh line (Fig. 2.7 a, b) [148, 149].

The classic theory of Raman scattering could be explained by vibrations of the electron shell of a molecule, which subsequently induces an alternating dipole

moment. If the electric strength E induces a dipole moment μ in the substance molecule, it can be represented as follows [149]:

$$\mu = \alpha E; \quad (3)$$

where α is the polarizability of the molecule. Assuming that the electric field experienced by each sample molecule varies as $E = E_o \cos \pi \nu t$, then [149]:

$$\mu = \alpha E = E_o \cos \pi \nu t; \quad (4)$$

where E_o is the ground state of amplitude of the electromagnetic wave.

Even though the polarizability of a molecule depends on the distance between the nuclei of atoms therefor, for the small displacement from equilibrium position, the polarizability is given as follows [149]:

$$\alpha = \alpha_0 + (q - q_{eq}) \frac{\partial \alpha}{\partial q}, \quad (5)$$

and the equation of motion for a harmonic displacement may be represented as follows:

$$q - q_0 = q_{max} \cos \pi \nu_{vib} t; \quad (6)$$

where α_0 is equilibrium polarizability, q_{eq} - equilibrium vibrational coordinates, q - instant vibrational coordinates, ν_{vib} - vibrational frequency of a molecule, and q_{max} - maximum distance between atoms relative equilibrium vibrational coordinates. Then, the polarizability of molecule α can be represented as follows [149]:

$$\alpha = \alpha_0 + \left(\frac{\partial \alpha}{\partial q} \right) q_{max} \cos \pi \nu_{vib} t, \quad (7)$$

and μ has the following form:

$$\mu = E_o \cos \pi \nu t \left[\alpha_0 + \left(\frac{\partial \alpha}{\partial q} \right) q_{max} \cos \pi \nu_{vib} t \right], \quad (8)$$

or

$$\mu = \alpha_0 E_o \cos \pi \nu t + E_o \left(\frac{\partial \alpha}{\partial q} \right) q_{max} \cos \pi \nu t \cos \pi \nu_{vib} t, \quad (9)$$

or

$$\mu = \alpha_0 E_o \cos \pi \nu t + \frac{E_o}{2} q_{max} \left(\frac{\partial \alpha}{\partial q} \right) \cos[2\pi(\nu - \nu_{vib})t] + \frac{E_o}{2} q_{max} \left(\frac{\partial \alpha}{\partial q} \right) \cos[2\pi(\nu + \nu_{vib})t]. \quad (10)$$

The frequencies appearing in the scattered spectrum $(\nu - \nu_{vib})$ and $(\nu + \nu_{vib})$ belong to Stoke and Anti-Stoke scattering, respectively. The Rayleigh scattering is represented by the excitation frequency [149].

Raman spectrum can give rich information of analyte molecules, and in Via spectrometer was used to obtain the Raman spectra (Renishaw, Gloucestershire, UK) (Fig. 2.8). The device consists of several key components. 1) Monochromatic light (laser) sources in this study were used as excitation beam from a diode laser of 532 nm wavelength, and at the sample surface, laser power varied from 1.75 mW to

3.5 mW. The detecting signals were accumulated five times, and further signals were averaged. The integration time was from 15 to 30 seconds. 2) Waveplates were used to control the directions of the incident laser. 3) Incident laser was 4 microns (μm) in diameter, and a microscope was used to focus the laser beam on the sample by using a $50\times$ objective ($\text{NA} = 0.75$, Leica). 4) The exact coordinates for the investigation samples were controlled in-situ by the movable stage. 5) Rayleigh part of the spectrum was filtered by a dielectric filter. 6) The diffraction grating (2400 grooves/mm) was used for dispersing the Raman Stokes scattered signal. 7) The data was detected (recorded) by using a Peltier cooled charge-coupled device (CCD) detector (1024 \times 256 pixels). Raman spectroscopy measurements were performed at the Institute of Material Science (IMS) of Kaunas University of Technology. Detailed and specific performance characteristics of the InVia Renishaw spectrometer are given in Table 2.7.

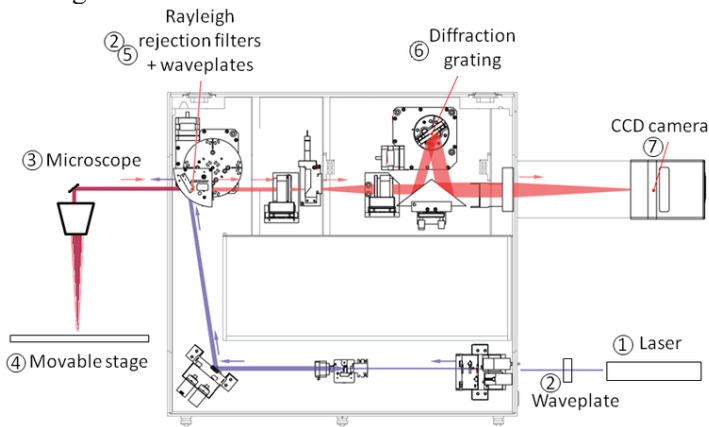


Fig. 2.8. Illustration of the key components of Renishaw inVia confocal Raman microscope [151]

Table 2.7. InVia Renishaw general specifications, adapted from [152]

Wavelength range	200 nm to 2200 nm	
Spectral resolution	0.3 cm^{-1} (FWHM)	Highest (typically necessary): 1 cm^{-1}
Stability	$<\pm 0.01 \text{ cm}^{-1}$	
Low wavenumber cut-off	5 cm^{-1}	Lowest (typically necessary): 100 cm^{-1}
High wavenumber cut-off	30.000 cm^{-1}	Standard: 4.000 cm^{-1}
Spatial resolution (lateral)	0.25 μm	Standard: 1 μm
Spatial resolution (axial)	$<1 \mu\text{m}$	Standard: $<2 \mu\text{m}$ Depend on the objective and laser
Detector size (standard)	1024 \times 256 pixels	Other available options

Detector operating temperature	-70 °C	
Supply voltage	110 V AC to 240 V AC +10% -15%	
Supply frequency	50 Hz or 60 Hz	
Typical power consumption (spectrometer)	150 W	

The spectral resolution of using systems is about 1 cm⁻¹. The calibrations of the Raman setup in both Raman wavenumber and spectral intensity were performed using Silicon (Si), because the peak of silicon is very well known, and it is expressed at 520 cm⁻¹. The intensity and position of the Raman spectra peaks were identified by fitting the data to the Lorentz line shape with the OriginPro 2016 software, peak fit function. The illustrations of Raman spectra fitting are presented at supplementary materials of this work in the Appendix. The overlapped background-corrected Raman spectral bands were fitted with Lorentz contours by using least-squares fitting software. The identification was supported by the calculations of the phase ratios, issuing the following formula [126, 134, 153, 154]:

$$\vartheta_c = \frac{I_c}{k(I_m + I_t + I_\beta) + I_c}; \quad (11)$$

where I_m , I_t , I_β , and I_c represent scattering intensity of cubic, tetragonal, rhombohedral, and monoclinic Raman peaks, and the coefficient $k = 0.97$ is the factor required to convert the Raman intensities to the XRD intensities of the reference material.

2.8. Electrochemical impedance spectroscopy (EIS)

The electrolyte has total electrical conductivity, which is the sum of electronic (electron/hole) and ionic conductivities. The electrical conductivity of electrolytes is normally measured by the DC four-probe method, but this can cause errors because of the effect of grain boundaries and electrodes, which can cover the proper behavior of bulk. Electrical impedance spectroscopy can overcome this error [52, 155–157]. The ideal equivalent circuit and impedance spectrum for a polycrystalline ZrO₂-based electrolyte can be seen in Fig. 2.9 a, b [158]. This spectrum normally consists of low-frequency semicircle that corresponds to the electrode response (double-layer capacitance C_e and electrode resistance R_e), intermediate-frequency semicircle that corresponds to grain-boundary (grain-boundary capacitance C_{gb} and resistance R_{gb}), and high-frequency semicircle that corresponds to the grain interior (grain-interior capacitance C_{gi} and resistance R_{gi}). The electrode response is only found for isotropic electrolyte due to the effect of relaxation behavior at higher temperatures. The high-frequency intercept on the real axis represents the electrolyte resistance, while the sum of electrolyte resistance and area-specific resistance (ASR) is represented by the low-frequency intercept on the real axis. The entire impedance spectrum can be observed at a certain temperature, and the impedance spectrum is

affected by the electrode material and its fabrication process, connection technique of electrodes, and the performance of instruments [52].

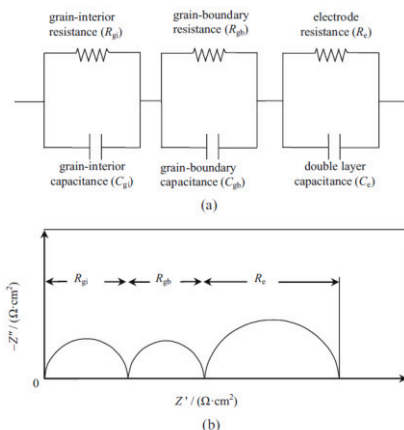


Fig. 2.9. (a) Ideal equivalent circuit and (b) impedance spectrum [52]

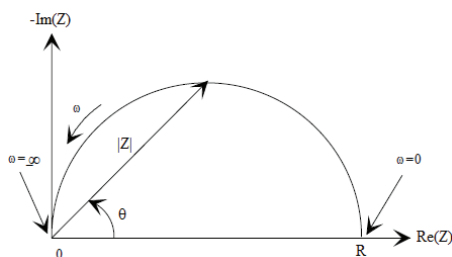


Fig. 2.10. Nyquist scheme of the complex impedance

The ionic conductivity measurements of formed thin ceramic films were carried out by using an electrochemical impedance spectrometer (EIS) Probostat® (Norecs AS, Oslo, Norway). The impedance spectroscopy method allows obtaining detailed data on the nature of electrical conductivity of ceramics based on the complex oxide systems. The essence of the method is the study of response from the imposition of a disturbing sinusoidal pulse of small amplitude on the system. The measuring of the impedance spectrum was performed in parallel (in-plane) to the coating surface. Two Pt electrodes were overlaid on the thin film tops through a mask, repeating the electrode geometry (a two-probe method). [159]. The essence of the method consists of the application of a current of a certain frequency and measuring the amplitude and phase shift or imaginary and real part of the resulting current at that frequency. Electrochemical impedance is a vector quantity. The complex impedance of the system can be expressed by formula (12) and represented graphically using Cartesian or polar coordinates at any frequency (Fig. 2.10). The measured complex impedance is displayed on a Nyquist plot to form a semicircle.

$$Z = Z' + jZ'' \quad \text{Complex impedance} \quad (12)$$

$$Re(Z) = Z' + |Z| \cos \theta \quad \text{Real part} \quad (13)$$

$$Im(Z) = Z'' + |Z| \sin \theta \quad \text{Imaginary part} \quad (14)$$

$$\theta = \tan^{-1} Z'' / Z' \quad \text{Phase angle of the impedance} \quad (15)$$

The samples were painted with platinum paste with a brush before impedance measurements; then, the applied platinum mass had a thermal treatment at 900 °C for 20 min. The rectangular electrodes were 1 cm × 0.5 cm in size, 1 cm apart. The impedance was measured in the air within the temperature range between 400 and 900 °C. These measurements were obtained over the frequency range of 0.1 Hz to 1 MHz (13 points per decade).

Furthermore, the impedance data that was acquired was analyzed, and Nyquist plots were modeled using “Z-view 2” software. The total conductivity was calculated as follows:

$$\sigma = \frac{L_e}{R_s A} = \frac{L_e}{R_s h l_e}; \quad (16)$$

where L_e is the distance between the Pt electrodes, R_s is the resistance obtained from the impedance spectra, A is the cross-sectional area of the electrodes, h is the thickness of the thin films, and l_e is the length of the electrodes.

The activation energy was determined from the Arrhenius equation:

$$\sigma T = \sigma_0 e^{\frac{-E_a}{kT}}; \quad (17)$$

where σ is the ionic conductivity, T - temperature of measurement, σ_0 - pre-exponential factor, E_a - activation energy, and k - Boltzmann constant ($0.86 \cdot 10^{-4}$ eV K^{-1}).

2.9. Thin film thickness via profilometer

The high sensitive contact profiler device can be used to recognize the surface geometry and roughness. It can as well be used to measure the thin film thickness. The formed thin film thickness measurements were obtained by using a contact profiler Ambios XP-200 (USA). A graphical representation of the result is shown below (Fig. 2.11). The main technical parameters of the XP-200 profilometer are presented in Table 2.8.

Table 2.8. Technical characteristics of Ambios XP-200 [160]

Height Ranges	2.5, 10, 100 μm
Minimum Resolution Step	1 nm (10 \AA)
Scan Length Maximum	55 mm
Stage Translation	150 x 178 mm
Stage Rotation	Manual operation, 180° in X-Y plane and tilt for slope correction
Camera Zoom Range	40 to 160 X (1 to 4 mm, field of view)
Sample Thickness	30 mm max
Stylus Tip	Radius 2.5 μm , Apex angle 60°, Bevel height 200 μm , Diamond
Stylus Force Range	0.03 to 10 mg

The Ambios XP-200 is a very high sensitive thin surface profilometer, and the working principles of measuring devices based on a diamond stylus (needle) are used as a probe, which moves along a certain line (track) relative to the surface. The irregularities cause mechanical vibrations of the needle, resulting in an electrical signal that is proportional to the size of the irregularities. Due to the small radius of curvature of the diamond needle, they provide high precision. The scanning of the border between the coating and the thin film substrate was obtained; the step of the profile and height of the step corresponds to the thickness of the road surface.

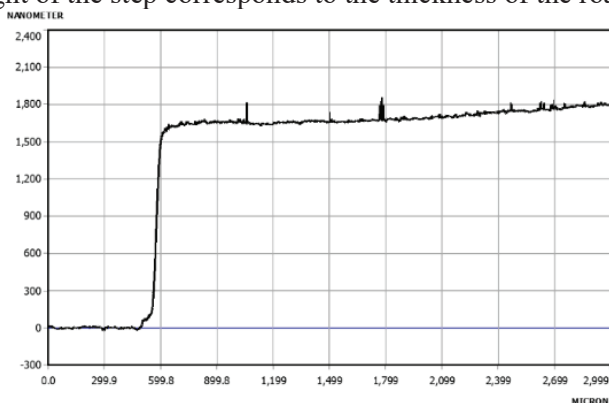


Fig. 2.11. Profile of ScSZAl thin films

RESULTS AND DISCUSSIONS

In order to get stabilized ceramic thin films, there were made a series of experiments, and the effect of evaporation parameters on the microstructural properties, chemical compositions, and phase content have been studied carefully. Firstly, scandia-doped zirconia (ScSZ) and scandia-alumina co-doped zirconia (ScSZAl) with different concentration were selected as primary candidates to forming stabilized ceramic thin films. The initial material was chosen because (ScSZAl) oxides are still considered under-researched issue. Moreover, the systematic studies of structure, electrochemical and influence of co-doping Al depending on the content of the concentrations were studied. Furthermore, the influences of technological parameters of ionic conductivity were analyzed in detail.

As a result of complex nature of evaporating material, different concentration of containing materials and different approaches of investigating methods, the result part was split into two sections:

- Structure and Conductivity Studies of $(\text{Sc}_2\text{O}_3)_{0.10}(\text{ZrO}_2)_{0.90}$ Scandia-Stabilized Zirconia and $(\text{Sc}_2\text{O}_3)_{0.10}(\text{Al}_2\text{O}_3)_{0.01}(\text{ZrO}_2)_{0.89}$ Scandia-Stabilized Zirconia Co-Doped with Alumina Thin Films;
- Structural and Electrochemical Properties of Scandia Alumina Stabilized Zirconia Thin Films $(\text{Sc}_2\text{O}_3)_{0.06}(\text{Al}_2\text{O}_3)_{0.01}(\text{ZrO}_2)_{0.93}$.

3. STRUCTURE AND CONDUCTIVITY STUDIES OF $(\text{Sc}_2\text{O}_3)_{0.10}(\text{ZrO}_2)_{0.90}$ SCANDIA-STABILIZED ZIRCONIA AND $(\text{Sc}_2\text{O}_3)_{0.10}(\text{Al}_2\text{O}_3)_{0.01}(\text{ZrO}_2)_{0.89}$ SCANDIA-STABILIZED ZIRCONIA CO-DOPED WITH ALUMINA THIN FILMS

3.1. X-ray diffraction analysis of initial powders and investigation of the crystalline structure of formed ScSZ and ScSZAl thin films

The investigation of the crystalline structure of the initial powder was carried out to make a comparison of structural analyses of formed thin films. The XRD patterns of ScSZ and ScSZAl of initial powders are presented in Fig. 3.1. The obtained XRD patterns displayed that ScSZ and ScSZAl powders are predominantly containing a rhombohedral (JCPDS No. 01-089-5482) phase, and it is presented by the sharp peaks at 003, 006, 012, 015, 021, 104, 101, 110, 113, and 202, and some bands expressed the corresponding presence of monoclinic (JCPDS No. 01-089-5474) phase [50]. It is visible, that the XRD pattern of powders contains a set of peaks corresponding to the rhombohedral and monoclinic phases [50].

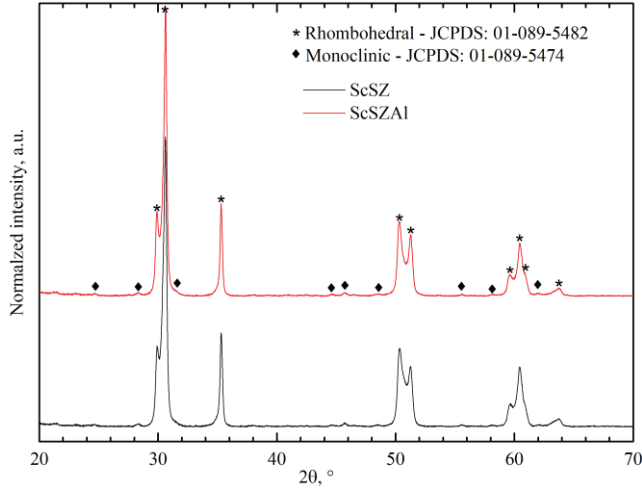
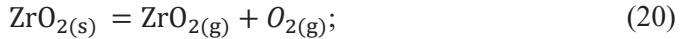


Fig. 3.1. X-ray diffraction patterns of initial powders: ScSZ and ScAlSZ [50]

The structure of evaporating material has a slight effect on the microstructural properties of zirconia-based materials (ScSZ, ScSZAl thin ceramics) as long as e-beam evaporation is used for the deposition. It is a well-known fact that the sublimations of Zirconium oxides proceed by the fragmentary decomposing during the electron beam deposition process [50, 103, 104].



where (s) is a solid-phase, (g) is a gas-phase.

The gas-phase of ScSZ and ScSZAl initial powders may contain a molecule, molecular fragments, and atoms of O, O₂, ZrO, ZrO₂, Sc, ScO, Sc₂O₂, Sc₂O₃, Al, AlO, Al₂O₂, Al₂O₃. The deposited atoms and molecules tend to grow on the surface of the lowest energy, i.e., $\gamma_{(111)} < \gamma_{(200)} < \gamma_{(220)} < \gamma_{(311)}$, and thin films form cubic structures. During the formation of thin films, the initial material atoms and molecules on the vapor phase primarily form the crystallization centers at substrate than by the competing growth around the center of crystallization form grains. A polycrystalline film for face-centered cubic has a predominant crystallographic grain orientation, e.g., (111), and such a thin film material is called textured. In the stage of formation of textured thin films, surface diffusion plays a very important role. For example, if adatoms are oriented randomly and deposited near grain boundaries due to the surface diffusion, they have a higher probability of being incorporated in a surface with a low diffusion coefficient, while adatoms on planes with a high diffusion coefficient have longer mean free paths with a correspondingly higher probability of leaving the plane and capture adjacent grains [50, 161].

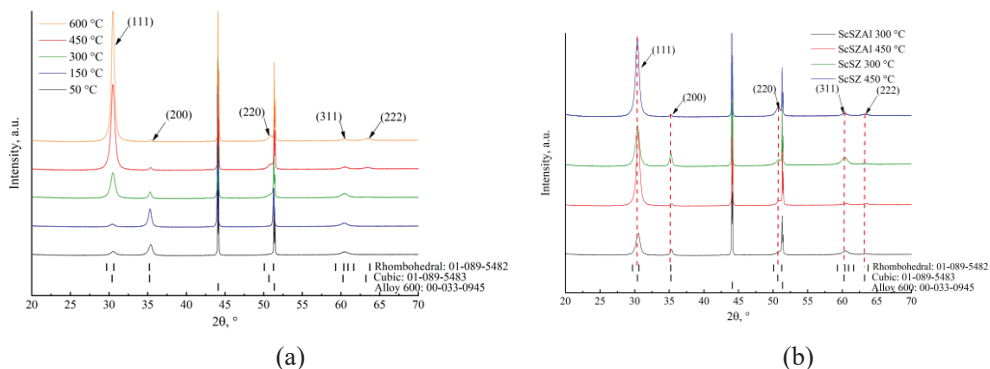


Fig. 3.2. X-ray diffraction patterns of thin films obtained by evaporation process (a) ScSZ and (b) ScSZAl; deposition rate: 0.4 nm/s; substrate: alloy 600 [50]

ScSZ and ScSZAl thin films were observed as a similar growing mechanism. At the same time, X-ray pattern analysis data (Fig. 3.2 a) at room temperature confirm the existence of the fluorite cubic phase, and it is expressed by a set of peaks of 111, 200, 220, 311, and 222 (JCPSD No. 01-089-5483) [50]. The XRD results of formed ScSZ and ScSZAl thin films are mainly presented by the presence of cubic phase and some minor presence of rhombohedral phase while the initial powder displayed predominantly a rhombohedral and some minor presence of monoclinic phase (Fig. 3.1, Fig. 3.2 a, b). Moreover, 200 preferential orientation was at (50–300 °C) and 111 at higher temperatures (450–600 °C) because of the high level of diffusion energy that facilitated the migrations processes of adatoms on the surface, and a part of adatoms was trapped into the material surface. At low deposition temperatures (50–300 °C), the diffusion path and time of atoms and molecules are short. Therefore, they are limited by the time of absorption in the low energy state, and thin films grow having a preferential orientation of (200). At high deposition temperatures (450–600 °C), the diffusion path and time of atoms and molecules are long. Thus, thin films grow is having a preferential orientation of (111). In addition, it has been discovered that XRD patterns of ScSZAl thin films peaks positions are shifted in the region of higher angles level (0.2°) in comparison with ScSZ thin films (Fig. 3.2 b). The shift of peaks positions appeared for the reason that the structure of thin films is largely distorted as a result of Al co-doping and segregation of various components of grains. The Al is 0.53 Å ion, which is not as much as the Zr - 0.84 Å ion. The lattice constants were estimated for the cubic unit cell with TOPAS 4.1 commercial software. Therefore, the crystal lattice is deformed. The calculations of lattice constant were proved (Fig. 3.3). The lattice constant gets smaller after co-doping ScSZ with Al. The lattice constant of ScSZ is approximately 5.080Å, and the lattice constant of ScSZAl is approximately 5.075Å.

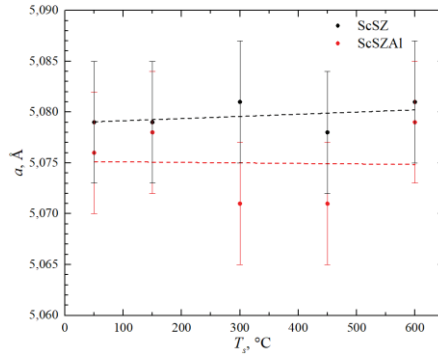


Fig. 3.3. The lattice constant against the substrate temperature of ScSZ and ScSZAl thin films deposited on SiO₂ substrates using 0.4 nm/s deposition rate

In order to refine the structure using the software approach called the Rietveld method, the calculated diffraction pattern (model) of ScSZAl thin films was obtained [162]. However, Rietveld's analysis of ScSZAl thin films (Fig. 3.4) has revealed that formed thin ceramics contains a mix of cubic and rhombohedral phases by 87.8% and 12.2%, respectively, with the same chance of pure cubic modifications. The match level of the experimental and calculated radiographs is evaluated by using the so-called R-factors (R-reliability). The "weighted-profile" R-factor (Rwp) is a factor in which only experimental points are used for the calculation, contributing to the diffraction peak [162]. The Rwp factor for pure cubic modifications is represented by 1.45, and the Rwp factor for the mixed phases is about 1.35. As a result, the cubic and rhombohedral phase peaks can overlap [50, 115, 116]. Under these circumstances, a complementary analysis is required, and Raman spectroscopy analysis as an option may be applied to appropriate solutions [117, 118].

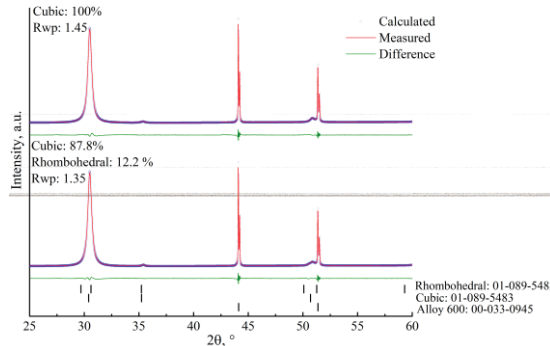


Fig. 3.4. Rietveld full-profile analysis of x-ray diffraction pattern from ScSZAl thin films; substrate: alloy 600; deposition rate: 0.4 nm/s [50]

The crystal size parameters had been calculated on the basis of experimental data obtained from the XRD analyses; the crystallite size parameters presented in Table 3.1 were calculated for ScAlSZ thin films deposited by 0.2 nm/s to 1.6 nm/s

deposition rates and the different substrate temperature ramping by 50 °C to 600 °C, respectively.

Table 3.1. Dependency of the crystallite size on the substrate temperatures of ScSZAl thin films; substrate: alloy 600; deposition rate: by 0.2 nm/s to 1.6 nm/s

Substrate temperature, °C	Deposition rate, (v_d) nm/s				
	0.2	0.4	0.8	1.2	1.6
	Crystallite size $\langle d \rangle$, nm				
50	19	19.7	17.4	19.2	18.5
150	29.4	29.3	24.4	35.6	28.8
300	60.8	65.4	48.3	69.9	43.5
450	31.9	31.2	29.5	44.6	40.8
600	40.9	48.4	37.2	46.3	47

The dependency of the crystallite size on the substrate temperatures exhibits non-linear performance (Fig. 3.5). Crystallite size evolution with increasing substrate temperature by 50 °C to 300 °C has a grow tendency (17.4–69.9 nm), while with the substrate temperature of 450 °C, the crystallite size of the thin films decreases (44.6–31.2 nm). This crystallite size decrease might be corresponding to the changes of preferential orientation. It is assumed that the crystallites are spherical in crystallite size calculations. However, such simplification is not always suitable for use. The dimensions of the crystallite can be different in x, y, z directions. Using standard θ - 2θ geometry, only out-of-plane diffraction is observed. The crystallite size calculations give values in one direction. If changes of preferential orientation are observed in the XRD pattern, the orientation of crystallites is changed for the substrate surface as well. It means that the crystallite size calculations give a distance between different crystallite surfaces than before the changes of orientation. Therefore, the obtained results show a decrease in the size of the crystallite.

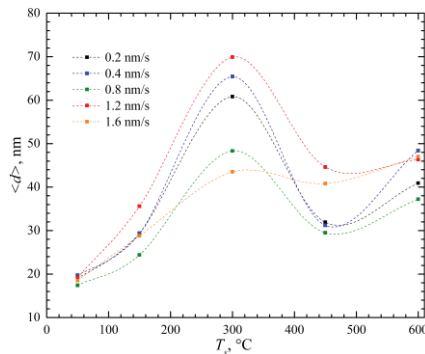


Fig. 3.5. Dependency of the crystallite size on the substrate temperatures of ScSZAl thin films; substrate: alloy 600; deposition rate: by 0.2 nm/s to 1.6 nm/s [50]

3.2. Analysis of Raman spectroscopy measurements data

Raman spectroscopy measurement is a very sensitive investigation method that differentiates the vibrations of various ZrO_2 phases, and it is a good support measurement for the XRD. Raman spectroscopy was used for a detailed analysis of phase composition of ScSZ and ScAlSZ initial powders and ScSZ and ScSZAl formed thin nanostructured films. The obtained Raman results of powders corresponded well with the X-ray diffraction analyses (Fig. 3.6). Raman spectra of the ScSZ and ScSZAl powders contain 13- Raman peaks. The peaks at $507\text{--}517\text{ cm}^{-1}$, $552\text{--}554\text{ cm}^{-1}$, 585 cm^{-1} , 597 cm^{-1} are the characteristics of β -rhombohedral phase [130]; the peaks at $147\text{--}148\text{ cm}^{-1}$, $259\text{--}260\text{ cm}^{-1}$, $315\text{--}321\text{ cm}^{-1}$, $384\text{--}386\text{ cm}^{-1}$, 422 cm^{-1} , 547 cm^{-1} , 551 cm^{-1} , 640 cm^{-1} are the presence of tetragonal phase, and 176 cm^{-1} , 190 cm^{-1} , 191 cm^{-1} , $469\text{--}473\text{ cm}^{-1}$ belong to the monoclinic phase [126, 131]. In general, cubic zirconia should be presented by the broad bands between 605 cm^{-1} and 630 cm^{-1} , which is the corresponding mode of F_{2g} vibrations. At Raman spectra of ZrO_2 powder, no vibrations were detected corresponding to the cubic phase [10, 117, 118, 126, 130]. In addition, the peaks were detected at 147, 148, 176, 190, 191, 259, 260, 315, 321, 384, 386, 422, 471, 473, 507, 517, 552, 554, 585, 597, 640 cm^{-1} , and around 800 to 1100 cm^{-1} . The Raman bands around 800 cm^{-1} are expressed by the presence of polymorphism in the lattice of powders, and it might be corresponding to any of the rhombohedral, tetragonal, or monoclinic phases of this material. The obtained Raman results of powders are in good respect by the results provided by other authors [10, 116]. ZrO_2 based ceramics doping with up to 9 mol% of Sc_2O_3 mainly should consist of rhombohedral phases [34, 135]. The Raman spectroscopy analysis of powders indicates that Raman peaks corresponding to the tetragonal phase are deformed, and dominant concentrations of this phase are primarily in the grain boundary [117].

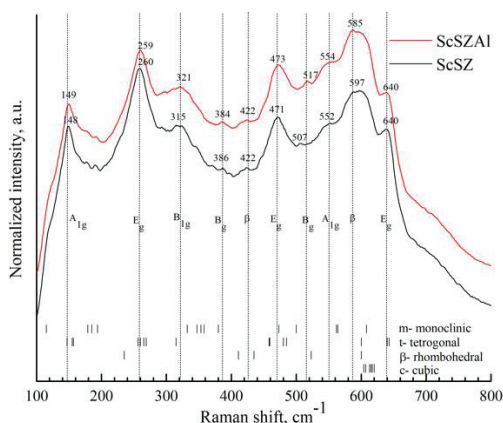


Fig. 3.6. Raman spectra of initial powder (ScAlSZ - red, ScSZ- black) [50], monoclinic [130, 126, 131], tetragonal [10, 117, 118, 131, 133], rhombohedral [130, 10], cubic [130, 10, 126, 117]

The Raman spectra analysis of ScSZ and ScSZAl thin films were done to characterize the structural changes against the temperature specimens ramping by 50, 150, 300, 450 and 600 °C (Fig. 3.7 a, b). ScSZ and ScSZAl specimen exhibits typical 10-Raman peaks maxima presented by 140, 262, 354, 382, 475, 540, 618, 726, 954, and 1000 cm^{-1} , respectively. According to the literature data, the Raman peaks maxima at 354, 382 cm^{-1} corresponding to the monoclinic phase [126, 130, 131] and characteristic bands for tetragonal phase were detected near 147, 260, and 475 cm^{-1} [10, 117, 118, 131, 133]. The expression of tetragonal peaks, not the results of predominates tetragonal phase in these films, might result from the defects of the initial material processing (powder).

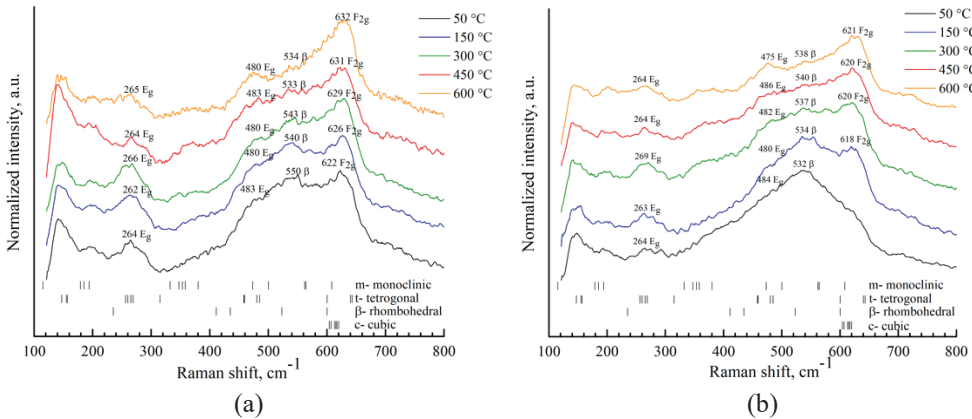


Fig. 3.7. Raman spectra of (a) ScSZ and (b) ScSZAl thin films; substrate: alloy 600; deposition rate: 0.4 nm/s [50]; monoclinic [126, 130, 131]; tetragonal [10, 117, 118, 131, 133]; rhombohedral [10, 130]; cubic [10, 117, 126, 130]

In addition, there are some Raman bands at 540 cm^{-1} that stand for the rhombohedral phase; these peaks are coming from the initial powder presented between 552–554 cm^{-1} ; moreover, these peaks are matched by the other author's data [10, 130]. The broad peaks for formed ScSZ and ScSZAl thin films with a maximum around 620 cm^{-1} could be a result of the merges of several peaks corresponding to the monoclinic (m), tetragonal (t), and mainly for cubic (c) phases, respectively; however, these peaks are not expressed in Raman spectra of initial powder (Fig. 3.6) and could be explained by the phase transition from the polymorphic material to the fluorite type cubic structure [10, 117, 126, 130]. At the same time, Raman maxima at 620 cm^{-1} could be shifted as a result of disorders in oxygen sub-lattice, which may arise when exposed to Sc dopant and Al co-dopants. The substitution of Zr^{4+} by Sc^{3+} has a significant effect, which leads to the creation of high numbers of oxygen vacancies [128]. A high level of vacancies can lead to a violation of the selection rules, and hence, it could enable the appearance of additional vibration modes, which are assigned to the changes in oxygen vacancy vibrations. Such changes in the lattice prevented the fluorite cubic structure lattice vibration. [129]. At the same time, Raman peaks at around 480 cm^{-1} line with the maximum of 484 cm^{-1} corresponds to the metastable tetragonal phase, which is

characterized by the pseudo-fluorite cubic structure. However, in contrast thereto, the t-phase is characterized by a slight displacement of oxygen ions relative to the position of oxygen ions in the crystal lattice with a fluorite structure [163, 164]. The investigating Raman spectra of initial powders and formed thin films do not contain the peaks around $\sim 418 \text{ cm}^{-1}$, corresponding to Al_2O_3 [134].

Raman spectroscopy patterns of ScSZ and ScSZAl have a similar shape, and both spectra contain the presence of peaks of around 620 cm^{-1} (Fig. 3.7 a, b). It suggests the cubic phase in both ScSZ and ScSZAl thin films. However, the peaks at 620 cm^{-1} for the ScSZAl are relatively lower than ScSZ thin films. It was noted that for samples doped with Al (Fig. 3.7 b), the cubic phase starts to stabilize and form at temperatures above $50 \text{ }^\circ\text{C}$, the subsequent ramping of the temperature does not have any significant effect on the formation and amount of the cubic phase. It suggests that when co-doped with Al, it retards the formation of the cubic phase and stabilizes it at substrate temperatures above $300 \text{ }^\circ\text{C}$.

The features of the phase composition revealed by the Raman measurements for the formed ScSZ and ScAlSZ thin films initiated a more detailed analysis, as quantitative calculations of the phase composition. However, the phase transition of the formed thin films during temperature ramping was calculated using formula (11) and listed in Table 3.2. It has been noted that during the increasing of substrate temperature, the phase transition from rhombohedral phase to phase cubic occurred in this step, and it can be characterized by the stabilization of the ceramic by the temperature of the substrates.

Table 3.2. Evaluation of containing phase ratio for ScSZ and ScSZAl thin films [50]

Substrate temperature, $^\circ\text{C}$	Cubic %	Tetragonal %	Rhombohedral %
ScSZ			
50 $^\circ\text{C}$	43%	15%	42%
150 $^\circ\text{C}$	42%	19%	39%
300 $^\circ\text{C}$	45%	18%	37%
450 $^\circ\text{C}$	46%	17%	37%
600 $^\circ\text{C}$	53%	17%	30%
ScSZAl			
50 $^\circ\text{C}$	-	22%	78%
150 $^\circ\text{C}$	41%	13%	46%
300 $^\circ\text{C}$	42%	19%	39%
450 $^\circ\text{C}$	43%	20%	37%
600 $^\circ\text{C}$	43%	23%	34%

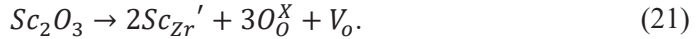
The quantitative calculations support the same conclusion of Raman peaks expressions of ScSZ and ScSZAl thin films. The cubic phase modifications ratio to tetragonal and rhombohedral phase ranges from 42% to 53% for ScSZ, and nearly 42% for ScSZAl. According to the calculations, by increasing the substrate temperature, the quantity of cubic phase rises by 10% and 2% for ScSZ and ScAlSZ, respectively. Finally, Raman examination reveals that thin films contain a

combination of mainly cubic (~44%), which is accompanied by tetragonal (18%), and rhombohedral (38%) phases. Hence, the produced thin films underwent a polymorphous transition from rhombohedral to cubic phase, which is typical for doped ZrO₂ [165]. The rhombohedral phase of ZrO₂ is not considerably represented in the XRD spectra, and the tetragonal phase is not observed, although Raman spectra indicate high amounts of both phases, implying that both phases could be found near grain boundaries [50, 117, 165].

3.3. Investigation of electrical properties of the formed thin films (EIS)

The investigations of the electrical properties and effect of the impurity composition of formed conductive thin-film were performed with a ProboStat™ device. The formed ScSZ and ScAlSZ thin films were investigated by the two-probe method in (1–10⁶) Hz electric fields at (200–1000) °C temperatures. The temperature range was chosen by the operating temperatures of the formed thin film electrolytes. A feature of these formed thin films materials is their multi-phase composition: according to the data of X-ray diffraction studies and Raman spectroscopy analyses, which were presented, the thin films were in a cubic, tetragonal, and rhombohedral phases.

The ionic conductivity of ScSZ systems is due to the presence of oxygen vacancies V_o , which are formed by the replacement of Zr⁴⁺ cations with Sc³⁺ cations; the reactions could be presented by the following equations [166]:



The stabilization of ZrO₂ lattice could be reached by doping, and one of the promising dopant is Sc₂O₃ oxide [166].

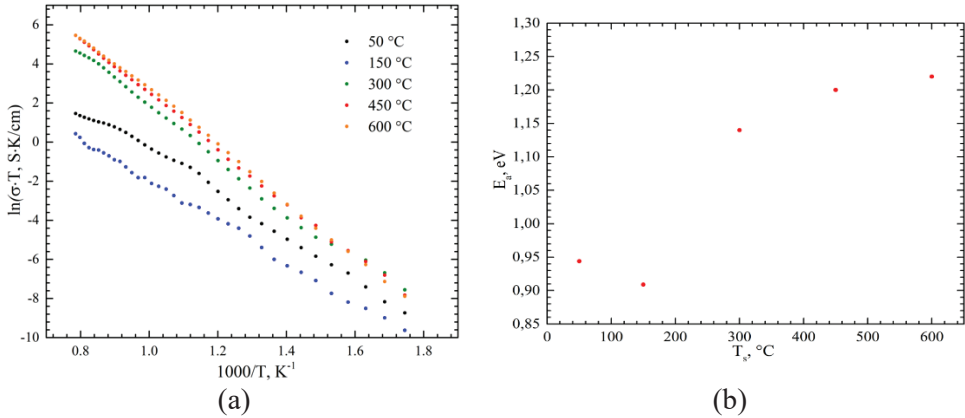


Fig. 3.8. (a) Arrhenius plots of ScSZAl thin films, (b) vacancy activation energy of ScSZAl thin films against the substrate temperature; substrate: Al₂O₃; deposition rate: 0.4 nm/s [50]

Arrhenius plots of ScSZAl thin films that have been formed at different substrate temperatures are presented in Fig. 3.8 a, and it can be seen that they show linear dependences. There were no evident breaking or bending points on the plots,

indicating that no phase transitions occurred during the experiments. Furthermore, ionic conductivity is depending on the substrate temperature. In the thin films formed on higher substrate temperature, there was found higher ionic conductivity (Table 3.3). The greatest ionic conductivity value of 4.2×10^{-3} S/cm (substrate temperature - 600 °C, and deposition rate - 0.4 nm/s) is comparable to the results of other authors that are presented as 7×10^{-3} S/cm [10, 29, 167], 2.9×10^{-3} S/cm [168], and 4.6×10^{-3} S/cm [29]. The crystallite size has a similar temperature dependence. The crystals grow (from 17.4 nm to 69.9 nm) as the substrate temperature (from 50 °C to 300 °C) increases during the deposition. At a temperature of 450 °C, the crystallite size decreases sharply (~45 nm to 30 nm). This may be the result of changes in preferential orientation and phase relations. It has been established that ionic conductivity strongly depends on the size of the crystallite. Based on the bricklayer model representation, high ionic conductivity can be achieved in materials that contain larger crystallites, as grain boundaries decelerate the oxygen ion diffusion [169–171].

Table 3.3. Ionic conductivity (S/cm) of ScSZ and ScSZAl thin films deposited using different substrate temperature and 0.4 nm/s deposition rate [50]

Thin Films	Substrate temperature				
	50 °C	150 °C	300 °C	450 °C	600 °C
ScSZ	1.7×10^{-5}	2.5×10^{-5}	7.4×10^{-4}	3.6×10^{-3}	4.2×10^{-3}
ScSZAl	4.1×10^{-5}	2.3×10^{-4}	1.1×10^{-3}	1.9×10^{-3}	2.4×10^{-3}

It has been found that the activation energy increases from 0.909 eV to 1.22 eV by increasing the substrate temperature (Fig. 3.8 b). The activation energy changes could be caused by the change in conduction mechanism in high- and low-temperature range [168]. Moreover, an increase of activation energy could appear due to the phase transition, which other authors as well found in the Scandia-zirconia system around 600 °C [43, 168]. However, taking into account the obtained results of XRD and Raman study data of ScSZAl, the sudden increases of the activation energy by 0.944 eV at sample formed at 50 °C substrate temperature could occur due to the existence of higher amount of tetragonal phases in the formed thin films by 22% of the tetragonal phase and the highest content of β -phase 78% (pseudo-fluorite cubic structure). The evaluation of containing phase ratio for ScSZAl thin films is presented in Table 3.2. The activation energy that has been determined from the temperature dependences of conductivity for these temperature ranges for ZrO_2 - Al_2O_3 - Sc_2O_3 crystals, and it is presented in Table 3.4 according to formula (22). Moreover, there has not been observed any tendentious change in the ionic conductivity depending on the activation energy:

$$\sigma = A/T^{-1} \exp(E_a/kT); \quad (22)$$

where A is the pre-exponential factor, T is the absolute temperature (usually in kelvins), and k is the reaction rate coefficient, E_a - activation energy.

Table 3.4. Activation energy (E_a , eV) of ScSZAl thin films deposited using different substrate temperature and 0.4 nm/s deposition rate

T_s , °C	E_a , eV
50	0.944
150	0.909
300	1.14
450	1.2
600	1.22

In addition, it has been found that the Al co-doping has an insignificant (minor) effect on the formation of the cubic phase and the stabilization of the crystallite structure, the consequence of which affects the ionic conductivity. Although ScSZAl thin films results in a slightly lower conductivity at higher substrate temperature, the reduced ionic conductivity is a result of the higher quantities of tetragonal phase, as lower quantities of cubic phase (Table 3.2).

3.4. Results and conclusions

The investigation methods, the preparation of initial materials, thin film formation, and the study of the microstructure and electrochemical properties were determined in accordance with the aim and objectives of this study. ScSZ and ScSZAl thin films were deposited by E-beam physical vapor deposition system, which produces a dense and homogeneous thin film. The produced thin films structure and conductivity were investigated. It has been discovered that the structure of the formed thin films differs from that of the evaporating material. The evaporated powders of ScSZ and ScSZAl reveal a polymorphism of ZrO₂ monoclinic, tetragonal by the Raman spectroscopy analysis and rhombohedral phases, according to the XRD patterns and Raman spectra. A conceptually new approach was used to analyze the crystallographic nature and phase content of formed thin ceramics. The XRD results of the obtained thin ceramic films that are presented as a pure cubic face-centered phase by 200 preferential orientations were at (50–300 °C) and 111 at higher temperatures (450–600 °C) in the course of the work. Moreover, the same behavior was established: the crystallite size depends on the substrate temperatures and changes of preferential orientation. The crystals grow large (from 17.4 nm to 69.9 nm) as the substrate temperature (50–300 °C) increases, and when the temperature reaches 450 °C, the crystallite size decreases sharply (from 44.6 nm to 31.2 nm). However, in order to meet the challenge of determining the influence Al co-doping and the exact quantitative phase ScSZAl composition, Rietveld analysis was made, and the results in a mixture of cubic and rhombohedral phases are 87.8% and 12.2%, respectively, with the same chance of pure cubic modifications. Raman spectroscopy analysis presented different polymorphic states for both ZrO₂ based thin films. Thus, the thin films are presented by the expression of Raman peaks, which is corresponding to 44% of cubic phase, 18% of tetragonal, and 38% of mixed phase, indicating as rhombohedral transitions phases. However, it has been determined that the influence of Al co-doping has a significant effect, and it slows down the stabilization of cubic shape by about 7%, and its results for ScSZ

are from 42% to 53%, and for ScSZAl, from 41% to 43%. At the same time, Arrhenius plots demonstrate linear dependence, and the highest ionic conductivity exhibits at 600 °C substrate temperature with a value of 4.2×10^{-3} S/cm. The predominant tetragonal phase in the results of specimen in vacancy activation energy increases from 0.91 eV to 1.22 eV at the higher temperature of substrate.

4. STRUCTURAL AND ELECTROCHEMICAL PROPERTIES OF SCANDIA ALUMINA STABILIZED ZIRCONIA $(\text{Sc}_2\text{O}_3)_{0.06}(\text{Al}_2\text{O}_3)_{0.01}(\text{ZrO}_2)_{0.93}$ THIN FILMS

4.1. Determination of elemental composition of Zr based thin films and influence on microstructure

4.1.1. Elemental analysis (EDS) of ScAlSZ thin films formed at 300 °C and 600 °C substrate temperatures

According to the EDS measurements, the content of elemental composition (elements) of formed ScAlSZ thin films surface, using various deposition parameters, are presented in Table 4.1. The concentration of Zr in thin films ranges from 25.3 to 36.0 at.% and O₂, Al, Sc are from 49.5 to 54.2 at.%, 3.0 to 20.2 at.%, 3.1 to 8.7 at.%, respectively. The atomic concentrations of containing elements are scattered in the mentioned intervals. The effect of the initial powder size on the elemental composition of ScAlSZ thin films has not been observed.

Table 4.1. The elemental composition (EDS) of the thin film surface of ScAlSZ, where v_d is the deposition rate, T_d - substrate temperature, and c_x - atomic concentration of investigating elements [102]

v_d , nm/s	$T_d = 300\text{ °C}$				$T_d = 600\text{ °C}$			
	c_{O} , at.%	c_{Al} , at.%	c_{Sc} , at.%	c_{Zr} , at.%	c_{O} , at.%	c_{Al} , at.%	c_{Sc} , at.%	c_{Zr} , at.%
0.2	51.4	20.2	3.1	25.3	54.2	12.2	3.6	30.0
0.4	49.5	12.4	3.6	34.5	49.8	12.5	3.4	34.3
0.8	53.4	3.8	7.4	35.4	50.6	15.8	3.6	30.0
1.2	51.5	6.4	8.7	33.5	53.6	8.0	6.7	31.8
1.6	54.1	3.0	6.8	36.0	51.2	7.1	7.1	34.5
Powder	52.0	12.6	3.9	32.5				

Furthermore, the effect of the deposition rate on the concentration of Al has been revealed. The concentration of Al for thin films formed at 300 °C substrates temperature fluctuates from 20.2 at.% to 3.0 at.% (Fig. 4.1 a), and for thin films formed at 600 °C substrates temperature, it fluctuates from 12.4 at.% to 7.1 at.% (Fig. 4.1 b). Moreover, it has been found that Al content for thin films formed at 600

°C is significantly higher, compared to thin films formed at 300 °C substrate temperature. However, Al content for initial powder were $c_{Al\ powder}=12.6\ at.\%$.

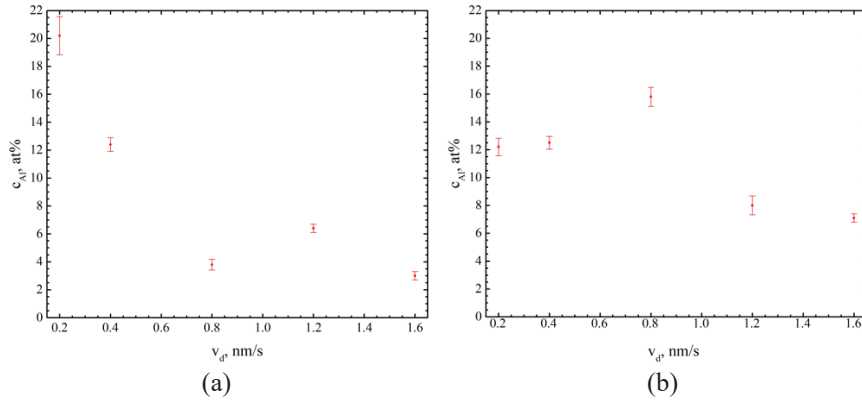


Fig. 4.1. Al concentration in ScAlSZ thin films against the deposition rate: (a) $T_d=300\ ^\circ\text{C}$ and (b) $T_d=600\ ^\circ\text{C}$ [102]

Al concentration changes non-homogeneously with an increase in the deposition rate and substrate temperature (Fig. 4.1 a, b). With an increase in deposition rate, the temperature in the crucible increases, influencing the changes in the evaporate ion rate and vapor concentrations of different elements atoms and atom clusters. The concentration differences can be related to the evaporation mechanism. It is known that Al_2O_3 , Sc_2O_3 , and ZrO_2 pass into the vapor phase during sublimation. The transition of Al_2O_3 into the vapor phase (sublimation) begins at 2072 °C, and in the case of Sc_2O_3 and ZrO_2 , (2485 °C) and (2715 °C), respectively. However, it has been noticed that the sublimation temperature is different. Due to the lower sublimation temperature of Al_2O_3 , the Al concentration in the vapor phase is higher than the concentration of the Sc and Zr. The Al concentration in the formed coatings differs significantly from the initial powder. Al_2O_3 oxide sublimates faster compared to Sc_2O_3 or ZrO_2 oxides. The formation of a thin film with a thickness of $\sim 1500\ \text{nm}$ at lower deposition rates takes a longer time, compared to the formation at higher deposition rates. As a result, given the same thickness of the thin films, a smaller quantity of Al sublimates at a higher deposition rate. Therefore, the existence of metallic Al or its compound phases in ScAlSZ thin films could be the presence of a high concentration of Al or exceeding the solubility limit of $\sim 7\ at.\%$ [172].

4.1.2. Elemental analysis (EDS) of ScAlSZ thin films formed at 450 °C substrate temperature

The content of elemental composition (elements) of ScAlSZ thin films formed at various deposition rates from 0.2 nm/s to 1.6 nm/s at 450 °C substrate temperature was done with the EDS measurements (Table 4.2). It has been found that the deposition rates have a major effect on the chemical composition of formed thin films. Aluminum concentrations were found to be reduced when the deposition rate was increased. When the deposition rate was 0.2 nm/s and 1.6 nm/s, the

concentration of aluminum (Al) was 15.9 at.% and 3.8 at.%, respectively. The content of Sc and Zr atoms is inversely proportional to the concentration of Al atoms. The concentration of Sc was 3.4–7.7 at.%, and the concentration of Zr was 27.4–34.4 at.% when deposition rate was 0.2–1.6 nm/s, respectively.

During the higher deposition rates, Al atom contents were lower, and it could be the result of higher sublimation rate of Al₂O₃. It has already been mentioned above that the melting temperature of the initial material has a significant effect on the resulting materials. Hence, the same thickness thin films could be formed faster at higher deposition rates. Consequently, the lower quantity of Al sublimates at a higher deposition rate [159].

Table 4.2. The elemental composition (EDS) of the thin film surface of ScAlSZ thin films formed at 450 °C substrates temperature, where v_d is the deposition rate, and c_x - atomic concentration of investigating elements [159]

v_d , nm/s	c_{O} , at.%	c_{Al} , at.%	$c_{Al^{3+}}$, at.%	c_{Sc} , at.%	c_{Zr} , at.%
0.2	53.3	15.9	11.8	3.4	27.4
0.4	50.2	22.2	20.1	3.4	24.2
1.2	55.6	1.6	1.4	7.4	35.4
1.6	54.1	3.8	3.5	7.7	34.4
Powder	52.0	12.6	-	3.9	32.5

The crystalline structure depends on the concentration of aluminum, which exceeded the solubility limit, more precisely on Al₂O₃ and Al concentrations. The amorphous phases of Al or Al₂O₃ in the grain boundaries of ScAlSZ crystallites acted as impurities and suppressed the formation of grains. ScAlSZ thin films were amorphous when Al concentration of thin films was 22.2 at.% and crystalline when Al concentration was lower, detailed explanations of the crystallinity of formed thin films was presented by XRD and Raman spectroscopy analyses.

4.2. Chemical analysis by X-ray photoelectron spectrometer XPS

The XPS measurements were set for ScAlSZ and supplemented the EDS analysis. The XPS analyses were performed to analyze the chemical compositions of ScAlSZ thin film. The surface profile of ScAlSZ thin film, containing the presence of OH groups and Sc, Zr, Al, C compounds, is presented in Fig. 4.2 a. Furthermore, a detailed analysis of O1s, Zr 3d, Al 2p, and Sc 2p regions leads to supplement information about the containing compounds (Fig. 4.2 b-e). The obtained core level peaks and literature data were compared, and it has been found that sub-oxide of ZrO_x: 3d_{5/2}, and ZrO_x: 3d_{3/2} peaks are at 181.96 eV BE (binding energy) and 184.36 eV BE and O1s at 530.05 eV BE. The oxygen vacancy peaks presented O1s at 531.40 eV, Sc₂O₃: 2p_{1/2} and Sc₂O₃: 2p_{3/2} are presented at 406.40 eV BE, 401.85 eV BE, respectively, and O1s at 529.65 eV BE, Al₂O₃: 2p at 73.69 eV BE and O1s at 530.85 eV BE. The metallic Al: 2p presented at 72.90 eV BE, AlO(OH) 2p at 74.82 eV BE, OH O1s - 532.70 eV BE, C–O: O1s at 533.17 eV BE, and C=O: O1s at 532.03 eV BE occurs on the ScAlSZ thin films surface [173–177].

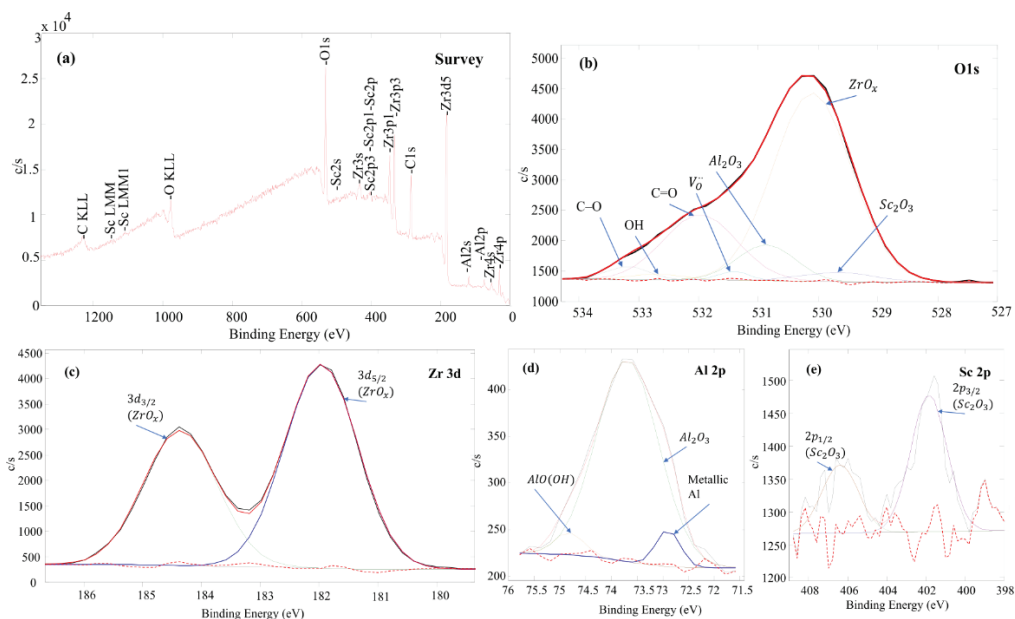


Fig. 4.2. XPS spectra of ScAlSZ thin films ($v_d = 0.2$ nm/s, $T_d = 300$ °C): (a) survey, (b) Zr O1s, (c) Zr 3d, (d) Al 2p, (e) Sc 2p [102]

Moreover, similar XPS spectra peak behaviors and identical Binding energy positions of ScSZ was reported in other authors' data [133]. The OH and CO groups are formed naturally in an ambient environment and do not have any influence on the bulk properties. The high concentrations of metallic Al and Al_2O_3 oxides may affect the structural properties of materials and the existence of ZrO_x and oxygen vacancies [178, 179].

The atomic concentrations calculations of Al^{3+} at ScAlSZ thin films deposited on 450 °C substrates were performed by using Al 2p spectra and survey results, and it was introduced in Table 4.2. The obtained core level Al 2p spectra contain AlO: OH, Al_2O_3 : Al^{3+} , and Al, and they are presented at ~ 75.3 eV BE, ~ 73.8 eV BE, and ~ 72.5 eV, respectively. The peak area ratio was used to calculate the Al_2O_3 : Al^{3+} fraction, which was then multiplied by the Al concentration found in the survey results. Al concentrations were decreasing from 11.8 at.% to 3.5 at.%, while the deposition rates were 0.2 nm/s and 1.6 nm/s, respectively.

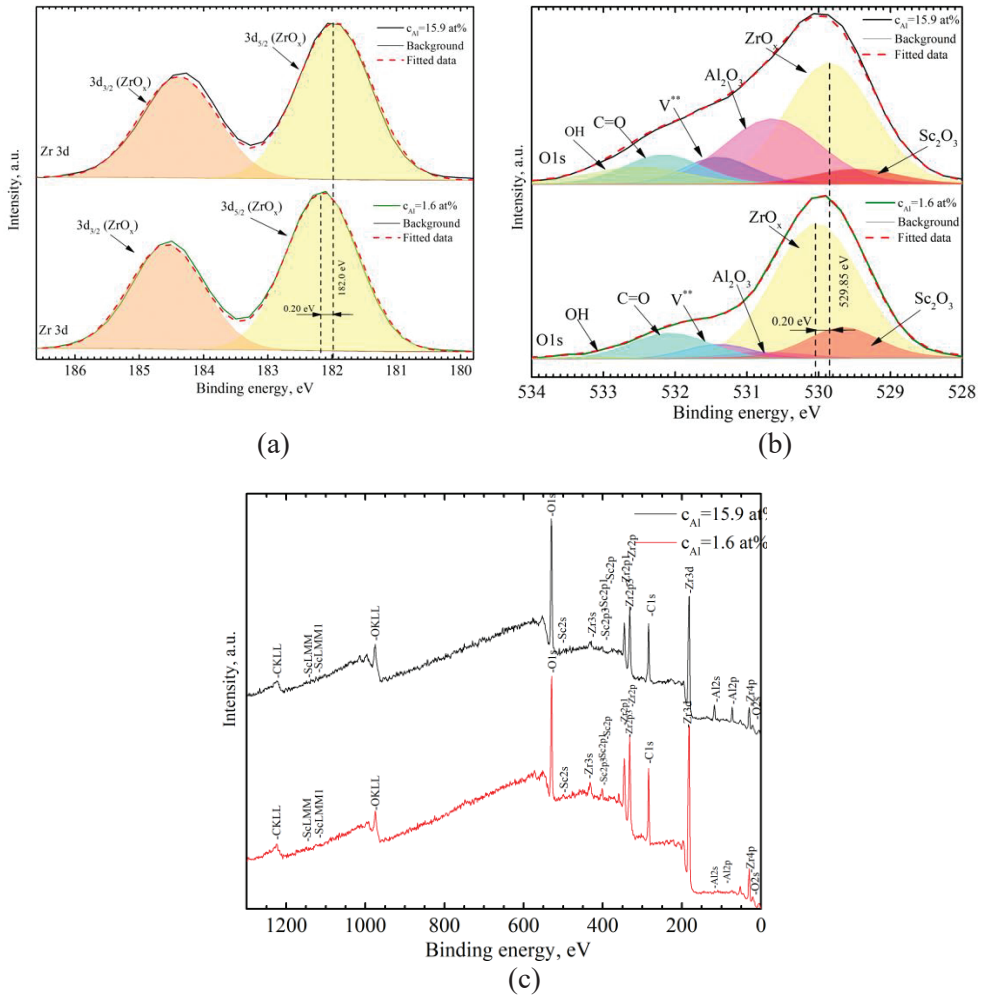


Fig. 4.3. XPS spectra of ScAlSZ thin films: (a) Zr 3d, (b) O 1s, and (c) full surveys of ScAlSZ thin films with 1.6 at.% and 15.9 at.% Al content [159]

The presence of OH groups and Zr compounds for both Al-containing 1.6 at.% and 15.9 at.% thin films is presented in Fig. 4.3 a, b, and the full surface profile of ScAlSZ is shown in Fig. 4.3 c. Zr $3d_{5/2}$ peak position belongs to the Zr^{3+} sub-oxides, and it is presented at ~ 182.0 eV BE. The presence of Zr^{3+} ions may indicate the presence of oxygen vacancies. The O1s core level spectra belongs to the C=O and OH groups, V_o : O^{2-} ions, which is on the oxygen-vacancy region of ZrO_x lattice, Al_2O_3 : Al^{3+} , and ZrO_x : O^{2-} ion [180–186]. Al_2O_3 and V_o peaks were a particularly important part of O1s core level spectra. The enlarged regions suppress a higher concentration of oxygen vacancies with an increase in Al content.

4.3. X-ray diffraction analysis and investigation of the crystal structure of formed thin films

4.3.1. X-ray diffraction analysis of the initial powder

ScAlSZ initial powder was investigated by using X-ray diffractions. The obtained XRD patterns of ScAlSZ powder have a mixed phase. The monoclinic and cubic phases are presented by the data of JCPDS No. 04-014-8566 and JCPDS No. 01-089-5485. The consistence of Al_2O_3 existed in the presence of rhombohedral phases and was presented by the data of JCPDS No. 04-015-8608. Accordingly, all containing peaks and phases of initial powder are marked in the Fig. 4.4. It has been observed that the initial powders mainly contained monoclinic and cubic phases, and it was expressed by sharp peaks at (111), (200), (122), (222), and insignificant peaks at (011), (012), (002), (110), (211), (113), (024), (202), (116), (300) [102].

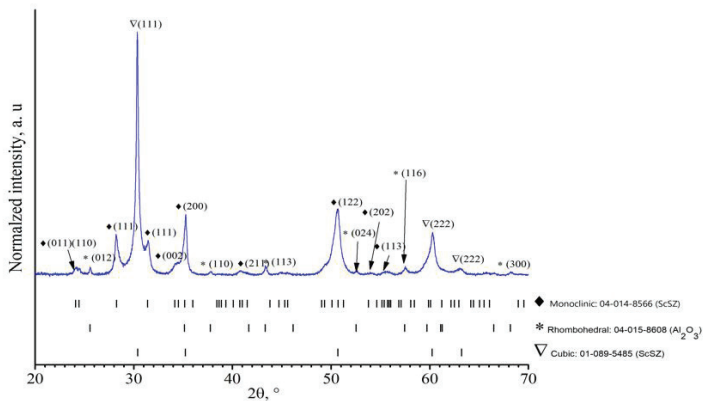


Fig. 4.4. X-ray diffraction (XRD) patterns of ScAlSZ powders [102]

4.3.2. X-ray diffraction analysis and crystallinity ScAlSZ thin films

Oxygen vacancies and other defects in ZrO_2 lattice due to the doping of Sc^{3+} and Al cannot be characterized by the XRD measurements. Furthermore, in this work, X-ray diffraction techniques were used as an additional method for phase determinations of the initial powders and formed thin films ceramics. The Raman spectroscopy techniques were further employed to study the phase of ScAlSZ formed thin films. The XRD diffraction patterns of the deposited ScAlSZ thin films on Alloy-600 at different substrate temperatures and different deposition rates are presented in Fig. 4.5 a, b. The substrate temperature and deposition rate influence the thin ceramic film growth.

The XRD analysis of ScAlSZ thin films formed using a substrate temperature of 600 °C shows that the crystalline structure was observed at all deposition rates, but the thin films deposited at a lower substrate temperature of 300 °C substrates are amorphous at lower deposition rates (0.2–0.4 nm/s) and polycrystalline structure only at higher (0.8–1.6 nm/s) deposition rates. It can be related to the energy of

deposited particles and kinetic energy of the arriving atoms. When the arriving atoms have higher energy, they form a crystalline structure [130, 187]. As it is seen in Fig. 4.5 a, b, the substrate temperature influences the crystallographic orientation. The dominating (200) orientation at a substrate temperature of 300 °C changes to (111) orientation when the temperature is 600 °C. The analysis of the XRD pattern by the search-match approach was obtained that the examining patterns would have peaks corresponding to the cubic phase of Scandia stabilized zirconia and presented by the data of JCPDS No. 01-089-5485. The tetragonal phases were as well recognized during the measurement, and it is presented by JCPDS No. 00-053-0549, corresponding to alumina stabilized zirconia. Moreover, JCPDS No. 01-084-9828 were characterized by the presence of tetragonal phase for pure zirconia. No characteristic peaks of pure Al₂O₃ were observed during the analysis of XRD patterns of ScAlSZ thin films. In addition, it is difficult to unambiguously determine the corresponding phase content and compounds of investigating patterns as a consequence of shift in the peak position and overlapping of those peaks.

Table 4.3. The dependence of crystallite size ($\langle d \rangle$, nm) with substrate temperature 300 °C and 600 °C at different deposition rate for thin films formed on alloy 600

Deposition rate, (v_g) nm/s	Crystallographic orientation				$\langle d \rangle$, nm (200)
	(111)	(200)	(220)	(311)	
Deposition on Alloy600, $\langle d \rangle$ nm, Substrate temperature 300 °C					
0.2	Amorphous structure				
0.4	Amorphous structure				
0.8	16.5	25.3	8	16.5	25.3
1.2	17.8	23.2	12	17.8	23.2
1.6	17.7	22.8	16	17.7	22.8
Deposition on Alloy600, $\langle d \rangle$ nm, Substrate temperature 600 °C					
0.2	11.3	—	—	—	11.3
0.4	16.8	—	—	—	16.8
0.8	16.3	—	—	—	16.3
1.2	17.7	19.3	—	9.8	15.6
1.6	20.0	24.8	—	12.0	18.9

The crystallite size of the ScAlSZ thin ceramic films deposited at 300 °C and 600 °C at different deposition rates for thin films formed on Alloy 600 was calculated from the XRD measurements, and it is presented in Table 4.3. The crystallite size increases with increasing deposition rate and substrate temperature. The deposition rate that is higher than 0.4 nm/s has a minor influence on the crystallite size for the samples deposited at 300 °C substrate temperature. The formed ScAlSZ thin films are amorphous at the lowest deposition rates, i.e., at 0.2 nm/s and 0.4 nm/s. It is possible to see a similar effect when the substrate temperature is 600 °C, i.e., the crystallite size does not change when the deposition rate is 0.4÷1.2 nm/s. The largest crystallites size (18.9 nm) was obtained when the substrate temperature is 600 °C, and the deposition rate is 1.6 nm/s, and the smallest crystallite size was when the deposition rate was 0.2 nm/s. All these crystallite size changes and the dependences could be related to the kinetics surface migration

energy, i.e., evaporating particles have more energy with increasing deposition rate, and that influences their higher mobility and longer surface diffusion length on the substrate surface. The deposited atoms have more energy to migrate and can form the biggest crystallite at higher temperatures [130, 187]. A higher deposition rate can as well cause evaporation of large clusters rather than individual particles, and that as well influences the formation of large crystallites and thin film morphology. However, thin film crystallinity is related to Al concentration and substrate temperature. This means that by decreasing the Al concentration, the crystallinity of the thin films increases, and the same effects occur with an increase in the substrate temperatures. Amorphous phases of Al or Al₂O₃ may occur in ScAlSZ crystallite grain borders and act as impurities. As a result, at high Al concentrations, grain growth was inhibited. However, the decreases in crystallinity were observed due to the Al concentrations increase in ZrO₂ thin films deposited by an atomic layer deposition technique [188].

Furthermore, it has been found that thin films with amorphous phase structure grow while concentrations of Al are 9.7% [189]. At the same time, Ishii [29] reported that increasing Al₂O₃ concentration can lead to the destruction of the oxygen vacancy ordering phenomena of the low-temperature rhombohedral phase. The cubic phase stabilization was obtained at 0.5% [29]. Moreover, the variations of the oxygen content may affect the grain size and phase content [190].

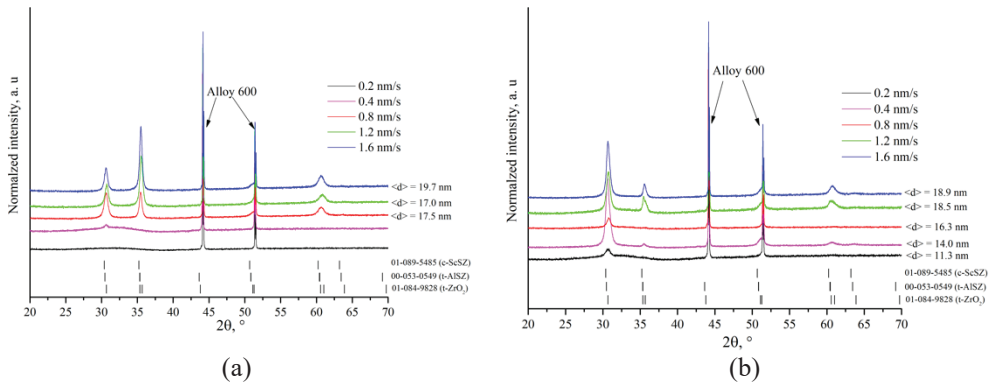


Fig. 4.5. XRD patterns (measured at room temperature) of ScAlSZ thin films deposited on alloy 600 substrates using (a) 300 °C and (b) 600 °C substrate temperature and different deposition rate from 0.2 nm/s to 1.6 nm/s [102]

4.3.3. X-ray diffraction analysis of ScAlSZ thin films at different Al concentrations

The additional XRD diffraction analyses of formed thin films depending on the Al concentrations have been made for deeper investigation of Al co-dopant influence on the phase stabilizations.

The analysis of the results obtained by the XRD method for ScAlSZ thin films has shown that their crystal structure corresponds to the amorphous modification when Al concentration in thin films was 22.2 at.% and crystalline structure when Al concentration was 1.6 at.%, 3.8 at.%, and 15.9 at.%, respectively (Fig. 4.6).

However, the XRD pattern of ScAlSZ thin films containing 15.9 at.% of Al consisted of peaks belonging to the tetragonal phase of zirconia and were detected (JCPDS No. 01-084-9828), and there was detected the (110) orientation, which is forbidden in the cubic crystal lattice and allowed in the tetragonal phase. ScAlSZ thin films with a low concentration of aluminum (1.6 at.% and 3.8 at.%) had a characteristic peak belonging to the cubic phase of scandia stabilized zirconia (JCPDS No. 01-089-5485) and the characteristic peaks of the tetragonal phase of zirconia (JCPDS No. 01-084-9828).

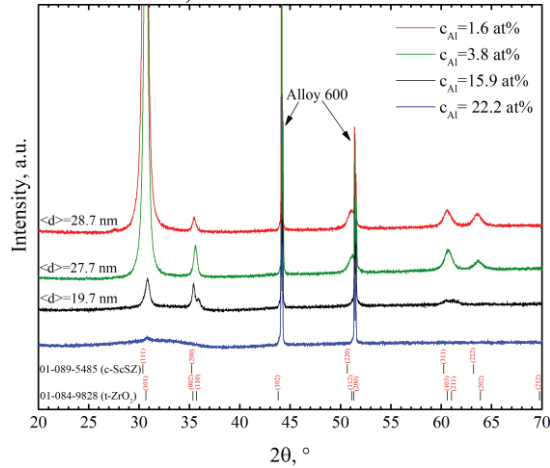


Fig. 4.6. XRD patterns (measured at room temperature) of ScAlSZ thin films deposited on alloy 600 substrates using 450 °C substrate temperature and different Al concentration: 1.6 at.%, 3.8 at.%, 15.9 at.%, and 22.2 at.% [159]

4.3.4. XRD analysis of thin films after thermal annealing

In order to study the phase formation, a cycle of thermal X-ray diffraction of ScAlSZ thin films was formed at 450 °C substrate temperature; in the range of temperature from 30 °C to 900 °C, it was carried out to investigate the changes in the crystalline structure in-situ, while the heating rate was 1 °C per minute. The diffraction patterns of formed thin films during annealing process containing 15.9 at.% and 22.2 at.% Al concentration were presented in Fig. 4.7. Thermal X-ray diffraction patterns show that with relatively rapid heating of the sample, the phase transition and increase of crystallinity does not occur up to 500 °C temperature. However, at the temperature above 500 °C, the corresponding peak in the XRD patterns appeared, and the peak intensity was increased. X-ray phase analysis data confirm the improvement of the crystalline structure; however, due to the overlapping of peaks of the cubic, tetragonal, monoclinic, and rhombohedral phases, it is impossible to determine the exact nature of the phase transition of the investigated samples. Thus, from the data analysis, it can be assumed that the amount of the tetragonal phase increases when the Al concentration is 15.9 at.%, and the amorphous phase transforms into a mixture of cubic, tetragonal, and rhombohedral phases when Al concentration is 22.2 at.%.

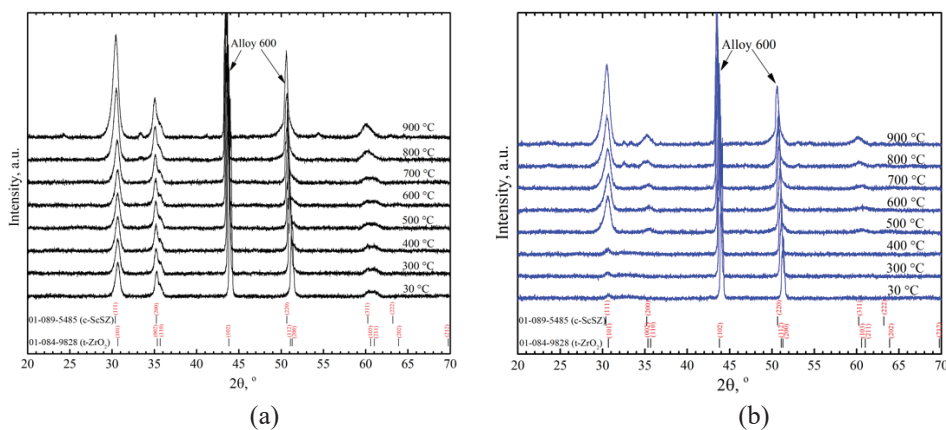


Fig. 4.7. XRD patterns of ScAlSZ thin films during annealing process containing different Al concentration: (a) 15.9 at.%, (b) 22.2 at.% [159]

4.4. Surface roughness analysis of formed thin films

Atomic force microscopy was done in order to study the influence of Al concentration on the parameters of roughness of the nanostructured surface relief of the formed thin films before and after the thermal annealing. AFM pictures show that the concentrations of Al have a major influence on the surface structure and roughness. The roughness parameters of nanostructured surfaces with low Al concentrations thin films (e.g., 1.6 at.%) have a fiber-like structure and roughness of 4.0 nm (Fig. 4.8 a, Fig. 4.10, Table 4.4). However, by increasing the Al concentrations (e.g., 3.8 at.% 15.9 at.%, and 22.2 at.%), there was reached a transition from fiber-like structure to the grained structure, and the surface roughness has decreased to 2.6, 2.2, and 1.9 nm, respectively (Fig. 4.8 b, c, d). Due to the inhibitory influence of Al or Al_2O_3 phases in the grain boundaries, the columns of ScAlSZ thin films with high Al concentrations consist of small grains (globulars) (Fig. 4.8 b, Fig. 4.8 c, d) rather than fibers as in low Al concentration 1.6 at.% case.

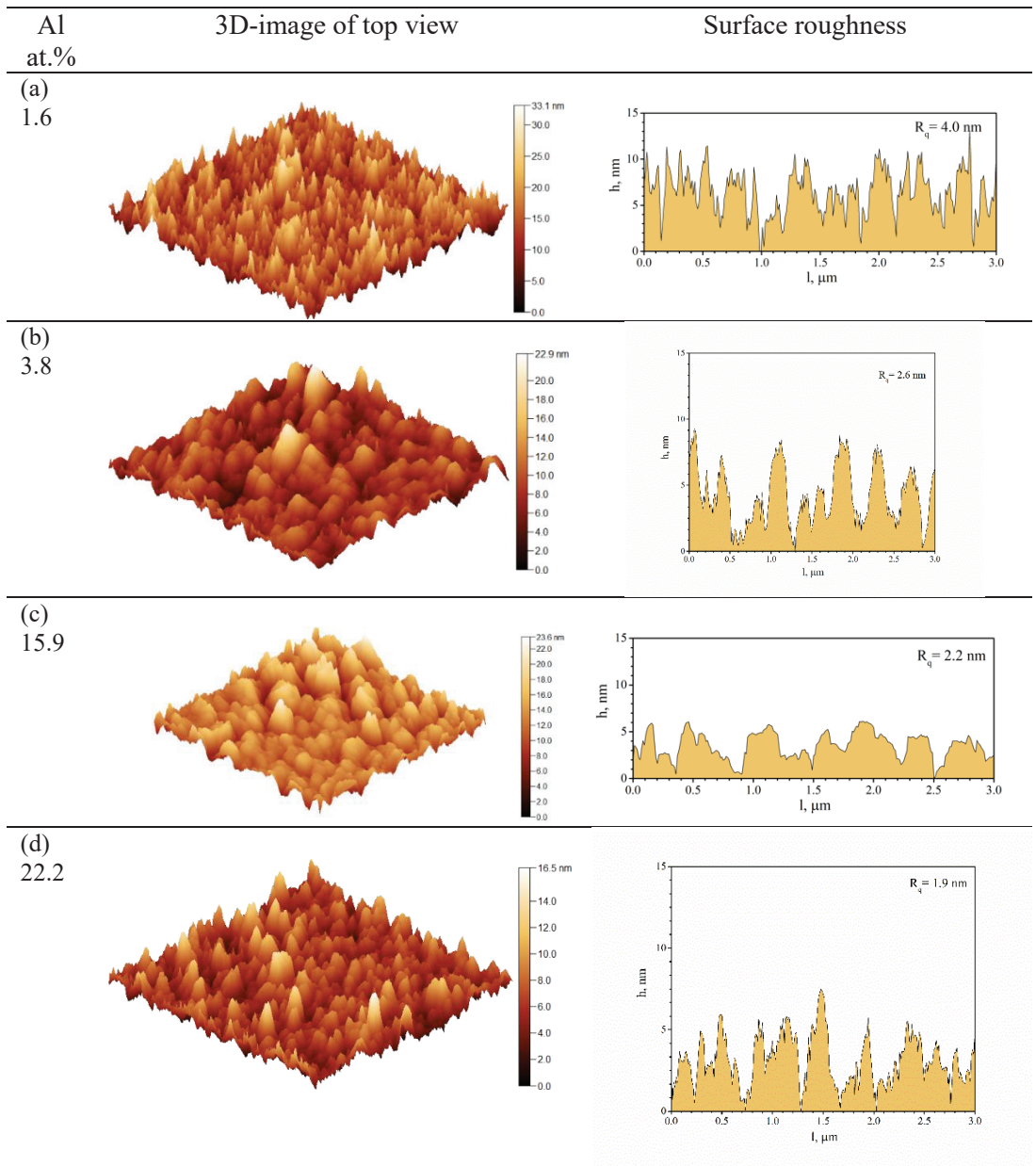


Fig. 4.8. 3D-images of top view and surface roughness (AFM) of ScAlSZ thin films: a) $c_{Al} = 1.6$ at.%, b) $c_{Al} = 3.8$ at.%, c) $c_{Al} = 15.9$ at.%, d) $c_{Al} = 22.2$ at.% [159]

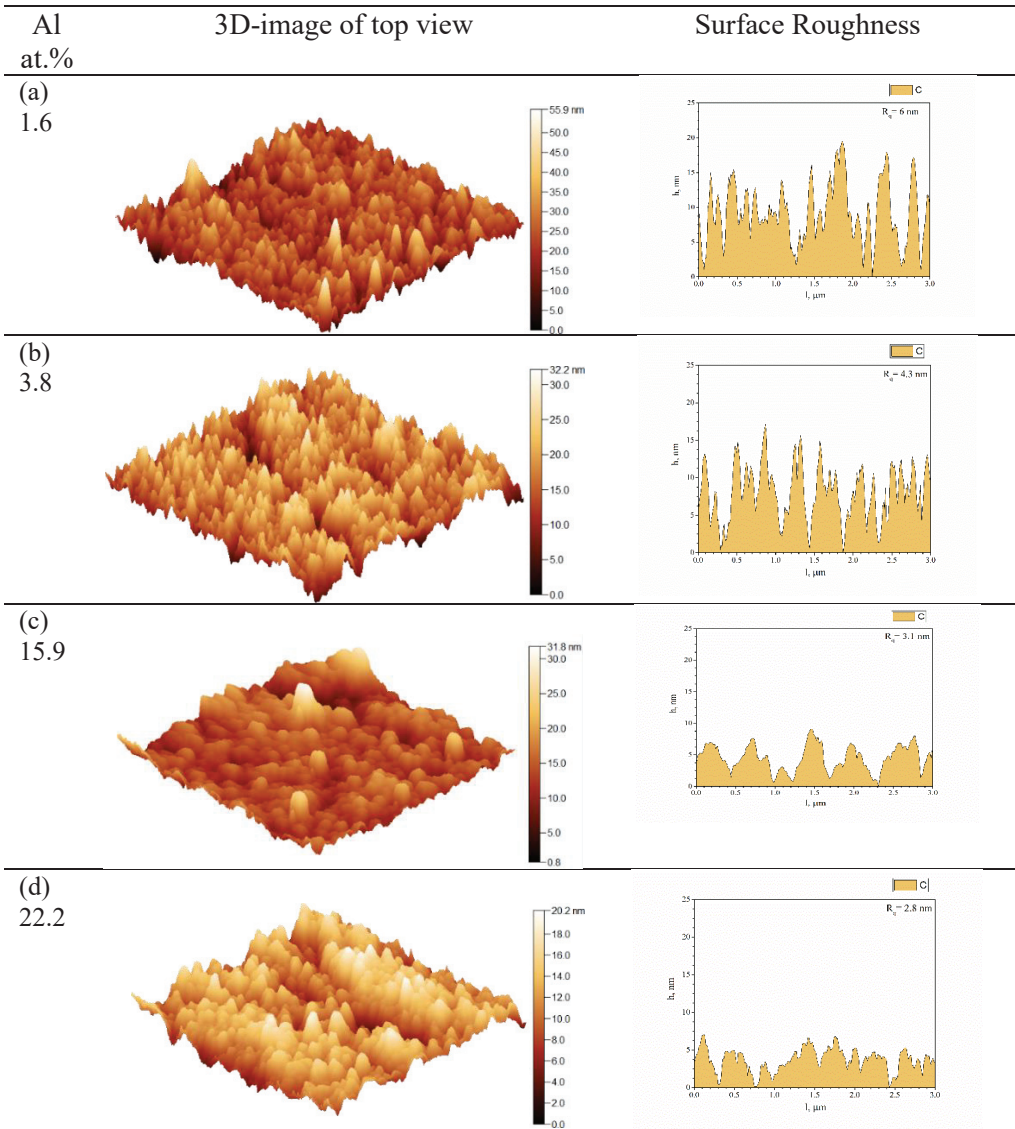


Fig. 4.9. 3D-images of top view and surface roughness (AFM) of SCAISZ thin films after annealing: a) $c_{Al} = 1.6$ at.%, b) $c_{Al} = 3.8$ at.%, c) $c_{Al} = 15.9$ at.%, d) $c_{Al} = 22.2$ at. %

Table 4.4. Surface roughness of ScAlSZ thin films ○ as-deposited and ○ after annealing samples

Al concentration, at. %	○ as-deposited R_q , nm	○ after annealing R_q , nm
1.6	3.966	5.967
3.8	2.572	4.288
15.9	2.179	3.121
22.2	1.94	2.845

After annealing, the microstructure of ScAlSZ thin films was examined. The surface roughness of ScAlSZ thin films increased 1.5 times for all thin films, according to the AFM measurements (Fig. 4.9 a, b, c, d, Fig. 4.10, Table 4.4). With increasing Al content from 1.6 at.% to 22.2 at.%, the surface roughness fell from 6.0 nm to 2.8 nm. The increases in the surface roughness after thermal annealing might be explained by the mobility of adatoms on the surface under temperature during thermal annealing. At high temperatures, the mobility of adatoms is high enough for them to be incorporated between each other, preconditioning a predominant grain growth. Accordingly, with grain growth, the average value of the measured deviations of individual heights and depths from the mean line (Root mean square roughness, R_q) increases as well. Moreover, a similar tendency of surface roughness increase by temperature ramping was reported by other authors [191, 192].

There were no additional alterations in the microstructure. Thin films remained consistent with no obvious splits or pores.

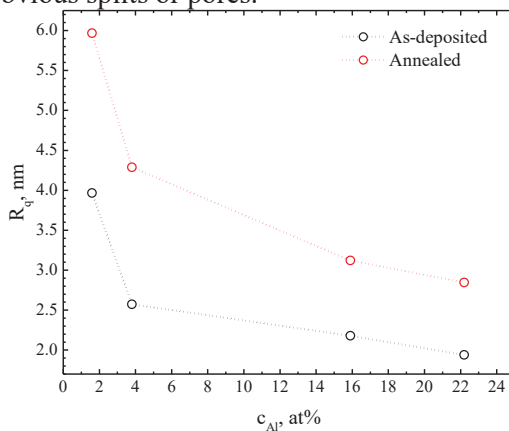


Fig. 4.10. Surface roughness of ScAlSZ thin films: ○ as-deposited and ○ after annealing [159]

4.5. Analysis of Raman spectra

It should be noted that in contrast to the XRD method, which is an integral method, the Raman spectroscopy method is the most sensitive to the local environment of oxygen ions in these structures. Therefore, the Raman spectroscopy method is as well used in this work to reveal the features of the phase composition of $Sc_2O - ZrO_2$ and $ZrO_2 - Sc_2O_3 - Al_2O_3$ crystals. For the excitation of the Raman

spectra in this work, the radiation with $\lambda = 532$ nm wavelength diode green laser was chosen, because the radiation with different wavelength leads to the excitation of ion luminescence.

4.5.1. Raman spectra analysis of ScAlSZ initial powder and formed thin films

Raman spectroscopy measurements of initial ScAlSZ powder are represented by the expression of peaks: 147, 178, 190, 221, 261, 332, 381, 418, 473, 536, 559, 620, 635 cm^{-1} and around 750–1000 cm^{-1} positions, and the spectra were compared with the data from the literature (Fig. 4.11). The obtained Raman results were in good agreement with the XRD analysis of initial powder (Fig. 4.4) and show the same behavior on structural properties. The Raman spectra of ScAlSZ powders contain mixed phases and are represented by (m-ZrO₂), (c-ZrO₂), (t-ZrO₂), and β -rhombohedral phases, which are initiated by Al₂O₃ oxide. The tetragonal phases were not observed during the XRD analysis of the powder. Nevertheless, the tetragonal phases were detected by using Raman spectroscopy. Raman spectra consist of several peaks assigned for monoclinic ZrO₂ and represented by: 3-A_g modes at 178–190 cm^{-1} , 473 cm^{-1} , 559 cm^{-1} and 3-B_{1g} modes at 221 cm^{-1} , 332 cm^{-1} , 381 cm^{-1} [122, 126, 130–132]. The expression of Tetragonal phases peaks are represented by B_{1g} at 147 cm^{-1} , E_g at 261 $\text{cm}^{-1}, A_{1g} at 635 cm^{-1} [10, 117, 118, 131, 133]. The Raman mode of cubic phase (Fm3m) has not been observed, and it should be containing only one Raman active vibration peak presented at F_{2g} mode, expressed between ~ 605 and 630 cm^{-1} [10, 50, 117, 126, 130, 134]; however, the investigated Raman spectra do not contain peaks at around ~ 418 cm^{-1} , corresponding to Al₂O₃ [134].$

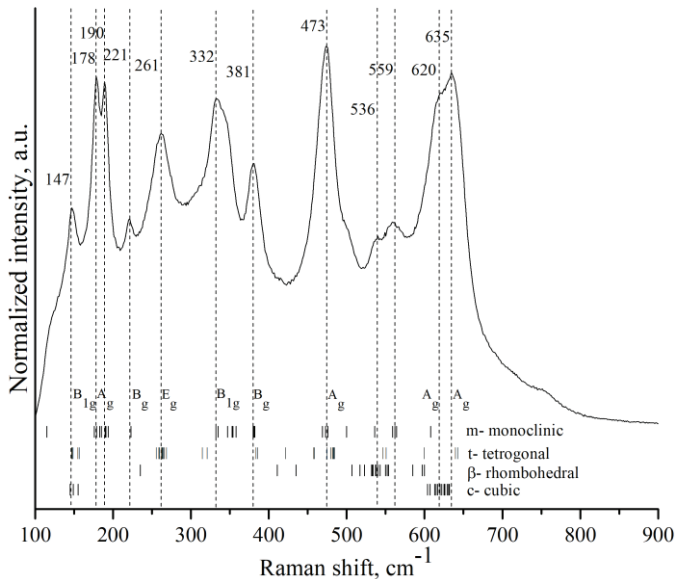


Fig. 4.11. Raman spectra of ScAlSZ initial powder [102], monoclinic [10, 50, 122, 126, 130–132, 133], tetragonal [10, 50, 117, 118, 122, 126, 131, 132, 133], rhombohedral [50, 130, 154], Cubic [10, 50, 117, 122, 126, 130–132]

The peak at 261 cm^{-1} is purely attributed to t-ZrO₂, while the peak at 178 cm^{-1} is attributed to m-ZrO₂. There are two Raman bands at 473 and 635 cm^{-1} , corresponding to both monoclinic and tetragonal phases. In such cases, the attention should be paid to the intensity of these bands. For instance, if the Raman bands at 473 cm^{-1} are stronger than the bands at 635 cm^{-1} , this may belong to monoclinic phases and vice versa for tetragonal phases. In addition, the monoclinic phase bands expressed between 473 and 635 cm^{-1} are not detected in the tetragonal phase [193].

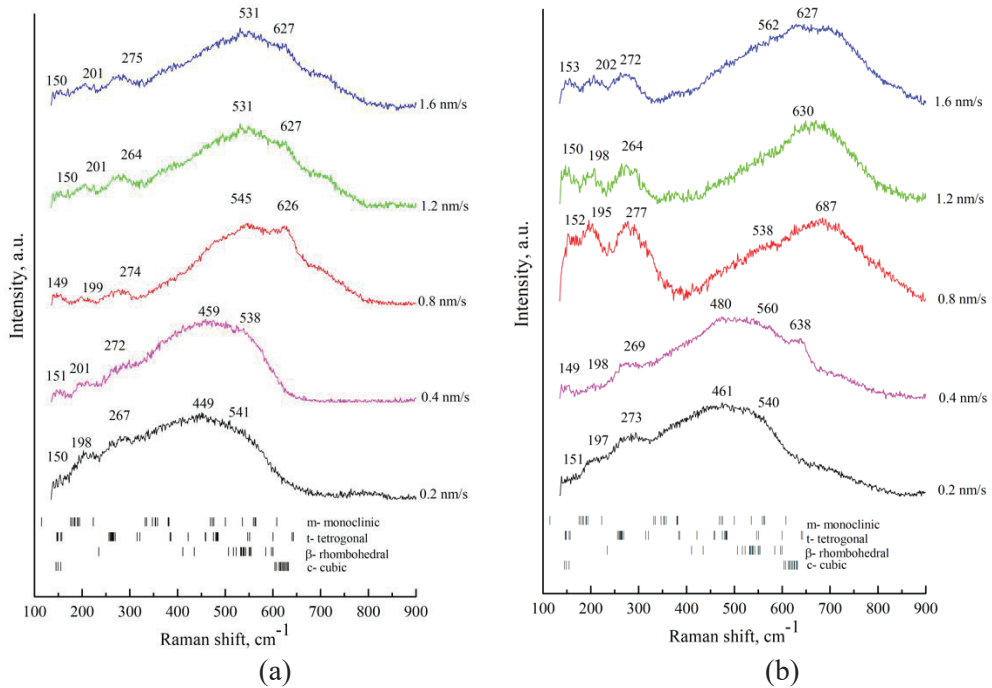


Fig. 4.12. Raman spectra of ScAlSZ thin films deposited on alloy 600 substrates using (a) $300\text{ }^{\circ}\text{C}$ and (b) $600\text{ }^{\circ}\text{C}$ substrate temperature and different deposition rate from 0.2 nm/s by 1.6 nm/s [102], monoclinic [10, 50, 122, 126, 130–133], tetragonal [10, 50, 117, 118, 122, 126, 131–133], rhombohedral [50, 130, 154], Cubic [10, 50, 117, 122, 126, 130–132]

Raman measurements were used to completely characterize the structure of ScAlSZ thin films. Raman spectra of ScAlSZ thin films contain a series of overlapping peaks that may indicate polymorphism. After extensive investigation of Raman, the peaks have been identified as the presence of monoclinic (m-ZrO₂), tetragonal (t-ZrO₂), rhombohedral (β -ZrO₂), and cubic (c-ZrO₂) phases (Fig. 4.12). Raman bands are represented by the expression of peaks: $150, 200, 264, 460, 540, 627, 638\text{ cm}^{-1}$, and the additional peaks expressed between $770\text{--}900\text{ cm}^{-1}$ may belong to the monoclinic and tetragonal phases. These peaks could be explained as a Raman active lattice phonon [122, 132]. Raman spectra shift within the peak positions can be explained by the presence of structural heterogeneity of the material. The band appears in the Raman spectra at above 800 cm^{-1} , the intensity of

which is poorly visible and can be assigned to the second-order active Raman mode [194]. By the presence of Raman peaks between 149 cm^{-1} and 277 cm^{-1} , which consist of several peaks, one can speak of the formation of different ZrO_2 phases. Raman band around 198 cm^{-1} A_g mode correspond to the peaks of monoclinic phase ZrO_2 [126, 130, 131]. The group theory describes the presence of six Raman modes ($A_{1g} + 2B_{1g} + 3E_g$) for tetragonal ZrO_2 , while the cubic phase shows the presence of one Raman mode F_{2g} (between 605 and 630 cm^{-1}), and some modes for the tetragonal phase may be absent. Raman peaks expressed around 540 cm^{-1} belong to the rhombohedral phase [10, 130]. Raman peaks in the low-frequency range 149 – 153 cm^{-1} and around 638 cm^{-1} correspond to the A_{1g} mode and can be as an indicator of the t- ZrO_2 phase [10, 117, 118, 131, 133]. The cubic (c) phase was presented by the weak broad peaks between 626 and 630 cm^{-1} (Fig. 4.12). It should be noted that some of the bands for the cubic phase are shifted towards the higher wavenumbers values of the Raman spectra, and it could be related to the oxygen sub-lattice disorder caused by Sc_2O_3 and Al_2O_3 doping and co-doping [10, 117, 126, 130]. Furthermore, wavenumber shifting can be caused by a variety of factors, including changes in atomic distances, lattice contraction, and expansion. As a result, thin films ScAlSZ are polymorphic and contain monoclinic (m- ZrO_2), tetragonal (t- ZrO_2), rhombohedral (β - ZrO_2), and cubic (c- ZrO_2) phases. The cubic symmetry must be expressed by a broad band about 620 – 630 cm^{-1} , which is not detected in Raman spectra of ScAlSZ thin films deposited at 0.2 nm/s and 0.4 nm/s at $300\text{ }^\circ\text{C}$ and 0.2 nm/s , 0.4 nm/s , 0.8 nm/s at $600\text{ }^\circ\text{C}$, excluding the Raman peaks at those regions where the existence of the cubic phase has been proven. The peaks around 687 cm^{-1} can be interpreted as anomalous luminescence bands.

The low-intensity additional modes that should not appear for the cubic fluorite structure could be explained by the substitution of Zr^{4+} ions that are replaced by Sc^{3+} ; the excess of negative charges appears, which is compensated by the appearance of violation of the selection rules, which directly depends on the oxygen vacancies (V_o) [128, 129].

Table 4.5. The ratio of cubic, tetragonal, and monoclinic phases in the ScAlSZ thin films [102]

Deposition Rate (nm/s)	Substrate Temperature, $^\circ\text{C}$					
	300 $^\circ\text{C}$		600 $^\circ\text{C}$		300 $^\circ\text{C}$	
	monoclinic	tetragonal+ rhombohedral	monoclinic	tetragonal+ rhombohedral	monoclinic	cubic
0.2 nm/s	35%	28%	65%	72%	0%	0%
0.4 nm/s	19%	12%	81%	88%	0%	0%
0.8 nm/s	6%	54%	41%	46%	53%	0%
1.2 nm/s	19%	20%	26%	26%	55%	53%
1.6 nm/s	19%	18%	26%	23%	55%	59%

According to the Raman spectroscopy parameters obtained in this work, the ratios of the cubic phase to the monoclinic, tetragonal phases are from 53% to 59% for ScAlSZ and are generally around 55% (Table 4.5). The amount of cubic phase increases significantly when the depositing rate is increased. In agreement with the

Raman data, the cubic phase is not detected at 0.2 and 0.4 nm/s deposition rates. However, the existence of broad bands in Fig. 4.12, which indicate local disorder, could be due to a non-stoichiometric phase of ZrO_2 and a poorly crystallized Zr^{4+} and Sc^{3+} structure. It has been determined that thin films deposited at low deposition rates are of a mixed phase (m- ZrO_2) and (t- ZrO_2).

4.5.2. Raman spectra analysis of ScAlSZ thin films at different Al concentrations

The XRD analysis of ScAlSZ thin films, formed using 0.2, 0.4, 1.2, and 1.6 nm/s deposition rate at 450 °C substrate temperature with 1.6, 3.8, 15.9, and 22.2 at.% of Al concentrations, was supported by Raman spectroscopy measurements. Furthermore, it has been found that the monoclinic phase is presented in all thin films. Moreover, the thin films formed tetragonal and monoclinic phases at 22.2 at.% concentration of aluminum. Even though the XRD analysis revealed an amorphous phase, Raman measurements prove the presence of amorphous phases in this case. Raman spectrum of ScAlSZ thin film has a set of peaks, which belong to the monoclinic (m- ZrO_2), tetragonal (t- ZrO_2), and cubic (c- ZrO_2) phases (Fig. 4.13, Table 4.6). The cubic phase is represented by the detected peaks at 626 cm^{-1} and 628 cm^{-1} . Tetragonal phase is represented by: 148, 149, 150, 152, 264, 265, 273, 278, 337, 464, 463, 471, 483 cm^{-1} , while the peaks corresponding to the monoclinic phases can be found at 199, 200, 201, 202, 375, 382 cm^{-1} [10, 50, 122, 126, 130–134].

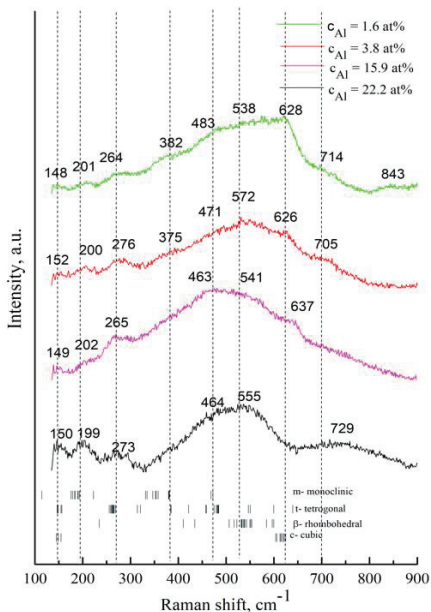


Fig. 4.13. Raman spectra of ScAlSZ thin films [159], monoclinic [50, 118, 122, 126, 130, 134], tetragonal [50, 118, 122, 126, 130, 132, 134], rhombohedral [50, 118], cubic [50, 118, 122, 126, 130, 134, 174]

Table 4.6. The ratio of monoclinic, tetragonal, and cubic phases of deposited ScAlSZ thin films [159]

ScAlSZ phase	$c_{Al} = 1.6$ at. %	$c_{Al} = 3.8$ at. %	$c_{Al} = 15.9$ at. %	$c_{Al} = 22.2$ at. %
Monoclinic	22%	18%	18%	31%
Tetragonal	42%	40%	82%	69%
Cubic	36%	42%	0%	0%

The presence of high concentrations of metallic Al can affect the structural properties of the thin film. It can be said that crystallinity can be directly associated with Al concentration. Thin films are polymorphic and normally consist of monoclinic, tetragonal, and cubic phases. Therefore, high Al concentration thin films restrain the cubic phase formation. The optimum conditions for thin films with stable cubic structures can be obtained by higher deposition rates and higher substrate temperature [102].

4.5.3. Raman spectra analysis of ScAlSZ thin films at different Al concentrations after thermal annealing

Since no evidence for the formation of cubic phase was found by Raman spectroscopy of formed thin films at 15.9 at.% and 22.2 at.% concentration of aluminum, in order to investigate any imperceptible phase transition and lattice distortion, Raman spectroscopy analyses of thin films after the thermal annealing process were utilized (Fig. 4.14). The Raman spectrum of the ScAlSZ annealed thin films displayed a different spectra shape compared to the deposited. It has been observed that the Raman spectrum contained several peaks belonging to tetragonal phases and was expressed by 150 cm^{-1} (A_{1g}), 265 cm^{-1} (E_g), 460 cm^{-1} (A_{1g}), 645 cm^{-1} (A_{1g}) [10, 102, 117, 118, 131], and the peaks at 202 cm^{-1} and 346 cm^{-1} can be assigned to the monoclinic (m-ZrO₂) phase [126, 130, 131]. Rhombohedral (β - ZrO₂) phase is presented in these spectra as weak broad peaks at approximately 535 cm^{-1} (B_g) and sharp peaks at about 560 cm^{-1} (A_g) [10, 50, 130]. A broad line peak between 600 cm^{-1} and 630 cm^{-1} should be described as a Raman active vibration (F_{2g}) of the cubic (c-ZrO₂) phase [50, 102, 133]. The Raman peaks at 621 cm^{-1} (F_{2g}) and 645 cm^{-1} (A_{1g}) are merged into one broad peak, possibly due to the impurities at the grain boundaries. The peaks indicating the cubic (c) phase of ZrO₂ are not prominently expressed [117]. Finally, peaks 695 cm^{-1} and 698 cm^{-1} could be explained by a Raman active lattice phonon and could be mixed phases.

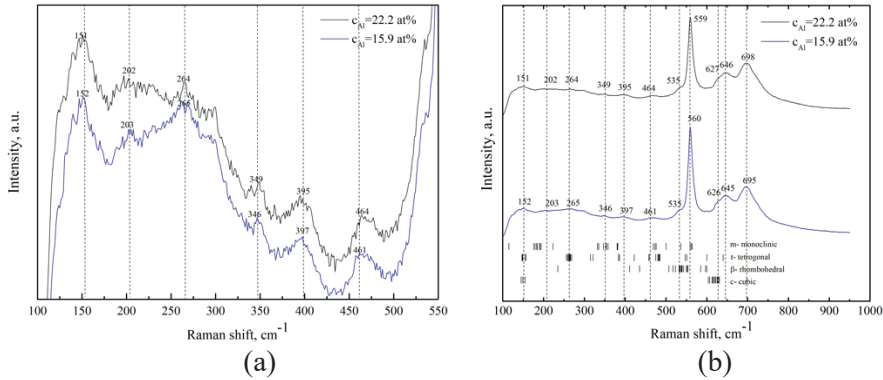


Fig. 4.14. Raman spectra measurements of ScAlSZ thin ceramic films deposited on Alloy600 in the annealing process (30–900 °C): containing 15.9 at.% and 22.2 at.% of Al consisted (a) range of 100 cm^{-1} to 550 cm^{-1} , (b) range of 100 cm^{-1} to 900 cm^{-1} [159], monoclinic [50, 118, 122, 126, 130, 134], tetragonal [50, 118, 122, 126, 130, 132, 134], rhombohedral [50, 118], cubic [50, 118, 122, 126, 130, 134, 174]

The calculations of phase composition ratio that were estimated from Raman spectra are presented in Table 4.7. According to the calculations of the phase ratio, tetragonal and rhombohedral phases account for 61% of the total, while cubic (24%) and monoclinic (16%) are lesser before the annealing process. The phase ratio of the monoclinic phase of formed thin films at 15.9 at.% and 22.2 at.% concentration of aluminum are decreased by -4% and -13%, respectively. However, the amount of cubic phase is increased by +24%, and the rhombohedral phase was formed. However, due to the overlapped peaks of tetragonal and rhombohedral phases in Raman spectra, the amount of rhombohedral phase could not be determined. Based on the performed studies, it can be concluded that after annealing thin ScAlSZ films containing 15.9 at.% and 22.2 at.% aluminum, thin films were presented in a presence of cubic and rhombohedral phases as well as monoclinic and tetragonal phases.

Table 4.7. The ratio of monoclinic, tetragonal and rhombohedral, and cubic phases of annealed ScAlSZ thin films [159]

ScAlSZ phase	$c_{\text{Al}} = 15.9 \text{ at.}\%$	$c_{\text{Al}} = 22.2 \text{ at.}\%$
Monoclinic	16%	15%
Tetragonal + Rhombohedral	61%	61%
Cubic	23%	24%

4.6. Investigation of the surface morphology of thin films by scanning electron microscopy

The surface morphology of the obtained thin coatings was studied by using scanning electron microscopy (SEM). In general, thin films have a similar porous surface morphology. It has been found that the surface morphology of formed thin films at 300 °C and 600 °C substrate temperature are homogenous and do not have

any visible cracks and defects (Fig. 4.15 a, b, c, d, e). The absence of cracks or any defect in formed thin films could be related to the phase content and internal stress of unit cells. The quantitative analysis of phase content was presented by the results of XRD and Raman spectroscopy analysis, and the content of the monoclinic phase is around ~20%. The formed thin films are mainly containing tetragonal or cubic phases. The monoclinic phase is formed from the tetragonal by shear deformation and large volume increase of the whole unit cell. The shear deformation and large volume collectively establish the internal stress, which could lead to the cracking of ceramics. The magnitude of internal stresses depends on the rate of atoms surface diffusivity. Hence, when the surface diffusivity rate is high, less internal stress occurs in the unit cells. As mentioned above, during the $t\text{-ZrO}_2 \leftrightarrow c\text{-ZrO}_2$ phase transitions, no essential restructuring occurs in the crystal lattice. In addition, thin films formed at 600 °C substrate temperature have an increase in grain size and grain boundaries.

The cross-section analysis shows that formed thin films have a columnar growth of the structure. The cross-section analysis presents that thin films were formed at 300 °C substrate temperatures and 1.6 nm/s deposition rate; the layer structure grows into small grains (Fig. 4.16, a). The grains increase with increasing temperature while thin films are formed at 600 °C substrate temperature and 1.6 nm/s deposition rate (Fig. 4.16 b); the grains begin to form columns by the mechanism grains that grow on top of each other.

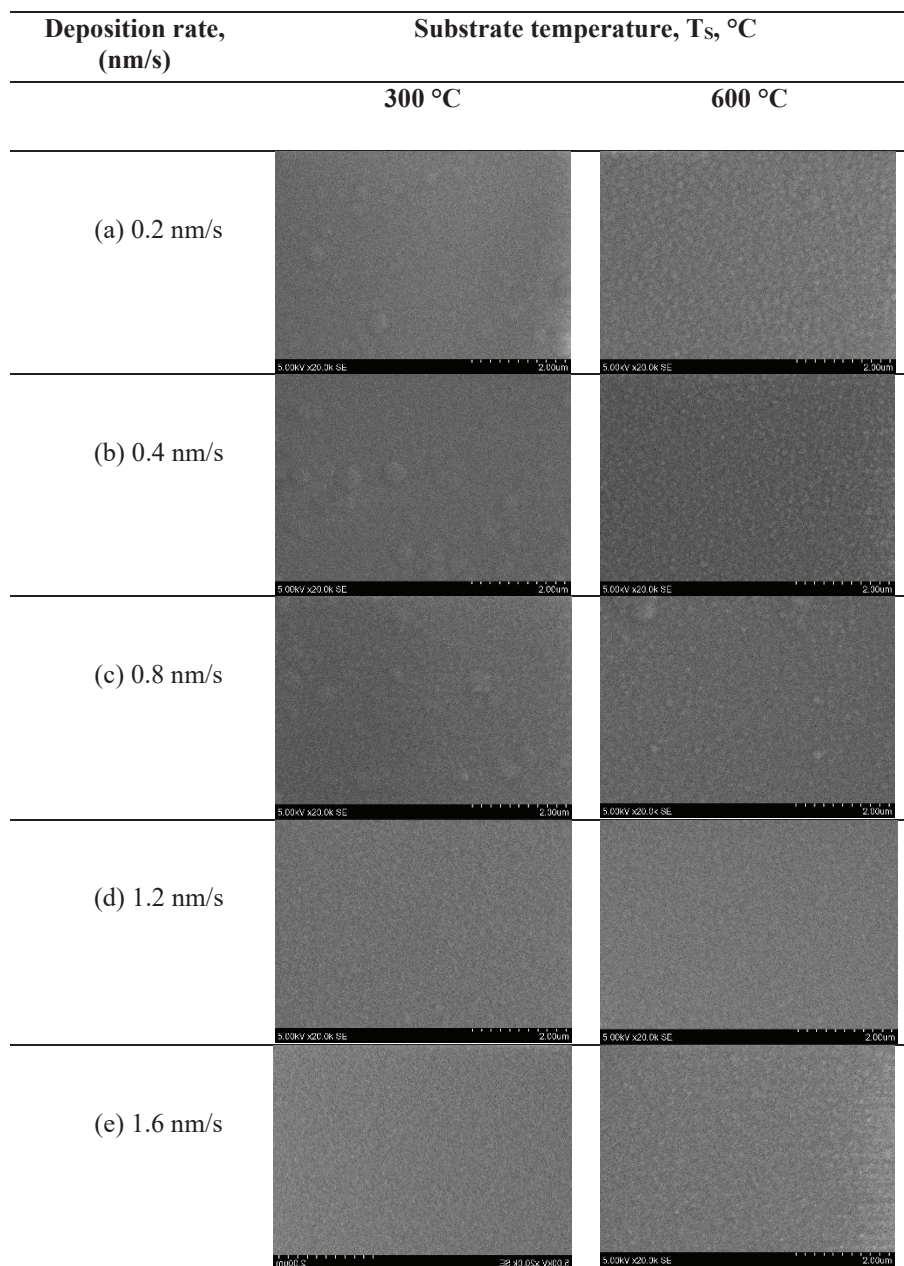


Fig. 4.15. Topographic images view (SEM) of ScAlSZ thin films formed at 300 °C and 600 °C at different deposition rate: (a) 0.2 nm/s, (b) 0.4 nm/s, (c) 0.8 nm/s, (d) 1.2 nm/s, (e) 1.6 nm/s

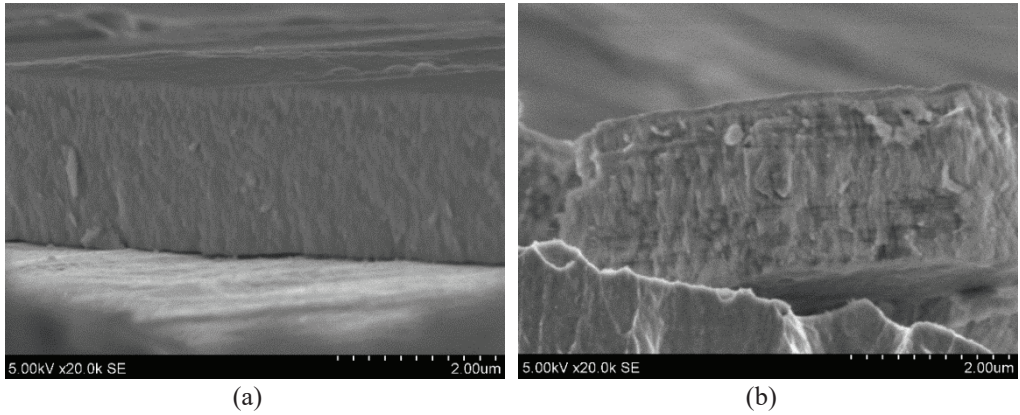


Fig. 4.16. Cross section images view (SEM) of ScAlSZ thin films formed at (a) 300 °C substrate temperature and 1.6 nm/s deposition rate, (b) 600 °C substrate temperature and 1.6 nm/s deposition rate

The surface morphology of the obtained thin films with different Al concentrations was as well studied by using scanning electron microscopy by surface view images and cross-section view (SEM) (Fig. 4.17). It has been established that thin films containing low Al concentrations were clearly presented with the bigger grains that thin films formed at higher Al concentrations. Cross-section analysis shows that the formed thin films have a columnar growth of the structure. The formed thin films preferential orientations of layer growth changes are presented in the XRD analysis.

Concentrations of Al, at. %	Topographic view	Cross section view
(a) 1.6 at. %		
(b) 3.8 at. %		

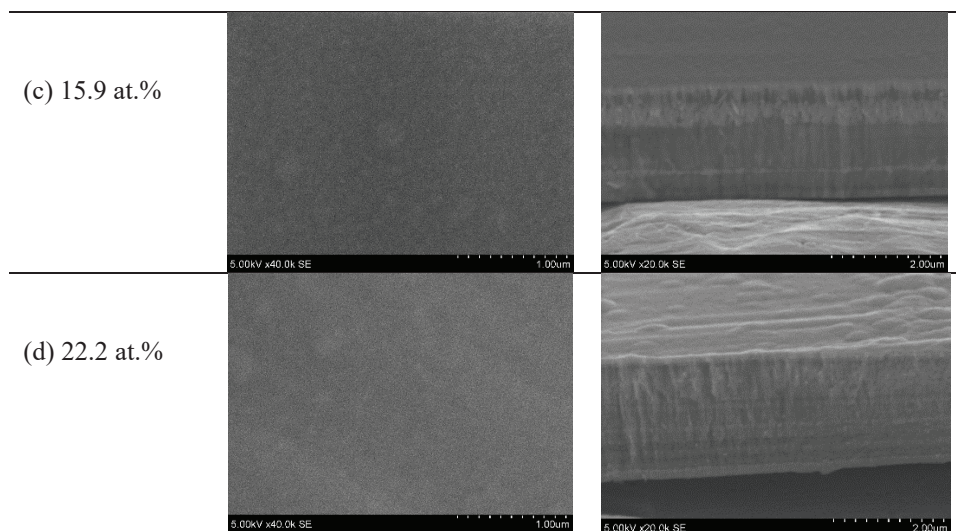


Fig. 4.17. Topographic and cross section images view (SEM) of ScAlSZ thin films formed with different Al concentrations in 300 °C and 600 °C at different deposition rate: (a) 0.2 1.6 at.%, (b) 3.8 at.%, (c) 15.9 at.%, (d) 22.2 at.%

4.7. Investigation of electrical properties of formed thin films

The electrolyte ionic conductivity depends on the dopant atomic radii, dopant concentration, electrostatic interactions between dopants and oxygen vacancies, and the composition of a phase. There are more phases that reduce the ionic conductivity. Alumina co-dopants as aliovalent dopants affect the ionic conductivity of zirconia-based ceramics by increasing the oxygen vacancy concentration after the co-doping.

4.7.1. Impedance for ScAlSZ thin films

The investigations of the electrical properties of ScAlSZ thin film formed at 300 °C and 600 °C substrate temperature were performed using a ProboStat device. The formed thin ceramic layers were investigated by the two-probe method. The impedance measurements were conducted in air over the temperature range between 200 and 1000 °C. These measurements were obtained over the frequency range of 0.1 Hz to 1 MHz. The complex resistance $Z = Z' + jZ''$ was measured in an electric field. The bulk ceramics conductivity was estimated of the formed ScAlSZ by impedance spectra. The grain boundary resistance is very small, for adding the same amount of Al_2O_3 , compared with the grain resistance, and it was considered that $R_{\text{bulk}} = R_{\text{g}} + R_{\text{gb}}$ [168].

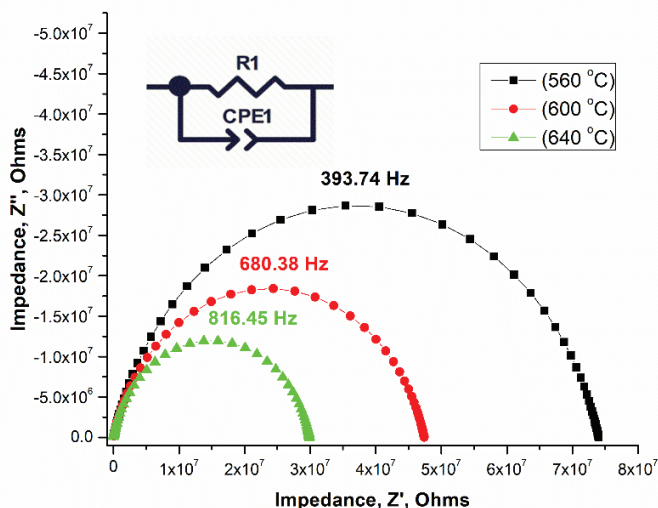


Fig. 4.18. Dependencies of $Im(Z) = Z''$ ($Re(Z) = Z'$) ScAlSZ formed thin films deposition rate of 0.4 nm/s at different temperatures

The change in the complex resistance by increasing the temperature is presented in Fig. 4.18. The relaxation frequency of the ceramics changes with the increasing temperature, shifting to a higher frequency range.

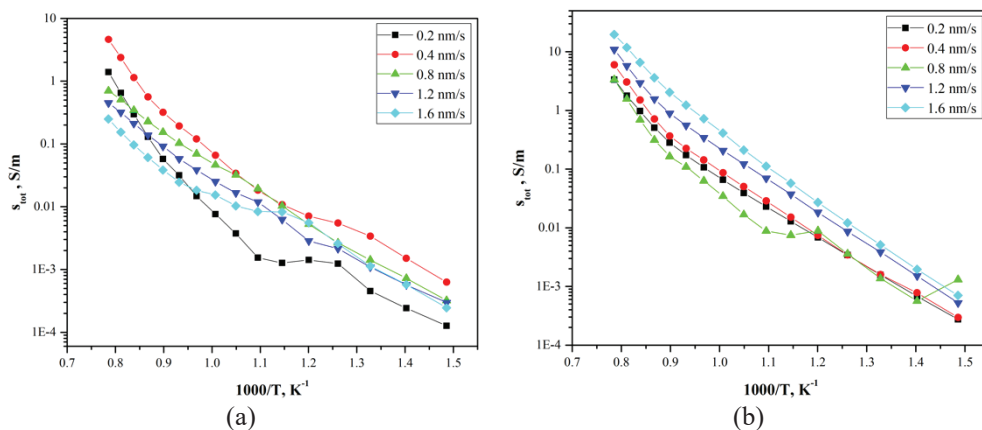


Fig. 4.19. The bulk ionic conductivity as a function of temperature at different deposition rates from 0.2 nm/s to 1.6 nm/s: (a) substrates temperature 300 °C, (b) substrates temperature 600 °C

The electrical properties of ZrO_2 based ceramics are significantly dependent on the temperature. The main information about the nature of temperature dependence is provided by the dependence of resistivity logarithm on the reciprocal temperature. Fig. 4.19 shows graphs of temperature dependences of formed thin films. The

activation energy for the diffusion of oxygen ions was determined from the values of ionic conductivity as a function of inverse temperature. The angle increase of the line with the abscissa: the activation energy monotonically increases. The diffusion activation energies are presented in Table 4.8. The bulk ScAlSZ conductivity is mainly composed of the grain conductivity, and the grain boundary conductivity cannot be estimated. The grain boundary resistance is very small, and it can be related to ScSZ co-doping by small amount of Al₂O₃ [114, 195]. The activation energy dependence on the crystallite size has been observed, and the activation energy increases as the crystallite size increases (Table 4.3, Table 4.8). The lowest activation energy was estimated when the temperature of the substrates was 300 °C. The best bulk ionic conductivity in these investigated samples was $\sigma_{bulk} = 1.01$ S/m at 800 °C temperature; the activation energy $E_a = 1.13$ eV was achieved when the deposition rate of 1.6 nm/s and temperature of the substrate was 600 °C.

Table 4.8. Bulk ionic conductivity (σ_{bulk}) at 800 °C temperature and their activation energy (E_a) of ScAlSZ thin ceramic films formed at different deposition rate

Deposition rate, nm/s	Temperature range			
	300 °C		600 °C	
	σ , S/m	E_a , eV	σ , S/m	E_a , eV
0.2		—	0.51	1.15
0.4		—	0.27	1.04
0.8	0.11	0.94	0.13	0.98
1.2	0.08	0.96	0.53	1.09
1.6	0.12	0.99	1.01	1.13

4.7.2. Impedance for ScAlSZ thin films formed with different Al concentration

Electrochemical Impedance Spectroscopy methods were used to study the electrical properties that take place in ScAlSZ, a thin film formed at 450 °C substrate temperature. The shape of the Nyquist plot, measured using platinum as the electrode material, was obtained from the measurement data (Fig. 4.20). Arrhenius plots as a function of temperature show that the amount of introduced Al affects the conductivity (Fig. 4.21). In order to perform this study, thin films were investigated in the air and in a range of temperatures, i.e., range 1 (400–560 °C) and range 2 (720–1000 °C). The Nyquist plot was irregular, indicating that there are two paths of oxygen diffusion as grain and grain boundary. The best results were seen with $R_g|CPE_g - R_{gb}|CPE_{gb}$ model, and subsequently, through data simulation, it was possible to fit the results properly. It has been proven that grain impedance was higher than grain boundary impedance for thin films with Al concentrations as low as <3.8 at.%. For thin films with high concentrations of Al (>3.8 at.%), the grain impedance was lower than that of the grain boundary.

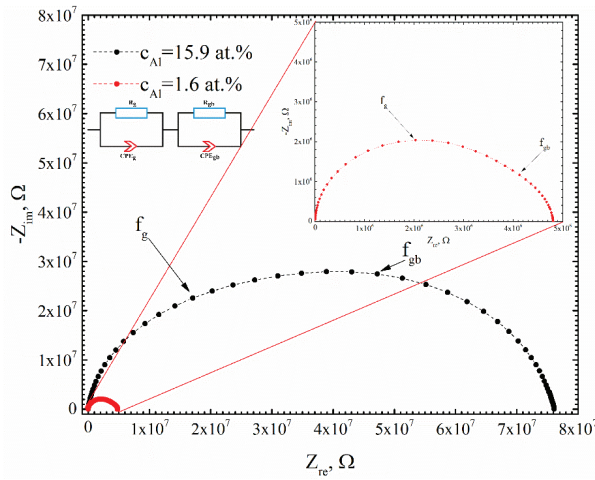


Fig. 4.20. Nyquist plots of ScAlSZ thin films with 15.9 at.% and 1.6 at.% of Al at 560 °C temperature [159]

The resistance for thin films with 1.6 at.% Al concentration is $R_g \sim 3.70E \times 10^6 \Omega$ and $R_{gb} \sim 1.11E \times 10^6 \Omega$, when thin films with 15.9 at.% Al concentration are $R_{gb} \sim 2.52E \times 10^7 \Omega$ and $R_g \sim 5.07E \times 10^7 \Omega$. Furthermore, for ScAlSZ thin films with 1.6 at.% 15.9 at.% Al concentration, the critical frequency of grain boundaries (f_g) decreased from 9.08×10^3 to 9.60×10^2 (9.08 kHz to 0.96 kHz) for thin films, and the critical frequency of grains (f_{gb}) decreased from 1.79×10^3 to 2.16×10^2 (1.79 kHz to 0.216 kHz) (Table. 4.9).

Table 4.9. Resistance and capacitance for grain and grain boundary process, the composition ScAlSZ thin films with 15.9 at.% and 1.6 at.% of Al at 560 °C temperature

	$c_{Al} = 1.6, \text{ at. \%}$	$c_{Al} = 15.9, \text{ at. \%}$
R_g, Ω	3.7×10^6	2.52×10^7
CPE_g, F	5.29×10^{-12}	1.11×10^{-11}
n_g	9.90×10^{-1}	9.40×10^{-1}
R_{gb}, Ω	1.11×10^6	5.07×10^7
CPE_{gb}, F	1.54×10^{-10}	2.99×10^{-11}
n_{gb}	9.30×10^{-1}	9.00×10^{-1}
$f_{gb}, \text{ Hz}$	9.08×10^3	9.60×10^2
$f_g, \text{ Hz}$	1.79×10^3	2.16×10^2

The Arrhenius plot (Fig. 4.21) shows that ScAlSZ thin films with 1.6 at.% and 3.8 at.% Al concentration have similar behavior and show linear dependences. Although there is a significant difference between the curves with higher Al concentration 15.9 at.% and 22.2 at.%, which appear to be nonlinear dependencies, for ScAlSZ thin films with 15.9% and 22.2 percent Al, the activation energy is greater at higher temperatures. The activation energies in the range 1 (400–560 °C) are ~1.10 eV, and in the range 2 (720–1000 °C), they are ~1.85 eV (Table 4.10).

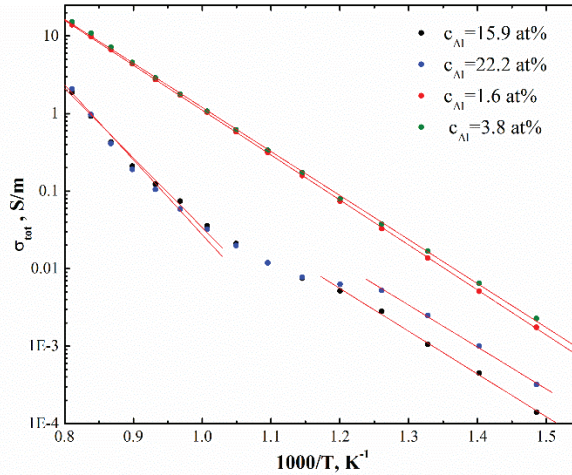


Fig. 4.21. Arrhenius plots of ScAlSZ thin films with different Al concentrations [159]

Table 4.10. Bulk ionic conductivity (σ_{bulk}) at 520 °C and 800 °C temperatures and their activation energy (E_a) of ScAlSZ thin ceramic films formed at the different aluminum concentration (c_{Al}) [159]

c_{Al} , at.%	Temperature range			
	Range 1		Range 2	
	σ , S/m	E_a , eV	σ , S/m	E_a , eV
1.6	0.033	1.16	2.74	1.16
3.8	0.038	1.14	2.89	1.14
15.9	0.0028	1.10	0.123	1.79
22.2	0.0025	1.08	0.105	1.93

The thin films containing 3.8 at.% Al had the highest total conductivity values. In the temperature range of 700 °C to 1000 °C, it ranged from 1.1 to 19.2 S/m (Fig. 4.21, Table 4.10). The comparison of the total conductivity of ScAlSZ thin films revealed that the total conductivity of thin films decreases with the high 15.9 at.% and 22.2 at.% of Al content, and it was 10 times lower than thin films containing 1.6 and 3.8 at.% of Al (Fig. 4.21). The overview of the ionic conductivity of Zr-based ceramics reported by many authors and comparison of the obtained results were summarized and presented at Table 4.11. ZrO_2 , $Mg_xSc_yZr_{1-x-y}O_2$, $Sc_xZr_{1-x}O_2$, $Ce_xSc_yZr_{1-x-y}O_2$, $Y_xZr_{1-x}O_2$, $Ga_xSc_yZr_{1-x-y}O_2$, $Al_xSc_yZr_{1-x-y}O_2$, $Al_xSc_yZr_{1-x-y}O_2$,

Yb_xSc_yZr_{1-x-y}O₂ ceramics conductivity at various temperatures were analyzed and compared with the obtained results in this study. Similarly, Guo et al. [168] reported high total ionic conductivity obtained for Al_{0.01}Sc_{0.10}Zr_{0.89}O₂ system by σ_{tot} value of 9.2 S/m at 800 °C. Haering et al. [196] reported that 1 mol% of Al₂O₃ co-doping to 10 mol% of ScSZ system has no significant effect on the ionic conductivity. However, further increase of Al₂O₃ up to 5.5 mol% content to the 10 mol% of ScSZ system has a negative impact by slowing down for 20% of conductivity, compared to alumina-free 10 mol% of ScSZ systems [196]. This may indicate that the introduction of alumina with a higher content, above 0.5 at.% of alumina, will not promote the ionic conductivity. However, some authors [168, 196] have noted that the optimal content of Al₂O₃ co-doping to exhibit the higher conductivity is 0.5 at.%. However, Ishii et al. [29] reported about the tendency of temperature dependence on ionic conductivity by different concentration of Al₂O₃ co-doping from 0 to 0.5 at.%, and the results assert that the samples with Al₂O₃ content from 0 to 0.4 at.% show a discontinuous change in ionic conductivity with a structural transition phase. The phase transition temperature has decreased from 660 °C to 500 °C [29]. The continuous change of ionic conductivity was obtained at the sample with 0.5 at.% Al₂O₃ content with a ionic conductivity value 12 S/m (Al_{0.005}Sc_{0.12}Zr_{0.88}O₂, cubic); at the same time, the sample with 0.1 at.% Al₂O₃ content was presented by ionic conductivity value of 10 S/m (Al_{0.001}Sc_{0.12}Zr_{0.88}O₂, rhombohedral) [29]. In general, the conductivity values of the reviewed literature vary from 1 S/m to 31 S/m, and the temperature interval was found in the range of 700–1000 °C. The total conductivity was lower than the results reported in literature (Table 4.11). However, it was on the same order of magnitude.

Table 4.11. Total conductivities of ZrO₂ based compounds (σ_{tot}), highest total conductivities in the study ($\sigma_{3.8 \text{ at.}\%}$) [159]

Compound	Phase	σ_{tot} , S/m	$\sigma_{3.8 \text{ at.}\%}$, S/m	T _m , °C	Formation method	Ref.
ZrO ₂	tetragonal	3	1.8	750	caustic fusion method	[197]
Doped ZrO₂						
Sc _{0.7} Zr _{0.93} O ₂	tetragonal + cubic	25	19.2	1000	solid-state reaction	[196]
Sc _{0.08} Zr _{0.92} O ₂	cubic	25.8	15.2	950	sol-gel	[198]
Sc _{0.09} Zr _{0.91} O ₂	cubic + tetragonal	31	19.2	1000	solid-state reaction	[196]
Sc _{0.10} Zr _{0.90} O ₂	rhombodral	6	1.8	750	solid-state reaction	[114]
Sc _{0.11} Zr _{0.89} O ₂	cubic	9.3	2.9	800	co-precipitation combined with supercritical	[199]

$Y_{0.7}Zr_{0.93}O_2$	tetragonal + cubic	5.5	10.9	900	ethanol drying route skull melting	[200]
$Y_{0.08}Zr_{0.92}O_2$	monoclinic +cubic	1	1.1	700	sol-gel	[201]
$Y_{0.09}Zr_{0.91}O_2$	monoclinic +cubic	1.5	2.9	800		[135]
$Y_{0.10}Zr_{0.90}O_2$	cubic	6.2	10.9	900	skull melting crystalline	[200]
$Y_{0.11}Zr_{0.89}O_2$	cubic	6.5	16.2	950	sample oxide-mixing method	[202]
Co-doped ZrO₂						
$Al_{0.01}Sc_{0.10}Zr_{0.89}O_2$	cubic	9.2	2.9	800	conventional tape-casting method	[168]
$Al_{0.001}Sc_{0.12}Zr_{0.88}O_2$	rhombohedral	10	4.6	850	solid-state reaction	[29]
$Al_{0.005}Sc_{0.12}Zr_{0.88}O_2$	cubic	12	4.6	850	solid-state reaction	[29]
$Ga_{0.01}Sc_{0.10}Zr_{0.89}O_2$	cubic	13	10.9	900	sol-gel	[202]
$Ga_{0.07}Sc_{0.04}Zr_{0.89}O_2$	monoclinic + tetragonal	1.6	10.9	900	sol-gel	[202]
$Yb_{0.01}Sc_{0.10}Zr_{0.89}O_2$	cubic	31	19.2	1000	solid-state reaction	[196]
$Yb_{0.02}Sc_{0.10}Zr_{0.88}O_2$	cubic	24	19.2	1000	solid-state reaction	[196]
$Ce_{0.01}Sc_{0.10}Zr_{0.89}O_2$	cubic	7.9	10.9	900	self- combustion synthesis	[130]
$Mg_{0.03}Sc_{0.08}Zr_{0.89}O_2$	cubic	10	10.9	900	sol-gel	[203]

4.8. Results and conclusions

Nanostructured (~2 μm) thin ceramic films based on ScAlSZ systems with different structural and electrochemical characteristics were deposited by electron beam evaporation. It has been found that the formed thin coatings show individual structural and chemical properties, which are different compared to the initial material. The elemental concentrations were as follows: thin ceramics formed at 300 °C substrate temperature and were presented by O₂, Al, Sc, and Zr, and the concentrations varied in the range from 49.5 to 54.1 at.%, from 3.0 to 20.2 at.%, from 3.1 to 8.7 at.%, from 25.3 to 36.0 at.%, and thin ceramics formed at 600 °C substrate temperature were presented by O₂, Al, Sc, and Zr, and the concentrations varied in the range from 49.8 to 54.2 at.%, from 7.1 to 12.5 at.%, from 3.4 to 7.1 at.%, and from 30.0 to 34.5 at.%. The chemical composition of formed thin ceramics at 450 °C substrate temperature were presented by O₂, Al, Al³⁺, Sc, and Zr, and the

concentrations varied in the range from 50.2 to 55.6 at.%, from 1.6 to 22.2 at.%, from 1.4 to 20.1 at.%, from 3.4 to 7.7 at.%, from 27.4 to 34.4 at.%. The EDS analysis established that Al concentration depends on the deposition rate and substrate temperature. Al concentrations increase during higher substrate temperature, while at higher deposition rates, Al concentrations decrease. It could be explained by the difference melting temperature of initial powder-containing materials, i.e., Al_2O_3 melting point 2072 °C, whereas Sc_2O_3 and ZrO_2 melting points are 2485 °C and 2715 °C, respectively. The XPS analysis determined the surface profile of ScAlSZ thin film containing presence OH groups and Sc, Zr, Al, C compounds. XPS spectra Al 2p, Zr 3d, and O1s stated the increases of oxygen vacancy and presence of ZrO_x caused by increasing the concentrations of Al and Al_2O_3 . The crystallographic nature of thin ceramics is not identical compared to the initial materials. The structures of initial materials were polymorphic and presented by the presence of monoclinic, tetragonal, and rhombohedral phases. The formed thin ceramics have a mixed phase modification of cubic, tetragonal, and monoclinic. Moreover, it has been discovered that the presence of cubic phase was in the range of 53–59% at thin ceramics formed at 300 and 600 °C substrate temperature. Furthermore, the content of the cubic phase was higher for thin films containing low Al concentrations: 1.6 at.% and 3.8 at.% have 36% and 42% of cubic phase content, while 15.9 at.% and 22.2 at.% are presented as a mixed phase of tetragonal and monoclinic. The analysis phase transition and microstructural changes of formed thin ceramics in the "in-situ" mode presented more stabilized thin ceramics with 15.9 at.% and 22.2 at.%, and the content of the cubic modifications were 23% and 24%, respectively. Hence, it could be firmly concluded that Al concentrations have a significant effect on the microstructural properties and crystallinity of thin ceramics. The AFM measurements revealed that formed thin ceramics are uniform and with lower roughness at higher Al concentrations. The electrochemical analysis has established that at a high concentration of Al, firstly happens low crystallinity caused by the presence of a large number of grain boundaries, second, amorphous phase of Al and Al_2O_3 in the grain boundaries, third, dopant vacancy complexes (vacancy dopant cation dipoles or tripoles) with high association energy suppressed diffusion of oxygen ions. Therefore, the Arrhenius plot has confirmed the nonlinear dependences with the Al concentrations of 15.9 and 22.2 atomic percentages of Al in ScAlSZ thin film. The activation energy was ~1.10 eV from 400 to 560 °C and ~1.85 eV in the range of 720–1000 °C substrate temperatures. The oxygen vacancy complexes dissociation can be the reason of increase in conductivity and activation energies. The annealed ScAlSZ thin films have the highest total ionic conductivity value ($S_{bulk} = 2.89 \text{ S/m}$ at 800 °C) of 3.8 at.% of Al.

MAIN RESULTS

In this work, the scandia alumina stabilized zirconia was used to prepare thin films with the help of e-beam physical vapor deposition technique. For the deposition process, the pellets were formed from the powder with the composition of $(\text{Sc}_2\text{O}_3)_{0.06}(\text{Al}_2\text{O}_3)_{0.01}(\text{ZrO}_2)_{0.93}$. The thin films prepared through the deposition process were found to have different chemical composition and structure compared to the powders of ScAlSZ. The concentration of Al in thin film was found to be associated with the deposition parameters, such as substrate temperature and deposition rate. If the deposition rate is higher, i.e., 1.6 nm/s, the Al concentration becomes lower 3.0 at.% and slightly higher 7.1 at.% with higher 600 °C substrate temperature.

The XPS measurement was performed, and it has been observed that thin film surface consisted of compounds, such as: Sc, Zr, Al and C, OH group, and the oxygen vacancy. The structural properties of the thin film were observed to be affected by the presence of oxygen vacancies, ZrO_x , and a high concentration of alumina and metallic aluminum. The higher deposition rates and deposition temperatures were used to make greater crystallinity of thin films. Hence, the crystallinity was directly associated with the substrate temperature and aluminum concentration.

Raman method was used to identify the crystal structures of powder, which was identified as polymorphic crystalline structure and monoclinic, cubic, tetragonal and rhombohedral phases. The peaks were detected around 140 cm^{-1} , 262 cm^{-1} , 354 cm^{-1} , 382 cm^{-1} , 475 cm^{-1} , 540 cm^{-1} , 618 cm^{-1} , 726 cm^{-1} , 954 cm^{-1} , and 1000 cm^{-1} , which indicated the presence of cubic, tetragonal, and rhombohedral phases with ~44%, ~18%, and ~38% percentages, respectively, and that a transition has occurred from rhombohedral to the cubic phase. Furthermore, the concentration of the cubic phase was greater than the tetragonal phase with a higher deposition rate. It is clear that higher Al concentration in thin film restrains the development of the cubic phases. The most stabilized cubic phase in thin film can be obtained in the most optimal conditions of high substrate temperature and high deposition rate.

XRD was performed on a deposited thin film of scandia alumina stabilized zirconia. The XRD analysis was carried out on the initial evaporated powders of ScSZ and ScSZAl, which was confirmed to have polymorphism of ZrO_2 with the tetragonal, monoclinic, and rhombohedral phases by Raman spectroscopy. In contrast to the evaporating material structure, the XRD pattern of ScSZ and ScSZAl thin films has shown that only pure ZrO_2 face-centered cubic phase with the preferred orientation of (200) at the temperature up to 450 °C has existed and changed at higher temperatures, compared to the preferred orientation of (100). The Rietveld analysis was then carried out to examine the effect of Al dopant, which has shown that a pure cubic phase exists in the ScSZAl thin film with an equal chance of being a mixed structure of cubic and rhombohedral phase with 87.8% and 12.2% percentages, respectively. The co-doping with Al in the ScSZAl thin films has been observed to delay and slow down the creation of cubic phases and stabilize it at greater than 300 °C temperature of substrate temperature. The percentage of cubic

phase was from 42% to 53% in ScSZ and around 42% in ScSZAl thin film from the tetragonal and rhombohedral phases. It can be understood that the crystallite size is dependent on the substrate temperatures and shows a nonlinear behavior. The crystallites were observed to grow longer from 17.4–69.9 nm with an increase in substrate temperatures from 50 to 300 °C and a rapid decrease in size at the deposition temperature of 450 °C from ~45 to 30 nm because of the change in preferred orientations and phase ratios.

The Arrhenius plot has shown linear dependences and having the highest ionic conductivity value, which is 4.2×10^{-3} S/cm for the thin film with 600 °C substrate temperature and the deposition rate of 0.4 nm/s. The vacancy activation energy has been affected by the increase in the concentration of the tetragonal phase formed in thin film, and it increased from 0.91 to 1.22 eV with the higher substrate temperatures.

The effect of the concentration of Al on the structural, chemical, and electrochemical properties of ScAlSZ thin films has been determined with the help of XPS analysis. The XPS spectra (Al 2p, Zr 3d, and O 1s) have shown that the concentration of oxygen vacancies has increased with the increase in Al concentrations. The crystallinity and the microstructure of ScAlSZ thin films were observed to be dependent on the Al concentrations. ScAlSZ thin film has been observed to have low crystallinity with the increase in Al concentrations (28.7 nm for 1.6 at.% of Al and 19.7 nm for 15.9 at.% of Al). Furthermore, the structure of thin films at the lower Al concentrations (1.6 and 3.8 at.%) consisted of cubic, monoclinic, and tetragonal phases, whereas the thin film had a monoclinic and tetragonal phase at a higher Al concentration (15.9 and 22.2 at.%). Nevertheless, after annealing, the cubic phase has been created in a thin film with a higher Al concentration, and it has shown higher oxygen vacancies concentration.

The AFM measurements have shown that thin film has uniformity and homogeneity without the formation of cracks and visible porosity and has a lower roughness at higher Al concentration. The electrochemical analysis has shown the existence of a heavy amount of grain boundaries (lower crystallinity), amorphous Al, and Al₂O₃ phases at the grain boundary, and dopant vacancy complexes with the higher association energy with concealed oxygen ions diffusion at the higher Al concentration. As a result, the impedance of grain boundaries was greater than the grain impedance, and the total ionic conductivity was lower but greater than the 10 times of thin films having higher Al concentration of more than 3.8 at.%. Furthermore, the Arrhenius plot has confirmed the nonlinear dependences with the Al concentrations of 15.9 and 22.2 atomic percentages in ScAlSZ thin film. The activation energy was ~1.10 eV in 400–560 °C and ~1.85 eV in the range of 720–1000 °C substrate temperatures. The oxygen vacancy complexes dissociation can be the reason of increase in conductivity and activation energies. The annealed ScAlSZ thin films have the highest total ionic conductivity value ($S_{bulk} = 2.89$ S/m at 800 °C) of 3.8 at.% of Al.

CONCLUSIONS

1. The XRD results of ScSZ and ScSZAl thin films formed on Alloy 600 substrates using a 0.4 nm/s deposition rate were presented by cubic (JCPDS No. 01-089-5483) and rhombohedral (JCPDS No. 01-89-5482); however, as a much more sensitive for small displacement of atoms, the Raman analysis of both ScSZ and ScSZAl were presented by different polymorphic states: 44% of cubic phase, 18% of tetragonal, and 38% of mixed phase, indicated as rhombohedral transitions phases.
2. ScSZ and ScSZAl thin films crystallinity is directly associated with the substrate temperature: a crystal grows large (from 17.4 nm to 69.9 nm) as the substrate temperature (from 50 °C to 300 °C) increases, and when the temperature reaches 450 °C, the crystallite size decreases sharply (from 44.6 nm to 31.2 nm).
3. The rietveld analysis of ScSZ and ScSZAl thin films results in the mixture of cubic and rhombohedral phases of 87.8% and 12.2% with the same chance of pure cubic modifications.
4. It has been determined that the oxygen sub-lattice disorder associated by Sc₂O₃ and Al₂O₃ doping and co-doping leads to the Raman shift for the cubic phase of ScSZ and ScSZAl thin films toward higher wavenumber value from 622 cm⁻¹ to 632 cm⁻¹ and from 618 cm⁻¹ to 621 cm⁻¹.
5. The presence of cubic phase for ScAlSZ thin films was in the range of 53–59% at thin ceramics formed at 300 °C and 600 °C substrate temperature. The ScAlSZ thin films formed at 450 °C substrate temperature cubic phase were higher for thin films containing low Al concentrations, 1.6 at.% and 3.8 at.% have 36% and 42% of cubic phase content, while 15.9 at.% and 22.2 at.% were presented as a mixed phase of tetragonal and monoclinic.
6. Al co-doping slow down the stabilization of cubic shape by 7% and its results for ScSZ are from 42% to 53% and for ScSZAl, from 41% to 43%.
7. The ScAlSZ thin films are uniform and with lower roughness at higher 15.9 at.% and 22.2 at.% Al concentrations, as-deposited: 2.2 nm and 1.9 nm; as annealing: 3.1 nm and 2.8 nm, respectively.
8. The highest ionic conductivity exhibits for ScSZ thin films at 600 °C substrate temperature with a value of 4.2×10^{-3} S/cm. The predominant tetragonal phase in the specimens results of vacancy activation energy increases from 0.91 eV to 1.22 eV at higher temperature of the substrate. Arrhenius plot has confirmed the nonlinear dependences with the Al concentrations of 15.9 and 22.2 at.% in ScAlSZ thin film. The activation energy was ~1.10 eV in 400–560 °C and ~1.85 eV in the range of 720–1000 °C substrate temperatures. The annealed ScAlSZ thin films have the highest total ionic conductivity value ($S_{bulk} = 2.89$ S/m at 800 °C) of 3.8 at.% of Al.
9. The chemical composition of ScAlSZ thin ceramics at 300 and 600 °C substrate temperature presented by O₂, Al, Sc, and Zr and concentrations ranged from 49.5 to 54.2 at.%, from 3.0 to 20.2 at.%, from 3.1 to 8.7 at.%, from 25.3 to 36.0 at.% respectively.

10. The chemical composition of ScAlSZ thin ceramics at 450 °C substrate temperature presented by O₂, Al, Al³⁺, Sc, and Zr and concentrations varied in the range from 50.2 to 55.6 at.%, from 1.6 to 22.2 at.%, from 1.4 to 20.1 at.%, from 3.4 to 7.7 at.%, from 27.4 to 34.4 at.%, respectively.
11. ScAlSZ thin film contained OH groups and Sc, Zr, Al, C compounds. XPS spectra Al 2p, Zr 3d, and O1s stated the increases of oxygen vacancy and presence of ZrO_x caused by increasing the concentrations of Al and Al₂O₃.
12. ScAlSZ powders were not detected in the presence of tetragonal phases by XRD measurements; however, tetragonal phases peaks were represented by Raman analysis by B_{1g} at 147 cm⁻¹, E_g at 261 cm⁻¹, A_{1g} at 635 cm⁻¹.
13. The XRD results of ScAlSZ thin films formed at 300 and 600 °C were presented by cubic (JCPDS No. 01-089-5485) and tetragonal (JCPDS No. 00-053-0549), while the Raman analysis of ScAlSZ thin films formed at 300 and 600 °C was presented by monoclinic (m-ZrO₂) at 198 cm⁻¹ A_g, tetragonal (t-ZrO₂) at 149–153 cm⁻¹, 638 cm⁻¹, cubic (c-ZrO₂) between 626 and 630 cm⁻¹ F_{2g} mode.
14. The high concentration of Al co-dopant by 15.9 and 22.2 at.% slows down the stabilization of cubic shape, only after thermal annealing; thus, thin films reach the formation of cubic phase by 23 and 24%, respectively.

SANTRAUKA

IVADAS

Cirkonio oksidas, stabilizuotas skandžio oksidu (ScSZ), yra plačiai naudojamas kuro elementuose ir dujų jutikliuose [1–3] ir pasižymi dideliu stipriu, šiluminiu stabilumu bei geromis elektrocheminėmis savybėmis. Cirkonio oksido pagrindu pagaminta keramika yra laidi deguonies jonams plačiame slėgio ir temperatūrų ruože. Būtent ši savybė leidžia praktiškai pritaikyti šią medžiagą deguonies jutikliuose ir aukštatemperatūriniuose kuro elementuose. Cirkonio oksido pagrindo keramikose laidi dumas vyksta deguonies jonų vakansijomis, o vakansijų koncentracijos padidėjimas ir atitinkamai joninis laidumo padidėjimas pastebimi iki pakankamai aukštų temperatūrų (1200 °C).

Siekiant pagerinti cirkonio oksido stabilizuoto skandžio oksidu savybes, galima ScSZ legiruoti papildoma trečiaja priemaiša, dėl kurios įvyksta pokyčiai medžiagos struktūroje, kartu kinta ir kitos savybės, tokios kaip cheminis stabilumas, mechaninės savybės, jonų judris ir deguonies vakansijų koncentracija [4–6]. Trikomponenčių kietųjų tirpalų laidumą ir struktūros pokyčius lemiančios priežastys yra kompleksinės ir nepakankamai gerai ištirtos, nepaisant to, kad samprata apie įprastų dvikomponenčių kietųjų tirpalų savybes, taip pat ir papildomų priemaišinių oksidų savybes padeda prognozuoti trikomponenčių kietųjų tirpalų savybes [7]. Dėl didelio tarpkristalinių ribų skaičiaus polikristalinėse kietosiose medžiagose kristalinės struktūros parametrai gali netiesine priklausomybe skirtis nuo pradinių oksidų struktūros parametru. Mokslinėje literatūroje yra analizuojamos įvairios elementinės kompozicijos trikomponenčių elementų sistemos siaurame temperatūrų ruože arba mažos koncentracijos priemaišų įtaka plačiame temperatūrų intervale, bet pasigendama išsamios eksperimentinės statistikos apie trikomponenčių oksidų sistemų fazių sudėtį plačiame temperatūrų intervale [8]. Papildoma priemaiša gali pakeisti elektrolito kristalinės gardelės struktūrą ir turėti didelę įtaką bendram elektrolito laidumui. Taigi, kietosios keramikos, pagamintos cirkonio oksido pagrindu, kubinės fazės stabilizavimas legiruojant cirkonio oksidą cerio ir skandžio oksidais arba aliuminio ir skandžio oksidais nulemia tarpkristalinių ribų laidumo indėlį į bendrą keramikos laidumą [9,10].

Pagrindinis šios disertacijos darbo tikslas – ištirti aliuminio priemaišos įtaką skandžiu stabilizuoto cirkonio oksido plonų dangų, suformuotų naudojant garinimą elektronų spinduliu, mikrostruktūrai, kristališkumui ir joniniam laidumui, t. y. ištirti tokias trinares sistemas, kaip:

- $(\text{Sc}_2\text{O}_3)_{0,10}(\text{ZrO}_2)_{0,90}$ (10% Sc_2O_3 , 90% ZrO_2) cirkonio oksidas, stabilizuotas skandžio oksidu (ScSZ)
- $(\text{Sc}_2\text{O}_3)_{0,10}(\text{Al}_2\text{O}_3)_{0,01}(\text{ZrO}_2)_{0,89}$ (10% Sc_2O_3 , 1% Al_2O_3 , 89% ZrO_2) cirkonio oksidas, stabilizuotas skandžio ir aliuminio oksidais (ScSZAl)
- $(\text{Sc}_2\text{O}_3)_{0,06}(\text{Al}_2\text{O}_3)_{0,01}(\text{ZrO}_2)_{0,93}$ (6% Sc_2O_3 , 1% Al_2O_3 , 93% ZrO_2) cirkonio oksidas, stabilizuotas skandžio ir aliuminio oksidais (ScAlSZ)

Tyrimo problema

Pagrindinė tyrimo problema – nėra išsamios fizikinių ir technologinių savybių analizės, komponentų santykio, dalelių morfologijos, fazinės sudėties, fazių kristalinės struktūros įtakos $\text{Sc}_2\text{O}_3 - \text{ZrO}_2 - \text{Al}_2\text{O}_3$ sistemų plonoms dangoms, suformuotoms garinant elektronų pluošteliu esant skirtingoms nusodinimo temperatūroms ir skirtingam ir nusodinimo greičiui.

Disertacijos tikslas ir uždaviniai

Pagrindinis darbo tikslas – ištirti aliuminio priemaišų įtaką skandžio oksidu stabilizuoto cirkonio oksido plonų dangų, suformuotų garinant elektronų pluošteliu, mikrostruktūrai, kristališkumui ir joniniam laidumui.

Siekiant įgyvendinti šį tikslą, buvo sprendžiami žemiau nurodyti **darbo uždaviniai**:

1. Suformuoti $\text{Sc}_2\text{O}_3 - \text{ZrO}_2 - \text{Al}_2\text{O}_3$ sistemų plonas keramines dangas naudojant garinimą elektronų spinduliu bei keičiant technologinius parametrus, tokius kaip padėklo temperatūra ir nusodinimo greitis.
2. Ištirti pradinių miltelių $(\text{Sc}_2\text{O}_3)_{0,06}(\text{Al}_2\text{O}_3)_{0,01}(\text{ZrO}_2)_{0,93}$, $(\text{Sc}_2\text{O}_3)_{0,10}(\text{Al}_2\text{O}_3)_{0,01}(\text{ZrO}_2)_{0,89}$, $(\text{Sc}_2\text{O}_3)_{0,10}(\text{ZrO}_2)_{0,90}$ įtaką suformuotų plonų dangų kristalinei fazei, kristalinei gardelei ir mikrostruktūrai.
3. Ramano spektroskopijos metodu ištirti suformuotų $\text{ZrO}_2 - \text{Sc}_2\text{O}_3$ ir $\text{ZrO}_2 - \text{Sc}_2\text{O}_3 - \text{Al}_2\text{O}_3$ sistemų plonų dangų kristalinės fazės sudėtį.
4. Naudojant rentgeno spindulių difrakciją (XRD) ištirti suformuotų $\text{ZrO}_2 - \text{Sc}_2\text{O}_3$ ir $\text{ZrO}_2 - \text{Sc}_2\text{O}_3 - \text{Al}_2\text{O}_3$ sistemų kristalografiją.
5. Ištirti suformuotų $\text{ZrO}_2 - \text{Sc}_2\text{O}_3$ ir $\text{ZrO}_2 - \text{Sc}_2\text{O}_3 - \text{Al}_2\text{O}_3$ sistemų plonų dangų joninį laidį.

Darbo naujumas ir praktinė reikšmė

Nepaisant to, kad dviejų komponentų cirkonio oksido pagrindu $\text{ZrO}_2 - \text{M}_x\text{O}_y$ sistemos yra ištirtos gana išsamiai, informacijos apie trijų komponentų oksidų sistemas yra labai mažai. Trijų komponentų sistemų struktūra ir savybės negali būti laikomos griežtai adityvia atskirų komponentų struktūros ir savybių funkcija. Atskirai reikėtų pažymėti galimą priemaišų poveikį tarpkristalinių ribų struktūrai ir laidumui, kuris aiškiai pasireiškia $\text{Al}_2\text{O}_3 - \text{ScSZ}$ sistemos atveju. Naudojantis Ramano spektroskopijos duomenimis buvo detalai aprašytos ScAISZ sistemos, suformuotos garinant elektronų pluošteliu, įvertinant keramikų fazinę sudėtį ir mikrostruktūrinės savybes. Be to, buvo ištirta ScAISZ polikristalinio elektrolito struktūros įtaka jo laidumui. Taip pat buvo ištirta aliuminio koncentracijos įtaka plonų dangų, suformuotų garinant elektronų pluošteliu, paviršiaus šiurkštumui.

Ginamieji teiginiai

1. Kubinė fazė ScSZAl dangose pradeda stabilizuotis ir formotis esant didesnėms nei 50 °C temperatūroms. Tolimesnis temperatūros didinimas kubinės fazės formavimuisi ir kiekiui didelės įtakos neturi.
2. Nedidelis atomų poslinkis $\text{ZrO}_2 - \text{Sc}_2\text{O}_3 - \text{Al}_2\text{O}_3$ sistemos fluorito struktūroje gali būti nustatytas naudojant Ramano spektroskopinę analizę.

3. ScAlSZ plonosios plėvelės yra tolygios ir pasižymi mažesniu paviršiaus šiurkštumu esant didesnei 15,9 % ir 22,2 % Al koncentracijai.
4. Aukštesnėmis joninio laidžio vertėmis pasižymi $ZrO_2 - Sc_2O_3 - Al_2O_3$ sistemų plonos dangos, suformuotos esant aukštesnei 600 °C padėklo temperatūrai ir mažesnėms aliuminio koncentracijoms.
5. Kubinės fazės Ramano smailės padėties poslinkis link aukštesnių verčių atsiranda dėl deguonies subgardelės netvarkos, kuri atitinkamai yra susijusi su legiravimu Sc_2O_3 ir Al_2O_3 priemaišomis.
6. Didelė Al priemaišų koncentracija (15,9 ir 22,2 at.%) lėtina kubinės fazės stabilizavimąsi.

Disertacijos sandara ir apimtis

Disertaciją sudaro įvadas, literatūros apžvalga, priemonės ir metodai, rezultatai ir jų aptarimas bei išvados. Pirmajame skyriuje pateikiama literatūros apžvalga apie ZrO_2 pagrindu pagamintą keramiką, apimanti jos struktūrą, medžiagas, formavimo būdus. Antrame skyriuje pristatomos šiame darbe naudotos priemonės ir metodai. Dėl sudėtingos garinamos medžiagos prigimties ir skirtingų tyrimo metodų buvo nuspręsta rezultatų dalį padalyti į du skyrius. 3 ir 4 skyriuose pateikiami gauti rezultatai ir jų aptarimas. Pagrindinių rezultatų išvados pateikiamos paskutiniame skyriuje. Disertacijos pabaigoje pateikiama disertacijos santrauka lietuvių kalba, literatūros sąrašas, autoriaus gyvenimo aprašymas, publikacijų ir mokslinių konferencijų sąrašas. Disertacijos apimtis – 156 puslapiai, kuriuos sudaro 60 paveikslėlių, 30 lentelių, 22 lygtys ir 203 literatūros šaltiniai.

Autoriaus ir kitų asmenų indėlis

Autoriaus indėlis:

Autoriaus indėlis: šio darbo autorius atliko didžiąją dalį eksperimentinių darbų, keraminių sistemų nusodinimą, tyrimus, matavimus ir skaičiavimus. Autoriaus indėlį sudaro:

- $Sc_2O_3 - ZrO_2 - Al_2O_3$ plonasluoksnių keraminių sistemų nusodinimas ir elektrocheminės impedanso spektroskopijos matavimai, bendradarbiaujant su dr. D. Virbuku.
- Tyrimai ir duomenų analizė, naudojant skenuojamąjį elektroninį mikroskopą, bendradarbiaujant su dr. M. Sriubu.
- Ramano spektrų matavimus, tyrimus ir gautų duomenų skaitinę analizę atliko autorius.
- Atlikti atominių jėgų mikroskopijos tyrimai ir gautų duomenų analizė, bendradarbiaujant su dr. M. Sriubu.
- Bendra gautų rezultatų analizė ir interpretacija. Mokslinių straipsnių rengimas ir rezultatų pristatymas mokslinėse konferencijose.

Bendraautorijų indėlis:

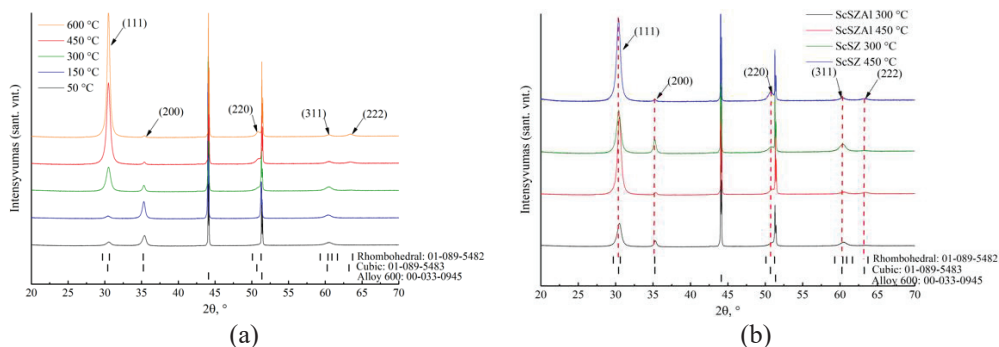
Šiam darbui vadovavo prof. dr. G. Laukaitis. Prie eksperimentų ir metodologijos planavimo prisidėjo mokslinių straipsnių bendra autoriai dr. K.

Bočkutė, doc. dr. Ž. Rutkūnienė ir prof. dr. G. Laukaitis. Nusodinimo tyrimus ir analizę, elektrocheminės impedanso spektroskopijos matavimus atliko dr. D. Virbukas. Rentgeno spindulių difrakcijos, rentgeno spindulių energijos dispersijos spektrometrijos, rentgeno spindulių fotoelektroninės spektroskopijos tyrimai ir analizė buvo atlikta bendradarbiaujant su dr. M. Sriubu ir dr. D. Virbuku. Skenuojamojo elektroninio mikroskopo matavimus atliko dr. M. Sriubas.

PAGRINDINIAI REZULTATAI IR JŲ APTARIMAS

Legiravimo aliuminiu įtaka ScSZ dangų struktūrai ir laidumui

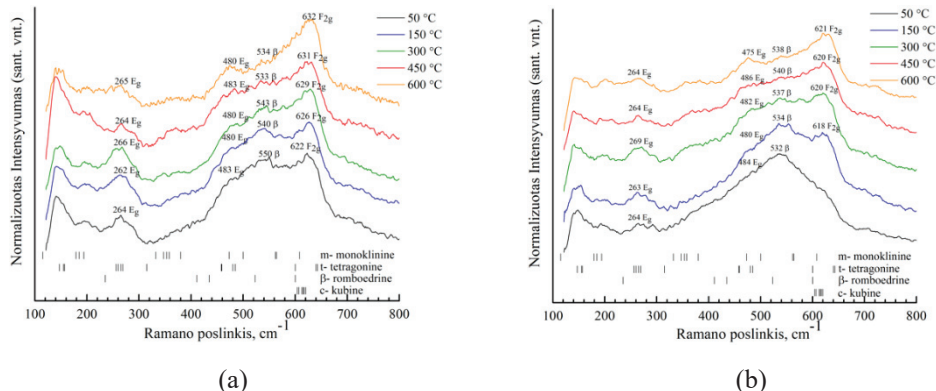
ScSZ ir ScSZAl plonų dangų kristalinės struktūros tyrimas



1 pav. Suformuotų dangų Rentgeno difrakcijos spektrai: a) ScSZ, b) ScSZAl, nusodinimo greitis: 0,4 nm/s; padėklas: Alloy 600 [50]

Rentgeno difrakcijos tyrimų duomenys (1 pav., a) kambario temperatūroje patvirtina, kad egzistuoja fluorito kubinė fazė, kurią išreiškia (111), (200), (220), (311) ir (222) smailės (JCPDS Nr. 01-089-5483) [50]. Be to, dominuojanti (200) orientacija buvo esant žemoms temperatūroms (50 °C – 300 °C), o (111) aukštesnėje temperatūroje (450 °C – 600 °C) dėl to, kad aukštas difuzijos energijos lygis palengvino adatomų migracijos procesus paviršiuje, o dalis adatomų įstrigo medžiagos paviršiuje. Esant žemai nusodinimo temperatūrai (50 °C – 300 °C), atomų ir molekulių difuzijos kelias ir laikas yra trumpi, todėl jų absorbcijos laikas mažos energijos būsenos yra ribotas ir plonos dangos auga turėdamos dominuojančią orientaciją (200). Esant aukštai nusodinimo temperatūrai (450 °C – 600 °C), atomų ir molekulių difuzijos kelias ir laikas pailgėja, taigi, plonos dangos auga turėdamos dominuojančią orientaciją (111). Be to, buvo nustatyta, kad ScSZAl dangų XRD smailių pozicijos pasislinko į didesnių verčių sritį per 0.2° lyginant su ScSZ dangomis (1 pav., b). Kristalitų dydžio priklausomybė nuo padėklo temperatūros rodo netiesinę priklausomybę. Kristalitų dydžio kitimas, didėjant padėklo temperatūrai nuo 50 °C iki 300 °C, turi augimo tendenciją (17,4 nm – 69,9 nm), o, esant 450 °C padėklo temperatūrai, plonų dangų kristališkumas mažėja (44,6 nm – 31,2 nm).

ScSZ ir ScAlSZ dangų Ramano spektrų tyrimas



2 pav. (a) ScSZ ir (b) ScSZAl plonų dangų Ramano spektrai; padėklas – Alloy 600; nusodinimo greitis – 0,4 nm/s [50]; monoklininė [126,130,131]; tetragoninė [10,117,118,131,133]; romboedrinė [10,130]; kubinė [10,117,126,130]

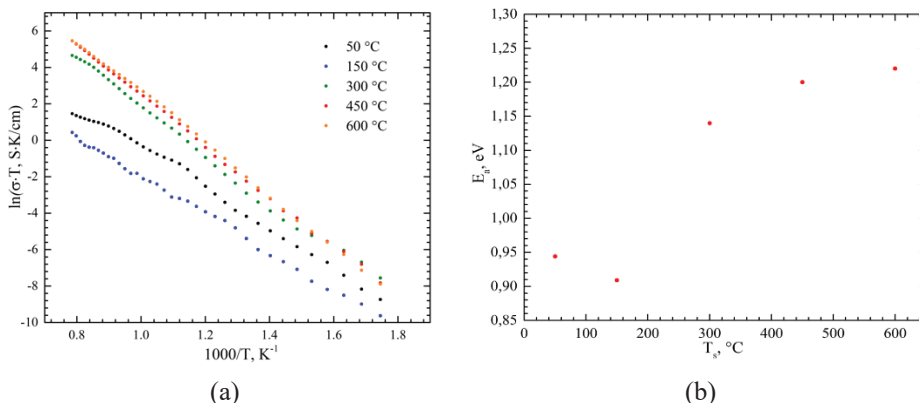
ScSZ ir ScSZAl plonų sluoksnių Ramano spektrų analizė buvo atlikta siekiant apibūdinti struktūrinius pokyčius keičiant padėklo temperatūrą 50, 150, 300, 450 ir 600 °C (2 pav., a, b). ScSZ ir ScSZAl dangos turi 10 būdingų Ramano smailių: 140, 262, 354, 382, 475, 540, 618, 726, 954 ir 1000 cm^{-1} . Remiantis literatūra, Ramano smailės maksimumai ties 354, 382 cm^{-1} atitinka monoklininę fazę [126,130,131], o tetragoninei fazei būdingos juostos aptinkamos ties 147, 260 ir 475 cm^{-1} [10,117,118,131,133]. Tetragoninių smailių atsiradimas gali būti ne dėl vyraujančios tetragoninės fazės šiose dangose, o gali atsirasti dėl pradinio medžiagos apdorojimo (miltelių) defektų. Be to, yra keletas Ramano smailių ties 540 cm^{-1} , kurios atitinka romboedrinę fazę, taip pat šios smailės sutampa su kitų autorių duomenimis [10,130]. Plačios smailės, kurių maksimumas yra apie 620 cm^{-1} , gali būti kelių smailių, atitinkančių monoklinę (m), tetragoninę (t) ir kubinę (c) fazes, persiklojimo rezultatas.

1 lentelė. ScSZ ir ScSZAl dangų fazinė sudėtis [50]

Padėklo temperatūra, °C	Kubinė %	Tetragoninė %	Romboedrinė %
ScSZ			
50 °C	43%	15%	42%
150 °C	42%	19%	39%
300 °C	45%	18%	37%
450 °C	46%	17%	37%
600 °C	53%	17%	30%
ScSZAl			
50 °C	-	22%	78%
150 °C	41%	13%	46%
300 °C	42%	19%	39%
450 °C	43%	20%	37%
600 °C	43%	23%	34%

Suformuotų dangų, fazinių pokyčių dėl temperatūros skaičiavimai buvo atlikti naudojantis (11) formule ir pateikti (1 lentelėje). Pastebėta, kad, didinant padėklo temperatūrą, šiame etape įvyko fazinis virsmas iš romboedrinės fazės į kubinę fazę, ir tai galima apibūdinti kaip keramikos fazės stabilizavimąsi dėl padėklo temperatūros. Kubinės fazės modifikacijų santykis su tetragonine ir romboedrine faze ScSZ atveju svyruoja nuo 42% iki 53%, o ScSZAl atveju – beveik 42%. Remiantis skaičiavimais, didinant padėklo temperatūrą, kubinės fazės kiekis ScSZ ir ScAlSZ padidėja atitinkamai 10% ir 2%. Galiausiai Ramano spektroskopijos tyrimai parodė, kad plonose dangose yra daugiausiai kubinės (~ 44%) fazės, kurią papildė tetragoninė (18%) ir romboedrinė (38%) fazės.

Plonų dangų elektrinių savybių tyrimas (EIS)



3 pav. (a) ScSZAl dangų Arenijaus grafikai; (b) ScSZAl dangų vakancijų aktyvacijos energijos priklausomybės nuo padėklo temperatūros; padėklas: Al_2O_3 , nusodinimo greitis: 0,4 nm/s [50]

Ant skirtingų temperatūrų padėklų suformuotų ScSZAl plonų dangų Arenijaus grafikai pateikti (3 pav., a). Didžiausia joninio laidumo vertė – $4,2 \times 10^{-3} \text{ S/cm}$ (padėklo temperatūra 600 °C, o nusodinimo greitis 0,4 nm/s) yra panaši į kitų autorių gautus rezultatus – $7 \times 10^{-3} \text{ S/cm}$ [10,29,167], $2,9 \times 10^{-3} \text{ S/cm}$ [168] ir $4,6 \times 10^{-3} \text{ S/cm}$ [29]. Nustatyta, kad, didinant padėklo temperatūrą, aktyvacijos energija didėja nuo 0,909 eV iki 1,22 eV (3 pav., b). Aktyvacijos energijos pokyčius gali lemti laidumo mechanizmo pasikeitimas aukštų ir žemų temperatūrų diapazone [168]. Be to, aktyvacijos energijos padidėjimas galėjo atsirasti dėl fazinio virsmo, kurį kiti autoriai taip pat nustatė skandžio cirkonio sistemoje apie 600 °C temperatūroje [43,168].

Skandžiu ir aliuminiu stabilizuotų cirkonio plonų dangų struktūra ir elektrocheminės savybės

ScAlSZ plonų dangų elementinė analizė

Elementinės analizės (EDS) matavimų rezultatai pateikti 2 lentelėje. Zr koncentracija plonosiose dangose svyruoja nuo 25,3 iki 36,0 at.%, o O₂, Al, Sc yra atitinkamai 49,5 iki 54,2 at.%, 3,0 iki 20,2 at.%, 3,1 iki 8,7 at.%. Sudėtyje esančių elementų atominės koncentracijos yra išsibarsčiusios minėtuose intervaluose.

2 lentelė. ScAlSZ plonų dangų paviršiaus elementinė sudėtis (EDS), kur v_d – nusodinimo greitis, T_d – padėklo temperatūra, c_x – tiriamųjų elementų atominė koncentracija [102]

v_d , nm/s	$T_d=300\text{ }^\circ\text{C}$				$T_d=600\text{ }^\circ\text{C}$			
	c_{O} , at.%	c_{Al} , at.%	c_{Sc} , at.%	c_{Zr} , at.%	c_{O} , at.%	c_{Al} , at.%	c_{Sc} , at.%	c_{Zr} , at.%
0,2	51,4	20,2	3,1	25,3	54,2	12,2	3,6	30,0
0,4	49,5	12,4	3,6	34,5	49,8	12,5	3,4	34,3
0,8	53,4	3,8	7,4	35,4	50,6	15,8	3,6	30,0
1,2	51,5	6,4	8,7	33,5	53,6	8,0	6,7	31,8
1,6	54,1	3,0	6,8	36,0	51,2	7,1	7,1	34,5
Powder	52,0	12,6	3,9	32,5				

Al koncentracija plonosiose dangose, suformuotose esant 300 °C padėklo temperatūrai, svyruoja nuo 20,2% iki 3,0%, o plonosiose plėvelėse, suformuotose esant 600 °C padėklo temperatūrai, svyruoja nuo 12,4% iki 7,1 %. Be to, nustatyta, kad Al kiekis plonosiose plėvelėse, suformuotose 600°C temperatūroje, yra gerokai didesnis $c_{\text{Al}600} = 11,1$ at.%, palyginti su plonosiomis plėvelėmis, suformuotomis 300 °C padėklo temperatūroje: $c_{\text{Al}300} = 9,2$ at.%. Tačiau abiem atvejais Al kiekis yra mažesnis nei pradiniuose milteliuose: $c_{\text{Al milteliai}} = 12,6$ at.%.

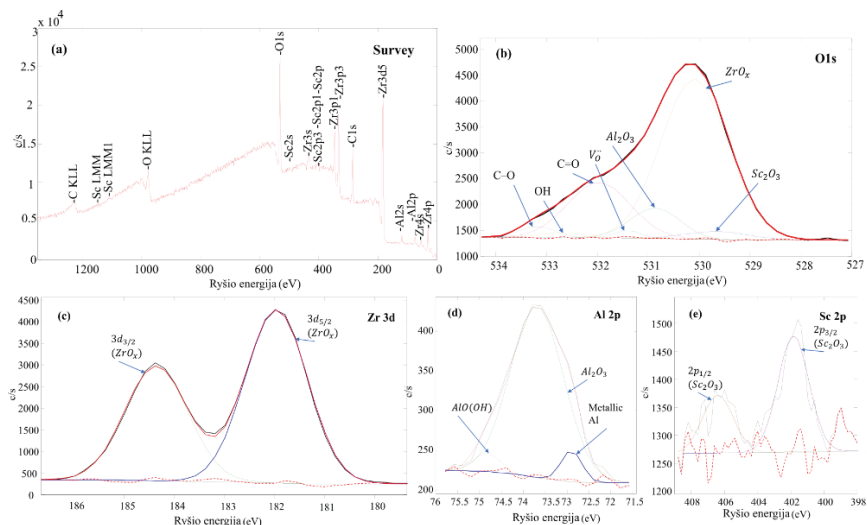
Skirtingais nusodinimo greičiais nuo 0,2 nm/s iki 1,6 nm/s, esant 450 °C padėklo temperatūrai, suformuotų ScAlSZ plonų dangų elementinės sudėtis buvo nustatyta atliekant EDS matavimus (3 lentelė). Nustatyta, kad nusodinimo greičiai turi didelę įtaką suformuotų plonų dangų cheminei sudėčiai. Taip pat nustatyta, kad, didinant nusodinimo greitį, mažėja aliuminio koncentracija. Kai nusodinimo greitis buvo 0,2 nm/s ir 1,6 nm/s, aliuminio (Al) koncentracija buvo atitinkamai 15,9 at.% ir 3,8 at.%. Sc ir Zr atomų kiekis atvirkščiai proporcingas Al atomų koncentracijai. Kai nusodinimo greitis buvo 0,2 nm/s – 1,6 nm/s, Sc koncentracija buvo atitinkamai 3,4 % – 7,7 %, o Zr – 27,4 % – 34,4 %. Esant didesniam nusodinimo greičiui, Al atomų kiekis buvo mažesnis, ir tai galėjo lemti didesnis Al₂O₃ sublimacijos greitis.

3 lentelė. ScAlSZ plonųjų dangų, suformuotų 450 °C temperatūroje, paviršiaus elementinė sudėtis (EDS), v_d – nusodinimo greitis ir c_x – tiriamųjų elementų atominė koncentracija [159]

v_d , nm/s	CO, at. %	c_{Al} , at. %	$c_{Al^{3+}}$, at. %	c_{Sc} , at. %	c_{Zr} , at. %
0,2	53,3	15,9	11,8	3,4	27,4
0,4	50,2	22,2	20,1	3,4	24,2
1,2	55,6	1,6	1,4	7,4	35,4
1,6	54,1	3,8	3,5	7,7	34,4
Powder	52,0	12,6	-	3,9	32,5

Cheminė analizė rentgeno spindulių fotoelektronų spektrometru

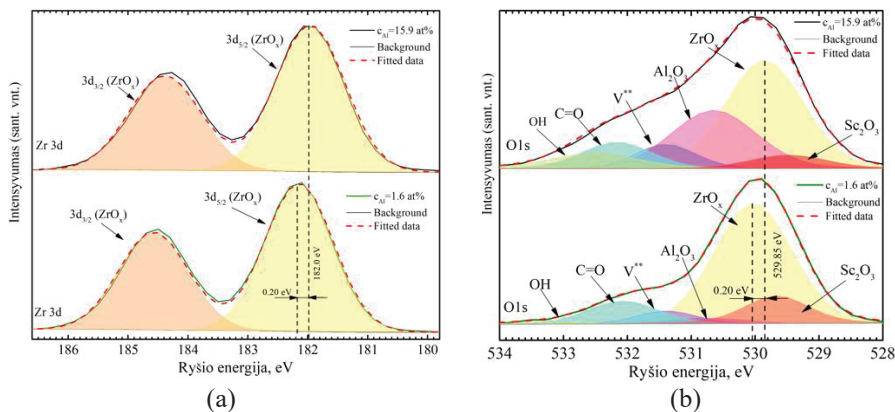
ScAlSZ dangų XPS matavimai papildė EDS analizę. XPS analizė buvo atlikta siekiant ištirti ScAlSZ plonųjų dangų cheminę sudėtį. ScAlSZ plonos dangos, kuriose yra OH grupių ir Sc, Zr, Al, C junginių, paviršiaus profilis pateiktas (4 pav., a). Be to, detali O1s, Zr 3d, Al 2p ir Sc 2p sričių analizė leidžia gauti papildomos informacijos apie jose esančius junginius (4 pav., b–e). Palyginus gautus pagrindinių energijos lygmenų smailių ir literatūros duomenis, nustatyta, kad ZrO_x suboksidas: $3d_{5/2}$ ir ZrO_x : $3d_{3/2}$ smailės yra ties 181,96 eV BE (ryšio energija) ir 184,36 eV BE, o O1s – ties 530,05 eV BE. Deguonies vakansijų smailės O1s spektre yra ties 531,40 eV, Sc_2O_3 : $2p_{1/2}$ ir $Sc_2O_3^-$: $2p_{3/2}$ rastos atitinkamai prie 406,40 eV BE, 401,85 eV BE ir O1s tie 529,65 eV BE, Al_2O_3 : 2p ties 73,69 eV BE ir O1s ties 530,85 eV BE. Metalinis Al: 2p ties 72,90 eV BE, $AlO(OH)$ 2p ties 74,82 eV BE, OH O1s – 532,70 eV BE, C-O: O1s – 533,17 eV BE ir C=O: O1s – 532,03 eV BE ScAlSZ plonųjų sluoksnių paviršiuje [173–177].



4 pav. ScAlSZ plonųjų dangų XPS spektrai ($v_d=0,2$ nm/s, $T_d=300$ °C): (a) bendrinis spektras, (b) Zr O1s, (c) Zr 3d, (d) Al 2p, (e) Sc 2p [102]

Be to, panašų XPS spektro smailių elgesį ir identiškas ScSZ ryšio energijų pozicijas pateikė ir kiti autoriai [133]. OH ir CO grupės natūraliai susidaro aplinkoje ir neturi jokios įtakos tūrinėms savybėms. Didelė metalinių Al ir Al₂O₃ oksidų koncentracija gali turėti įtakos medžiagų struktūrinėms savybėms ir ZrO_x bei deguonies vakansijų egzistavimui [178,179].

Al³⁺ atominių koncentracijų skaičiavimai ScAlSZ plonosiose plėvelėse, nusodintose ant 450 °C temperatūros substratų, buvo atlikti naudojant Al 2p spektrą ir yra pateikti (3 lentelėje). Gautame pagrindinių energijos lygmenų smailės Al 2p spektre yra AlO: OH, Al₂O₃: Al³⁺ ir Al, jie rasti atitinkamai ties ~75,3 eV BE, ~73,8 eV BE ir ~72,5 eV. Smailės ploto santykis buvo naudojamas apskaičiuoti Al₂O₃: Al³⁺ frakcija, kuri buvo padauginta iš tyrimo rezultatuose nustatytos Al koncentracijos. Al koncentracija mažėja nuo 11,8 at.% iki 3,5 at.%, o nusodinimo greičiai buvo atitinkamai 0,2 nm/s ir 1,6 nm/s.



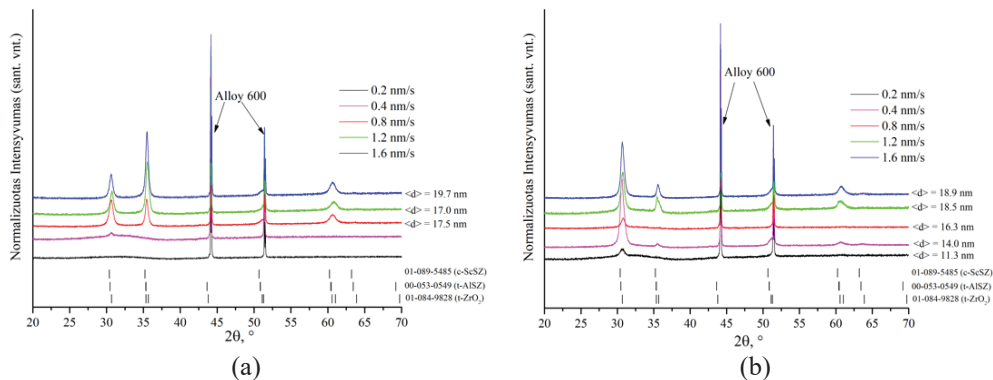
5 pav. ScAlSZ plonų dangų XPS spektrai: (a) Zr 3d, (b) O 1s [159]

OH grupių ir Zr junginių buvimas abiejose 1,6 at.% ir 15,9 at.% Al turinčiose plonosiose plėvelėse pateiktas (5 pav, a, b). Zr 3d_{5/2} smailė priklauso Zr³⁺suboksidams ir yra ties ~182,0 eV BE. Zr³⁺ jonų buvimas gali reikšti deguonies vakansijų buvimą. O1s pagrindinių energijos lygmenų smailių spektrai priklauso C=O ir OH grupėms, V_o: O²⁻ jonams, kurie yra ZrO_x gardelės deguonies vakansijos srityje, Al₂O₃: Al³⁺ ir ZrO_x: O²⁻ jonai [180–186]. Al₂O₃ ir V_o smailės buvo ypač svarbios O1s spektre. Didėjant Al kiekiui, išsiplėtusios sritys slopina didesnę deguonies vakansijų koncentraciją.

ScAlSZ rentgeno difrakcijos ir Ramano spektrų analizė

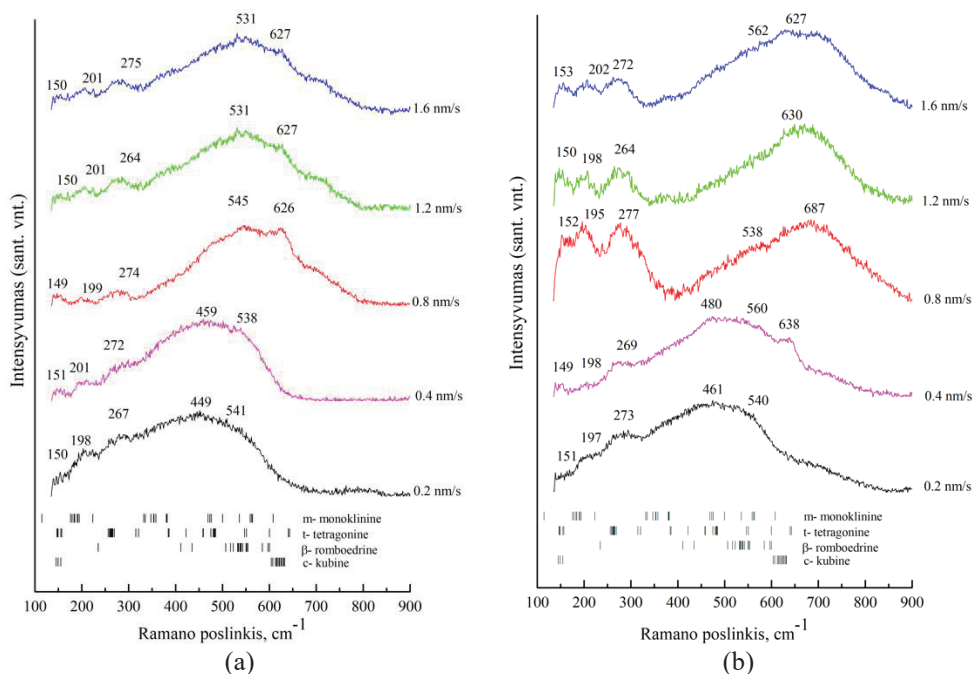
ScAlSZ plonų dangų, nusodintų ant Alloy 600 lydinio, esant skirtingoms padėklo temperatūroms ir skirtingiems nusodinimo greičiams, rentgenogramos pateiktos (6 pav., a, b). ScAlSZ plonų dangų, suformuotų naudojant 600 °C padėklo temperatūrą, XRD analizė rodo, kad kristalinė struktūra pastebima esant visiems nusodinimo greičiams, tačiau plonos dangos, nusodintos esant žemesnei 300 °C padėklo temperatūrai, yra amorfinės esant mažesniems nusodinimo greičiams (0,2 nm/s – 0,4 nm/s) ir polikristalinės struktūros tik esant atitinkamai didesniems (0,8 –

1,6 nm/s) nusodinimo greičiams. Atlikus XRD analizę pagal paieškos ir atitikimo metodą, gauta, kad nagrinėjamuose modeliuose yra smailės, atitinkančios kubinę skandžio stabilizuoto cirkonio fazę ir atitinka (JCPSD Nr. 01-089-5485) duomenis. Matavimų metu taip pat buvo rasta tetragoninės fazės, kuri atitinka aliuminio oksidu stabilizuotą cirkonį (JCPSD Nr. 00-053-0549). Taip pat buvo rasta gryno cirkonio tetragoninės fazė (JCPSD Nr. 01-084-9828). Analizuojant ScAlSZ plonųjų dangų rentgenogramas, gryno Al_2O_3 būdingų pikų nepastebėta. Be to, dėl smailės padėties poslinkio ir tų smailių persidengimo sunku vienareikšmiškai nustatyti atitinkamą fazės kiekį ir junginius tiriant rentgenogramas.



6 pav. ScAlSZ plonųjų dangų, nusodintų ant Alloy 600 padėklų, XRD kreivės (išmatuotos kambario temperatūroje), naudojant (a) 300 °C ir (b) 600 °C padėklų temperatūrą ir skirtingą nusodinimo greitį nuo 0,2 nm/s iki 1,6 nm/s [102]

XRD analizė parodė, kad kristalitų dydis didėja didėjant nusodinimo greičiui ir padėklų temperatūrai. Didžiausias kristalitų dydis (18,9 nm) gautas, kai padėklų temperatūra yra 600 °C, o nusodinimo greitis 1,6 nm/s, o mažiausias kristalitų dydis (11,3 nm) – kai nusodinimo greitis buvo 0,2 nm/s. Kristalito dydžio pokyčio priklausomybė gali būti susijusi su paviršiaus migracijos energijos kinetika, t. y., didėjant nusodinimo greičiui, garuojančios dalelės turi daugiau energijos, o tai lemia didesnę jų judrumą ir ilgesnį difuzijos kelią padėklų paviršiuje. Nusodinti atomai turi daugiau energijos migruoti ir aukštesnėje temperatūroje gali suformuoti didžiausius kristalitus [130,187]. Kita vertus, plonųjų dangų kristališkumas susijęs su Al koncentracija ir padėklų temperatūra. Jis didėja, mažėjant Al koncentracijai ir didėjant padėklų temperatūrai. ScAlSZ kristalitų grūdelių ribose gali atsirasti amorfinių Al arba Al_2O_3 fazių, kurios veikia kaip priemaišos. Dėl to, esant didelei Al koncentracijai, grūdelių augimas buvo stabdomas. Be to, nustatyta, kad plonos dangos su amorfinės fazės struktūra auga, kai Al koncentracija yra 9,7% [189]. Taip pat Ishii [29] pastebėjo, kad didėjanti Al_2O_3 koncentracija gali lemti deguonies vakansijų žematemperatūrinėje romboedrinėje fazėje išnykimą. Kubinės fazės stabilizacija gauta esant 0,5% [29]. Be to, deguonies kiekio pokyčiai gali turėti įtakos grūdelių dydžiui ir fazinei koncentracijai [190].



7 pav. ScAlSZ plonų dangų, nusodintų ant Alloy 600 padėklų, Ramano spektrai naudojant (a) 300 °C ir (b) 600 °C padėklo temperatūrą ir skirtingą nusodinimo greitį nuo 0,2 nm/s iki 1,6 nm/s [102]; monoklininė [10,50,122,126,130–133]; tetragoninė [10,50,117,118,122,126,131–133]; romboedrinė [50,130,154]; kubinė [10,50,117,122,126,130–132]

Siekiant visapusiškai apibūdinti ScAlSZ plonų dangų struktūrą, buvo atlikti Ramano matavimai. Plonų ScAlSZ dangų Ramano spektruose yra keletas persidengiančių smailių, kurios gali rodyti polimorfizmą. Po išsamių Ramano tyrimų buvo nustatyta, kad smailės yra monoklininės (m-ZrO₂), tetragoninės (t-ZrO₂), romboedrinės (β-ZrO₂) ir kubinės (c-ZrO₂) fazių (7 pav.). Pagal Ramano smailės tarp 149 cm⁻¹ ir 277 cm⁻¹, kurių sudaro kelios smailės, buvimą galima kalbėti apie skirtingų ZrO₂ fazių susidarymą. Ramano juosta apie 198 cm⁻¹ A_g moda atitinka monoklininės fazės ZrO₂ smailės [126,130,131]. Grupinė teorija aprašo šešių Ramano modų (A_{1g} + 2B_{1g} + 3E_g) buvimą tetragoniniame ZrO₂, o kubinė fazė rodo vienos Ramano modos F_{2g} buvimą (tarp 605 ir 630 cm⁻¹), o kai kurių modų tetragoninei fazei gali ir nebūti. Ramano smailės žemo dažnio diapazone, tokia kaip 149–153 cm⁻¹ ir apie 638 cm⁻¹, atitinka A_{1g} modą ir gali būti t-ZrO₂ fazės indikatorius [10,117,118,131,133]. Kubinę (c) fazę rodė silpnos plačios smailės tarp 626 ir 630 cm⁻¹ (7 pav.). Kubinei fazei būdingos Ramano juostos pasislinkusios į aukštesnį bangų skaičiaus intervalą, ir tai gali būti susiję su deguonies subplokštelės netvarka, kurią sukelia legiravimas Sc₂O₃ ir Al₂O₃ [10,117,126,130]. Be to, smailių poslinkį gali lemti įvairūs veiksniai, įskaitant tarpatominių atstumų pokyčius, gardelės susitraukimą ir išsiplėtimą. Dėl to plonosios ScAlSZ dangos yra polimorfinės, jose yra monoklininės (m-ZrO₂), tetragoninės (t-ZrO₂), romboedrinės (β-ZrO₂) ir kubinės (c-

ZrO₂) fazės. Smailė apie 687 cm⁻¹ gali būti interpretuojama kaip anomalios liuminescencinės juostos. Mažo intensyvumo papildomas modas, kurios nebūdingos kubinei fluorito struktūrai, galima paaiškinti tuo, kad, Zr⁴⁺ jonus pakeitus Sc³⁺, atsiranda neigiamo krūvio perteklius, kurį kompensuoja atrankos taisyklės, tiesiogiai priklausančios nuo deguonies vakansijų (V_o) [128,129].

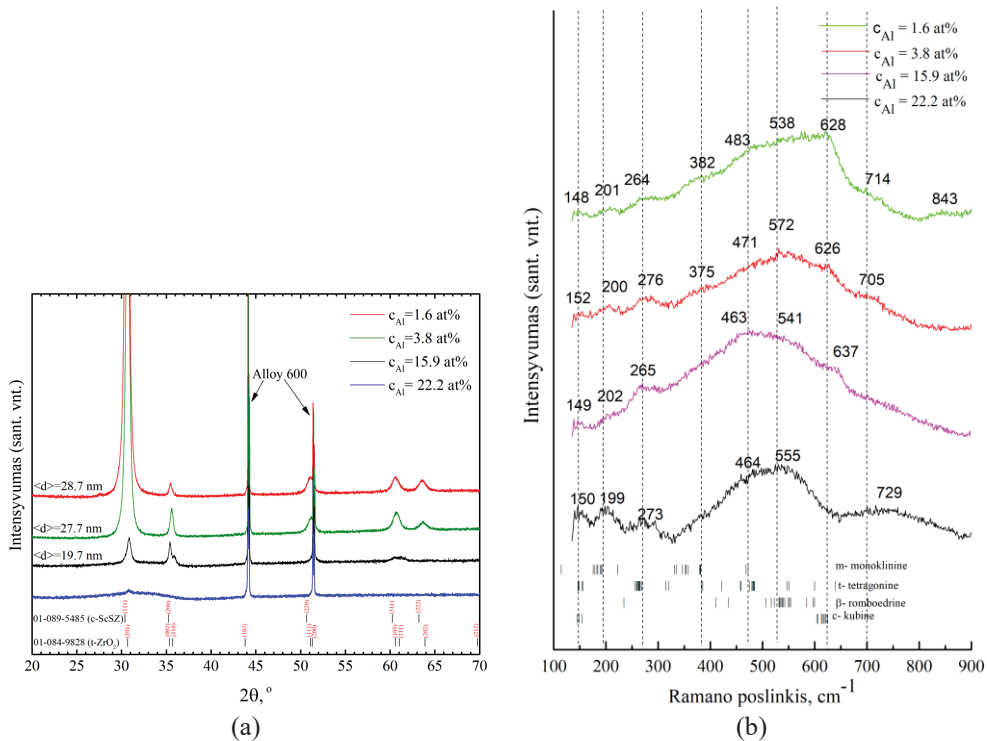
4 lentelė. Kubinių, tetragoninių ir monoklininių fazių santykis ScAlSZ plonosiose plėvelėse [102]

Nusodinimo greitis (nm/s)	Padėklo temperatūra, °C					
	300 °C		600 °C		300 °C	
	monoklininė		tetragoninė + romboedrinė		kubinė	
0,2 nm/s	35%	28%	65%	72%	0%	0%
0,4 nm/s	19%	12%	81%	88%	0%	0%
0,8 nm/s	6%	54%	41%	46%	53%	0%
1,2 nm/s	19%	20%	26%	26%	55%	53%
1,6 nm/s	19%	18%	26%	23%	55%	59%

Remiantis šiame darbe gautais Ramano spektroskopijos rezultatais, kubinės ir monoklininės, tetragoninės fazių santykis ScAlSZ atveju yra nuo 53% iki 59% (4 lentelė). Kubinės fazės kiekis smarkiai padidėja, kai didėja nusodinimo greitis. Pagal Ramano spektrų duomenis, kubinė fazė neaptinkama esant 0,2 ir 0,4 nm/s nusodinimo greičiui. Tačiau (7 pav.) egzistuojančios plačios juostos, kurios rodo vietinę netvarką, gali būti susijusios su nestechiometrine ZrO₂ faze ir blogai kristalizuota Zr⁴⁺ ir Sc³⁺ struktūra. Mums pavyko nustatyti, kad plonos dangos, nusodintos esant mažam nusodinimo greičiui, yra mišrios fazės (m-ZrO₂) ir (t-ZrO₂).

Skirtingos Al koncentracijos ScAlSZ plonų dangų rentgeno spindulių difrakcijos ir Ramano spektrų analizė

Siekiant nuodugnai ištirti legiravimo Al įtaką fazių stabilizacijai, buvo atlikta papildoma suformuotų plonų dangų XRD difrakcinė analizė, keičiant Al koncentraciją. XRD metodu gautų ScAlSZ plonųjų dangų rezultatų analizė parodė, kad jų kristalinė struktūra atitinka amorfinę modifikaciją, kai Al koncentracija plonosiose dangose buvo 22,2 at.%, ir kristalinę struktūrą, kai Al koncentracija buvo atitinkamai 1,6 at.%, 3,8 at.% ir 15,9 at.% (8 pav., a). Tačiau ScAlSZ plonų dangų, kuriose yra 15,9 at.% Al, XRD rentgenogramą sudarė smailės, priklausančios tetragoninei cirkonio fazei, ir atitiko (JCPDS Nr. 01-084-9828) bei buvo aptikta (110) orientacija, kuri yra draudžiama kubinėje kristalinėje gardelėje ir leidžiama tetragoninėje fazėje. ScAlSZ plonos dangos su maža aliuminio koncentracija (1,6 at.% ir 3,8 at.%) pasižymėjo būdingomis smailėmis, priklausančiomis kubinei skandžio stabilizuoto cirkonio fazei (JCPDS Nr. 01-089-5485), ir būdingomis tetragoninės cirkonio fazės smailėmis (JCPDS Nr. 01-084-9828).



8 pav. (a) XRD rentgenogramos (išmatuotos kambario temperatūroje) ir (b) ScAlSZ plonų dangų, nusodintų ant Alloy 600 padėklų, Ramano spektrai, naudojant 450 °C padėklo temperatūrą ir skirtingą Al koncentraciją: 1,6 %, 3,8 %, 15,9 % ir 22,2 %; b) plonų ScAlSZ dangų Ramano spektrai [159]; monoklininė [50,118,122,126,130,134]; tetragoninė [50,118,122,126,130,132,134]; romboedrinė [50,118]; kubinė [50,118,122,126,130,134,174]

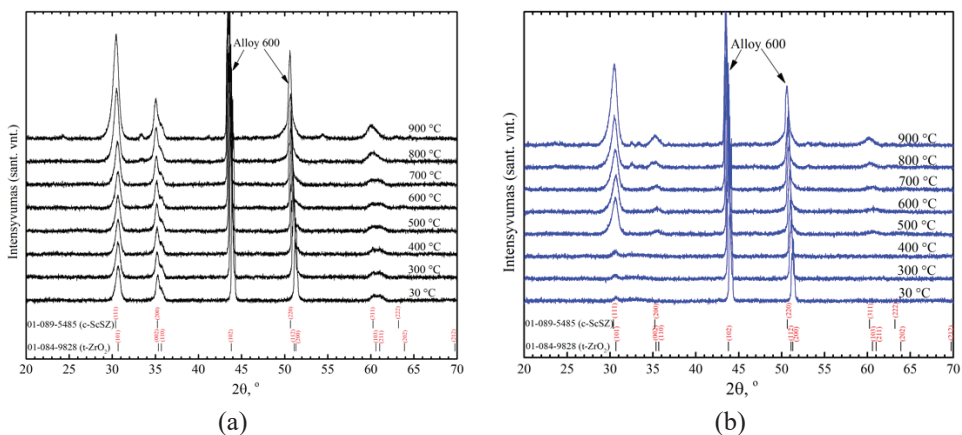
Suformuotų ScAlSZ plonų dangų su 1,6, 3,8, 15,9 ir 22,2% Al koncentracija XRD analizę patvirtino Ramano spektroskopijos matavimai. Be to, nustatyta, kad visose plonosiose dangose yra monoklininė fazė. Be to, esant 22,2% aliuminio koncentracijai plonose dangose susidarė tetragoninė ir monoklininė fazės. Nors atlikus XRD analizę nustatyta amorfinė fazė, Ramano matavimai įrodo, kad ScAlSZ plonų dangų Ramano spektre yra smailės, priklausančios monoklininei (m-ZrO₂), tetragoninei (t-ZrO₂) ir kubinei (c-ZrO₂) fazėms (8 pav., b, 5 lentelė). Kubinei fazei atstovauja aptiktos 626 cm⁻¹ ir 628 cm⁻¹ smailės. Tetragoninei fazei atstovauja: 148, 149, 150, 152, 264, 265, 273, 278, 337, 464, 463, 471, 483 cm⁻¹, o smailės, atitinkančios monoklinines fazes, aptinkamos ties 199, 200, 201, 202, 375, 382 cm⁻¹ [10,50,122,126,130–134].

5 lentelė. Suformuotų ScAlSZ plonų dangų monoklininių, tetragoninių ir kubinių fazių santykis [159]

ScAlSZ fazė	$c_{Al}=1,6$ at. %	$c_{Al}=3,8$ at. %	$c_{Al}=15,9$ at. %	$c_{Al}=22,2$ at. %
Monoklininė	22%	18%	18%	31%
Tetragoninė	42%	40%	82%	69%
Kubinė	36%	42%	0%	0%

Plonų dangų XRD analizė ir Ramano spektrai po terminio atkaitinimo

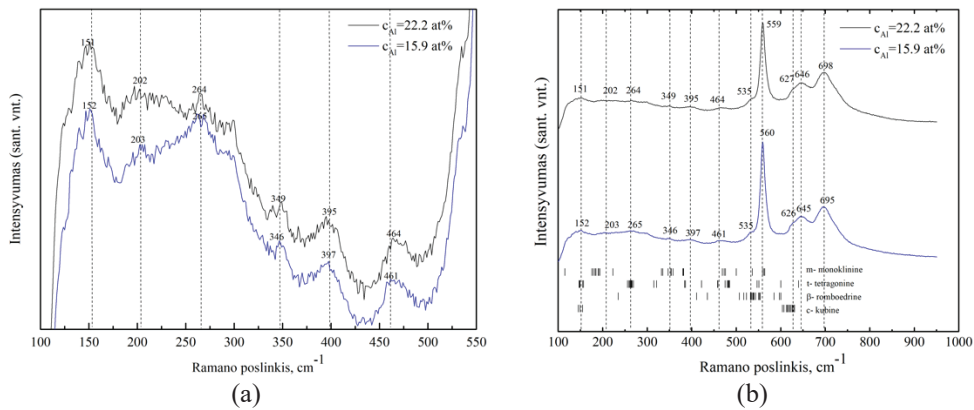
Siekiant ištirti fazių susidarymą, buvo tiriami suformuotų plonų dangų kristalinės struktūros pokyčiai *in situ* temperatūroje nuo 30 °C iki 900 °C, o kaitinimo greitis buvo 1 °C per minutę. Atkaitinimo proceso metu suformuotų plonų dangų rentgenogramos, kuriose yra 15,9 at.% ir 22,2 at.% Al koncentracijos yra pateiktos (9 pav.). Rentgeno spinduliuotės difrakcijos kreivės, gautos kintant temperatūrai, rodo, kad, palyginti greitai kaitinant bandinį, iki 500 °C temperatūros fazinis perėjimas ir kristalimumo padidėjimas nevyksta. O, temperatūrai viršijant 500 °C, XRD kreivėse atsirado atitinkama smailė ir padidėjo smailės intensyvumas. Rentgeno fazinės analizės duomenys patvirtina kristalinės struktūros pagerėjimą, tačiau dėl kubinės, tetragoninės, monoklininės ir romboedrinės fazių smailių persidengimo neįmanoma tiksliai nustatyti tiriamųjų bandinių fazinio perėjimo pobūdžio. Taigi iš analizės duomenų galima daryti prielaidą, kad tetragoninės fazės kiekis didėja, kai Al koncentracija yra 15,9 at.%, o kai Al koncentracija yra 22,2 at.%, amorfinė fazė virsta kubinės, tetragoninės ir romboedrinės fazių mišiniu.



9 pav. ScAlSZ plonų dangų XRD rentgenogramos atkaitinimo proceso metu, esant skirtingai Al koncentracijai: (a) 15,9 %, (b) 22,2 % [159]

Kadangi Ramano spektroskopijos metu nebuvo nustatyta kubinės fazės susidarymo požymių suformuotose plonose dangose, kuriose aliuminio koncentracija yra 15,9% ir 22,2%, siekiant ištirti bet kokią nepastebimą fazinį

perėjimą ir gardelės iškraipymą, buvo panaudota plonų dangų po temperatūrinio atkaitinimo Ramano spektroskopijos analizė (10 pav.). Atkaitintų ScAlSZ plonųjų dangų Ramano spektras pasižymėjo kitokia spektro forma, palyginti su neatkaitintomis dangomis. Pastebėta, kad Ramano spektre yra kelios smailės, priklausančios tetragoninėms fazėms ties 150 cm^{-1} (A_{1g}), 265 cm^{-1} (E_g), 460 cm^{-1} (A_{1g}), 645 cm^{-1} (A_{1g}) [10,102,117,118,131], o smailės ties 202 cm^{-1} ir 346 cm^{-1} gali būti priskirtos monoklininei ($m\text{-ZrO}_2$) fazei [126,130,131]. Romboedrinė ($\beta\text{-ZrO}_2$) fazė šiuose spektruose randama kaip silpna plati smailė maždaug apie 535 cm^{-1} (B_g) ir aštri smailė su centru apie 560 cm^{-1} (A_g) [10,50,130] Plati smailė tarp 600 cm^{-1} ir 630 cm^{-1} atitinka kubinės ($c\text{-ZrO}_2$) fazės Ramano aktyviają vibraciją (F_{2g}) [50,102,133]. Ramano smailės ties 621 cm^{-1} (F_{2g}) ir 645 cm^{-1} (A_{1g}) susilieja į vieną plačią smailę, galbūt dėl priemaišų ties grūdelių ribomis. Kubinę (c) ZrO_2 fazę rodančios smailės spektre nėra ryškiai išreikštos [117]. Galiausiai smailės 695 cm^{-1} ir 698 cm^{-1} gali būti paašškintos Ramano aktyviuoju gardelės fononu ir gali būti mišrios fazės.



10 pav. ScAlSZ plonų dangų, nusodintų ant Alloy600 atkaitinimo procese ($30\text{--}900\text{ }^\circ\text{C}$), Ramano spektrų matavimai: turinčių $15,9\text{ at.}\%$ ir $22,2\text{ at.}\%$ Al (a) diapazonas nuo 100 cm^{-1} iki 550 cm^{-1} . (b) diapazonas nuo 100 cm^{-1} iki 900 cm^{-1} [159]; monoklininė [50,118,122,126,130,134]; tetragoninė [50,118,122,126,130,132,134]; romboedrinė [50,118]; kubinė [50,118,122,126,130,134,174]

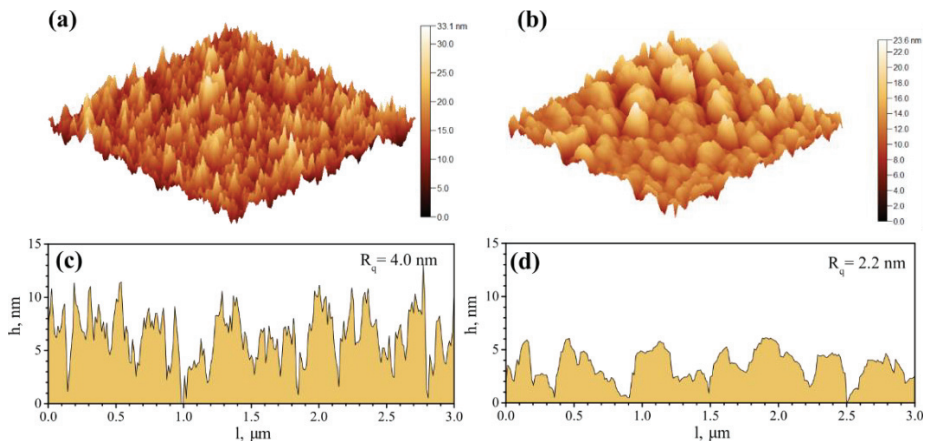
Fazinės sudėties apskaičiavimai pagal Ramano spektrus pateikti (6 lentelėje).

6 lentelė. Monoklininių, tetragoninių ir romboedrinųjų bei kubinių fazių santykis atkaitintose ScAlSZ plonose dangose [159]

ScAlSZ fazė	$c_{Al}=15,9\text{ at.}\%$	$c_{Al}=22,2\text{ at.}\%$
Monoklininė	16%	15%
Tetragoninė + Romboedrinė	61%	61%
Kubinė	23%	24%

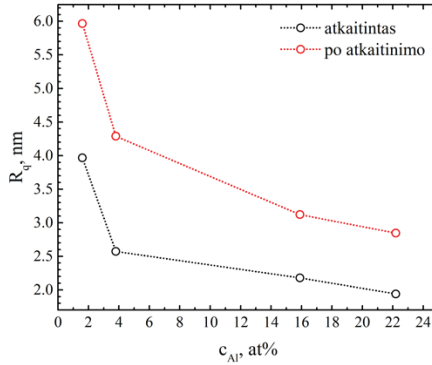
Plonų dangų paviršiaus šiurkštumo tyrimas

Atominių jėgų mikroskopu buvo tiriama Al koncentracijos įtaka suformuotų plonų dangų nanostruktūrinio paviršiaus reljefo šiurkštumo parametrams. Tyrimai buvo atliekami prieš atkaitinimą ir po jo. Iš AFM nuotraukų matyti, kad Al koncentracija turi didelę įtaką paviršiaus struktūrai ir šiurkštumui. Mažos Al koncentracijos plonų dangų (pvz., 1,6 at.%) nanostruktūrizuotų paviršių šiurkštumo parametrai turi pluoštinę struktūrą ir 4,0 nm šiurkštumą (11 pav., a, c, ir 12 pav.). Tačiau didinant Al koncentraciją (pvz., 15,9 at.%) pereinama nuo pluoštinės struktūros prie grūdėtos struktūros, o paviršiaus šiurkštumas sumažėja iki 2,2 nm (11 pav., b, d). Dėl slopinančio Al arba Al_2O_3 fazių poveikio grūdelių ribose ScAlSZ plonose dangose, kuriose yra didelė Al koncentracija, stulpeliai sudaryti iš smulkių grūdelių (rutuliukų), o ne skaidulų, kaip mažos Al koncentracijos 1,6 at.% atveju.



11 pav. ScAlSZ plonų dangų AFM vaizdai: a), c) Al=1,6 at% ir b), d) Al=15,9 at% [159]

Po atkaitinimo taip pat buvo tiriama ScAlSZ plonų dangų mikrostruktūra. Visų ScAlSZ plonų dangų paviršiaus šiurkštumas padidėjo 1,5 karto (12 pav.). Didėjant Al kiekiui nuo 1,6 at.% iki 22,2 at.%, paviršiaus šiurkštumas sumažėjo nuo 6,0 nm iki 2,8 nm. Paviršiaus šiurkštumo padidėjimą po terminio atkaitinimo galima paaiškinti adatomų judrumu paviršiuje per žemą temperatūrą terminio atkaitinimo metu. Aukštoje temperatūroje adatomų judrumas yra pakankamai didelis ir sudaro sąlygas vyraujančiam grūdelių augimui. Atitinkamai, augant grūdeliams, didėja ir išmatuotų atskirų aukščių ir gylių nuokrypių nuo vidutinės linijos vidutinė vertė (vidutinis kvadratinis šiurkštumas, R_q). Panašią paviršiaus šiurkštumo didėjimo tendenciją didinant temperatūrą pastebėjo ir kiti autoriai [191,192]. Jokių papildomų mikrostruktūros pakitimų nepastebėta. Plonos dangos išliko vientisos, be akivaizdžių skilimų ar porų.

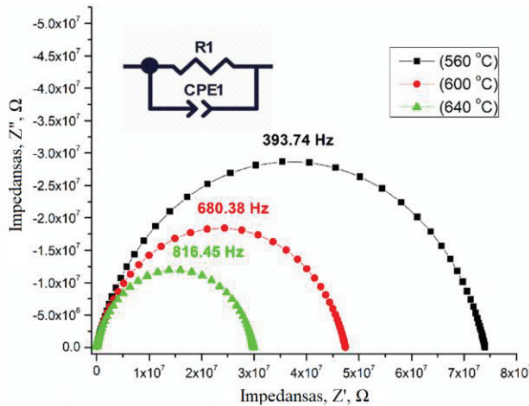


12 pav. ScAlSZ plonų dangų paviršiaus šiurkštumas: ○ atkaitintas ○ po atkaitinimo [159]

Suformuotų plonų dangų elektrinių savybių tyrimas

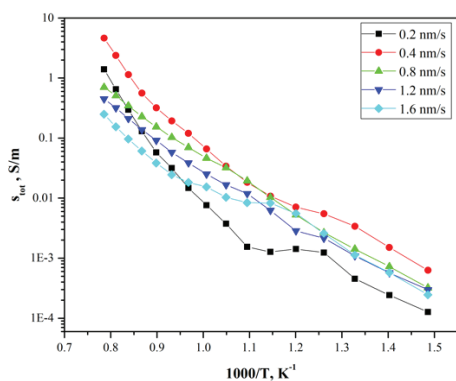
ScAlSZ plonųjų dangų impedanso matavimo rezultatai

Suformuotų ScAlSZ tūrinis keramikos laidumas buvo įvertintas pagal impedanso spektrus. Grūdelių ribų varža yra labai maža, palyginti su grūdelių varža, todėl buvo laikoma, kad $R_{\text{bulk}} = R_g + R_{\text{gb}}$ [168].

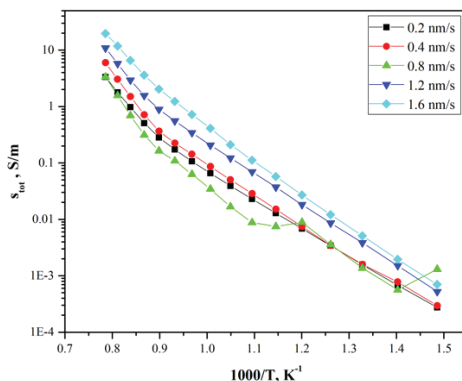


13 pav. Suformuotų ScAlSZ plonų dangų $\text{Im}(Z) = Z''$ ($\text{Re}(Z) = Z'$) kreivės, esant 4 nm/s nusodinimo greičiui ir skirtingoms temperatūroms

Kompleksinės varžos kitimas didinant temperatūrą yra pateiktas 13 pav. Keramikos relaksacijos dažnis kinta didėjant temperatūrai, pereidamas į aukštesnį dažnių diapazoną.



(a)



(b)

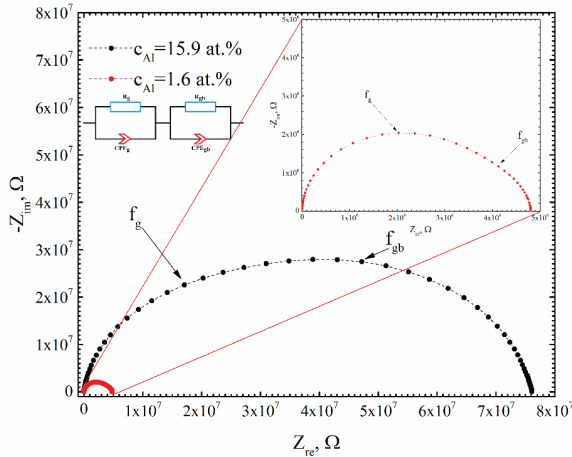
14 pav. Tūrinio joninio laidumo priklausomybė nuo temperatūros esant skirtingiems nusodinimo greičiams nuo 0,2 nm/s iki 1,6 nm/s: (a) padėklų temperatūra 300 °C, (b) padėklų temperatūra 600 °C

ZrO₂ pagrindu pagamintos keramikos elektrinės savybės labai priklauso nuo temperatūros. Pagrindinę informaciją apie priklausomybės nuo temperatūros pobūdį suteikia varžos priklausomybė nuo atvirkštinės temperatūros. (14 pav.) pateikti suformuotų plonų dangų temperatūrinių priklausomybių grafikai. Deguonies jonų difuzijos aktyvacijos energija buvo nustatyta iš joninio laidumo verčių, atitinkamai priklausančių nuo atvirkštinės temperatūros. Didėjant tiesės kampo su abscisių ašimi kampui, aktyvavimo energija monotoniškai didėja. Pateiktos difuzijos aktyvavimo energijos. Tūrinį ScAlSZ laidumą daugiausia sudaro grūdelių laidumas, o grūdelių ribos laidumo negalima įvertinti. Grūdelių ribų varža yra labai maža ir gali būti susijusi su ScSZ kolegiravimu nedideliu Al₂O₃ kiekiu [114,195]. Pastebėta aktyvacijos energijos priklausomybė nuo kristalito dydžio. Aktyvacijos energija didėja didėjant kristalito dydžiui (nuo 11,3 nm iki 18,9 nm). Mažiausia aktyvacijos energija apskaičiuota, kai padėklų temperatūra buvo 300 °C. Geriausias tūrinis jonų laidumas šiuose tiriamuosiuose bandiniuose buvo ($\sigma_{bulk} = 1,01$ S/m 800 °C temperatūroje, aktyvavimo energija $E_a = 1,13$ eV) pasiektas, kai nusodinimo greitis buvo 1,6 nm/s, o padėklo temperatūra 600 °C.

ScAlSZ plonųjų dangų su skirtinga Al koncentracija impedanso matavimo rezultatai

Elektrocheminės impedanso spektroskopijos metodu buvo tiriamos ScAlSZ dangų elektrinės savybės. Iš matavimo duomenų buvo gauta Naikvisto grafiko forma, išmatuota naudojant platiną kaip elektrodo medžiagą (15 pav.). Arenijaus grafikai kaip temperatūros funkcija rodo, kad įvesto Al kiekis turi įtakos laidumui (16 pav.). Atliekant šį tyrimą, plonos dangos buvo tiriamos ore, esant įvairioms temperatūroms: 1 diapazono (400 °C – 560 °C) ir 2 diapazono (720 °C – 1000 °C). Naikvisto grafiko forma buvo netaisyklinga, o tai rodo, kad egzistuoja du deguonies difuzijos keliai – grūdelių ir grūdelių ribomis. Geriausi rezultatai gauti taikant $R_g|CPE_g - R_{gb}|CPE_{gb}$ modelį. Iš modelio matome, kad plonose dangose, kuriose yra

maža Al koncentracija (<3,8 %), grūdelių varža buvo didesnė už grūdelių ribos varžą. Plonų dangų, kuriose yra didelė Al koncentracija (>3,8 at.%), grūdelių impedansas buvo mažesnis už grūdelių ribos impedansą.



15 pav. ScAlSZ plonų dangų su 15,9 % ir 1,6 % Al Naikvisto diagramos 560 °C temperatūroje [159]

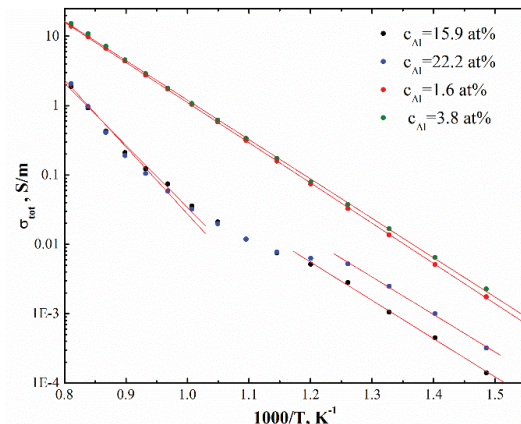
Plonų dangų su 1,6 % Al koncentracija varža $R_g \sim 3,70E \times 10^6 \Omega$ ir $R_{gb} \sim 1,11E \times 10^6 \Omega$, o plonų dangų su 15,9 % Al koncentracija $R_{gb} \sim 2,52E \times 10^7 \Omega$ ir $R_{gb} \sim 5,07E \times 10^7 \Omega$. Be to, ScAlSZ plonų dangų su 1,6 at.% 15,9 at.% Al koncentracija kritinis grūdelių ribų dažnis (f_g) dangose sumažėjo nuo $9,08 \times 10^3$ iki $9,60 \times 10^2$ (9,08 kHz iki 0,96 kHz), o kritinis grūdelių dažnis (f_{gb}) atitinkamai nuo $1,79 \times 10^3$ iki $2,16 \times 10^2$ (1,79 kHz iki 0,216 kHz) (7 lentelė).

7 lentelė. ScAlSZ dangų su 15,9 % ir 1,6 % Al, užaugintų 560 °C temperatūroje grūdelių ir grūdelių ribų varžos ir talpos

	$c_{Al}=1,6 \text{ at.}\%$	$c_{Al}=15,9 \text{ at.}\%$
R_g, Ω	$3,7 \times 10^6$	$2,52 \times 10^7$
CPE_g, F	$5,29 \times 10^{-12}$	$1,11 \times 10^{-11}$
n_g	$9,90 \times 10^{-1}$	$9,40 \times 10^{-1}$
R_{gb}, Ω	$1,11 \times 10^6$	$5,07 \times 10^7$
CPE_{gb}, F	$1,54 \times 10^{-10}$	$2,99 \times 10^{-11}$
n_{gb}	$9,30 \times 10^{-1}$	$9,00 \times 10^{-1}$
f_{gb}, Hz	$9,08 \times 10^3$	$9,60 \times 10^2$
f_g, Hz	$1,79 \times 10^3$	$2,16 \times 10^2$

Arenijaus grafikas (16 pav.) rodo, kad ScAlSZ plonos dangose su 1,6% ir 3,8% Al koncentracijos pasižymi panašia elgsena ir tiesine priklausomybe. Nors kreivės su didesne Al koncentracija 15,9 at.% ir 22,2 at.% labai skiriasi ir atrodo, kad jos yra netiesinės priklausomybės. ScAlSZ plonų dangų su 15,9% ir 22,2% Al aktyvacijos energija yra didesnė aukštesnėse temperatūrose. Aktyvacijos energija 1

intervale (400 °C – 560 °C) yra ~1,10 eV, o 2 intervale (720 °C – 1000 °C) – ~1,85 eV (8 lentelė).



16 pav. ScAlSZ plonų dangų su skirtingomis Al koncentracijomis Arenijaus diagramos [159]

8 lentelė. ScAlSZ plonų keraminių dangų, suformuotų esant skirtingai aliuminio koncentracijai (c_{Al}), tūrinis joninis laidumas (σ_{bulk}) 520 °C ir 800 °C temperatūroje ir jų aktyvavimo energija (E_a) [159]

c_{Al} , at. %	Temperatūros intervalas			
	Intervalas 1		Intervalas 2	
	σ , S/m	E_a , eV	σ , S/m	E_a , eV
1,6	0,033	1,16	2,74	1,16
3,8	0,038	1,14	2,89	1,14
15,9	0,0028	1,10	0,123	1,79
22,2	0,0025	1,08	0,105	1,93

Didžiausias suminis laidumas buvo plonų dangų, kurių sudėtyje yra 3,8% Al. Temperatūros intervale nuo 700 °C iki 1000 °C jis svyravo nuo 1,1 iki 19,2 S/m (16 pav. ir 8 lentelė). Palyginus ScAlSZ plonų dangų bendrąjį laidumą nustatyta, kad dangų, kuriose yra 15,9 at.% ir 22,2 at.% Al, bendrasis laidumas buvo 10 kartų mažesnis nei dangų, kuriose yra 1,6 ir 3,8 at.% Al (16 pav.).

IŠVADOS

1. ScSZ ir ScSZAl plonų sluoksnių, suformuotų ant Alloy 600 padėklų, naudojant 0,4 nm/s nusodinimo greitį, remiantis Rentgeno struktūrine analizės (XRD) rezultatais, yra kubinės (JCPDS Nr. 01-089-5483) ir romboedrinės fazės (JCPDS Nr. 01-89-5482). Atlikta Ramano analizė, kaip jautresnė mažam atomų poslinkiui, parodė, kad suformuoti ScSZ ir ScSZAl sluoksniai yra sudaryti iš skirtingų polimorfinių būsenų: 44% kubinės fazės, 18% tetragoninės ir 38% mišrios fazės, rodančios romboedrinį fazės perėjimą.
2. ScSZ ir ScSZAl plonų sluoksnių kristališkumas tiesiogiai susijęs su padėklo temperatūra: kristalitų matmenys didėja nuo 17,4 nm iki 69,9 nm didėjant padėklo temperatūrai nuo 50 °C iki 300 °C, o kai temperatūra yra 450 °C, kristalito dydis sumažėja nuo 44,6 nm iki 31,2 nm.
3. Rietveldo analizė parodė, kad suformuotos ScSZ ir ScSZAl plonos plėvelės, sudarytos iš kubinės ir romboedrinės fazių mišinio atitinkamai 87,8 % ir 12,2 %, su tokia pačia grynosios kubinės fazės tikimybe.
4. Ramano smailės padėtis ScSZ ir ScSZAl plonų dangų kubinėje fazėje pasislenka link didesnės banginio skaičiaus vertės atitinkamai iš 622cm⁻¹ į 632cm⁻¹ ir iš 618 cm⁻¹ į 621cm⁻¹. ir tai gali būti dėl deguonies subgardelės išsikraipymo, sukkelto legiravimu Sc₂O₃ ir Al₂O₃.
5. Kai ScAlSZ keramika buvo suformuota ant 300 °C ir 600 °C temperatūros padėklų, dangose kubinės fazės buvo 53–59%, o dangose, suformuotose ant 450 °C temperatūros padėklų, kubinės fazės buvo daugiau dangose, kuriose buvo maža Al koncentracija. Kai Al koncentracija buvo 1,6 at.% ir 3,8 at.%, dangose buvo 36% ir 42% kubinės fazės, o kai Al buvo 15,9 at.% ir 22,2 at.%, dangose buvo tetragoninės ir monoklininės fazių mišinys.
6. Legiravimas Al sulėtino kubinės fazės stabilizavimąsi apie 7 %, dėl ko pasikeitė kubinės fazės dalis ScSZ nuo 42% iki 53% ir ScSZAl nuo 41% iki 43%.
7. Suformuotos plonos ScAlSZ dangos yra tolygios ir mažesnio šiurkštumo esant didesnei Al koncentracijai (15,9 ir 22,2 at.%). Nusodintų dangų šiurkštumas kinta nuo 2,2 iki 1,9 nm, o po terminio atkaitinimo – nuo 3,1 iki 2,8 nm.
8. Didžiausia ScSZ plonųjų dangų joninio laidumo vertė buvo 4,2×10⁻³ S/cm, kai padėklo temperatūra buvo 600 °C. Bandiniuose vyraujanti tetragoninė fazė atsiranda dėl vakansijos aktyvacijos energijos padidėjimo nuo 0,91 eV iki 1,22 eV esant aukštesnei padėklo temperatūrai. Arenijaus grafikai patvirtino netiesines priklausomybes, kai ScAlSZ dangose Al koncentracija yra 15,9 ir 22,2 at.%. Aktyvacijos energija buvo ~1,10 eV 400–560 °C temperatūroje ir ~1,85 eV 720–1000 °C padėklo temperatūrų intervaluose. Atkaitintose ScAlSZ dangose didžiausia bendrojo joninio laidumo vertė $S_{\text{bulk}} = 2,89$ S/m, gauta esant 800°C temperatūrai, kai dangose yra 3,8 at % Al.
9. ScAlSZ suformuotas plonas dangas, kai padėklo temperatūros buvo 300 °C ir 600 °C, sudarė O₂, Al, Sc ir Zr, o šių elementų koncentracijos atitinkamai

kito nuo 49,5 iki 54,2 at.%, nuo 3,0 iki 20,2 at.%, nuo 3,1 iki 8,7 at.%, nuo 25,3 iki 36,0 at.%.

10. ScAlSZ dangose suformuotose ant 450 °C temperatūros padėklų O₂, Al, Al, Al³⁺, Sc ir Zr ir koncentracijos svyravo atitinkamai nuo 50,2 iki 55,6 at.%, nuo 1,6 iki 22,2 at.%, nuo 1,4 iki 20,1 at.%, nuo 3,4 iki 7,7 at.%, nuo 27,4 iki 34,4 at.%.
11. ScAlSZ dangoje, kurioje yra OH grupių ir Sc, Zr, Al, C junginių, XPS spektro Al 2p, Zr 3d ir O1s smailės parodė, kad, didėjant Al ir Al₂O₃ koncentracijai, didėja deguonies vakansijų ir ZrO_x.
12. ScAlSZ kermainiuose milteliuose Rentgeno struktūrinės analizė (XRD) nenustatė tetragoninės fazės, tačiau šių miltelių tetragonaliųjų fazių smailės yra matomos iš Ramano analizės, t.y. B_{1g} ties 147 cm⁻¹, E_g ties 261 cm⁻¹, A_{1g} ties 635 cm⁻¹.
13. Remiantis Rentgeno struktūrinės analizės rezultatais, ScAlSZ plonos dangos, suformuotos 300 ir 600 °C temperatūroje, yra kubinės (JCPSD Nr. 01-089-5485) ir tetragoninės (JCPSD Nr. 00-053-0549) fazės, kai Ramano spektrų analizė parodė, kad 300 ir 600 °C temperatūrose susidaro monoklininės (m-ZrO₂) 198 cm⁻¹ A_g, tetragoninės (t-ZrO₂) 149-153 cm⁻¹, 638 cm⁻¹, kubinės (c-ZrO₂) 626-630 cm⁻¹ F_{2g} fazės.
14. Didelė 15,9 ir 22,2 at.% Al koncentracija sulėtina kubinės formos stabilizavimąsi tik po terminio atkaitinimo, todėl dangose pasiekiamas atitinkamas 23 ir 24% kubinės fazės susidarymas.

REFERENCES

- [1] C.A.J. Fisher, H. Matsubara, The influence of grain boundary misorientation on ionic conductivity in YSZ, *J Eur Ceram Soc.* 19 (1999) 703–707. [https://doi.org/10.1016/S0955-2219\(98\)00300-8](https://doi.org/10.1016/S0955-2219(98)00300-8).
- [2] N.Q. Minh, Ceramic Fuel Cells, *Journal of the American Ceramic Society.* 76 (1993) 563–588. <https://doi.org/10.1111/j.1151-2916.1993.tb03645.x>.
- [3] Y. Liu, L.E. Lao, Structural and electrical properties of ZnO-doped 8 mol% yttria-stabilized zirconia, *Solid State Ion.* 177 (2006) 159–163. <https://doi.org/10.1016/j.ssi.2005.10.002>.
- [4] V.G. Zavodinsky, The Mechanism of Ionic Conductivity in Stabilized Cubic Zirconia, *Physics of the Solid State.* 46 (2004) 453–457. <https://doi.org/10.1134/1.1687859>.
- [5] S.P.S. Badwal, F.T. Ciacchi, Oxygen-ion conducting electrolyte materials for solid oxide fuel cells, *Ionics (Kiel).* 6 (2000) 1–21. <https://doi.org/10.1007/BF02375543>.
- [6] I. Nettleship, R. Stevens, Tetragonal zirconia polycrystal (TZP)—A review, *International Journal of High Technology Ceramics.* 3 (1987) 1–32. [https://doi.org/10.1016/0267-3762\(87\)90060-9](https://doi.org/10.1016/0267-3762(87)90060-9).
- [7] F.M. Spiridonov, L.N. Popova, R.Y. Popil'skii, On the phase relations and the electrical conductivity in the system $ZrO_2Sc_2O_3$, *J Solid State Chem.* 2 (1970) 430–438. [https://doi.org/10.1016/0022-4596\(70\)90102-7](https://doi.org/10.1016/0022-4596(70)90102-7).
- [8] J. Chevalier, L. Gremillard, A. V. Virkar, D.R. Clarke, The tetragonal-monoclinic transformation in zirconia: Lessons learned and future trends, *Journal of the American Ceramic Society.* 92 (2009) 1901–1920. <https://doi.org/10.1111/j.1551-2916.2009.03278.x>.
- [9] M. Liu, C. He, J. Wang, W.G. Wang, Z. Wang, Investigation of $(CeO_2)_x(Sc_2O_3)_{(0.11-x)}(ZrO_2)_{0.89}$ ($x = 0.01-0.10$) electrolyte materials for intermediate-temperature solid oxide fuel cell, *Undefined.* 502 (2010) 319–323. <https://doi.org/10.1016/J.JALLCOM.2009.12.134>.
- [10] A. Kumar, A. Jaiswal, M. Sanbui, S. Omar, Scandia stabilized zirconia-ceria solid electrolyte $(xSc_1CeSZ, 5 < x < 11)$ for IT-SOFCs: Structure and conductivity studies, *Scr Mater.* 121 (2016) 10–13. <https://doi.org/10.1016/j.scriptamat.2016.04.023>.
- [11] R.H.J. Hannink, Transformation Toughening in Ceramics., *Journal of the American Ceramic Society.* 83 (2000) 461–487.

- [12] J.P. Brog, C.L. Chanez, A. Crochet, K.M. Fromm, Polymorphism, what it is and how to identify it: a systematic review, *RSC Adv.* 3 (2013) 16905–16931. <https://doi.org/10.1039/C3RA41559G>.
- [13] I. Subuki, M.F. Mohsin, M.H. Ismail, F.S.M. Fadzil, Study of the synthesis of zirconia powder from zircon sand obtained from zircon minerals malaysia by caustic fusion method, *Indonesian Journal of Chemistry.* 20 (2020) 782–790. <https://doi.org/10.22146/IJC.43936>.
- [14] V. V. Rodaev, A.O. Zhigachev, A.I. Tyurin, S.S. Razlivalova, V. V. Korenkov, Y.I. Golovin, An engineering zirconia ceramic made of baddeleyite, *Materials.* 14 (2021). <https://doi.org/10.3390/ma14164676>.
- [15] Baddeleyite: Mineral information, data and localities., (n.d.). <https://www.mindat.org/min-480.html>.
- [16] X. Zhao, D. Vanderbilt, Phonons and lattice dielectric properties of zirconia, *Phys Rev B Condens Matter Mater Phys.* 65 (2002) 1–10. <https://doi.org/10.1103/PhysRevB.65.075105>.
- [17] V.G. Zavodinsky, A.P. Kuzmenko, Electronic structure of carbon nanotubes interacting with Cu and Li atoms, *Journal of Materials Engineering and Applications.* 2 (2018).
- [18] A. H. Heuer, Science and Technology of Zirconia (*Advances in Ceramics*), Amer Ceramic Society (October 1, 1981), 1981.
- [19] A.G. Karaulov, E.I. Zoz, I.N. Rudyak, T.E. Sudarkina, Structure and properties of solid solutions in the systems ZrO₂-MgO, ZrO₂-CaO, and ZrO₂-Y₂O₃, *Refractories.* 24 (1983) 452–458. <https://doi.org/10.1007/BF01386515>.
- [20] F.A. Olga Fabrichnaya, Assessment of thermodynamic parameters in the system ZrO₂ – Y₂O₃ – Al₂O₃, *Inorganic Materials.* 49 (2013) 389–394. <https://doi.org/10.7868/s0002337x13030160>.
- [21] D.R. Clarke, C.G. Levi, Materials design for the next generation thermal barrier coatings, *Annu Rev Mater Res.* 33 (2003) 383–417. <https://doi.org/10.1146/annurev.matsci.33.011403.113718>.
- [22] C.K. Ng, S. Ramesh, C.Y. Tan, A. Muchtar, M.R. Somalu, Microwave sintering of ceria-doped scandia stabilized zirconia as electrolyte for solid oxide fuel cell, *Int J Hydrogen Energy.* 32 (2016) 14184–14190. <https://doi.org/10.1016/J.IJHYDENE.2016.06.146>.
- [23] Y.S. Hong, H.H. Yoon, Y.S. Hong, H.H. Yoon, Preparation of Scandia-Stabilized Zirconia Electrolyte Thin Films for Intermediate Temperature-Solid Oxide Fuel Cells by Electron Beam Vapor Deposition, *JaJAP.* 50 (2011) 01BE09. <https://doi.org/10.1143/JJAP.50.01BE09>.

- [24] V. V. Kharton, *Solid State Electrochemistry I: Fundamentals, Materials and their Applications*, *Solid State Electrochemistry I: Fundamentals, Materials and Their Applications*. (2009) 1–506. <https://doi.org/10.1002/9783527627868>.
- [25] O. V. Tiunova, O.Y. Zadorozhnaya, Y.K. Nepochatov, I.N. Burmistrov, I.E. Kuritsyna, S.I. Bredikhin, Ceramic membranes based on scandium-stabilized ZrO₂ obtained by tape casting technique, *Russian Journal of Electrochemistry*. 50 (2014) 719–724. <https://doi.org/10.1134/S1023193514080138>.
- [26] A.J. Feighery, *Zirconia-based electroceramic materials for SOFC applications*, (1999).
- [27] R.E. Mistler, E.R. Twiname, *Tape casting: Theory and practice.*, The American Ceramic Society, Westerville OH, 2000.
- [28] S. Zhuiykov, *Electrochemistry of Zirconia Gas Sensors*, *Electrochemistry of Zirconia Gas Sensors*. (2007). <https://doi.org/10.1201/9781420047622>.
- [29] T. Ishii, Structural phase transition and ionic conductivity in 0.88ZrO₂(0.12 - x)Sc₂O₃xAl₂O₃, *Solid State Ion.* 78 (1995) 333–338. [https://doi.org/10.1016/0167-2738\(95\)00118-P](https://doi.org/10.1016/0167-2738(95)00118-P).
- [30] S. Omar, A. Belda, A. Escardino, N. Bonanos, Ionic conductivity ageing investigation of 1Ce10ScSZ in different partial pressures of oxygen, *Solid State Ion.* 184 (2011) 2–5. <https://doi.org/10.1016/j.ssi.2010.09.042>.
- [31] D.Z. de Florio, Sintering and thermal ageing studies of zirconia - yttria ceramics by impedance spectroscopy, (1998) 119.
- [32] M. Mogensen, D. Lybye, N. Bonanos, P. V. Hendriksen, F.W. Poulsen, Factors controlling the oxide ion conductivity of fluorite and perovskite structured oxides, *Solid State Ion.* 174 (2004) 279–286. <https://doi.org/10.1016/J.SSI.2004.07.036>.
- [33] E.M. Soares, C. Tomás, Characterisation of the ceria and yttria co-doped scandia zirconia; produced by an innovative sol-gel and combustion process, (2010).
- [34] Y. Arachi, H. Sakai, O. Yamamoto, Y. Takeda, N. Imanishai, Electrical conductivity of the ZrO₂–Ln₂O₃ (Ln=lanthanides) system, *Solid State Ion.* 121 (1999) 133–139. [https://doi.org/https://doi.org/10.1016/S0167-2738\(98\)00540-2](https://doi.org/https://doi.org/10.1016/S0167-2738(98)00540-2).
- [35] R.D. Shannon, Revised effective ionic radii and systematic studies of interatomic distances in halides and chalcogenides, *Acta Crystallographica Section A.* 32 (1976) 751–767. <https://doi.org/10.1107/S0567739476001551>.

- [36] V. V. Kharton, F.M.B. Marques, A. Atkinson, Transport properties of solid oxide electrolyte ceramics: A brief review, *Solid State Ion.* 174 (2004) 135–149. <https://doi.org/10.1016/J.SSI.2004.06.015>.
- [37] Y. Li, M. Liu, J. Gong, Y. Chen, Z. Tang, Z. Zhang, Grain-boundary effect in zirconia stabilized with yttria and calcia by electrical measurements, *Mater Sci Eng B Solid State Mater Adv Technol.* 103 (2003) 108–114. [https://doi.org/10.1016/S0921-5107\(03\)00162-4](https://doi.org/10.1016/S0921-5107(03)00162-4).
- [38] D. Lee, I. Lee, Y. Jeon, R. Song, Characterization of scandia stabilized zirconia prepared by glycine nitrate process and its performance as the electrolyte for IT-SOFC, *Solid State Ion.* 176 (2005) 1021–1025. <https://doi.org/10.1016/J.SSI.2005.01.004>.
- [39] Y. Yin, B.B. Argent, Basic and Applied Research: Section I Phase Diagrams and Thermodynamics of the Systems ZrO₂-CaO and ZrO₂-MgO, (n.d.).
- [40] N. Mahato, A. Gupta, K. Balani, Doped zirconia and ceria-based electrolytes for solid oxide fuel cells: a review, *Nanomaterials and Energy.* 1 (2012) 27–45. <https://doi.org/10.1680/nme.11.00004>.
- [41] M. Yashima, M. Kakihana, M. Yoshimura, Metastable-stable phase diagrams in the zirconia-containing systems utilized in solid-oxide fuel cell application, *Solid State Ion.* 86–88 (1996) 1131–1149. [https://doi.org/10.1016/0167-2738\(96\)00386-4](https://doi.org/10.1016/0167-2738(96)00386-4).
- [42] S.P.S. Badwal, Grain boundary resistivity in zirconia-based materials: effect of sintering temperatures and impurities, *Solid State Ion.* 76 (1995) 67–80. [https://doi.org/10.1016/0167-2738\(94\)00236-L](https://doi.org/10.1016/0167-2738(94)00236-L).
- [43] S.P.S. Badwal, F.T. Ciacchi, D. Milosevic, Scandia–zirconia electrolytes for intermediate temperature solid oxide fuel cell operation, *Solid State Ion.* 136–137 (2000) 91–99. [https://doi.org/10.1016/S0167-2738\(00\)00356-8](https://doi.org/10.1016/S0167-2738(00)00356-8).
- [44] T.I. Politova, J.T.S. Irvine, Investigation of scandia–yttria–zirconia system as an electrolyte material for intermediate temperature fuel cells—influence of yttria content in system (Y₂O₃)_x(Sc₂O₃)_(11-x)(ZrO₂)₈₉, *Undefined.* 168 (2004) 153–165. <https://doi.org/10.1016/J.SSI.2004.02.007>.
- [45] Z. Lei, Q. Zhu, Low temperature processing of dense nanocrystalline scandia-doped zirconia (ScSZ) ceramics, *Solid State Ion.* 37–38 (2005) 2791–2797. <https://doi.org/10.1016/J.SSI.2005.09.005>.
- [46] A.R. West, *Basic Solid State Chemistry*, Chichester : John Wiley & Sons, 1999. [https://doi.org/10.1002/\(SICI\)1099-0739](https://doi.org/10.1002/(SICI)1099-0739).
- [47] S.P.S. Badwal, F.T. Ciacchi, S. Rajendran, J. Drennan, An investigation of conductivity, microstructure and stability of electrolyte compositions in the

- system 9 mol% (Sc₂O₃-Y₂O₃)-ZrO₂(Al₂O₃), *Solid State Ion.* 109 (1998) 167–186. [https://doi.org/10.1016/S0167-2738\(98\)00079-4](https://doi.org/10.1016/S0167-2738(98)00079-4).
- [48] S.C. Singhal, K. Kendall, *High-temperature solid oxide fuel cells: fundamentals, design, and applications*, Elsevier Advanced Technology, 2003.
- [49] D.S. Lee, W.S. Kim, S.H. Choi, J. Kim, H.W. Lee, J.H. Lee, Characterization of ZrO₂ co-doped with Sc₂O₃ and CeO₂ electrolyte for the application of intermediate temperature SOFCs, *Solid State Ion.* 176 (2005) 33–39. <https://doi.org/10.1016/j.ssi.2004.07.013>.
- [50] M. Sriubas, N. Kainbayev, D. Virbukas, K. Bočkute, Ž. Rutkuniene, G. Laukaitis, Structure and conductivity studies of scandia and alumina doped zirconia thin films, *Coatings.* 9 (2019) 1–10. <https://doi.org/10.3390/coatings9050317>.
- [51] S. Sarat, N. Sammes, A. Smirnova, Bismuth oxide doped scandia-stabilized zirconia electrolyte for the intermediate temperature solid oxide fuel cells, *J Power Sources.* 160 (2006) 892–896. <https://doi.org/10.1016/J.JPOWSOUR.2006.02.007>.
- [52] T. Liu, X. Zhang, X. Wang, J. Yu, L. Li, A review of zirconia-based solid electrolytes, *Ionics (Kiel).* 22 (2016) 2249–2262. <https://doi.org/10.1007/S11581-016-1880-1>.
- [53] J. Gong, Y. Li, Z. Tang, Z. Zhang, Ionic conductivity in the ternary system (ZrO₂)_{1-0.08x-0.12y}-(Y₂O₃)_{0.08x}-(CaO)_{0.12y}, *J Mater Sci.* 35 (2000) 3547–3551. <https://doi.org/10.1023/A:1004857312129>.
- [54] G. JH, L. Y, Z. ZT, T. ZL, ac impedance study of zirconia doped with yttria and calcia, *Journal of the American Ceramic Society.* 83 (2000) 648–650.
- [55] J. Gong, Y. Li, Z. Tang, Z. Zhang, Enhancement of the ionic conductivity of mixed calcia/yttria stabilized zirconia, *Mater Lett.* 46 (2000) 115–119. [https://doi.org/10.1016/S0167-577X\(00\)00152-X](https://doi.org/10.1016/S0167-577X(00)00152-X).
- [56] F.C. Fonseca, R. Muccillō'instituto, Impedance spectroscopy of (yttria-stabilized zirconia)-magnesia ceramic composites, *Solid State Ion.* 131 (2000) 301–309.
- [57] F.C. Fonseca, D.Z. De Florio, R. Muccillo, Impedance spectroscopy study of the sintering of yttria-stabilized zirconia/magnesia composites, *Solid State Ion.* 180 (2009) 822–826. <https://doi.org/10.1016/j.ssi.2009.02.010>.
- [58] Y. Shiratori, F. Tietz, H.J. Penkalla, J.Q. He, Y. Shiratori, D. Stöver, Influence of impurities on the conductivity of composites in the system (3YSZ)_{1-x}-(MgO)_x, *J Power Sources.* 148 (2005) 32–42. <https://doi.org/10.1016/J.JPOWSOUR.2005.01.036>.

- [59] J.G. Duh, M.Y. Lee, Fabrication and sinterability in Y₂O₃-CeO₂-ZrO₂, *Journal of Materials Science* 1989 24:12. 24 (1989) 4467–4474. <https://doi.org/10.1007/BF00544531>.
- [60] A.G. Belous, K. V. Kravchyk, E. V. Pashkova, O. Bohnke, C. Galven, Influence of the chemical composition on structural properties and electrical conductivity of Y-Ce-ZrO₂, *Chemistry of Materials*. 19 (2007) 5179–5184. <https://doi.org/10.1021/CM070319J>.
- [61] H. Naito, N. Sakai, T. Otake, H. Yugami, H. Yokokawa, Oxygen transport properties in ZrO₂-CeO₂-Y₂O₃ by SIMS analysis, *Solid State Ion*. 135 (2000) 669–673. [https://doi.org/10.1016/S0167-2738\(00\)00378-7](https://doi.org/10.1016/S0167-2738(00)00378-7).
- [62] F. Guo, P. Xiao, Effect of Fe₂O₃ doping on sintering of yttria-stabilized zirconia, *J Eur Ceram Soc*. 32 (2012) 4157–4164. <https://doi.org/10.1016/J.JEURCERAMSOC.2012.07.035>.
- [63] M. Jauneika, G. Laukaitis, J. Dudonis, Study of Samarium Doped Cerium Oxide Thin Films Formed by E-beam Technique, *Materials Science* . 15 (2009) 28–31.
- [64] S. Dey, G.C. Dhal, Cerium catalysts applications in carbon monoxide oxidations, *Mater Sci Energy Technol*. 3 (2020) 6–24. <https://doi.org/https://doi.org/10.1016/j.mset.2019.09.003>.
- [65] M. Sriubas, G. Laukaitis, The influence of the technological parameters on the ionic conductivity of samarium doped ceria thin films, *Materials Science* . 21 (2015) 105–110. <https://doi.org/10.5755/J01.MS.21.1.5700>.
- [66] R. V. Mangalaraja, S. Ananthakumar, K. Uma, R.M. Jimenez, S. Uthayakumar, M. Lopez, C. Camurri P., Synthesis and Characterization of Gd³⁺ and Sm³⁺ Ion Doped Ceria Electrolytes Through an In-situ Sulphated Combustion Technique, *Journal of Ceramic Processing Research*. 13 (2012) 15–22.
- [67] C.J. Fu, Q.L. Liu, S.H. Chan, X.M. Ge, G. Pasciak, Effects of transition metal oxides on the densification of thin-film GDC electrolyte and on the performance of intermediate-temperature SOFC, *Int J Hydrogen Energy*. 35 (2010) 11200–11207. <https://doi.org/10.1016/J.IJHYDENE.2010.07.049>.
- [68] J. Kimpton, T.H. Randle, J. Drennan, Investigation of electrical conductivity as a function of dopant-ion radius in the systems Zr_{0.75}Ce_{0.08}M_{0.17}O_{1.92} (M=Nd, Sm, Gd, Dy, Ho, Y, Er, Yb, Sc), *Solid State Ion*. 149 (2002) 89–98. [https://doi.org/10.1016/S0167-2738\(02\)00136-4](https://doi.org/10.1016/S0167-2738(02)00136-4).
- [69] V. Galkin, V. Konakov, A. Shorohov, E. Solovieva, 353 Synthesis of nanopowders in the systems of Ce SYNTHESIS OF NANOPOWDERS IN THE SYSTEMS OF Ce₂O₃-ZrO₂, Y₂O₃-ZrO₂ AND Y₂O₃-Ce₂O

3-ZrO₂ FOR FABRICATION OF OXYGEN SENSORS, Rev.Adv.Mater.Sci. 10 (2005) 353–356.

- [70] K.C. Radford, R.J. Bratton, Zirconia electrolyte cells Part 2 Electrical properties, J Mater Sci. 14 (1979) 66–69.
- [71] B. Kumar, & C. Chen, Ionic Conductivity of Scandia Stabilized Zirconia and Alumina Composites, Transactions of the Indian Ceramic Society. 66 (2007) 17–22. <https://doi.org/10.1080/0371750X.2007.11012238>.
- [72] E.P. BUTLER, J. DRENNAN, Microstructural Analysis of Sintered High-Conductivity Zirconia with Al₂O₃ Additions, Journal of the American Ceramic Society. 65 (1982) 474–478. <https://doi.org/10.1111/J.1151-2916.1982.TB10336.X>.
- [73] B. Kumar, J.S. Thokchom, Space charge-mediated ionic transport in yttria-stabilized zirconia-alumina composite membranes, Journal of the American Ceramic Society. 91 (2008) 1175–1181. <https://doi.org/10.1111/j.1551-2916.2008.02257.x>.
- [74] M. Miyayama, A. Yanagida, A. Asada, Effects of Al₂O₃ additions on resistivity and microstructure of yttria-stabilized zirconia, American Ceramic Society Bulletin. 65 (1986) 660–664.
- [75] M. Mori, T. Abe, H. Itoh, O. Yamamoto, Y. Takeda, T. Kawahara, Cubic-stabilized zirconia and alumina composites as electrolytes in planar type solid oxide fuel cells, Solid State Ion. 74 (1994) 157–164. [https://doi.org/10.1016/0167-2738\(94\)90206-2](https://doi.org/10.1016/0167-2738(94)90206-2).
- [76] B. Kumar, C. Chen, C. Varanasi, J.P. Fellner, Electrical properties of heterogeneously doped yttria stabilized zirconia, J Power Sources. 140 (2005) 12–20. <https://doi.org/10.1016/j.jpowsour.2004.08.016>.
- [77] M.M.R. Boutz, C.S. Chen, L. Winnubst, A.J. Burggraaf, Characterization of Grain Boundaries in Superplastically Deformed Y-TZP Ceramics, Journal of the American Ceramic Society. 77 (1994) 2632–2640. <https://doi.org/10.1111/J.1151-2916.1994.TB04654.X>.
- [78] Y. Ikuhara, P. Thavorniti, T. Sakuma, Solute segregation at grain boundaries in superplastic SiO₂-doped TZP, Acta Mater. 45 (1997) 5275–5284. [https://doi.org/10.1016/S1359-6454\(97\)00152-3](https://doi.org/10.1016/S1359-6454(97)00152-3).
- [79] M.L. MECARTNEY, Influence of an Amorphous Second Phase on the Properties of Yttria-Stabilized Tetragonal Zirconia Polycrystals (Y-TZP), Journal of the American Ceramic Society. 70 (1987) 54–58. <https://doi.org/10.1111/J.1151-2916.1987.TB04853.X>.
- [80] Y. IKUHARA, N. Y. Y. T, S. T, High-temperature behavior of SiO₂ at grain boundaries in TZP, INTERFACE SCIENCE. 7 (1999) 77–84.

- [81] J.-H. Lee, T. Mori, J.-G. Li, T. Ikegami, M. Komatsu, H. Haneda, Improvement of Grain-Boundary Conductivity of 8 mol % Yttria-Stabilized Zirconia by Precursor Scavenging of Siliceous Phase, *J Electrochem Soc.* 147 (2000) 2822. <https://doi.org/10.1149/1.1393612>.
- [82] X. Song, J. Lu, T. Zhang, J. Ma, Two-stage master sintering curve approach to sintering kinetics of undoped and Al₂O₃-doped 8 Mol% yttria-stabilized cubic zirconia, *Journal of the American Ceramic Society.* 94 (2011) 1053–1059. <https://doi.org/10.1111/J.1551-2916.2010.04199.X>.
- [83] R.I. Merino, J.I. Peña, Á. Larrea, G.F. De La Fuente, V.M. Orera, Melt grown composite ceramics obtained by directional solidification: structural and functional applications, *India Recent Res. Devel. Mat. Sci.* 37 (2003) 1–24.
- [84] P. Mondal, H. Hahn, Investigation of the complex conductivity of nanocrystalline Y₂O₃-stabilized zirconia, *Undefined.* 101 (1997) 1765–1768. <https://doi.org/10.1002/BBPC.19971011146>.
- [85] I. Kosacki, T. Suzuki, V. Petrovsky, H.U. Anderson, Electrical conductivity of nanocrystalline ceria and zirconia thin films, *Solid State Ion.* 136–137 (2000) 1225–1233. [https://doi.org/10.1016/S0167-2738\(00\)00591-9](https://doi.org/10.1016/S0167-2738(00)00591-9).
- [86] Kosacki, I., B. Gorman, H. Anderson, Microstructure and electrical conductivity in nanocrystalline oxide thin films, *Onic and Mixed Conducting Ceramics.* 3 (1998) 631–642.
- [87] H.L. Tuller, Ionic conduction in nanocrystalline materials, *Solid State Ion.* 131 (2000) 143–157. [https://doi.org/10.1016/S0167-2738\(00\)00629-9](https://doi.org/10.1016/S0167-2738(00)00629-9).
- [88] I. Kosacki, C.M. Rouleau, P.F. Becher, J. Bentley, D.H. Lowndes, Nanoscale effects on the ionic conductivity in highly textured YSZ thin films, *Solid State Ion.* 176 (2005) 1319–1326. <https://doi.org/10.1016/J.SSI.2005.02.021>.
- [89] A. Peters, C. Korte, D. Hesse, N. Zakharov, J. Janek, Ionic conductivity and activation energy for oxygen ion transport in superlattices - The multilayer system CSZ (ZrO₂ + CaO) / Al₂O₃, *Solid State Ion.* 178 (2007) 67–76. <https://doi.org/10.1016/J.SSI.2006.12.004>.
- [90] N. V. Gelfond, O.F. Bobrenok, M.R. Predtechensky, N.B. Morozova, K. V. Zherikova, I.K. Igumenov, Chemical vapor deposition of electrolyte thin films based on yttria-stabilized zirconia, *Inorganic Materials.* 45 (2009) 659–665. <https://doi.org/10.1134/S0020168509060144>.
- [91] X. He, B. Meng, Y. Sun, B. Liu, M. Li, Electron beam physical vapor deposition of YSZ electrolyte coatings for SOFCs, *Appl Surf Sci.* 254 (2008) 7159–7164. <https://doi.org/10.1016/J.APSUSC.2008.05.271>.

- [92] A. Marizy, T. Desaunay, D. Chery, P. Roussel, A. Ringuede, M. Cassir, Atomic Layer Deposition, a Key Technique for Processing Thin-Layered SOFC Materials - Case Of Epitaxial Thin Layers of CeO₂ Catalyst, *ECS Trans.* 57 (2013) 983–990. <https://doi.org/10.1149/05701.0983ECST>.
- [93] H. Hidalgo, A.L. Thomann, T. Lecas, J. Vulliet, K. Wittmann-Teneze, D. Damiani, E. Millon, P. Brault, Optimization of DC reactive magnetron sputtering deposition process for efficient YSZ electrolyte thin film SOFC, *Fuel Cells.* 13 (2013) 279–288. <https://doi.org/10.1002/FUCE.201200125>.
- [94] E. Gourba, A. Ringuede, M. Cassir, A. Billard, J. Päiväsääri, J. Niinistö, M. Putkonen, L. Niinistö, Characterisation of Thin Films of Ceria-Based Electrolytes for Intermediate Temperature - Solid Oxide Fuel Cells (IT-SOFC), *Ionics (Kiel).* 9 (2003) 15–20. <https://doi.org/10.2/JQUERY.MIN.JS>.
- [95] S.H. Shin, J.S. Park, H. Lee, S.W. Kong, J. Park, Y. Won, Y.B. Kim, Fabrication of Scandia-Stabilized Zirconia Thin Films by Instant Flash Light Irradiation, *Coatings* 2020, Vol. 10, Page 9. 10 (2019) 9. <https://doi.org/10.3390/COATINGS10010009>.
- [96] R.W. Schwartz, T. Schneller, R. Waser, Chemical solution deposition of electronic oxide films, *Comptes Rendus Chimie.* 7 (2004) 433–461. <https://doi.org/10.1016/J.CRCI.2004.01.007>.
- [97] R. Neagu, D. Perednis, A. Princivale, E. Djurado, Influence of the process parameters on the ESD synthesis of thin film YSZ electrolytes, *Solid State Ion.* 19–25 (2006) 1981–1984. <https://doi.org/10.1016/J.SSI.2006.05.052>.
- [98] Y. Zhang, J. Gao, D. Peng, M. Guanyao, X. Liu, Dip-coating thin yttria-stabilized zirconia films for solid oxide fuel cell applications, *Ceram Int.* 6 (2004) 1049–1053. <https://doi.org/10.1016/J.CERAMINT.2003.10.026>.
- [99] R. Peng, C. Xia, X. Liu, D. Peng, G. Meng, Intermediate-temperature SOFCs with thin Ce_{0.8}Y_{0.2}O_{1.9} films prepared by screen-printing, (n.d.).
- [100] Chukharev V.F., Specifics of YSZ nanopowders processing and electric conductivity of YSZ ceramics based on these powders, (n.d.) 58–77.
- [101] N.L. Savchenko, T.Y. Sablina, S.N. Kul'kov, Vacuum sintering of plasmochemical powders based on ZrO₂ II. Effect of sintering time at high temperature on the phase composition and mechanical properties of ceramics, *Powder Metallurgy and Metal Ceramics.* 34 (1995) 26–30. <https://doi.org/10.1007/BF00559848>.
- [102] N. Kainbayev, M. Sriubas, K. Bockute, D. Virbukas, G. Laukaitis, E-beam deposition of scandia-stabilized zirconia (ScSZ) thin films co-doped with Al, *Coatings.* 10 (2020) 2–11. <https://doi.org/10.3390/coatings10090870>.

- [103] Z. Xu, S. He, L. He, R. Mu, G. Huang, X. Cao, double-ceramic-layer systems deposited by electron beam physical vapor deposition, *J Alloys Compd.* 509 (2011) 4273–4283. <https://doi.org/10.1016/j.jallcom.2010.12.203>.
- [104] N.S. Jacobson, *Thermodynamic Properties of Some Metal Oxide-Zirconia Systems*, (1989).
- [105] A. Ivanov, Sputtering technology for thin films, *Modern Lighting Technology*. 1 (2010) 45–48.
- [106] Y.W. Yoo, W. Jeon, W. Lee, C.H. An, S.K. Kim, C.S. Hwang, Structure and Electrical Properties of Al-Doped HfO₂ and ZrO₂ Films Grown via Atomic Layer Deposition on Mo Electrodes, *ACS Appl Mater Interfaces*. 6 (2014) 22474–22482. <https://doi.org/10.1021/AM506525S>.
- [107] K.S. Yun, Y. il Kwon, J.H. Kim, S. Jo, C.Y. Yoo, J.H. Yu, J.H. Joo, Effects of Ni diffusion on the accelerated conductivity degradation of scandia-stabilized zirconia films under a reducing atmosphere, *J Eur Ceram Soc.* 36 (2016) 1835–1839. <https://doi.org/10.1016/J.JEURCERAMSOC.2016.02.007>.
- [108] G.Y. Cho, Y.H. Lee, S.W. Hong, J. Bae, J. An, Y.B. Kim, S.W. Cha, High-performance thin film solid oxide fuel cells with scandia-stabilized zirconia (ScSZ) thin film electrolyte, *Int J Hydrogen Energy*. 40 (2015) 15704–15708. <https://doi.org/10.1016/J.IJHYDENE.2015.09.124>.
- [109] Z. Zakaria, S.K. Kamarudin, Advanced modification of scandia-stabilized zirconia electrolytes for solid oxide fuel cells application—A review, *Int J Energy Res.* 45 (2021) 4871–4887. <https://doi.org/10.1002/er.6206>.
- [110] Q. Xue, X. Huang, J. Zhang, H. Zhang, Z. Feng, Grain boundary segregation and its influences on ionic conduction properties of scandia doped zirconia electrolytes, *Journal of Rare Earths*. 37 (2019) 645–651. <https://doi.org/10.1016/J.JRE.2018.11.006>.
- [111] P. Arunkumar, M. Meena, K.S. Babu, A review on cerium oxide-based electrolytes for ITSOFC, *Nanomaterials and Energy*. 1 (2012) 288–305. <https://doi.org/10.1680/NME.12.00015>.
- [112] Dipl.-P. Benjamin Butz, *Yttria-Doped Zirconia as Solid Electrolyte for Fuel-Cell Applications*, (2009). <https://doi.org/10.5445/IR/1000015724>.
- [113] J. Kondoh, T. Kawashima, S. Kikuchi, Y. Tomii, Y. Ito, Effect of Aging on Yttria-Stabilized Zirconia: I. A Study of Its Electrochemical Properties, *J Electrochem Soc.* 145 (1998) 1527–1536. <https://doi.org/10.1149/1.1838515/XML>.
- [114] C. Haering, A. Roosen, H. Schichl, M. Schnöller, Degradation of the electrical conductivity in stabilised zirconia system: Part II: Scandia-

- stabilised zirconia, *Solid State Ion.* 176 (2005) 261–268. <https://doi.org/10.1016/J.SSI.2004.07.039>.
- [115] S. Yarmolenko, J. Sankar, N. Bernier, M. Klimov, J. Kapat, N. Orlovskaya, Phase Stability and Sintering Behavior of 10mol%Sc₂O₃–1mol%CeO₂–ZrO₂ Ceramics, *J Fuel Cell Sci Technol.* 6 (2009) 21007–21008. <https://doi.org/10.1115/1.2971126>.
- [116] R.C. Garvie, The Occurrence of Metastable Tetragonal Zirconia as a Crystallite Size Effect, *J Phys Chem.* 69 (1965) 1238–1243. <https://doi.org/10.1021/j100888a024>.
- [117] Z. Wang, M. Cheng, Z. Bi, Y. Dong, H. Zhang, J. Zhang, Z. Feng, C. Li, Structure and impedance of ZrO₂ doped with Sc₂O₃ and CeO₂, *Mater Lett.* 59 (2005) 2579–2582. <https://doi.org/10.1016/j.matlet.2004.07.065>.
- [118] K. Nomura, Y. Mizutani, M. Kawai, Y. Nakamura, O. Yamamoto, Aging and Raman scattering study of scandia and yttria doped zirconia, *Solid State Ion.* 132 (2000) 235–239. [https://doi.org/10.1016/s0167-2738\(00\)00648-2](https://doi.org/10.1016/s0167-2738(00)00648-2).
- [119] K.N. Clausen, W. Hayes, Defect structure of yttria-stabilized zirconia and its influence on the ionic conductivity at elevated temperatures, *Phys Rev B Condens Matter Mater Phys.* 59 (1999) 14202–14219. <https://doi.org/10.1103/PhysRevB.59.14202>.
- [120] D.N. Argyriou, M.M. Elcombe, A.C. Larson, A neutron scattering investigation of cubic stabilised zirconia (CSZ) - I. The average structure of Y-CSZ, *Journal of Physics and Chemistry of Solids.* 57 (1996) 183–193. [https://doi.org/10.1016/0022-3697\(96\)80008-4](https://doi.org/10.1016/0022-3697(96)80008-4).
- [121] H. Kishimoto, N. Sakai, T. Horita, K. Yamaji, Y.P. Xiong, M.E. Brito, H. Yokokawa, Rapid phase transformation of zirconia in the Ni-ScSZ cermet anode under reducing condition, *Solid State Ion.* 179 (2008) 2037–2041. <https://doi.org/10.1016/j.ssi.2008.06.024>.
- [122] S.N. Basahel, T.T. Ali, M. Mokhtar, K. Narasimharao, Influence of crystal structure of nanosized ZrO₂ on photocatalytic degradation of methyl orange, *Nanoscale Res Lett.* 10 (2015). <https://doi.org/10.1186/s11671-015-0780-z>.
- [123] V. Vonk, N. Khorshidi, A. Stierle, H. Dosch, Atomic structure and composition of the yttria-stabilized zirconia (111) surface, *Surf Sci.* 612 (2013) 69–76. <https://doi.org/10.1016/j.susc.2013.02.014>.
- [124] C.N.R. Rao, Raman Spectra of Complex Metal Oxides., *Indian Journal of Pure and Applied Physics.* 16 (1978) 277–281.
- [125] A.S. Mokrushin, E.P. Simonenko, N.P. Simonenko, K.A. Bukunov, V.G. Sevastyanov, N.T. Kuznetsov, Microstructure, phase composition, and gas-sensing properties of nanostructured ZrO_{2-x}Y₂O₃ thin films and powders

- obtained by the sol-gel method, *Ionics* (Kiel). 25 (2019) 1259–1270. <https://doi.org/10.1007/s11581-018-2820-z>.
- [126] T. Hirata, E. Asari, M. Kitajima, Infrared and raman spectroscopic studies of zro2 polymorphs doped with y2o3 or ceo2, *J Solid State Chem.* 110 (1994) 201–207. <https://doi.org/10.1006/jssc.1994.1160>.
- [127] M. Yashima, K. Ohtake, H. Arashi, M. Kakihana, M. Yoshimura, Determination of cubic-tetragonal phase boundary in Zr1-XY XO2-X/2 solid solutions by Raman spectroscopy, *J Appl Phys.* 74 (1993) 7603–7605. <https://doi.org/10.1063/1.354989>.
- [128] D. Marrocchelli, P.A. Madden, S.T. Norberg, S. Hull, Structural disorder in doped zirconias, part II: Vacancy ordering effects and the conductivity maximum, *Chemistry of Materials.* 23 (2011) 1365–1373. <https://doi.org/10.1021/cm102809t>.
- [129] I. Kosacki, T. Suzuki, H.U. Anderson, P. Colomban, Raman scattering and lattice defects in nanocrystalline CeO2 thin films, *Solid State Ion.* 149 (2002) 99–105. [https://doi.org/10.1016/S0167-2738\(02\)00104-2](https://doi.org/10.1016/S0167-2738(02)00104-2).
- [130] H.P. Dasari, J.S. Ahn, K. Ahn, S.Y. Park, J. Hong, H. Kim, K.J. Yoon, J.W. Son, H.W. Lee, J.H. Lee, Synthesis, sintering and conductivity behavior of ceria-doped Scandia-stabilized zirconia, *Solid State Ion.* 263 (2014) 103–109. <https://doi.org/10.1016/j.ssi.2014.05.013>.
- [131] L. Li, W. Wang, Synthesis and characterization of monoclinic ZrO2 nanorods by a novel and simple precursor thermal decomposition approach, *Solid State Commun.* 127 (2003) 639–643. [https://doi.org/10.1016/S0038-1098\(03\)00521-0](https://doi.org/10.1016/S0038-1098(03)00521-0).
- [132] D. Gazzoli, G. Mattei, M. Valigi, Raman and X-ray investigations of the incorporation of Ca²⁺ and Cd²⁺ in the ZrO2 structure, *Journal of Raman Spectroscopy.* 38 (2007) 824–831. <https://doi.org/10.1002/jrs.1708>.
- [133] Q. XUE, X. HUANG, H. ZHANG, H. XU, J. ZHANG, L. WANG, Synthesis and characterization of high ionic conductivity ScSZ core/shell nanocomposites, *Journal of Rare Earths.* 35 (2017) 567–573. [https://doi.org/10.1016/S1002-0721\(17\)60949-9](https://doi.org/10.1016/S1002-0721(17)60949-9).
- [134] D.R. CLARKE, F. ADAR, Measurement of the Crystallographically Transformed Zone Produced by Fracture in Ceramics Containing Tetragonal Zirconia, *Journal of the American Ceramic Society.* 65 (1982) 284–288. <https://doi.org/10.1111/j.1151-2916.1982.tb10445.x>.
- [135] T. Liu, X. Zhang, X. Wang, J. Yu, L. Li, A review of zirconia-based solid electrolytes, *Ionics* (Kiel). 22 (2016) 2249–2262. <https://doi.org/10.1007/s11581-016-1880-1>.

- [136] J. Thapa, B. Liu, S.D. Woodruff, B.T. Chorpeneing, M.P. Buric, Raman scattering in single-crystal sapphire at elevated temperatures, *Appl Opt.* 56 (2017) 8598. <https://doi.org/10.1364/ao.56.008598>.
- [137] N. Kainbayev, M. Sriubas, D. Virbukas, I. Zivile Rutkuniene, B. Kristina, B. Saltanat, G. Laukaitis, *Thin Films, Coatings.* 10 (2020) 1–12. <https://doi.org/10.3390/coatings10050432>.
- [138] SOFC Powders - fuelcellmaterials, (n.d.). <https://fuelcellmaterials.com/products-overview/materials/sofc/powders/> (accessed November 20, 2021).
- [139] T. Vinodkumar, B.G. Rao, B.M. Reddy, Influence of isovalent and aliovalent dopants on the reactivity of cerium oxide for catalytic applications, *Catal Today.* 253 (2015) 57–64. <https://doi.org/10.1016/J.CATTOD.2015.01.044>.
- [140] U. König, R.S. Angélica, N. Norberg, L. Gobbo, Rapid X-ray diffraction (XRD) for grade control of bauxites, *Icsoba 2012.* (2012) 11.
- [141] H.S. Systems, Instruction Manual for Model S-3400N, (2004).
- [142] R.E. Smallman, A.H.W. Ngan, Characterization and Analysis, *Modern Physical Metallurgy.* (2014) 159–250. <https://doi.org/10.1016/B978-0-08-098204-5.00005-5>.
- [143] A.F. Microscope, O. Manual, NT-206, Gomel, 2004.
- [144] XPS Interpretation of Zirconium, (n.d.). <https://www.jp.xpssimplified.com/elements/>.
- [145] Electron Relaxation and Auger electron generation, (n.d.). <https://www.globalsino.com/EM/page4965.html> (accessed November 27, 2021).
- [146] PHI VersaProbe 4(XPS) Surface Analysis Instrument, (n.d.). <https://www.phi.com/surface-analysis-equipment/versaprobe.html#capabilities:fully-integrated-multi-technique-system-with-optional-accessories> (accessed November 21, 2021).
- [147] J. Mitra, G.J. Abraham, M. Kesaria, S. Bahl, A. Gupta, S.M. Shivaprasad, C.S. Viswanadham, U.D. Kulkarni, G.K. Dey, Role of substrate temperature in the pulsed laser deposition of zirconium oxide thin film, *Materials Science Forum.* 710 (2012) 757–761. <https://doi.org/10.4028/www.scientific.net/MSF.710.757>.
- [148] W. E. Smith; G. Dent, Chapter 1 Introduction, *Basic Theory and Principles*, 5 (n.d.) 1–21.
- [149] S. Kumar, P. Kumar, A. Das, C. Shakher Pathak, Surface-Enhanced Raman Scattering: Introduction and Applications, *Recent Advances in*

- Nanophotonics - Fundamentals and Applications. (2020). <https://doi.org/10.5772/intechopen.92614>.
- [150] R. Spectroscopy, R. Scattering, Application note - What is Raman Spectroscopy?, General Microtechnology and Photonics. (1928).
- [151] M.G.F. Nataf, New approaches to understand conductive and polar domain walls by Raman spectroscopy and low energy electron microscopy, PhD Thesis Guillaume f. Nataf. (2016) 143.
- [152] RENISHAW, inVia confocal Raman microscope, (2019) 28.
- [153] S.E. Porozova, A.A. Smetkin, I. V. Solnyshkov, Surface Composition and Structure of Highly Porous Materials Based Zirconia Stabilized with Ytria, Russian Journal of Non-Ferrous Metals. 58 (2017) 664–669. <https://doi.org/10.3103/S1067821217060098>.
- [154] L.D. Huy, P. Laffez, P. Daniel, A. Jouanneaux, N.T. Khoi, D. Siméone, Structure and phase component of ZrO₂ thin films studied by Raman spectroscopy and X-ray diffraction, Mater Sci Eng B Solid State Mater Adv Technol. 104 (2003) 163–168. [https://doi.org/10.1016/S0921-5107\(03\)00190-9](https://doi.org/10.1016/S0921-5107(03)00190-9).
- [155] I. Garbayo, A. Tarancón, J. Santiso, F. Peiró, E. Alarcón-LLadó, A. Cavallaro, I. Gràcia, C. Cané, N. Sabaté, Electrical characterization of thermomechanically stable YSZ membranes for micro solid oxide fuel cells applications, Solid State Ion. 181 (2010) 322–331. <https://doi.org/10.1016/J.SSI.2009.12.019>.
- [156] D.Y. Jang, H.K. Kim, J.W. Kim, K. Bae, M.V.F. Schlupp, S.W. Park, M. Prestat, J.H. Shim, Low-temperature performance of yttria-stabilized zirconia prepared by atomic layer deposition, J Power Sources. 274 (2015) 611–618. <https://doi.org/10.1016/J.JPOWSOUR.2014.10.022>.
- [157] E.B. Ramírez, A. Huanosta, J.P. Sebastian, L. Huerta, A. Ortiz, J.C. Alonso, Structure, composition and electrical properties of YSZ films deposited by ultrasonic spray pyrolysis, J Mater Sci. 42 (2007) 901–907. <https://doi.org/10.1007/S10853-006-0004-0>.
- [158] H. Inaba, H. Tagawa, Ceria-based solid electrolytes, Solid State Ion. 83 (1996) 1–16. [https://doi.org/10.1016/0167-2738\(95\)00229-4](https://doi.org/10.1016/0167-2738(95)00229-4).
- [159] M. Sriubas, D. Virbukas, N. Kainbayev, K. Bockute, G. Laukaitis, Structural and electrochemical properties of scandia alumina stabilized zirconia thin films, Coatings. 11 (2021). <https://doi.org/10.3390/coatings11070800>.
- [160] Ambios XP200 Profiler | McGill Nanotools - Microfab, (n.d.). <http://nmn.physics.mcgill.ca/content/ambios-xp200-profiler> (accessed November 21, 2021).

- [161] I. Petrov, P.B. Barna, L. Hultman, J.E. Greene, Microstructural evolution during film growth, *Journal of Vacuum Science & Technology A: Vacuum, Surfaces, and Films*. 21 (2003) S117–S128. <https://doi.org/10.1116/1.1601610>.
- [162] M.G. Krzhizhanovskaya, V.A. Firsova, R.S. Bubnova, Application of the Rietveld Method for Solving the Problems of Powder Diffractometry, (2016) 1–67.
- [163] Y. Hemberger, N. Wichtner, C. Berthold, K.G. Nickel, Quantification of yttria in stabilized zirconia by Raman spectroscopy, *Int J Appl Ceram Technol*. 13 (2016) 116–124. <https://doi.org/10.1111/ijac.12434>.
- [164] M. Yashima, S. Sasaki, M. Kakihana, Y. Yamaguchi, H. Arashi, M. Yoshimura, Oxygen-induced structural change of the tetragonal phase around the tetragonal–cubic phase boundary in ZrO₂–YO_{1.5} solid solutions, *Acta Crystallographica Section B*. 50 (1994) 663–672. <https://doi.org/10.1107/S0108768194006257>.
- [165] A. Spirin, V. Ivanov, A. Nikonov, A. Lipilin, S. Parandin, V. Khrustov, A. Spirina, Scandia-stabilized zirconia doped with yttria: Synthesis, properties, and ageing behavior, *Solid State Ion*. 225 (2012) 448–452. <https://doi.org/10.1016/J.SSI.2012.02.022>.
- [166] Q.N. Xue, L.G. Wang, X.W. Huang, J.X. Zhang, H. Zhang, Influence of codoping on the conductivity of Sc-doped zirconia by first-principles calculations and experiments, *Mater Des*. 160 (2018) 131–137. <https://doi.org/10.1016/J.MATDES.2018.09.001>.
- [167] M.I. Yusuke Ota Satomi Sakuragi, Yuki Iwama, Noriyuki Sonoyama, Shoitiro Ikeda, Atsushi Hirano, Nobuyuki Imanishi, Yasuo Takeda, Osamu Yamamoto, Crystal Structure and Oxygen Ion Conductivity of Ga³⁺ Co-Doped Scandia-Stabilized Zirconia, *J Electrochem Soc*. 157 (2010) B1707–B1712. <https://doi.org/doi:10.1149/1.3489377>.
- [168] C.X. Guo, J.X. Wang, C.R. He, W.G. Wang, Effect of alumina on the properties of ceria and scandia co-doped zirconia for electrolyte-supported SOFC, *Ceram Int*. 39 (2013) 9575–9582. <https://doi.org/10.1016/j.ceramint.2013.05.076>.
- [169] J. Maier, On the Conductivity of Polycrystalline Materials, *Berichte Der Bunsengesellschaft Für Physikalische Chemie*. 90 (1986) 26–33. <https://doi.org/10.1002/bbpc.19860900105>.
- [170] A. Tschöpe, E. Sommer, R. Birringer, Grain size-dependent electrical conductivity of polycrystalline cerium oxide: I. Experiments, *Solid State Ion*. 139 (2001) 255–265. [https://doi.org/10.1016/S0167-2738\(01\)00678-6](https://doi.org/10.1016/S0167-2738(01)00678-6).

- [171] J. Tao, A. Dong, J. Wang, The Influence of Microstructure and Grain Boundary on the Electrical Properties of Scandia Stabilized Zirconia, *Mater Trans.* 54 (2013) 825–832. <https://doi.org/10.2320/matertrans.M2012385>.
- [172] G. Lyamina, A. Ilela, O. Khasanov, M. Petyukevich, E. Vaitulevich, Synthesis of Al₂O₃-ZrO₂ powders from differently concentrated suspensions with a spray drying technique, in: *AIP Conf Proc*, American Institute of Physics Inc., 2016. <https://doi.org/10.1063/1.4964533>.
- [173] C. Morant, J.M. Sanz, L. Galán, L. Soriano, F. Rueda, An XPS study of the interaction of oxygen with zirconium, *Surf Sci.* 218 (1989) 331–345. [https://doi.org/10.1016/0039-6028\(89\)90156-8](https://doi.org/10.1016/0039-6028(89)90156-8).
- [174] A.P. Milanov, K. Xu, S. Cwik, H. Parala, T. De Los Arcos, H.W. Becker, D. Rogalla, R. Cross, S. Paul, A. Devi, Sc₂O₃, Er₂O₃, and Y₂O₃ thin films by MOCVD from volatile guanidinate class of rare-earth precursors, *Dalton Transactions.* 41 (2012) 13936–13947. <https://doi.org/10.1039/c2dt31219k>.
- [175] A. Ganguly, S. Sharma, P. Papakonstantinou, J. Hamilton, Probing the thermal deoxygenation of graphene oxide using high-resolution in situ X-ray-based spectroscopies, *Journal of Physical Chemistry C.* 115 (2011) 17009–17019. <https://doi.org/10.1021/jp203741y>.
- [176] J. Raja, C.P.T. Nguyen, C. Lee, N. Balaji, S. Chatterjee, K. Jang, H. Kim, J. Yi, Improved Data Retention of InSnZnO Nonvolatile Memory by H₂O₂ Treated Al₂O₃ Tunneling Layer: A Cost-Effective Method, *IEEE Electron Device Letters.* 37 (2016) 1272–1275. <https://doi.org/10.1109/LED.2016.2599559>.
- [177] J.S. Corsi, J. Fu, Z. Wang, T. Lee, A.K. Ng, E. Detsi, Hierarchical Bulk Nanoporous Aluminum for On-Site Generation of Hydrogen by Hydrolysis in Pure Water and Combustion of Solid Fuels, *ACS Sustain Chem Eng.* 7 (2019) 11194–11204. <https://doi.org/10.1021/acssuschemeng.9b00481>.
- [178] V. V Srdic´*srdic´*, M. Winterer, Aluminum-Doped Zirconia Nanopowders: Chemical Vapor Synthesis and Structural Analysis by Rietveld Refinement of X-ray Diffraction Data, (2003). <https://doi.org/10.1021/cm021303q>.
- [179] G.T. Dahl, S. Döring, T. Krekeler, R. Janssen, M. Ritter, H. Weller, T. Vossmeier, Alumina-Doped Zirconia Submicro-Particles: Synthesis, Thermal Stability, and Microstructural Characterization, *Materials.* 12 (2019) 2856. <https://doi.org/10.3390/ma12182856>.
- [180] A. Ganguly, S. Sharma, P. Papakonstantinou, J. Hamilton, Probing the thermal deoxygenation of graphene oxide using high-resolution in situ X-ray-based spectroscopies, *Journal of Physical Chemistry C.* 115 (2011) 17009–17019. <https://doi.org/10.1021/jp203741y>.

- [181] A.P. Milanov, K. Xu, S. Cwik, H. Parala, T. De Los Arcos, H.W. Becker, D. Rogalla, R. Cross, S. Paul, A. Devi, Sc 2O 3, Er 2O 3, and Y 2O 3 thin films by MOCVD from volatile guanidinate class of rare-earth precursors, Dalton Transactions. 41 (2012) 13936–13947. <https://doi.org/10.1039/c2dt31219k>.
- [182] J.S. Corsi, J. Fu, Z. Wang, T. Lee, A.K. Ng, E. Detsi, Hierarchical Bulk Nanoporous Aluminum for On-Site Generation of Hydrogen by Hydrolysis in Pure Water and Combustion of Solid Fuels, ACS Sustain Chem Eng. 7 (2019) 11194–11204. <https://doi.org/10.1021/acssuschemeng.9b00481>.
- [183] J. Raja, C.P.T. Nguyen, C. Lee, N. Balaji, S. Chatterjee, K. Jang, H. Kim, J. Yi, Improved Data Retention of InSnZnO Nonvolatile Memory by H₂O₂ Treated Al₂O₃ Tunneling Layer: A Cost-Effective Method, IEEE Electron Device Letters. 37 (2016) 1272–1275. <https://doi.org/10.1109/LED.2016.2599559>.
- [184] C. Morant, J.M. Sanz, L. Galán, L. Soriano, F. Rueda, An XPS study of the interaction of oxygen with zirconium, Surf Sci. 218 (1989) 331–345. [https://doi.org/10.1016/0039-6028\(89\)90156-8](https://doi.org/10.1016/0039-6028(89)90156-8).
- [185] J. Young Choi, S. Sig Kim, S. Yeol Lee, Effect of hafnium addition on Zn-Sn-O thin film transistors fabricated by solution process, Appl Phys Lett. 100 (2012). <https://doi.org/10.1063/1.3669700>.
- [186] G.X. Liu, A. Liu, Y. Meng, F.K. Shan, B.C. Shin, W.J. Lee, C.R. Cho, Annealing dependence of solution-processed ultra-thin ZrO_x films for gate dielectric applications, J Nanosci Nanotechnol. 15 (2015) 2185–2191. <https://doi.org/10.1166/jnn.2015.10228>.
- [187] D.A. Agarkov, M.A. Borik, S.I. Bredikhin, I.N. Burmistrov, G.M. Eliseeva, V.A. Kolotygin, A. V. Kulebyakin, I.E. Kuritsyna, E.E. Lomonova, F.O. Milovich, V.A. Myzina, P.A. Ryabochkina, N.Y. Tabachkova, T. V. Volkova, Structure and transport properties of zirconia crystals co-doped by scandia, ceria and yttria, Journal of Materiomics. 5 (2019) 273–279. <https://doi.org/10.1016/j.jmat.2019.02.004>.
- [188] Y.W. Yoo, W. Jeon, W. Lee, C.H. An, S.K. Kim, C.S. Hwang, Structure and electrical properties of Al-doped HfO₂ and ZrO₂ films grown via atomic layer deposition on Mo electrodes, ACS Appl Mater Interfaces. 6 (2014) 22474–22482. <https://doi.org/10.1021/am506525s>.
- [189] S. Spiga, R. Rao, L. Lamagna, C. Wiemer, G. Congedo, A. Lamperti, A. Molle, M. Fanciulli, F. Palma, F. Irrera, Structural and electrical properties of atomic layer deposited Al-doped ZrO₂ films and of the interface with TaN electrode, J Appl Phys. 112 (2012) 0–9. <https://doi.org/10.1063/1.4731746>.

- [190] N.E. Gorji, Oxygen incorporation into CdS/CdTe thin film solar cells, *Opt Quantum Electron.* 47 (2015) 2445–2453. <https://doi.org/10.1007/s11082-015-0122-5>.
- [191] L. Eftekhari, D. Raoufi, Crystallography characteristics of tetragonal nano-zirconia films under various oxygen partial pressure, *Surface Engineering.* 35 (2019) 618–626. <https://doi.org/10.1080/02670844.2018.1555913>.
- [192] A. v. Singh, M. Ferri, M. Tamplenizza, F. Borghi, G. Divitini, C. Ducati, C. Lenardi, C. Piazzoni, M. Merlini, A. Podestà, P. Milani, Bottom-up engineering of the surface roughness of nanostructured cubic zirconia to control cell adhesion, *Nanotechnology.* 23 (2012) 475101. <https://doi.org/10.1088/0957-4484/23/47/475101>.
- [193] M. Li, Z. Feng, P. Ying, Q. Xin, C. Li, Phase transformation in the surface region of zirconia and doped zirconia detected by UV Raman spectroscopy, *Physical Chemistry Chemical Physics.* 5 (2003) 5326–5332. <https://doi.org/10.1039/b310284j>.
- [194] G.G. Siu, M.J. Stokes, Y. Liu, Variation of fundamental and higher-order raman spectra of (formula presented) nanograins with annealing temperature, *Phys Rev B Condens Matter Mater Phys.* 59 (1999) 3173–3179. <https://doi.org/10.1103/PhysRevB.59.3173>.
- [195] J.-H. Lee, T. Mori, J.-G. Li, T. Ikegami, M. Komatsu, H. Haneda, Improvement of Grain-Boundary Conductivity of 8 mol % Yttria-Stabilized Zirconia by Precursor Scavenging of Siliceous Phase, *J Electrochem Soc.* 147 (2000) 2822. <https://doi.org/10.1149/1.1393612>.
- [196] W. Araki, T. Koshikawa, A. Yamaji, T. Adachi, Degradation mechanism of scandia-stabilised zirconia electrolytes: Discussion based on annealing effects on mechanical strength, ionic conductivity, and Raman spectrum, *Solid State Ion.* 180 (2009) 1484–1489. <https://doi.org/10.1016/J.SSI.2009.09.001>.
- [197] K. Apriany, I. Permadani, D.G. Syarif, S. Soepriyanto, F. Rahmawati, Electrical conductivity of zirconia and yttrium-doped zirconia from Indonesian local zircon as prospective material for fuel cells, *IOP Conf Ser Mater Sci Eng.* 107 (2016) 012023. <https://doi.org/10.1088/1757-899X/107/1/012023>.
- [198] M. Angeles-Rosas, M.A. Camacho-López, E. Ruiz-Trejo, Structure, conductivity and luminescence of 8 mol% scandia-doped zirconia prepared by sol-gel, *Solid State Ion.* 181 (2010) 1349–1354. <https://doi.org/10.1016/J.SSI.2010.07.032>.

- [199] Z. Lei, Q. Zhu, Low temperature processing of dense nanocrystalline scandia-doped zirconia (ScSZ) ceramics, *Solid State Ion.* 176 (2005) 2791–2797. <https://doi.org/10.1016/J.SSI.2005.09.005>.
- [200] M.A. Borik, S.I. Bredikhin, V.T. Bublik, A. V. Kulebyakin, I.E. Kuritsyna, E.E. Lomonova, P.O. Milovich, V.A. Myzina, V. V. Osiko, P.A. Ryabochkina, N.Y. Tabachkova, Structure and conductivity of yttria and scandia-doped zirconia crystals grown by skull melting, *Journal of the American Ceramic Society.* 100 (2017) 5536–5547. <https://doi.org/10.1111/JACE.15074>.
- [201] A. Zarkov, A. Stanulis, J. Sakaliuniene, S. Butkute, B. Abakeviciene, T. Salkus, S. Tautkus, A.F. Orliukas, S. Tamulevicius, A. Kareiva, On the synthesis of yttria-stabilized zirconia: a comparative study, *Undefined.* 76 (2015) 309–319. <https://doi.org/10.1007/S10971-015-3778-1>.
- [202] Y. Ota, M. Ikeda, S. Sakuragi, Y. Iwama, N. Sonoyama, S. Ikeda, A. Hirano, N. Imanishi, Y. Takeda, O. Yamamoto, Crystal Structure and Oxygen Ion Conductivity of Ga³⁺ Co-Doped Scandia-Stabilized Zirconia, (2010). <https://doi.org/10.1149/1.3489377>.
- [203] N. Sonoyama, S.G. Martin, U. Amador, N. Imanishi, M. Ikeda, N. Erfu, H. Tanimura, A. Hirano, Y. Takeda, O. Yamamoto, Crystal Structure and Electrical Properties of Magnesia Co-Doped Scandia Stabilized Zirconia, *J Electrochem Soc.* 162 (2015) F1397–F1401. <https://doi.org/10.1149/2.0231514JES>.

CURRICULUM VITAE

General information

Name, surname: **Nursultan Kainbayev**

Date and place of birth: **08 January 1993, Almaty, Kazakhstan**

Citizenship: **Kazakhstan (KZ)**

Languages: Kazakh (native), English (fluent), Russian (fluent), Turkish (good), Lithuanian (basic)

Education

Bachelor of Physics

2013–2015: Kaunas University of Technology, Faculty of Mathematics and Natural Sciences, Physics Department, Kaunas, Lithuania.

Applied Physics (612F30007)

Bachelor of Technics and Technologies

2011–2015: Al-Farabi Kazakh National University, Almaty, Kazakhstan.

Technical Physics (5B072300)

Master of Physics

2015–2017: Kaunas University of Technology, Faculty of Mathematics and Natural Sciences, Physics Department, Kaunas, Lithuania.

Applied Physics (621F30005)

PhD in Physics

2017–2022 Kaunas University of Technology, Faculty of Mathematics and Natural Sciences, Physics Department, Kaunas, Lithuania.

PhD Topic

Influence of alumina dopants on the microstructure and ionic conductivity of scandia stabilized zirconium oxide thin films.

Research and publications

ORCID iD: <https://orcid.org/0000-0001-7745-9782>

Scopus author ID: 57207885079

LIST OF PUBLICATIONS AND SCIENTIFIC CONFERENCES

Scientific papers directly related to the thesis (peer-reviewed and indexed in Clarivate Analytics Wos)

1. Sriubas, Mantas; Virbukas, Darius; **Kainbayev, Nursultan**; Bockute, Kristina; Laukaitis, Giedrius. Structural and electrochemical properties of scandia alumina stabilized zirconia thin films // *Coatings*. Basel: MDPI. ISSN 2079-6412. 2021, vol. 11, iss. 7, art. no. 800, p. 1-15.
2. **Kainbayev, Nursultan**; Sriubas, Mantas; Bockute, Kristina; Virbukas, Darius; Laukaitis, Giedrius. E-beam deposition of scandia-stabilized zirconia (ScSZ) thin films co-doped with Al // *Coatings*. Basel: MDPI. ISSN 2079-6412. 2020, vol. 10, iss. 9, art. no. 870, p. 1-10.
3. Sriubas, Mantas; **Kainbayev, Nursultan**; Virbukas, Darius; Bočkutė, Kristina; Rutkūnienė, Živilė; Laukaitis, Giedrius. Structure and conductivity studies of scandia and alumina doped zirconia thin films // *Coatings*. Basel: MDPI. ISSN 2079-6412. 2019, vol. 9, iss. 5, art. no. 317, p. 1-10.

Other scientific papers indirectly related to the thesis (peer-reviewed and indexed in Clarivate Analytics Wos)

1. **Kainbayev, Nursultan**; Sriubas, Mantas; Virbukas, Darius; Rutkuniene, Zivile; Bockute, Kristina; Bolegenova, Saltanat; Laukaitis, Giedrius. Raman study of nanocrystalline-doped ceria oxide thin films // *Coatings*. Basel: MDPI. ISSN 2079-6412. 2020, vol. 10, iss. 5, art. no. 432, p. 1-12.
2. Sriubas, Mantas; Bockute, Kristina; **Kainbayev, Nursultan**; Laukaitis, Giedrius. Influence of the initial powder's specific surface area on the properties of Sm-doped ceria thin films // *Crystals*. Basel: MDPI. ISSN 2073-4352. 2018, vol. 8, iss. 12, art. no. 443, p. 1-12.

Other scientific papers (conference proceedings)

1. **Kainbayev, Nursultan**; Sriubas, Mantas; Rutkuniene, Zivile; Bockute, Kristina; Bolegenova, Saltanat; Laukaitis, Giedrius. Formation and investigation of doped cerium oxide thin films formed using e-beam deposition technique / Recent advances in technology research and education: proceedings of the 17th international conference on global research and education Inter-Academia – 2018 / editor: Giedrius Laukaitis. Cham: Springer Nature, 2019. ISBN 9783319998336. p. 28-34.

Conferences directly related to the thesis

1. Virbukas, Darius; Sriubas, Mantas; **Kainbayev, Nursultan**; Bockute, Kristina; Laukaitis, Giedrius. Properties of Al and Ce co-doped scandia stabilized zirconia/14th international symposium on systems with fast ionic transport (ISSFIT14), 7–9 July 2021, Ljubljana.
2. **Kainbayev, Nursultan**; Sriubas, Mantas; Bockute, Kristina; Rutkuniene, Zivile; Laukaitis, Giedrius. Raman study of (Sc₂O₃)_{0.10} (ZrO₂)_{0.90} thin

- films/18th international conference on thin films & 18th joint vacuum conference, ICTF-JVC 2020, 22–26 November 2020, Budapest, Hungary.
3. **Kainbayev, Nursultan;** Sriubas, Mantas; Bockute, Kristina; Virbukas, Darius; Laukaitis, Giedrius. Influence of technological parameters on crystal phase stability of ceramic thin films/Advanced materials and technologies: book of abstracts of 22nd international conference - school, 24-28 August 2020, Palanga, Lithuania.
 4. **Kainbayev, Nursultan;** Sriubas, Mantas; Bockute, Kristina; Rutkuniene, Zivile; Laukaitis, Giedrius. Raman study of $(\text{Sc}_2\text{O}_3)_{0.10}(\text{Al}_2\text{O}_3)_{0.01}(\text{ZrO}_2)_{0.89}$ thin films/43-ioji Lietuvos nacionalinė fizikos konferencija, 2019 m. spalio 3-5 d., Kaunas.
 5. **Kainbayev, Nursultan.;** Bolegenova, S.; Laukaitis, Giedrius. Formation and investigation of doped cerium oxide thin films formed using e-beam deposition technique/Inter-Academia 2018: 17th international conference on global research and education, September 24-27, 2018 Kaunas, Lithuania.
 6. Sriubas, Mantas; **Kainbayev, Nursultan;** Bočkutė, Kristina; Rutkūnienė, Živilė; Laukaitis, Giedrius. Raman study of $(\text{Sc}_2\text{O}_3)_{0.10}(\text{Al}_2\text{O}_3)_{0.01}(\text{ZrO}_2)_{0.89}$ thin films // 13th international symposium on systems with fast ionic transport (ISSFIT-13), July 3-7, 2018, Minsk, Belarus.
 7. Sriubas, Mantas; **Kainbayev, Nursultan;** Laukaitis, Giedrius. Mikrostruktūros įtaka plonų SDC sluoksnių elektrinėms ir optinėms savybėms = Influence of microstructure on electrical and optical properties of SDC thin films//42-oji Lietuvos nacionalinė fizikos konferencija, 2017 m. spalio 4-6 d., Vilnius.
 8. **Kainbayev, Nursultan;** Sriubas, Mantas; Rutkūnienė, Živilė; Bočkutė, Kristina; Laukaitis, Giedrius. Plonasluoksnių cerio oksido dangų formavimas ir tyrimas Ramano spektrometrija = Formation and Raman study of doped cerium oxide thin films/42-oji Lietuvos nacionalinė fizikos konferencija, 2017 m. spalio 4-6 d., Vilnius.
 9. **Kainbayev, Nursultan;** Sriubas, Mantas; Rutkuniene, Zivile; Bockute, Kristina; Bolegenova, Saltanat A.; Laukaitis, Giedrius. Raman study of nanocrystalline doped ceria oxide thin films//Solid state ionics: 21st international conference, June 18-23., 2017, Padua, Italy: program guide and abstracts.

Appendix 1.

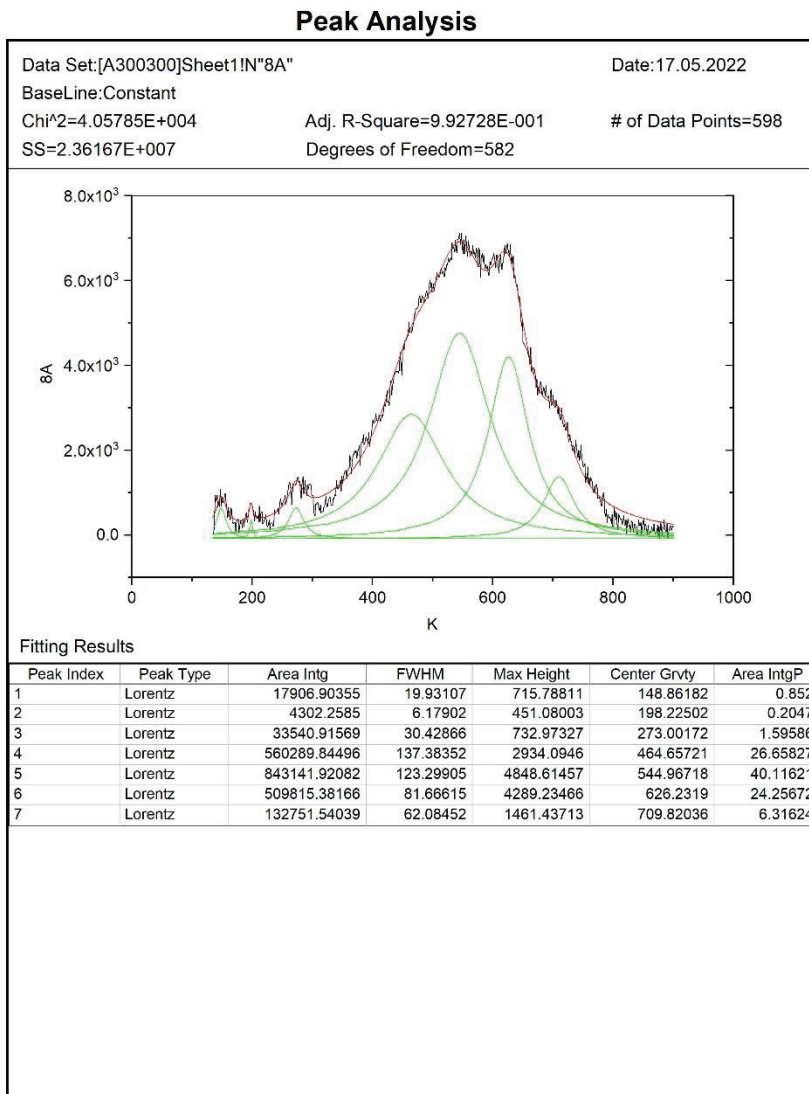


Fig. 1. Raman spectra fitting of ScAlSZ thin films deposited on alloy 600 substrates using 300 °C substrate temperature and 0.8 nm/s deposition rate

Peak Analysis

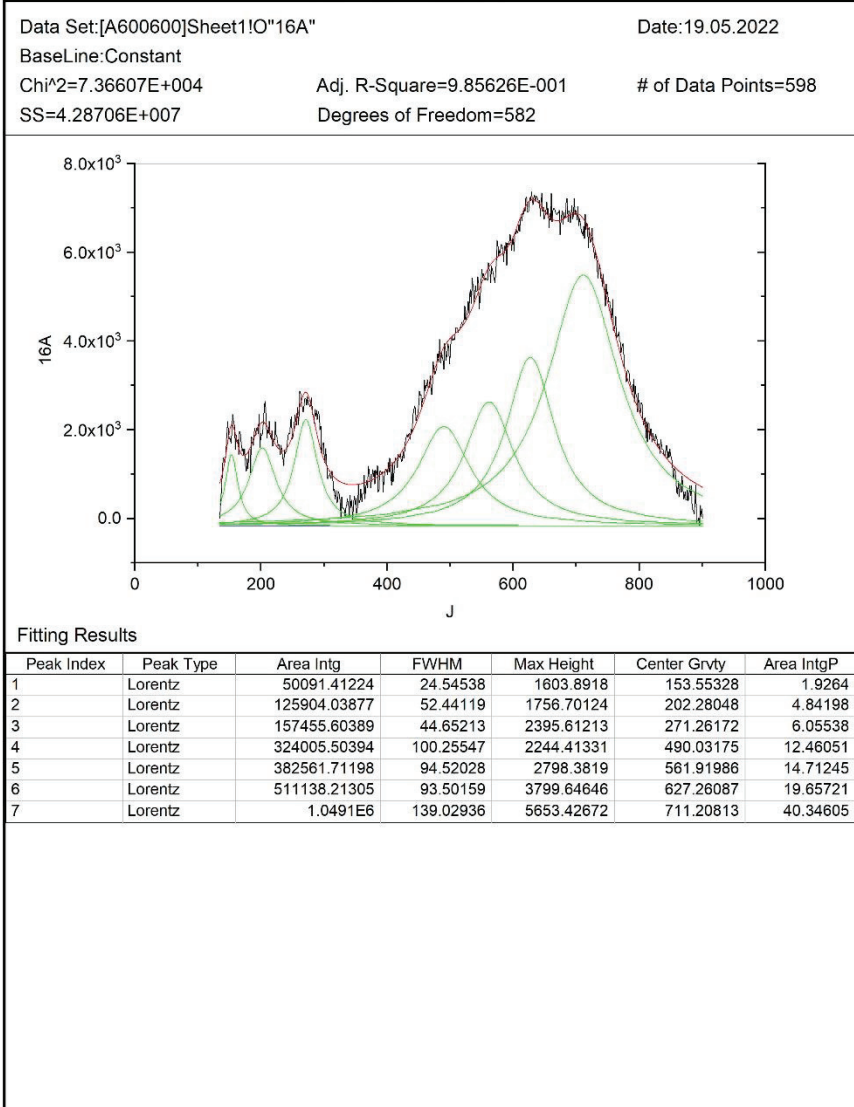


Fig. 2. Raman spectra fitting of ScAlSZ thin films deposited on alloy 600 substrates using 300 °C substrate temperature and 0.8 nm/s deposition rate

Peak Analysis

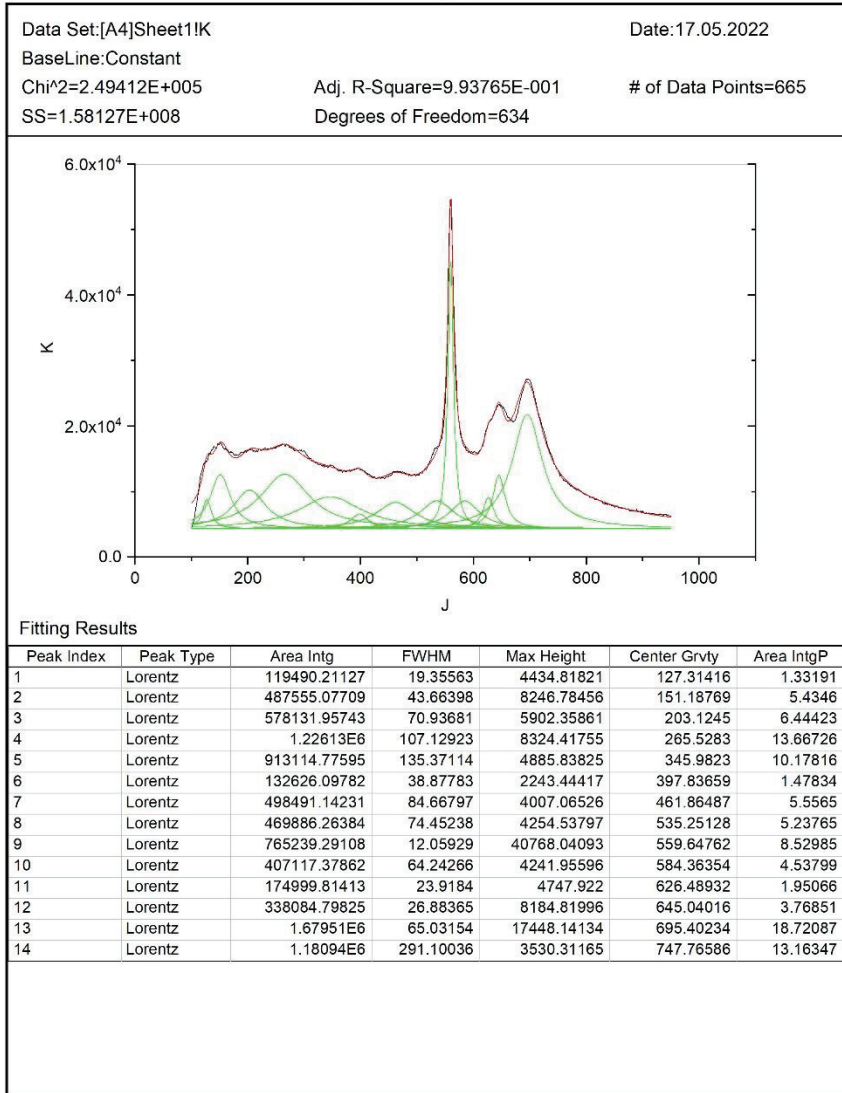


Fig. 3. Raman spectra fitting of ScAlSZ thin ceramic films deposited on alloy 600 at 450 °C substrate temperature, the annealing process (30–900 °C), containing 15.9 at.% of aluminum

UDK 539.216+544.654+621.352.6](043.3)

SL 344. 2022-11-07, 19,5 leidyb. apsk. I. Tiražas 14 egz. Užsakymas 231.
Išleido Kauno technologijos universitetas, K. Donelaičio g. 73, 44249 Kaunas
Spausdino leidyklos „Technologija“ spaustuvė, Studentų g. 54, 51424 Kaunas

